Doctoral theses at NTNU, 2020:368

John Fredrick Berntsen

Testing and modelling of multi-material joints

ISBN 978-82-326-5082-8 (printed ver.)
ISBN 978-82-326-5083-5 (electronic ver.)
ISSN 1503-8181

NTNU
Norwegian University of
Science and Technology

NTNU
Norwegian University of Science and Technology
Thesis for the Degree of
Philosophiae Doctor
Faculty of Engineering
Department of Structural Engineering

Doctoral theses at NTNU, 2020:368

NTNU
Norwegian University of
Science and Technology

John Fredrick Berntsen

Testing and modelling of multi-material joints

Thesis for the Degree of Philosophiae Doctor

Trondheim, December 2020

Norwegian University of Science and Technology
Faculty of Engineering
Department of Structural Engineering

NTNU
Norwegian University of
Science and Technology

NTNU
Norwegian University of Science and Technology

Thesis for the Degree of Philosophiae Doctor

Faculty of Engineering
Department of Structural Engineering

ISBN 978-82-326-5082-8 (printed ver.)
ISBN 978-82-326-5083-5 (electronic ver.)
ISSN 1503-8181

Doctoral theses at NTNU, 2020:368

Printed by NTNU Grafisk senter

Preface

This thesis is submitted to the Norwegian University of Science and Technology (NTNU) as part of the academic degree Philosophiae Doctor (PhD). The doctoral work has been carried out at the Department of Structural Engineering within the Structural Joints program of the Centre for Advanced Structural Analysis (CASA) in Trondheim, Norway. Supervision was provided by Associate Professor David Morin (NTNU), Professor Arild Holm Clausen (NTNU) and Professor Magnus Langseth (NTNU). Financial support of this thesis is from CASA, Centre for Research-based Innovation (SFI) at NTNU through the Norwegian Research Council with project number 237885. This thesis reports extensive experimental and numerical work. Minor parts of it have previously been reported by other researchers working on related projects. These contributions are clearly addressed in the relevant sections of the thesis.

Abstract

The trend towards lightweight design in the automotive industry has led to increasingly optimal and complex structures, where fundamentally different materials are combined. An effective way of combining these would be to use adhesives as they are compatible with a large range of materials unlike traditional joining methods such as spot-welds. Adhesives exhibit beneficial properties including increased stiffness and improved energy absorption at the structure level. Further, adhesives are beneficial with respect to noise and vibration in addition to acting as a corrosion barrier. Therefore, adhesives have been increasingly used in the automotive industry. This makes adhesives a relevant topic to study for this thesis as there is generally a lack of understanding with respect to both the behaviour and the modelling of adhesives.

This thesis is split into two parts, one for each of the two selected adhesives for this study. The first part treats a semi-structural two-component polyurethane adhesive that has not been thoroughly studied before. In order to investigate the behaviour of the adhesive it was performed several material tests on bulk adhesive test specimens. For a selection of these tests, field data was obtained for both deformations and temperature. Scanning electron microscopy was also used to look at the failure surface of one of the specimens. Three configurations of single lap joints, using two types of fibre reinforce polymers as adherents, were tested to see the behaviour of the adhesive in a joint setting. To model the adhesive, the Bergström-Boyce model was chosen as it proved to be able to capture the key phenomena governing the response of the adhesive. In addition, a modification of the model was implemented as a user subroutine in Abaqus to better capture the viscous response of the adhesive. Both models were calibrated based on the material tests and validated against the notched tension tests.

The second part of the thesis studies a structural toughened epoxy adhesive. Bulk adhesive material tests, bonded cross tests, hybrid single lap joint tests, hybrid peel tests and hybrid component tests were performed as a part of a related thesis. Additionally, bonded component tests were tested as a part of this thesis. Data from the material tests were used to calibrate a previously implemented meso-scale polymer model for the adhesive. This model was then validated against the bonded cross tests, hybrid benchmark tests and the bonded component tests.

A partial virtual laboratory calibration procedure was developed in order to calibrate macro-scale material models for the adhesive. The method was based on simulating

virtual benchmark tests using the meso-scale polymer model, then using the response of those simulations as target curves for reverse engineering of the macro-scale parameters. Three macro-scale models were calibrated using this approach including a baseline model MAT_240, a modified version of the baseline model and a Gurson-based cohesive zone model (GCZM). Additionally, the GCZM had to be implemented as a user subroutine in LS-DYNA. All three models were validated against the bonded component tests. There were made some adjustments to the calibration procedure, which led to new calibrations that were further validated against the hybrid benchmark tests and hybrid component tests. Finally, a study on the influence of the adherent properties on the calibrated material parameters of the macro-scale models were performed using the partial virtual calibration approach.

In conclusion, there was found a fundamental difference in the behaviour between the two adhesives that were studied in this thesis, which would imply significantly different modelling. The partial virtual laboratory calibration procedure was seen to give comparable results to what is obtained when using traditional calibration methods with physical experiments. Finally, the bending stiffness of the adherents were seen to have a larger influence on the calibrated macro-scale properties of the adhesive than the material of the adherents. However, both were seen to have a minor influence overall based on the cases studied in this thesis.

Acknowledgements

I would like to acknowledge and thank my supervisors for their support and guidance throughout the challenging journey this thesis has been. Associate Professor David Morin has been a constant source of good ideas and interesting discussions. Professor Arild Holm Clausen has provided his vast experimental knowledge as well as his attention to details that made a large difference. Professor Magnus Langseth has provided a clear perspective throughout the thesis based on his limitless experience.

My colleagues at the Department of Structural Engineering, especially at the SIMLab group, have been essential for my growth as an academic and for making these years memorable. In particular, I would like to thank: Bjørn Håkon Frodal, for our countless and long discussions regarding both academic topics and other topics of high importance. Joakim Johnsen, for sharing some of his vast knowledge with me and for showing me the way. Karoline Osnes, for all the fun times we have had both at the office and outside. Miguel Costas, for his inspiring attitude. Susanne Thomesen, for the cakes, obviously. Jianbin Xu, for his equally ridiculous office hours and good humour. Peter Karlsaune, for all your support throughout the years. Petter Henrik Holmström, for the numerous tips and tricks during my thesis. Trond Auestad and Tore Wisth, for their support with the experimental part of the thesis. Finally, a very special thanks to Matthias Reil for sharing my deep passion for structural adhesives and inspiring me to wear leather pants.

I would also like to thank my friends and family for being there for me. Especially my mom and dad, who have supported me through good times and especially during the tough times.

Contents

Part I.

Description of thesis

1. Introduction

1.1. Background and motivation

The research problem addressed in this thesis originates from the automotive industry, where the trend towards lightweight design has introduced new challenges. There are several key factors driving this trend including the concern for environmental impact, fuel economy, cost savings and regulations such as the Corporate Average Fuel Economy (CAFE). Recently, the emergence of battery electric vehicles has further emphasized this trend, as the heavy battery pack adds new requirements. Furthermore, efficiency is essential for the viability of electric vehicles for the general market. In order to achieve these goals, it requires significant changes to vehicle design as well as optimization. An effective approach for solving this problem is to use optimal materials for each part. Figure 1.1 shows that this is reflected in modern car bodies, where a range of materials is applied in the load-carrying structures. A consequence, however, is that materials that are fundamentally different in nature such as metals, polymers and composites have to be connected.

Thus, a result of this use of different materials is that it complicates the joining process. Traditionally, spot-welding has been the dominant joining method in the automotive industry. However, it requires process changes when joining different metals, and it is not feasible for joining of polymers and composites. Alternative joining methods, such as flow drill screws (FDS), self-piercing rivets (SPR) and adhesive bonding, have seen increased usage as a result of these trends. Adhesives are especially suitable for joining different materials as they can serve as a flexible bridge between two fundamentally different materials. Furthermore, adhesives can act as a corrosion barrier. Additionally, adhesively bonded joints could increase the overall stiffness of a component compared to using just mechanical fasteners in the joints. Fatigue life is also increased due to reduction of stress concentrations. It was seen in a study by Morin [1] that using adhesives in combination with mechanical fasteners could yield increased energy absorption or a reduction in number of mechanical fasteners.

It is therefore evident that adhesive bonding is suitable for joining multi-material joints. However, in order to achieve the potential described above, it is necessary to have a good understanding of the mechanical behaviour of adhesive joints subjected to a range of load-cases. It is also necessary to have numerical tools available that are sufficiently accurate

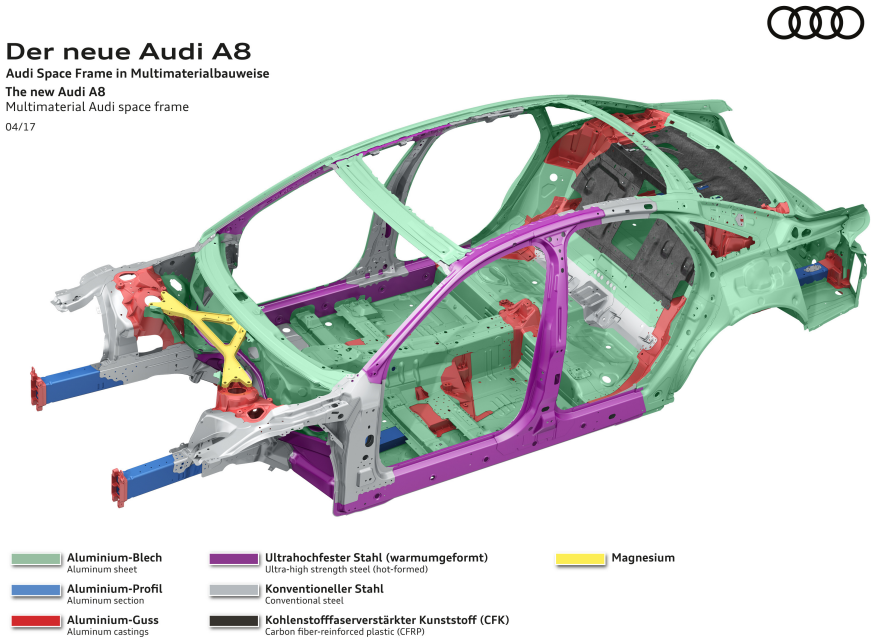

Figure 1.1.: Multi-material space frame of the Audi A8 [2].

and efficient for large-scale simulations. Validation of these numerical tools is essential for them to be trustworthy and therefore applicable. According to Martinsen et al. [3], there is currently a lack in both understanding of the behaviour of these types of joints and how to model them properly. In order to address these issues in this thesis, it has been performed experiments to gain a better understanding of the behaviour of this type of joints. They were then studied numerically, and new numerical methods were developed where it was deemed necessary.

1.2. Previous work

This section will give an overview of the literature published within the relevant fields of research. Experimental techniques to characterize materials, joints and components will be presented, as well as numerical methods for simulating these experiments. Details regarding specific experimental methods or numerical tools used in this work will not be covered in this chapter, as it is only the intention to provide context for the thesis.

1.2.1. Experimental techniques: Material characterization

Adhesives are polymers that come as one or two components in the form of viscous fluids. These fluids are then distributed at the surfaces to be bonded, and then the adhesive reticulates. Depending on the adhesive, the reticulation process can be driven by heat input, chemical reaction between two components, cooling, light, moisture and oxygen. During this process, the adhesive solidifies such that the substrates are bonded together. There are several phenomena that cause adhesion between the adhesive and the substrates including diffusion, chemical bonds and mechanical interlocking. In general, an adequate adhesive bonded to a properly treated surface should not experience adhesion failure [4]. Furthermore, adhesion failure typically causes significant scatter in test results, and it is therefore considered out of scope for this thesis.

In terms of mechanical properties, the adhesives studied in this thesis will be characterized in two different categories, namely structural and semi-structural adhesives. The key physical property differentiating the two types is the relation between the glass transition temperature of the adhesive and the operational temperature window. Semi-structural adhesives operate at temperatures above its glass transition temperature, giving them rubber-like properties such as low strength, low stiffness and high ductility. However, these adhesives are more versatile than structural adhesives, as they can be used as sealants as well as bond to a wider range of materials. The 2-component polyurethane adhesive BETAFORCE 2816L, which is studied in this thesis, is a semi-structural adhesive that is designed to bond to polymers, reinforced polymers and metals. It reticulates chemically through the mixing of the two components such that heat input is not needed to solidify. Therefore, it is suitable for joining materials that are sensitive to high temperatures.

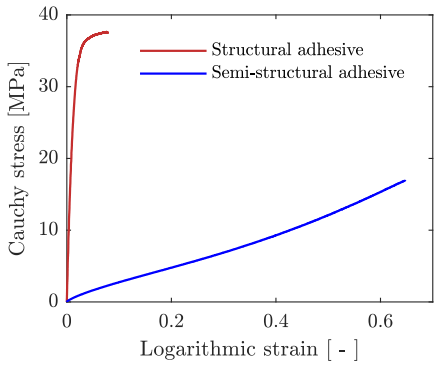

Figure 1.2.: Stress-strain curves of the structural adhesive SikaPower 498 and the semi-structural adhesive BETAFORCE 2816L.

In contrast, structural adhesives operate below its glass transition temperature, giving them high stiffness and strength at the cost of ductility. A comparison between the stress-strain

curves of a structural and a semi-structural adhesive is shown in Figure 1.2. The high strength and stiffness of structural adhesives make them excellent for increasing the overall stiffness of a car body as well as increasing energy absorption. In this thesis, the crash-stable single component epoxy adhesive SikaPower 498 was studied. It contains particles intended to arrest cracks propagating when exposed to extreme load conditions such as crash situations. However, its high curing temperature makes it unsuitable for joining polymers.

Structural adhesives have been investigated previously in literature, where the mechanical behaviour has been described. Dufour et al. [5] studied and modelled the behaviour of a structural epoxy adhesive. It was found that the elastic domain is rate sensitive, leading to viscoelastic behaviour. However, the elastic strains are still small compared to the plastic deformations due to the comparatively high elastic modulus. In the plastic domain, these adhesives exhibit pressure sensitivity indicated by the difference in yield stress between compression and tension. Unlike what is commonly assumed for metals, these adhesives also exhibit non-isochoric plastic flow [6]. Furthermore, it is evident that the plastic dilatation is accelerating with further deformation indicating ductile damage mechanisms with void growth and nucleation according to Morin et al. [6]. Strain-rate sensitivity in the plastic region is also an important phenomena for these types of adhesive as observed by both Morin et al. [6] and Goglio et al. [7]. It was reported an increase of initial yield stress with over a factor of 2 when going from a strain-rate of $5 \cdot 10^{-2}\,\mathrm{s}^{-1}$ to $400\,\mathrm{s}^{-1}$ for the epoxy adhesive studied by Morin et al. [6]. High strain-rates could also lead to adiabatic heating in the material [8]. Failure strain for an epoxy adhesive was seen to be dependent on both stress triaxiality and strain-rate, as reported by Morin et al. [9].

Looking at semi-structural adhesives, the most significant difference is the lack of plasticity as reported by Duncan and Dean [10]. Instead, these adhesives exhibit rubber-like behaviour, which includes large elastic deformations, incompressibility and viscoelasticity. It should be noted that going to high-rate loading or reducing temperature could lead to very different behaviour due to the glass transition, as observed in the experiments performed by Jia et al. [11].

In order to measure the previously mentioned phenomena, it is necessary to use advanced experimental techniques as the material could exhibit plastic dilatation, localization and temperature changes. To capture the temperature changes in a specimen, it is seen in the work by Johnsen et al. [8] that a thermal camera is applicable. Digital image correlation (DIC) is a tool that has been used by several authors ([5],[9]) with success in order to capture the previously mentioned behaviour. DIC also enables more complex post-processing methods such as the SEÈ method [12] for identifying rate sensitivity and the virtual fields method ([13],[14]) for parameter identification. Finally, it is also possible to use numerical methods in combination with experiments to obtain information that is unobtainable with only experiments. An example of that is seen in the work by Morin et al. [9], where the stress triaxiality in the notched region of a specimen was estimated using numerical simulations.

The most common material test is the uniaxial tension test, which comes in many shapes and sizes as long as there is a constant uniaxial stress state in the gage section. This specimen is typically used to calibrate plasticity parameters, strain-rate sensitivity and one point for failure. Pressure sensitivity of the material is usually determined through one or more additional tests in uniaxial compression, which are carried out on cylindrical compression test specimens. Compression tests could be applied at all strain-rates, but they have a significant drawback that the results are dependent on the friction between the specimen and the test machine. Notched tension test specimens are primarily used to investigate failure in the material as the location of failure is known. The notch alters the stress and strain fields of the specimen compared to a uniaxial specimen, such that there is an increased stress triaxiality in the notched region. This could be used to evaluate the pressure dependency of a yield surface or provide information on the stress triaxiality dependency of failure for the material.

A less common type of test is the shear tests. There are many versions of shear test specimens depending on material, strain-rate and available equipment. An Iosipescu shear test was performed by Morin et al. [6], while García et al. [15] used a torsion test to determine the shear properties of the material. If additional information is needed to calibrate a model, a biaxial test could be performed. Sasso et al. [16] performed a bulge test in order to investigate the behaviour of the material subjected to biaxial deformation.

Material tests are typically performed on servo-hydraulic test machines. These machines are used for low velocity testing, from quasi-static to strain-rates of about $1\,\mathrm{s}^{-1}$, as higher velocity would introduce vibrations in the test machine. In order to run tests at higher strain-rates, split Hopkinson bar [17] techniques are commonly used. These techniques rely on stress waves travelling through the specimens, enabling testing at strain-rates over $10^3\,\mathrm{s}^{-1}$. Most of these bars are made of steel as they yield uniaxial stress waves, making it easy to post-process. However, when testing softer materials like structural adhesives and especially semi-structural adhesives, there is a large impedance difference between the bars and the specimens. This difference could cause large signal to noise ratios making the test data inaccurate. Remedies for this issue, such as pulse shaping and alternative materials for the bars, was studied by several authors ([18],[19]). Successful characterization of structural adhesives at high strain-rates were performed by Morin et al. [6] and Goglio et al. [7]. For intermediary strain-rates, it was suggested by Tarigopula et al. [20] to use a hydro-pneumatic machine, achieving strain-rates between $1\,\mathrm{s}^{-1}$ and $100\,\mathrm{s}^{-1}$.

1.2.2. Experimental techniques: Joint characterization

The most common joint assemblies are single lap joints (SLJ) and double lap joints (DLJ), and the argument is that they are the simplest ones. While the setup is simple in terms of geometry and production, the behaviour is non-trivial. For a bonded lap joint, the shear stress distribution is highly non-linear, and there are significant peel stresses that reaches

peak values at the ends of the overlap region [21]. These edge effects were seen to be strongly dependent on the edge geometry, and according to Hildebrand [22] have a large impact on the peak force of the joint. Furthermore, there are significant rotations of the substrates caused by the eccentricities of the loading. A range of configurations of multi-material SLJ were tested by the authors Nassar and Sakai [23], Goudarzi and Khedmati [24] and Ozel et al. [25]. The authors observed significant scatter in the tests where adhesion failure was critical. A key observation in terms of the effects of multi-material joining is that the peak force is dependent on the bending stiffness of the substrates [25], as it changes the stress field in the adhesive layer. Kelly [26] tested hybrid SLJ with bolts and two types of adhesives. It was found that changing from a structural adhesive to a semi-structural adhesive significantly altered how the joint carried the load.

Peel tests are a common test setup for evaluation of a primarily macroscopic tension loading, which would generally be peeling for adhesive layers. These tests can also be used as fracture mechanics tests to determine mode I behaviour. A problem with the typical T-peel test is that the substrates have to be bent, which is normally unfeasible for polymer substrates. This issue could be circumvented by using a modified configuration of the peel test, such as the one proposed by Lambiase [27].

Butt joints represent a different test setup typically used to test macroscopic tension in adhesively bonded joints. While the macroscopic loading mode is tension, the local stress field is strongly non-homogeneous. There is often a strong edge effect for these joints, leading to early failure. Furthermore, this configuration is highly constrained, leading to large stress triaxiality depending on the geometry and material of the specimen. It was shown by Zhao and Xu [28] that there is also a significant size effect to these joints. Spaggiari et al. [29] designed a tubular butt joint with grooves, in order to alleviate the issues with the edge effects and saw good results. Although these joints are typically between metal adherents, it is possible to bond a different material to one or both faces of the metal adherents to make a multi-material joint [21].

The general idea behind the Arcan type tests, originally presented by Arcan [31], is to use a joint configuration that can be tested in different macroscopic loadings. Figure 1.3 shows a typical Arcan type fixture with the two plates that allows for testing along different axes. Depending on the setup, this would allow for testing in macroscopic tension to macroscopic shear and even combined compression and shear. Stamoulis et al. [32] and Cognard et al. [33] tested bonded butt joints in an Arcan style test setup. Cognard et al. [33] found that adding beaks to the butt joints significantly reduced the edge effects for these tests. A multi-material bonded joint was tested in different orientations in an Arcan type setup by Jiang et al. [34].

A versatile joint configuration for this purpose is the cross test specimen. The plates of the specimens could easily be exchanged for different materials like CFRP plates or polymer plates, making it easy to test multi-material configurations. Furthermore, the connector itself can also be adhesive bonding, SPR, FDS and spot-welds. However, it has a significant

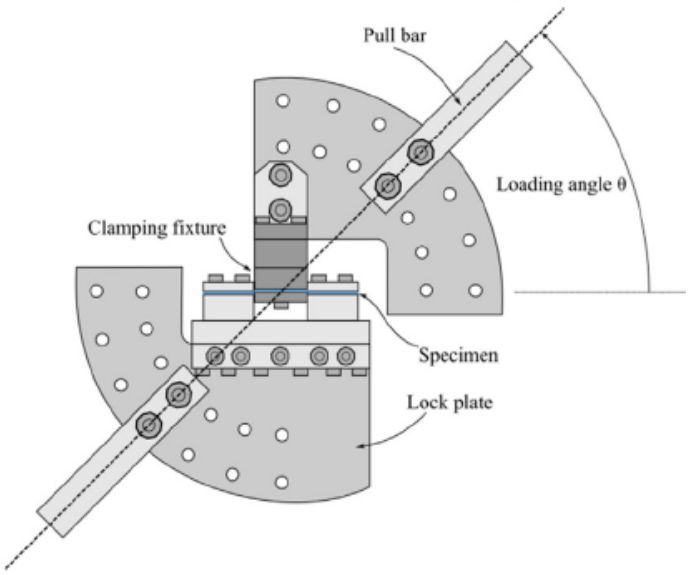

Figure 1.3.: Arcan type fixture [30] .

drawback, as the fasteners typically block vision of the joint itself, making it difficult to obtain detailed information regarding local displacements and deformation. These cross specimens were tested by Sønstabø et al. [30] in a traditional Arcan test setup, and in a cross test rig [35]. The cross test rig is a constrained Arcan type rig, where the displacements are accurately prescribed.

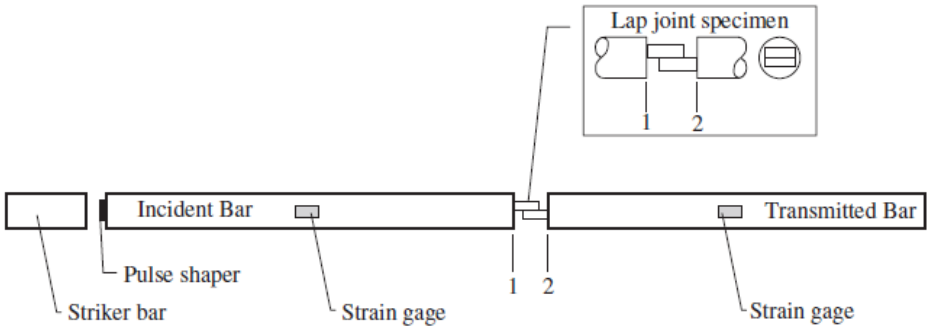

Figure 1.4.: Split Hopkinson pressure bar (SHPB) test setup for testing of SLJ [36].

One of the most common devices for dynamic testing is the split Hopkinson bars of different types, as it is possible to achieve high velocities in a controlled manner. These setups are primarily used for material testing, as it is difficult to maintain equilibrium for larger test

specimens. Therefore, the joints tested are typically very simple and have compact designs such as the one displayed in Figure 1.4. Compact lap joint test specimens have been tested in split Hopkinson pressure bars (SHPB) by multiple authors ([21],[36],[37],[38]). Multi-axial testing in a split Hopkinson tension bar (SHTB) was performed by Brefort [39] by using butt joints cut at different angles. Multi-axial testing was also achieved in a SHPB by using the DODECA specimens designed by Janin et al. [40]. Shear-dominated behaviour was investigated by Yokoyama and Shimizu [41] using a SHPB to test pin and collar joint specimens. Using a split Hopkinson torsion bar, Raykhere et al. [42] tested multi-material tubular butt joints. Inspired by the aerospace industry, they tested aluminium-to-aluminium joints as well as aluminium to glass fibre reinforced polymer (GFRP) joints with 4 different adhesives. Sato and Ikegami [43] tested tubular butt joints in combined tension and shear, using a unique split Hopkinson bar setup that was preloaded in both tension and torsion.

The Instron VHS testing machine allows for controlled high velocity testing, while being suitable for much larger specimens and fixtures than what is possible to test in a split Hopkinson bar setup. This machine uses a clamping system to ensure almost constant velocity during the tests, reaching loading velocities up to 25 $\mathrm{m/s}$. Dufour et al. [5] used this machine to test adhesively bonded butt joints in a modified Arcan fixture. This modified Arcan fixture was designed in order to reduce inertia effects, making it much more suitable for dynamic testing than a typical Arcan fixture. Using the same Instron VHS machine, Dufour [44] performed dynamic peel tests on bonded specimens consisting of an omega profile and a flat plate. A considerably less controlled approach to dynamic testing of joints is impact testing. Impact tests typically exhibit significant noise and variable velocity during the test duration. Goglio and Rossetto [45] instrumented a classical Charpy test machine with a single lap joint specimen. The tests exhibited significant amount of scatter, as expected with these type of tests.

Fracture mechanics is based on the concept of determining the energy required to propagate a crack through a material. In the context of joints, fracture mechanics is typically used to determine the fracture mechanics properties of the adhesive layer. There are three basic failure modes in fracture mechanics, mode I is linked to tension or peel deformation, while mode II and III are shear modes. Typically, mode III is ignored, such that only mode I and II as well as a combination of those two are considered. A fundamental problem with fracture mechanics tests is that two different tests intended to determine the same energy release rate could give different results [46]. There are many fracture mechanics tests available and used by a large number of authors, such as the ones performed by Hasegawa et al. [47] on a polyurethane adhesive and Fernandes et al. [48] on an epoxy adhesive. Dynamic fracture mechanics testing have also been performed by several authors, but it is still an active field of research as it is significantly more complicated than quasi-static testing. Impact loading has been used by Simon et al. [49] and Sun et al. [50] to perform dynamic fracture mechanics tests. However, both authors observed significant noise in their results as expected with impact tests. A high velocity servo-hydraulic machine was used by Blackman et al. [51] and May et al. [38] with more success. Oshima et al. [52] used a SHPB to induce a controlled high velocity load to test both mode I and mixed mode

fracture.

1.2.3. Experimental techniques: Validation

Validation is an important step in the process of evaluating new modelling techniques, as it provides trust in the methods such that they could be utilized in other applications. Models are validated by performing experiments that require a given model to perform outside of the domain used for calibration. This can be done at different scales and with multiple stages. Sønstabø et al. [53] used a multi-stage validation approach to validate macroscopic models calibrated based on cross tests. The models were first validated against benchmark tests such as lap shear tests and peel tests, which subjected the model to primarily one type of macroscopic loading each. Further, the models were validated against component tests, which subjected the connector models to a large range of loading modes. This section will focus on experiments that can be used for validation at a component level.

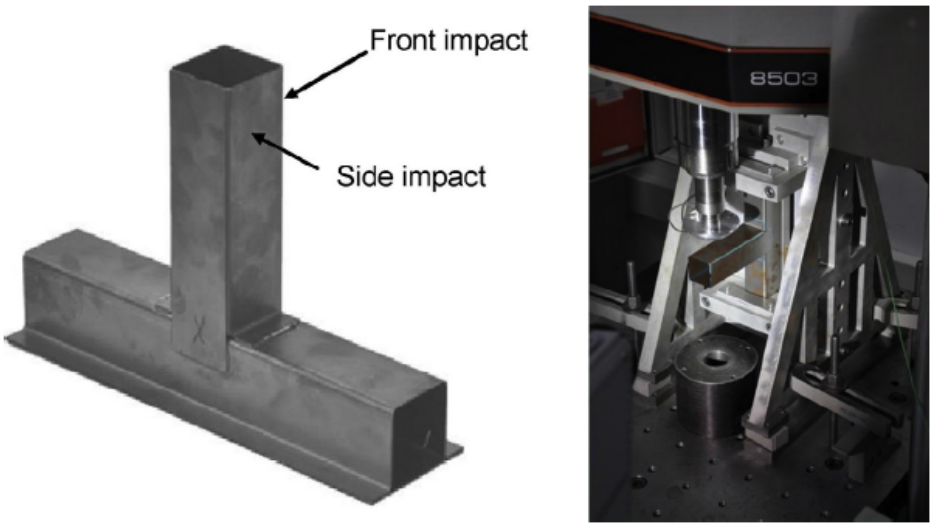

Figure 1.5.: Bonded T-component test [38].

A common component test used for validation cases is the T-component test. There are many configurations made with different joining techniques such as adhesive bonding, SPR and FDS. It can also be tested in different load-cases both quasi-static and dynamic. Clarke et al. [54] studied a T-component where the two profiles were bonded together on 3 flanges. One flange was primarily dominated by shear loading while the other two were dominated by peel loading. The components were tested in 3 configurations with just one type of flanges bonded at a time and all 3 flanges bonded. There was observed very large scatter in the case with only peel flanges bonded, which indicated problems related to production of

the specimens. Figure 1.5 shows a similar type of T-component that was tested by May et al. [38]. This component was tested for front and side impact in a servo-hydraulic machine with loading velocities up to 5 m/s. Consistent results were found for all configurations of this setup. Sønstabø et al. [35] tested and simulated T-component tests joined with flow drill screw (FDS). The simulations revealed that loading mode for each FDS varied significantly, indicating that this type of component test is a good validation case.

Another component used in literature for validation purposes is the closed-hat-section component, where a flat plate is joined to a hat profile. The simplicity of the component makes it easily expandable to multi-material joining and arbitrary joining techniques. Morin et al. [55] tested 3 variations of this component with adhesive bonding, SPR and a hybrid of the two. The axial crushing of these components were then used to validate a macroscopic model for adhesive bonding and investigate the potential in adhesive bonding. A similar setup was used by Sønstabø et al. [30], where FDS were used to join the 2 profiles. It was observed a range of failure modes for the FDS, indicating that this component is suitable for validation purposes.

Carlberger and Stigh [56] performed dynamic 3-point bending tests on H-beam specimens consisting of two closed-hat-sections bolted together. These closed-hat-sections consisted of an aluminium hat-section and a steel plate which were joined with bolts, adhesives or a combination of them. The specimens were designed to fail in the joints, which were loaded in both peel and shear, providing a suitable validation case. A multi-material product level test was used to validate a modelling strategy for a semi-structural adhesive by Lubowiecka et al. [57]. The product consisted of a polyurethane fender bonded to an aluminium plate. However, products are typically used as the last stage in the validation process as it may be difficult to correlate any issues to the model being validated.

1.2.4. Numerical methods: Overview

This section intends to give an overview of the three modelling length scales relevant for this thesis. Models of the different relevant length-scales are presented in Figure 1.6, showing how a bonded joint can be represented with three different modelling strategies. Micro-scale modelling will not be discussed in detail in the current work, but it provides necessary background for larger scale models. In micro-scale models, details on a micrometre length-scale are considered, such as voids and particles in an epoxy adhesive or crystallographic texture in metals. An example of a micro-scale model is given in Figure 1.6, where a representative volume element of a porous material with a given void volume fraction is subjected to shear deformation within periodic boundary conditions. Information from such a unit cell could then be used to obtain information regarding yielding and failure of the studied material for use in higher level models.

For mesoscopic models, these micro-scale details are homogenized into a continuous

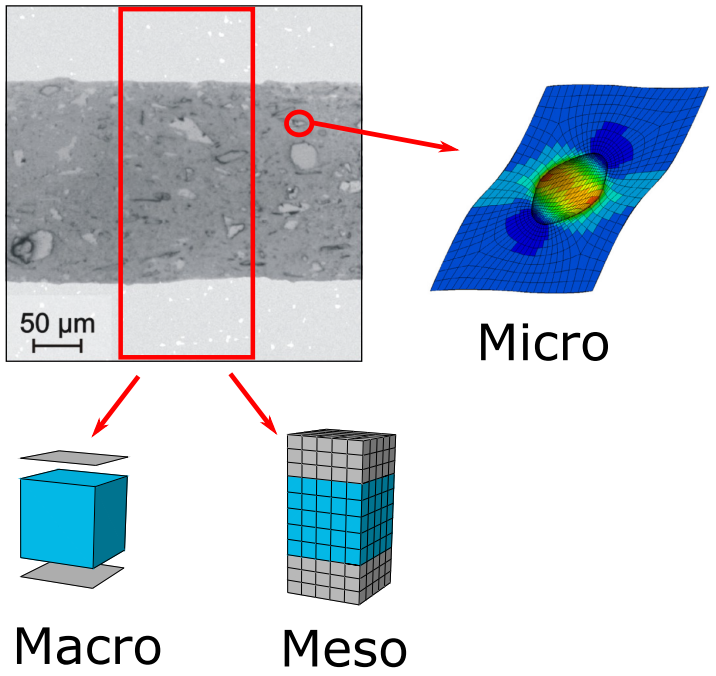

Figure 1.6.: Figure showing the different modelling scales based on a micrograph of the cross-section of a joint between two aluminium profiles bonded with a toughened epoxy adhesive [58]. The macro-scale model is represented by a shell element for each adherent and one cohesive element for the adhesive. For the meso-scale model, each material is represented by a fine mesh of solid elements. Finally, the micro-scale model [59] consists of a representative volume element with a void, that could represent one of the particles of this epoxy adhesive.

material in order to satisfy the continuum hypothesis. A mesoscopic model is discretized into a fine mesh, where the local material behaviour is described in each integration point by a constitutive relation. The constitutive relation describes the stress evolution in each integration point depending on the deformation state, rate of deformation, temperature, and potentially a range of history variables. Micromechanical phenomena such as voids and void growth could be indirectly captured in a constitutive model using a series of assumptions and then tracked through additional history variables. Mesoscopic models are suitable for simulating smaller assemblies, such as a peel specimen or a single lap joint. An adhesive layer typically has a thickness between 0.1 mm to 1.5 mm, which is discretized with several elements as seen in Figure 1.6. This makes it too computationally expensive to run larger simulations on components or full-scale vehicles. The small element size means that the there will be too many elements, and especially for explicit simulations, the critical time-step will be too small to run the simulation within a reasonable time-frame.

In contrast, a macroscopic model considers a mechanical fastener or an adhesive layer effectively as a spring or a cluster of springs between the two parts involved in the connection. The fine mesh of the mesoscopic models is replaced with a single point connector model or cohesive elements, as shown in Figure 1.6, which are described by a traction separation law. It is evident that macroscopic models represent a very simplified description of the joint behaviour compared to a mesoscopic model. However, the computational cost of macroscopic models is considerably smaller than mesoscopic models. Especially for explicit simulation, the critical time-step is larger, making them feasible for large-scale simulations. A comparison between the two approaches from a mathematical point of view was presented by Leuschner et al. [60]. While the mesoscopic models are typically too computationally costly to apply to full-scale simulations, they could be applied in a multi-scale modelling approach. Okereke et al. [61] discuss how models at different scales can be used as virtual tests in order to calibrate higher-level models. An attempt at this method for adhesives will be presented in this thesis.

1.2.5. Numerical methods: Mesoscopic modelling

This section will be dedicated to numerical methods used in meso-scale modelling of joints. This means presenting an overview of the relevant constitutive models that are typically used in mesoscopic models for different materials. It will be presented models for modelling of metals, then for semi-structural adhesives and finally for structural adhesives. A typical constitutive model for metals consists of an elastic component and a plastic component. Due to the small elastic deformations present in metals, it is common to assume isotropic hypo-elasticity in the elastic domain. For the plastic domain, several of the most common plasticity models will be presented. Key constituents are yield function, hardening and failure modelling.

The first component necessary is the yield function. The most common is the von Mises yield function, which typically gives satisfactory results. If higher accuracy is needed, the Hershey [62] Hosford [63] high exponent yield function could be used. Furthermore, some aluminium alloys exhibit anisotropic plasticity which could be modelled with a Hill yield function [64] or Barlat yield function [65]. A micromechanically based porous plasticity model was originally developed by Gurson [66], which assumes the metal as a composite of spherical voids and a von Mises matrix material. This model was extended by Tvergaard [67] to behave better in shear dominated load cases. A further extension was made by Nahshon and Hutchinson [68], adding a shear contribution to the void nucleation.

Hardening is typically described by a simple exponential function, i.e. Ludwig's hardening model, or with a more flexible model in Voce hardening. For industry applications, tabulated linear piecewise plasticity is commonly applied, such as MAT_24 [69]. MAT_24 also includes the possibility to add viscoplasticity in the form of a Cowper-Symonds rate term or tabulated scaling of the yield stress. In academic literature, the Johnson-Cook model

[70] is one of the most common models as it includes exponential hardening, logarithmic strain-rate sensitivity and temperature dependency. There are many other models, such as kinematic hardening, which is considered out of scope for this work.

Failure modelling in metals is generally split into phenomenological models and micromechanically based models. Phenomenological models are based on a damage parameter that is gradually accumulated throughout the test. The Cockcroft-Latham criterion [71] is one of the simplest failure models, with only a single critical energy parameter. It is defined by integrating the first principle stress over the plastic strain, such that it implicitly contains a Lode and stress triaxiality dependence. Therefore, it has been shown by many authors to provide good results, especially when combined with regularization as shown by Costas et al. [72]. Another popular failure model is the Johnson-Cook failure criteria [70], which is dependent on stress triaxiality, strain-rate and temperature. However, this failure model requires five parameters.

Micromechanically based ductile failure is based on the idea that failure is caused by void nucleation, void growth and coalescence of voids [46]. Lemaitre [73] suggested that the damage variable is linked to the void volume fraction, introducing the idea of effective stress and thus damage coupling. Therefore, a non-isochoric plastic flow is required for damage to evolve. This means that it is necessary to use a pressure dependent yield function, such as the porous plasticity models mentioned previously.

The behaviour of semi-structural adhesives is described in Section 1.2.1, and it is evident that there are two significant differences that define the suitable modelling techniques. One key characteristic of rubber-like materials is the large elastic deformations. Modelling this response using a hypo-elastic model would lead to significant spurious elastic dissipation. This problem is solved by deriving the elastic constitutive relation from a Helmholtz free energy potential, yielding a hyperelastic constitutive equation. Furthermore, there are insignificant permanent deformations for these types of materials, meaning any dissipation has to be done through viscous effects.

There are two types of energy potentials, either phenomenological or micromechanically based. Phenomenological potentials are typically based on functions of the invariants of the deformation tensors. The Yeoh [74], Mooney-Rivlin ([75],[76]) and Neo-Hookean [77] potentials are all functions of the first and second invariants of the right Cauchy-Green deformation tensor. Additionally, there is a term with the determinant of the deformation gradient to account for volumetric deformation. The Neo-Hookean model is the most common as it the simplest, with only a linear term of the first invariant. There is also the Ogden [78] potential, which is based on a general polynomial of the principal stretches and determinant of the deformation gradient. These higher order models are very flexible and fit to most test data. However, there is an issue that they could provide unphysical results, such as tensile stress when subjected to large compression deformation.

The most common of the micromechanically-based models for rubber-like materials is

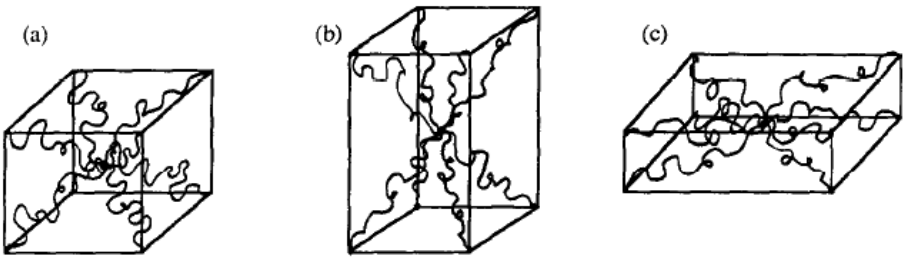

Figure 1.7.: Eight chain rubber model in different configurations [79]. a) Undeformed. b) Uniaxial extension. c) Biaxial extension.

the Arruda-Boyce [79] eight chain model. This model considers the potential energy related to the change of entropy of a representative volume of eight polymer chains when subjected to deformations as depicted in Figure 1.7. When the chains are fully extended, the model locks such that the stress will tend towards infinity. As a direct consequence of being related to the entropy, the model is also dependent on temperature. Another micro-mechanically based model is the extended tube model [80], which considers three energy contributions. One contribution comes from the cross-linking of the network, the second one from the confining tube constraints, and the third one is related to the energy from volumetric deformations. Unlike the phenomenological models, these models will provide physical results outside of the test regime used to calibrate them. Furthermore, it is discussed by Bergström [81] that these models generally provide better accuracy compared to the number of parameters that needs to be calibrated.

In order to account for the rate sensitivity of these materials, the hyperelastic model is combined with some type of viscous model. The most common approach is to use linear viscoelasticity, where the response is the sum of the initial hyperelastic model and one or more Maxwell elements. Each Maxwell element has its own relaxation time and stiffness. In order to properly cover a large range of strain-rates from quasi-static to impact problems, it could be necessary to use 5 to 15 Maxwell elements in parallel [82]. Khajehsaeid et al. [83] proposed using one Maxwell element with a dynamic relaxation time dependent on the strain-rate, in order to capture the whole domain. The Bergström-Boyce model is commonly used to model rubber-like materials, as it is based on the micromechanics of rubbers. Bergström and Boyce [84] suggested that the response was a sum of a time independent and a time dependent response. The time independent response was assumed to be governed by entropic stiffness according to the eight-chain model. Further, the time dependent response was based on affine stretching and then relaxation of free chains based on reptation motion.

A key characteristic of these types of adhesives is the lack of plasticity, which yields a brittle fracture mechanism despite large deformations. Therefore, the commonly used ductile failure models are not viable. Brittle failure is typically considered in a fracture

mechanics framework, which is not feasible for mesoscopic modelling. Osnes et al. [85] used a critical first principal stress and an estimation of the stress intensity factor combined with node splitting to model brittle fracture. This method would likely give reasonable results for a semi-structural adhesive as well. The weakest link mechanism described in the book by Anderson [46] indicates that the problem is length-scale dependent. This has to be accounted for by mesh regularization. Further, assuming the failure is initiated in a flaw, the critical value should also be stochastically distributed. It should be noted that this is still an active field of research.

Lubowiecka et al. [57] performed experiments and simulated joints between similar and dissimilar adherents bonded by a semi-structural polyurethane adhesive. It was found that both a Neo-Hookean model and an Arruda-Boyce eight-chain model gave satisfactory results for the given adhesive subjected to quasi-static loading. Furthermore, it was shown by comparing the simulations of the AL-AL joint with the simulations of the AL-PU joint that there was a significant effect of using dissimilar adherents. An Ogden model combined with linear viscoelasticity was used to model a similar type of adhesive by Golaz et al. [86]. The modelling approach was seen to give good results for a range of strain-rates for that specific adhesive.

According to Figure 1.2, structural adhesives behave significantly different to semi-structural ones. From a modelling point of view, one of the key differences is that the elastic deformations are typically much smaller in structural adhesives, such that hyperelastic models are not necessary. Further, there are large plastic deformations that have been seen to be pressure sensitive. The behaviour of these adhesives are dominated by the plastic domain, which will be the primary focus in this section. In terms of failure, structural adhesives exhibit ductile damage mechanisms, which could be modelled in a similar way as with metals.

There is a selection of pressure dependent yield functions available in literature, with the most basic one being a Drucker-Prager yield surface. A more advanced pressure sensitive yield surface that has been implemented in various polymer models is the Raghava [87] yield surface. It is possible to define the pressure sensitivity parameter directly from a tension and compression test. Similar to metals, a porous plasticity type model is also viable for structural adhesives, as there are both particles and voids that function as an initial void content. However, it may be required to use a more complex porous plasticity model than the one presented by Tvergaard, as the volume change due to void growth might not be sufficient. An extension of that porous plasticity model with a Drucker-Prager material in the matrix was developed by Jeong et al. [88]. This model was initially developed in order to study failure in the process zone of a rubber-toughened epoxy adhesive, where it was seen to give good results. Unlike typical porous plasticity models, it is non-symmetric in terms of pressure, such that it can also capture the difference in initial yield stress for a tension and compression test.

A complete polymer model was presented by Polanco-Loria et al. [89]. The model

assumes two primary contributions, a viscoplastic intermolecular part and a hyperelastic network resistance. The viscoplastic component is defined by a Raghava yield function with non-associated plastic flow, such that the plastic dilatation can be fitted separately. Although the presented model is elastic-perfectly-plastic in Part A, it is easily extended to include isotropic hardening for instance. A more advanced model was presented by Balieu et al. [90], which also allows for a different plastic dilatation parameter in tension and compression. Additionally, it has 6 parameters for isotropic hardening as well as damage coupling.

Damage and failure are believed to be governed by void nucleation, growth, and coalescence for structural adhesives, similar to metals. Therefore, the same ideas regarding porous plasticity models are also viable for structural adhesives. A critical void volume fraction failure criterion can also be used in combination with other polymer models due to the plastic dilation that is characteristic for these materials. There has also been some efforts in order to reduce mesh sensitivity with regards to failure. García et al. [15] and de Moura and Chousal [91] both determined a critical failure strain based on the critical energy release rate and the characteristic element length. A more advanced non-local method was implemented by Balieu et al. [92], where the rate of the damage variable was corrected by a penalty factor based on an intrinsic influence length. This method proved successful when simulating a mineral filled semi-crystalline polymer.

An extension of the model implemented by Balieu et al. [90] was used by Dufour et al. [5] to simulate the previously mentioned Arcan style experiments. The material model was calibrated based on tension tests and compression tests as well as dynamic mechanical analysis for the viscoelastic properties. Good agreement between the tests and simulations was found using this methodology to simulate the structural adhesive SikaPower 498.

1.2.6. Numerical methods: Macroscopic modelling

On a macroscopic level, adhesives are typically modelled using cohesive zone models (CZM) that are described by their traction separation law. This section will give a brief introduction to CZM and give an overview of some relevant traction separation laws used for modelling of adhesives. CZM are also called element-based models, as the tractions and separations are linked to the finite element (FE) model through a cohesive element. Figure 1.8 shows how the nodal positions are used to define the relative separation for each corner as well as the midsurface and the local coordinate system. The relative separations are then interpolated across the midsurface of the element and used as input to the CZM in each integration point. Tractions obtained from the CZM is then integrated over the element to obtain the nodal forces. There are variations of this formulation that also accounts for the thickness of adjacent shell elements [93].

The initial idea behind the CZM stems from the study by Dugdale [94] on the size of the

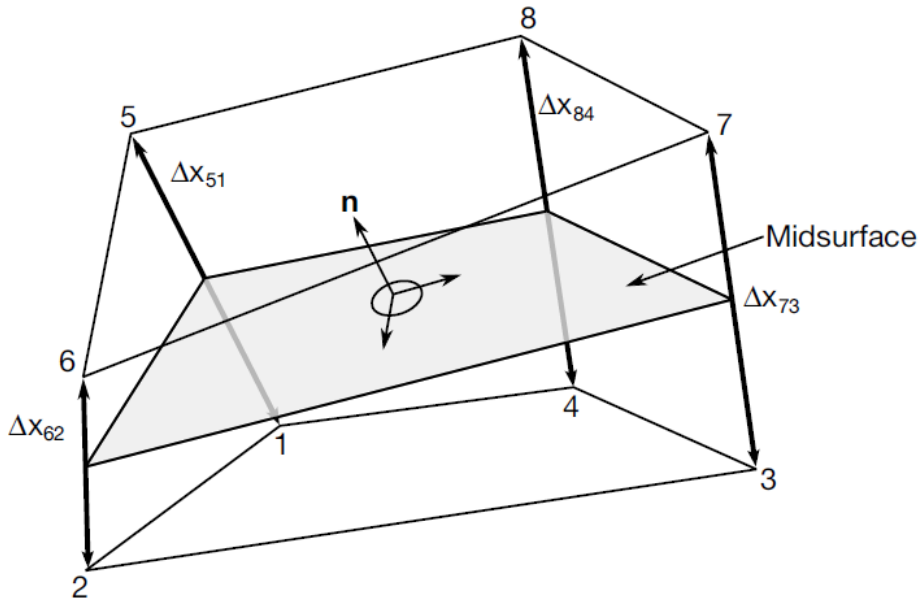

Figure 1.8.: Definitions of separations for cohesive solid element in LS-DYNA [93].

plastic zone next to a crack. Hillerborg et al. [95] implemented a 2D version for mode I fracture, thus providing the foundation for CZM in simulations. An extension of that model, which also accounts for mixed mode tractions and separations, was presented by Needleman [96]. The inclusion of mixed mode damage was described by Tvergaard [97]. Finally, Tvergaard and Hutchinson [98] proposed a typical elastic-plastic traction separation law such as the ones found in modern FE solvers.

Bi-linear traction separation laws represent the most common and simplest models. Depending on the required accuracy and scale of the model, these could provide good results as well. Zadpoor et al. [99] was able to predict the peak load for specimens bonded with an epoxy adhesive using this simple model. An extension of this model, with damage softening in the elastic regime, was introduced by Alfano and Crisfield [100]. This model was then used by Camanho et al. [101] to model mixed-mode delamination of composites in fracture mechanics test configurations. Marques et al. [102] used it to model the adhesive in hybrid welded and bonded joints. Further, Hasegawa et al. [103] used the same CZM to model the interface of a thick layer of a semi-structural polyurethane adhesive between a steel and a composite substrate.

The plastic deformations exhibited by structural adhesives indicate that a trapezoidal traction separation law could be better suited. Further, strain-rate sensitivity is also a key phenomenon for adhesives in general. Marzi et al. [104] implemented a CZM with strain-

rate sensitivity for both the flow stress and fracture energy. A state-of-the-art CZM model was developed by Morin et al. [55], which accounted for strain-rate sensitivity, hardening, pressure sensitive yielding and crack propagation velocity. This model was specifically designed to model structural adhesives, and it was seen to give good results for the validation case presented in the article. Another study using a trapezoidal traction separation law was performed by Pinto et al. [105]. Multi-material SLJ of 5 different materials in 9 different combinations were tested and simulated. Satisfactory correlation between experiments and simulations was found for most configurations.

Recently, a porous plasticity based CZM was developed by Said Schicchi and Caggiano [106], with the intent of modelling fracture in metals. Although it was developed for metals, it was discussed in Section 1.2.5 that porous plasticity models capture some key elements of the behaviour of structural adhesives as well. The model was derived from a typical porous plasticity model by reducing the number of strain components to one normal component and a shear component. These components were then directly linked to the separations through the thickness of the cohesive element. This model is implemented and validated as a part of this thesis, in order to model the structural adhesive SikaPower 498. Further details regarding this model will be presented in Chapter 5.

1.3. Objectives

It is the overarching objective of this thesis to provide new insight into the behaviour and modelling of bonded multi-materials joints subjected to a range of loadings. This will be achieved through a set of objectives:

- Perform an extensive experimental campaign in order to identify and characterize the phenomena governing the mechanical behaviour of a semi-structural adhesive.
- Evaluate the feasibility of currently available meso-scale constitutive models for adhesives and propose improvements or new models based on the experimental results.
- Evaluate the suitability of current and new models for large-scale simulations of bonded joints.
- Explore the feasibility of a multi-scale modelling approach in order to reduce the number of mechanical tests required for calibration of macro-scale numerical models.
- Validate the investigated numerical models against suitable validation tests.

1.4. Scope

There will only be studied two adhesives as a part of this thesis, BETAFORCE 2816L representing a semi-structural adhesive and SikaPower 498 representing a structural adhesive. Hybrid joints with adhesives and mechanical fasteners will be mentioned in this work, but they are considered out of scope. The adherent materials are limited to steel, aluminium, carbon fibre reinforced polymers (CFRP) and sheet moulding compounds (SMC). Further, only the steel and aluminium alloys will be modelled. Simulations have been performed using Abaqus Unified FEA and LS-DYNA.

Further limitations:

- All tests are performed at room temperature.
- Isothermal conditions have been assumed for all simulations.
- Simulations have been limited to meso-scale and macro-scale.
- Only cohesive failure has been considered.
- Only ductile failure mechanisms have been modelled.
- All materials have been considered isotropic in the current work.
- All macro-scale simulations, benchmark tests and component tests are assumed to be quasi-static.

A further list of topics considered out of scope for this thesis include:

- Fatigue.
- Ageing.
- Environmental effects.
- Process parameters.

1.5. Research strategy

The general research strategy for this project is based on first performing experiments, then using the results as a basis for numerical investigations and finally validate the numerical approach. It can be summarized in these steps:

1. Use state-of-the-art experimental techniques to study in detail the behaviour of adhesives subjected to a range of loading conditions.

2. Use the observations from the experimental campaign to find, and potentially develop, suitable numerical models for meso-scale modelling of adhesives.

3. Validate meso-scale modelling techniques using benchmark tests.

4. Use the validated meso-scale modelling techniques to develop a numerically based multi-scale calibration procedure for macro-scale modelling.

5. Validate macro-scale models on benchmark tests and component tests.

1.6. Contributions

Scientific contributions from the work performed during this thesis has been published in an international peer-reviewed journal as well as presented at international conferences.

Journal article:

I J. F. Berntsen, D. Morin, A. H. Clausen, M. Langseth, *Experimental investigation and numerical modelling of the mechanical response of a semi-structural polyurethane adhesive*, International Journal of Adhesion and Adhesives **95** (2019) 102395. doi: 10.1016/j.ijadhadh.2019.102395.

Conference contributions:

II J. F. Berntsen, D. Morin, A. H. Clausen, M. Langseth, *Mechanical behaviour of a ductile polyurethane adhesive*. In: 17th International Conference on Deformation, Yield and Fracture of Polymers (DYFP2018), Kerkrade, Netherlands, 26-29 April 2018.

III J. F. Berntsen, D. Morin, A. H. Clausen, M. Langseth, *Modelling of bonded component tests - Comparing MAT_240 to state-of-the-art model*. In: 12th European

LS-DYNA conference, Koblenz, Germany, 14-16 May 2019.

1.7. Outline of thesis

The thesis is structured as follows:

Part I: Introduction

Chapter 1 provides motivation, context, strategy and outline of the thesis.

Part II: Semi-structural two-component polyurethane adhesive

Chapter 2 describes the experimental techniques and presents the results of the studies performed on bulk adhesive specimens and joints bonded with the semi-structural adhesive BETAFORCE 2816L.

Chapter 3 gives an outline of the relevant numerical methods for meso-scale simulations and details the implementation and results of this approach applied to the results of Chapter 2.

Part III: Structural epoxy adhesive

Chapter 4 describes the experimental techniques and presents the results of the studies performed on bulk adhesive specimens and joints bonded with the structural adhesive SikaPower 498. Additionally, a meso-scale polymer model will be described and calibrated based on the test data and then validated against the experiments.

Chapter 5 describes how the meso-scale modelling presented in Chapter 4 can be used in a multi-scale approach to calibrate macro-scale models as well as implementation and validation of macro-scale models.

Chapter 6 uses the results from the previous two chapters to further study the influence of the meso-scale models on the multi-scale calibration approach. Additionally, there will be performed a study of the influence of the adherents on the macro-scale response of the adhesive. Finally, there will be validation on hybrid benchmark and component tests.

Part IV: Conclusions and outlook

Chapter 7 provides concluding remarks and an outlook for the future.

Part II.

Semi-structural two-component polyurethane adhesive

2. Experimental campaign: Polyurethane adhesive

2.1. Introduction

This section will provide a brief introduction to this chapter by giving a general description of the chapter and put it in context of the rest of the thesis. There will also be given a brief background into creation of bulk adhesive specimens, as it was not specifically covered in Section 1.2.

2.1.1. Chapter description

Based on the objectives of this thesis presented in Section 1.3, this chapter presents a detailed description of experimental methods and results of a study performed on the semi-structural two-component polyurethane adhesive BETAFORCE 2816L. The experimental results are evaluated in order to determine the key phenomena governing the mechanical behaviour for the studied adhesive. Furthermore, the data obtained through these experiments are directly used in this thesis as a basis for evaluating suitable numerical models and calibration of these models in line with the research strategy presented in Section 1.5.

The chapter is separated in different sections for each type of experiment. Each experimental section is further subdivided into a structure of first describing how the specimens were produced, then describing the test setup, further describing the post-processing methods and finally presenting the results. After a brief introduction the bulk adhesive testing on tension test specimens, compression test specimens and notched tension test specimens will be presented in Sections 2.2, 2.3 and 2.4 respectively. A simple unit test in the form of a single lap joint (SLJ) test will be presented in Section 2.5. Finally, the results will be discussed and conclusions drawn in relation to recent literature and the rest of the thesis in Section 2.6.

2.1.2. Background: Creation of bulk adhesive specimens

In order to characterize the adhesive material itself, it is necessary to produce test specimens of high quality. A critical parameter describing the quality of bulk adhesive specimens is the void content of the specimens. A large number of voids would heavily influence specimen failure, as the voids lead to stress concentrations that could initiate early crack growth. Furthermore, the voids could also be an additional source of error when calculating the stresses in the specimens. With that in mind, there are two primary approaches to creating these specimens. First method is to either pour or inject an adhesive into a mould, while the second method would be to make a plate of adhesive material and then machine out the specimens from that plate.

Both pouring and injection will entrap air bubbles in the specimens, such that it is necessary to post-process the specimens after the adhesive is inside the mould. It is suggested by da Silva et al. [21] that using a centrifuge on the specimens before they are reticulated would significantly reduce the void content in the specimens.

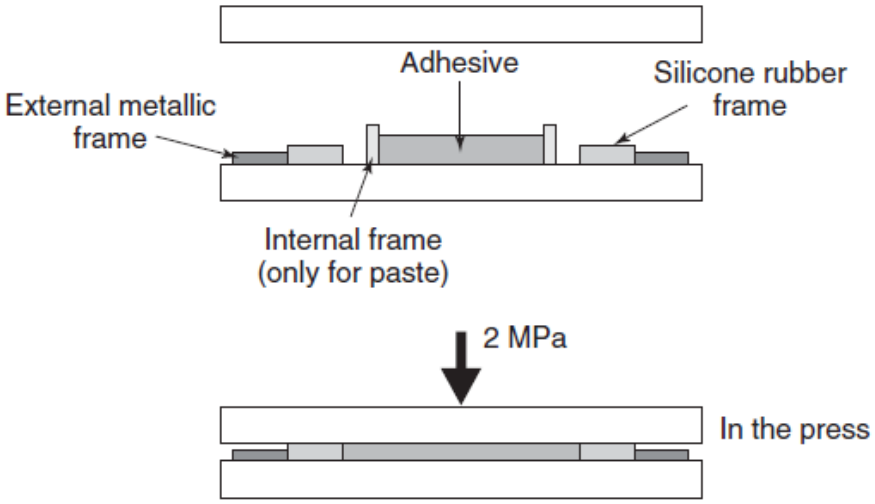

Figure 2.1.: Manufacturing of bulk adhesives plates [21].

The second approach is to make the plates using hydrostatic pressure in order to remove the voids. Both da Silva et al. [21] and Jia et al. [11] had success making bulk adhesives plates without voids following the principles outlined in the French standard NF T 76-142 [107]. Figure 2.1 presents a setup to apply these principles. Machining specimens from these plates could generate imperfections on the cut surfaces of the specimens. These imperfections could further influence the failure of the specimens as reported in the current

work. Furthermore, machining specimens of semi-structural adhesives with low stiffness requires different machining methods as proposed by previous authors [21] as well as in the current work. The second approach was chosen to make the tension and notched tension test specimens for this thesis due to its simplicity and proven record. However, due to their thickness, the compression test specimens had to be made using a different approach outlined in Section 2.3.1.

2.2. Uniaxial tension tests

2.2.1. Test specimens

An initial study was performed to find how to best distribute the adhesive in order to avoid voids. The adhesive was both mixed and distributed using the electric adhesive gun BETAGUN, which used a dynamic mixing bridge to mix the adhesive. This initial study found that keeping the nozzle in contact with adhesive volume, thus expanding the volume from within, ensured the lowest number of voids in the plates. It was evident that plates with an acceptable number of voids could be produced without applying pressure when using this technique.

Figure 2.2.: Bulk adhesive plate used for specimen machining.

In order to ensure the correct thickness and further reduce the volume of voids, a method

based on the one presented in Section 2.1.2 was implemented with some modifications. The mould used to make the plates in this thesis consisted of 3 components, a thin steel plate at the bottom, a Teflon spacer and a thick steel plate on the top. Both steel plates were coated with a Teflon spray on the contact surface for the adhesive. The bottom steel plate had a thickness of 8 mm, while the top plate had a thickness of 40mm to keep it from bending when applying the load. The Teflon spacer was cut in to a rectangular shape with outer dimensions of 250 mm × 250 mm, internal dimensions 200 mm × 200 mm and a thickness of 2 mm.

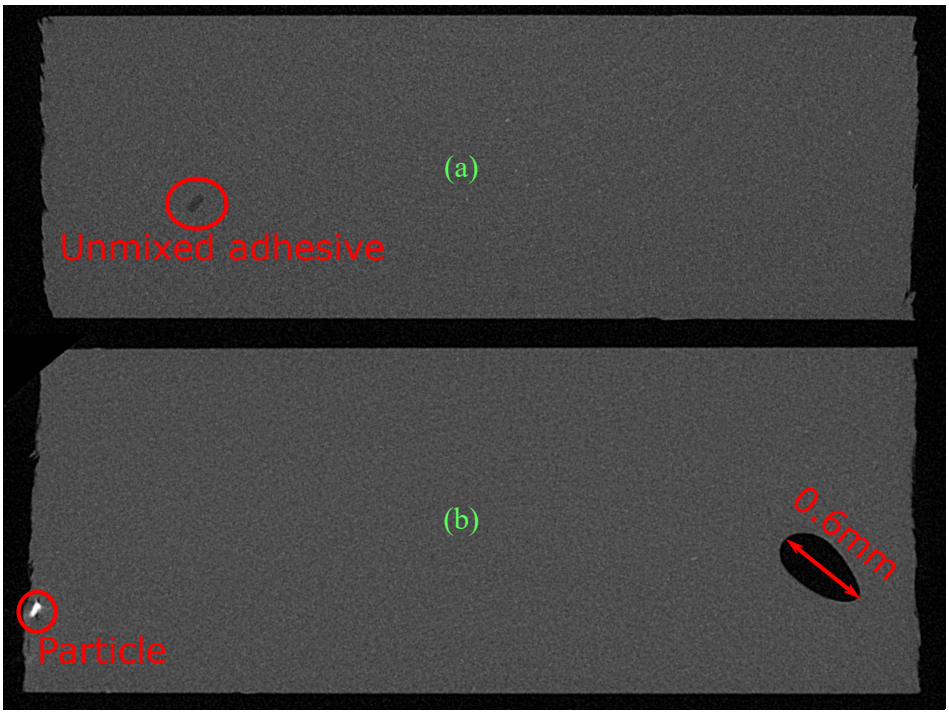

Figure 2.3.: Examples of cross-sections obtained from computed tomography scans of 3 uniaxial tension test specimens. (a) A typical cross-section with a spot that has a similar density to unmixed adhesive. (b) View of critical cross-section, showing the only void found from these scans.

When making the plates, approximately the correct volume of adhesive was added to the mould in the previously mentioned manner. Then, the top steel plate was added and the mould was moved to a servo-hydraulic machine with a capacity up to 100 kN. A load of roughly 90 kN, yielding a pressure of roughly 1.5 MPa, was applied to the mould for a few seconds. Finally, the mould was put to rest for at least a week before the plate was removed from the mould. An example of one of the plates can be seen in Figure 2.2. It can be seen that one of the edges are slightly bent, which is likely due to too much adhesive forcing the

Teflon spacer to bend.

As the adhesive material is 2 orders of magnitude softer than a structural adhesive and 4 orders of magnitude softer than metals, traditional machining methods are unsuitable. Therefore, the test specimens were cut using a waterjet cutting machine, which cuts using a jet of high-pressure water mixed with fine sand particles. This method reduces the deformations and vibrations of the plates during machining, yielding better results.

A key parameter for evaluating the quality of the specimens is the void content. In order to obtain a good indication on the void content, 3 tension test specimens were scanned using x-ray computed tomography (CT). Two examples of cross-sections obtained from this scan can be seen in Figure 2.3. A voxel size of 0.0058 mm was achieved with this scan, giving an indication on the size of features that could be resolved, such that voids on the micro-scale is would not be visible. Figure 2.3a represents a cross-section that could be considered typical for the studied volume. There is spot which is likely to be a pocket of unmixed adhesive as the estimated density is similar to that of one of the components of the adhesive. These pockets of unmixed adhesive are not seen in every cross-section, and they are generally smaller than the one seen in this figure. Figure 2.3b show the only cross-section where there was found a void in the gage section of the 3 scanned specimens. Assuming an ellipsoidal shape of the void, the void represented roughly 0.001% of the studied volume. Furthermore, the void represented roughly 1% of the cross-section area of the given specimen. Particles, such as the one visible in Figure 2.3b, are also distributed throughout the specimen. It is not known what those particles are made of.

The behaviour of the volumes of what is likely to be unmixed adhesive is unknown, although it could be assumed as a flaw with the effect being similar to that of a void. The volume fraction of these pockets of unmixed adhesive has not been estimated, as there are a lot of them with different sizes. However, it is clear that they represent a significantly smaller percentage of a critical cross-section than the single void. Therefore, they likely have a smaller impact on the results than any potential void would have.

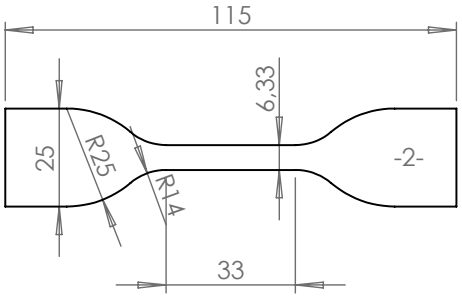

Figure 2.4.: Geometry of the tension test specimens, based on the ISO 37 standard [108].

It is evident from the Figure 2.3 that the surfaces of the specimens are rough compared to typical specimens from stiffer materials. This is an effect of machining the specimens using a waterjet cutting machine. However, this is likely better than what could have been obtained using more traditional methods. These rough surfaces could lead to early failure for specimens, especially for the notched tension test specimens that will be presented in Section 2.4.

The geometry of the tension test specimens is depicted in Figure 2.4, which is based on the Type 1 dumb-bell specimen described in the ISO 37 standard [108]. Initial tension tests on more generic specimens indicated a rubber-like material behaviour. Therefore, the specimen geometry was chosen based on previous experience using the ISO 37 specimen for testing of rubber materials.

The tension test specimens were produced in 3 different batches. It was made 15 specimens from the first batch, then another 5 from the second batch and finally 6 more specimens from the last batch. The reason for using these different batches was that the original batch was made with adhesive that was slightly out of date, such that it was necessary to make new specimens to confirm that it would not be an issue. It was spotted a significant difference between the first and second batch, which is why the third batch was made. However, results from the third batch indicated that the original batch was representative for the material.

2.2.2. Test setup

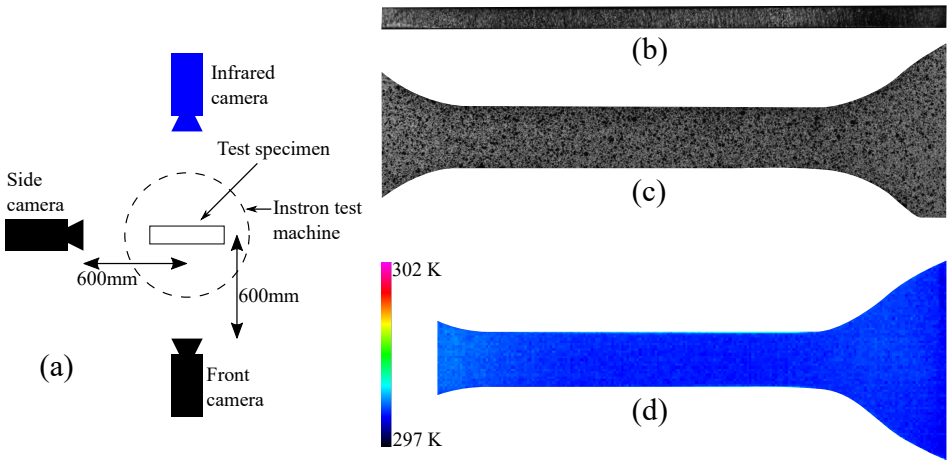

Figure 2.5.: Tension test setup. (a) Schematic of the tension test setup, as seen from above. (b) View from side camera. (c) View from front camera. (d) View from infrared camera.

To test the tension test specimens, a servo-hydraulic Instron 5944 machine equipped with a 2 kN load-cell was used. In order to capture the large deformations of the specimens and potentially identify any inhomogeneities in the deformation field, digital image correlation (DIC) techniques were applied. Therefore, it was used two perpendicular cameras of the type Prosilica GC2450, each located 600 mm away from the surface of the specimens as seen in Figure 2.5a. Furthermore, the surfaces visible to these two cameras were spray-painted with white paint to create a fine speckled pattern for DIC, as visible in Figures 2.5b and 2.5c. The imaging frequency of the cameras for these tests were 1 Hz, 10 Hz and 15 Hz for the nominal strain-rates $10^{-3}\,s^{-1}$, $10^{-2}\,s^{-1}$ and $10^{-1}\,s^{-1}$ respectively. A thermal camera of type FLIR SC 7500 was used to monitor the surface temperature of the specimens. The surface of the specimens exposed to the thermal camera was covered with a matte black spray-paint to obtain a similar emissivity to the calibrated value of the camera. Figure 2.5d shows the view from the thermal camera in the initial configuration.

The first batch of tension tests was run with 5 repetitions at nominal strain-rates of $10^{-3}\,s^{-1}$, $10^{-2}\,s^{-1}$ and $10^{-1}\,s^{-1}$ corresponding to cross-head velocities of 1.98 mm/min, 19.8 mm/min and 198 mm/min respectively. Additional 3 repetitions from the second batch were run at a nominal strain-rate of $10^{-3}\,s^{-1}$, as well as 2 more repetitions at a strain-rate of $10^{-2}\,s^{-1}$. Finally, the third batch consisted of 3 repetitions at a strain-rate of $10^{-2}\,s^{-1}$ and $10^{-1}\,s^{-1}$.

2.2.3. Post-processing techniques

DIC represents the key post-processing tool used for these experiments and throughout this thesis. The DIC software used is an element based software, which was developed as a part of the thesis of Fagerholt [109]. It was run initial DIC analyses to investigate the general behaviour of the specimens to determine the optimal DIC element size and formulation. Figure 2.6a shows the results of one such analysis, where it is evident that the strain field is close to homogeneous in the gage section. Therefore, the optimal solution would be to use large linear elements. The tension tests were analysed using linear DIC elements with a size of 50 px × 50 px equal to 1.8 mm × 1.8 mm for both cameras, as seen in Figures 2.6b and 2.6c. Furthermore, the noise was reduced by using virtual extensometers averaging the measure across most of the gage section, as seen in Figures 2.6b and 2.6c. The ends of the virtual extensometers were purposefully chosen to be away from the nodes in the DIC mesh to further reduce noise.

It was observed that the deformation field was homogeneous in the gage section as well as the initial temperature field being homogeneous for the whole specimen. Therefore, it was possible to obtain a more accurate temperature measurement by averaging the measurement from a region in the gage section that stayed within the gage section for the whole test. This region is highlighted in Figure 2.7.

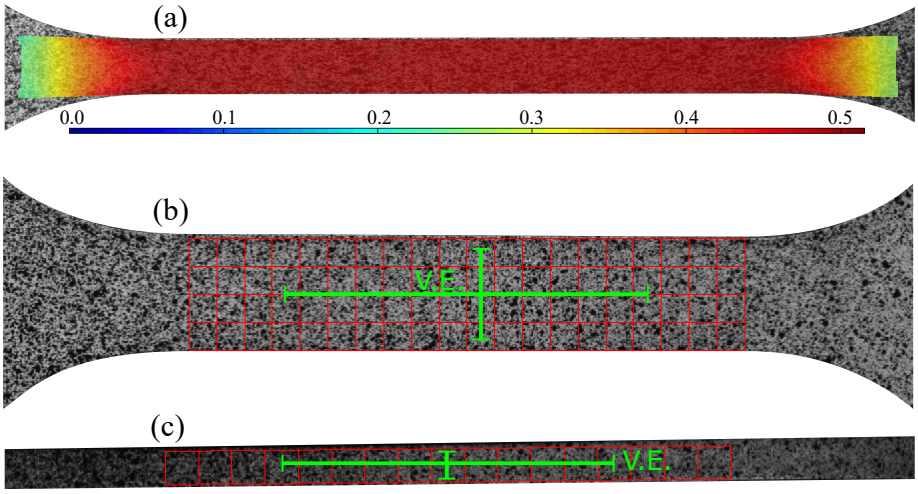

Figure 2.6.: Digital image correlation (DIC) on tension tests. (a) Example of homogeneous strain field. (b) DIC mesh and virtual extensometers (VE) applied to the front surface. (c) DIC mesh and VE applied to the side surface.

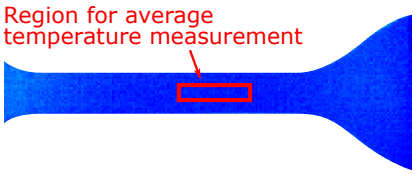

Figure 2.7.: Visualization of region where the averaged temperature measurements were measured.

2.2.4. Test results

The strain measures to be presented in this section are all logarithmic strain measures, while the stress measures will all be Cauchy stress. The Cauchy stress, σ, was calculated based on the equation:

$$\sigma = F/A \tag{2.1}$$

where F is the force measured by the load-cell and A is the current cross-section area of the gage section. Based on the transverse strain measurements obtained from DIC, the current area, A, could be calculated using this equation:

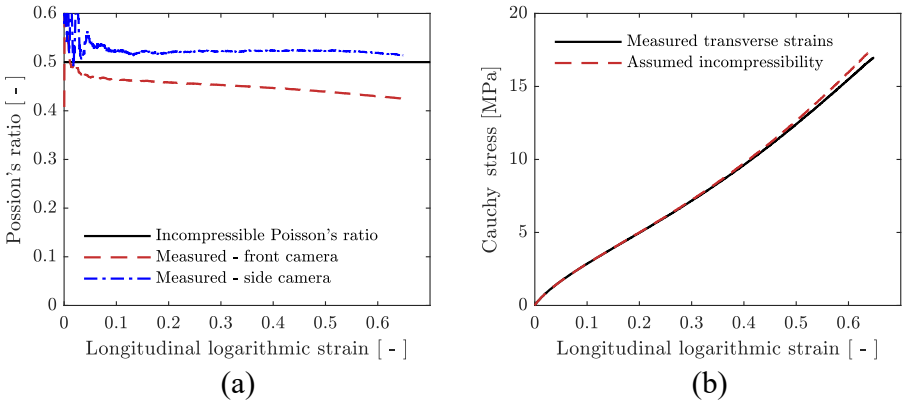

Figure 2.8.: Evaluation of incompressibility assumption. (a) Plot of Poisson's ratio measured from front and side cameras. (b) Comparison between the Cauchy stress calculated based on the measured transverse strains and the assumption of incompressibility.

$$A = A_0 \exp(\varepsilon_{22} + \varepsilon_{33}) \tag{2.2}$$

where A_0 is the initial cross-section area, ε_{22} is the transverse strain measured on the front surface of the specimen and ε_{33} is the transverse strain measured on the side surface of the specimen. It can be seen in Figure 2.8a that the specimen behaves in a close to incompressible manner. Assuming incompressibility, the current area, A, can be estimated using this equation:

$$A = A_0 \exp(-\varepsilon_{11}) \tag{2.3}$$

where ε_{11} is the longitudinal logarithmic strain. Figure 2.8b shows a comparison between the Cauchy stress using the two different definitions of the current area, further suggesting that the material behaves in a close to incompressible manner. Therefore, the assumption of incompressibility will be used to determine the Cauchy stress for the rest of the chapter.

Figure 2.9a shows the representative Cauchy stress versus longitudinal logarithmic strain curves obtained from the first batch of specimens. An apparent phenomenon is the strain-rate sensitivity of the material, going from a nominal strain-rate of $10^{-3}\,\mathrm{s}^{-1}$ to $10^{-1}\,\mathrm{s}^{-1}$ gives approximately a 15 % increase in the Cauchy stress. Furthermore, the viscous overstress is seen to behave in multiplicative manner, as it is approximately linearly increasing with increasing strains. There was not observed any localization in the specimens nor any softening, thus making the virtual extensometers valid until failure of the specimen. While there were large strains at failure, the failure mechanism itself is seemingly brittle. The

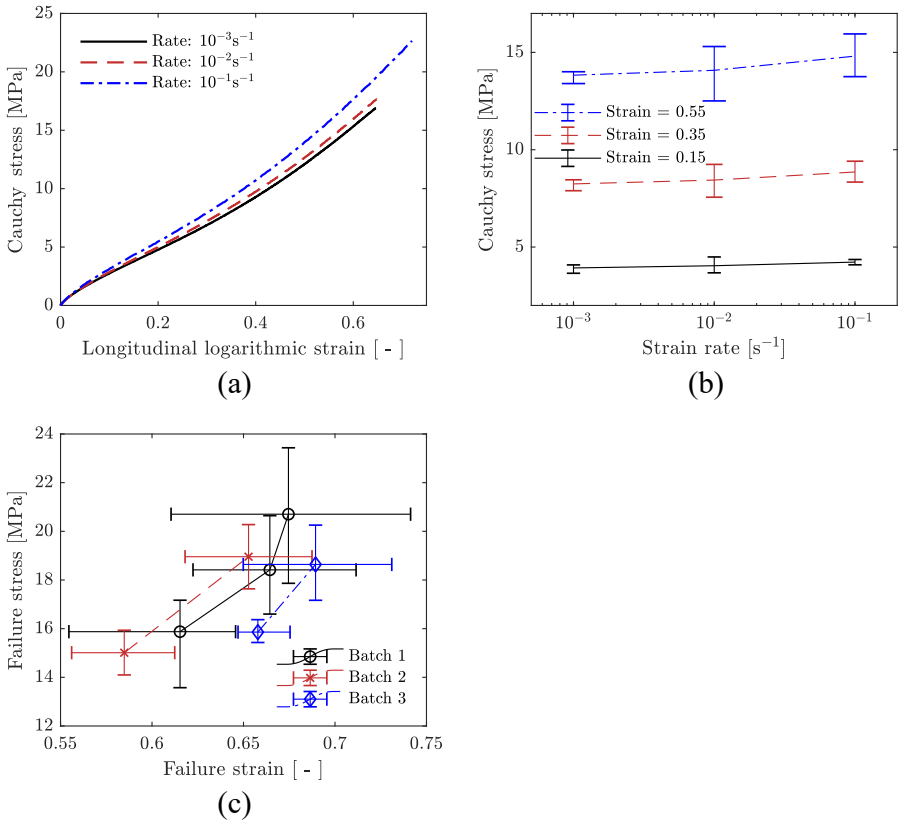

Figure 2.9.: Tension test results. (a) Representative stress-strain curves for 3 different nominal strain-rates. (b) Scatter in tensile stress at three strain levels for three different nominal strain-rates. (c) Scatter in failure strain and failure stress for the three different batches and different nominal strain-rates.

residual strains were measured to be negligible, with an upper bound on 1 %, further suggesting that there are negligible plastic deformations in this material.

Scatter in the stress level at different strain levels as a function of nominal strain-rate is presented in Figure 2.9b, showing a deviation of up to 10 %. This amount of scatter is on the same magnitude as the strain-rate sensitivity. However, it is important to note that this plot includes data from all 3 batches of specimens. This is clearly seen by the fact that the scatter is largest for the nominal strain-rate of $10^{-2}\,s^{-1}$, where there are tests from all 3 batches. The scatter within each batch is significantly smaller, such that the strain-rate sensitivity is as evident as shown in Figure 2.9a.

Scatter in failure strain and Cauchy stress at failure is presented in Figure 2.9c, where each point represents a specific nominal strain-rate for a specific batch. It is evident that there is significantly more scatter related to failure than to that of stress level. Furthermore, there is also a close to linear relationship between failure stress and strain. There is also a slight trend with increasing failure strain at increasing nominal strain-rate. The results presented in Figure 2.9c further suggest that the initial batch of specimens represent the average response of the material.

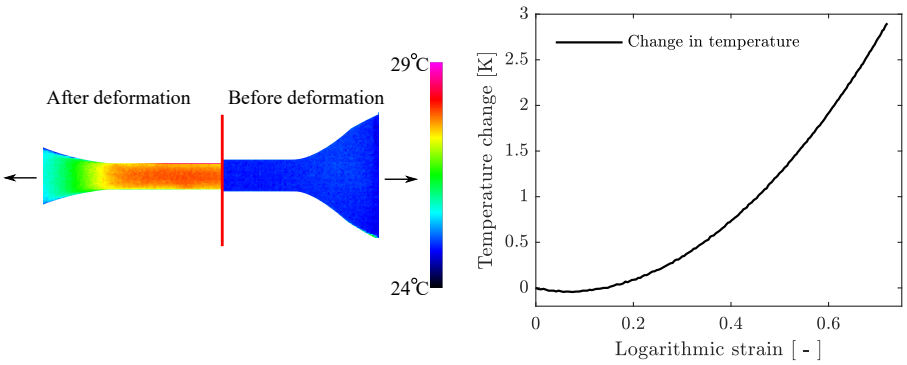

Figure 2.10.: Temperature measurements from a tension test run at a nominal strain rate of $10^{-1}\,\mathrm{s}^{-1}$. (a) Comparison of view from infrared camera in initial configuration and right before fracture. (b) Measured average change in temperature based on Figure 2.7.

Figure 2.10a shows the view from the thermal camera in the initial configuration and right before failure for a tension test run at a nominal strain-rate of $10^{-1}\,\mathrm{s}^{-1}$. The temperature field is seen to be close to homogeneous in the gage section and dropping off rapidly into the grips. This suggests low thermal conductivity, which would strengthen a hypothesis of adiabatic heating for the tests at this nominal strain-rate. This is consistent with what was found in a previous study [8]. The temperature measurements presented in Figure 2.10b are measured on the same specimen as Figure 2.10a using the method described in Section 2.2.3. A total change in temperature of 2.9 K was measured, which represents roughly a 1 % increase in absolute temperature. For a material with purely entropic stiffness, this effect would be within the scatter, suggesting that temperature changes due to adiabatic heating is negligible for this material. Furthermore, it serves as an additional indication of negligible plastic deformations. The temperature change does not start increasing before a logarithmic strain of 0.07, the reason for this has not been investigated further. It should be noted that from that point onwards, the temperature change can be fitted to a quadratic polynomial without a linear term. Assuming adiabatic conditions and a constant Taylor-Quinney coefficient, this would suggest a close to linear increase of the dissipative stress with increasing logarithmic strain. Therefore, it serves as an additional indication of a multiplicative viscous overstress.

2.3. Uniaxial compression tests

2.3.1. Test specimens

Figure 2.11.: Part of initial bulk adhesive cylinder, with slices of the cylinder and final test specimens.

Unlike the tension test specimens, the compression test specimens were cut from a cylindrical bulk of adhesive with a diameter of 51 mm which is depicted in Figure 2.11. This cylinder was created by pouring the adhesive into a mould, while keeping the nozzle of the adhesive gun in contact with the rising surface as was done previously. As the cylinder is much thicker than a typical adhesive layer in a joint, the heat generation during reticulation becomes significant. In order to cool down the specimen, the mould was put into a bath of water over night. Similar to the bulk adhesive plates, the cylinder was laid to rest in the mould for more than a week before extracting it from the mould.

The steps in the machining process is shown in Figure 2.11. Due to the thickness of the cylinder, it is possible to cut it into 10 mm thick slices with traditional machining tools and receive good results. From these slices, compression test specimens were cut using the previously mentioned waterjet cutting machine. It was made a total of 15 specimens

from 3 slices in a single batch. The geometry of the compression specimens is given in Figure 2.12, with the diameter to length ratio chosen to allow for large deformation without barrelling or buckling.

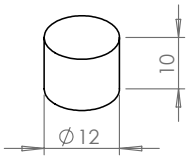

Figure 2.12.: Geometry of compression test specimens.

Visual inspection of the compression test specimens revealed similar surface defects as with the tension test specimens including a thin ridge along the length of the specimen. There was also observed a void on one of the surfaces. A more significant flaw of the specimens were the slanted edges due to the waterjet being conical, which was not properly accounted for. Numerical simulations were run to investigate the effect of these slanted edges. The results of these simulations indicated that there would be a gradient on the surface of the specimens. However, it was seen that an average strain measure across the height of the specimen and an average stress measure closely represented the material response. Furthermore, it should be noted that the purpose of the compression tests is to investigate if there is a pressure sensitivity as well as performing high strain-rate testing in a split Hopkinson pressure bar (SHPB) setup. For these purposes, it would be acceptable with more scatter than for the tension tests.

2.3.2. Test setup

The same servo-hydraulic Instron 5944 machine with a 2 kN load-cell was used to test the first 2 series of compression tests. A schematic of the test setup is presented in Figure 2.13a. The same two perpendicular cameras were used as with the tension tests, but now located 350 mm away from the specimens. It was also applied a speckled pattern to the compression tests using white spray-paint for DIC, as can be seen in the view from both camera angles in Figures 2.13b and 2.13c. In order to reduce friction between the machine and the test specimens, it was applied Teflon tape to the top and bottom of the compression test specimens. The first 2 series with 5 repetitions each were run at nominal strain-rates of $10^{-3}\,\mathrm{s}^{-1}$ and $5 \cdot 10^{-2}\,\mathrm{s}^{-1}$ corresponding to cross-head velocities of 0.6 mm/min and 30 mm/min respectively. Camera recording frequencies for the 2 test series were 1 Hz and 15 Hz respectively.

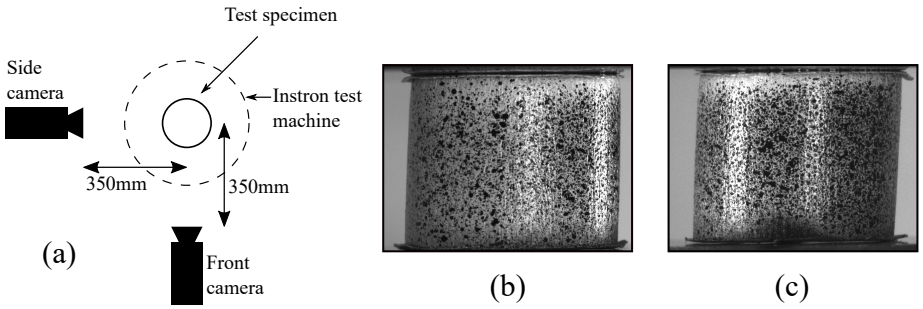

Figure 2.13.: Compression test setup in the servo-hydraulic test machine. (a) Schematic of the compression test setup, as seen from above. (b) View from front camera. (c) View from side camera.

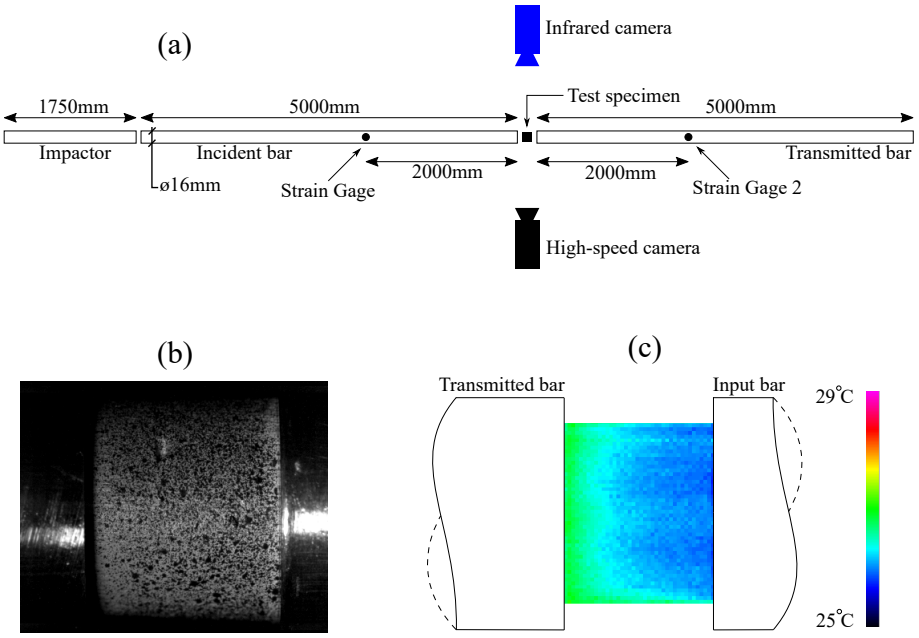

Figure 2.14.: Compression test setup in the split Hopkinson pressure bar (SHPB). (a) Schematic of SHPB setup. (b) View from high-speed camera. (c) View from thermal camera.

A split Hopkinson pressure bar (SHPB) was used to test the last series of 5 compression test specimens. The Hopkinson bars used in this setup consisted of two 5000 mm long steel bars with a diameter of 16 mm, as seen in Figure 2.14a. An impactor with length 1750 mm,

accelerated by pressurized air, was used to incite stress waves in the system. Two strain gages, each 2000 mm away from the specimen on the incident bar and transmitted bar, were used to record the stress waves assuming 1 dimensional elastic stress waves.

As shown in Figure 2.14a, a high-speed camera and a thermal camera were used to record the deformation of the specimen and the temperature change in the specimen. The high-speed camera of type Phantom v161 was recording at a frequency of 75000 Hz for all tests. Figure 2.14b show the view from the high-speed camera. Temperature measurements were done with the FLIR SC 7500 camera, recording at a frequency of 1125 Hz. It can be seen from Figure 2.14c that the resolution of the thermal camera had to be significantly reduced in order to record at the given frequency. Similar to the tension tests, these compression test specimens were covered with a white spray-paint to create speckled pattern for DIC and matte black spray-paint on the back surface for the thermal camera. It was not used any Teflon tape for the specimens tested in the SHPB.

The impactor velocity chosen for the test series was significantly lower than what was typically used to reduce noise in the response of the tests. A target impactor velocity of 3 m/s, with an actual velocity of 3.46 m/s, was used for the first repetition. However, due to observation of significant noise, the next 4 repetitions were run with a target impactor velocity of 2 m/s, giving impactor velocities between 2.27 m/s and 2.47 m/s. There was not observed any significant reduction in noise by reducing the target impactor velocity. The nominal strain-rate was estimated using DIC on the specimen, measuring a nominal strain-rate of roughly $350\,\mathrm{s}^{-1}$ for the first repetition and roughly $200\,\mathrm{s}^{-1}$ for the rest of the tests.

2.3.3. Post-processing techniques

Preliminary DIC analyses were run to investigate optimal mesh size and formulation for the compression tests. Figure 2.15a show the chosen mesh using linear elements with a size of $100\,\mathrm{px} \times 100\,\mathrm{px}$ equal to $1.5\,\mathrm{mm} \times 1.5\,\mathrm{mm}$. These elements were chosen to mitigate the expected effect of a gradient going from top to bottom of the specimen due to the slanted edges. The large linear elements increase the accuracy of the nodes and smoothing the strain field, leading to more accurate estimates of an average strain measure. Figure 2.15b show the gradient consistent with the expectations established in Section 2.3.1. The peak values of the principal stress are likely due to DIC error, which is emphasized at nodes on the edge of the mesh. Similar to the tension tests, the average strain was obtained using virtual extensometers as seen in Figure 2.15a. The transverse strain measurements obtained from these virtual extensometers were only used as an additional control of incompressibility, as a better measure of the transverse strains were obtained through edge tracing.

An edge tracing technique is able to track the diameter of the specimen with high accuracy, which in turn can be used to determine the transverse strains with high accuracy assuming

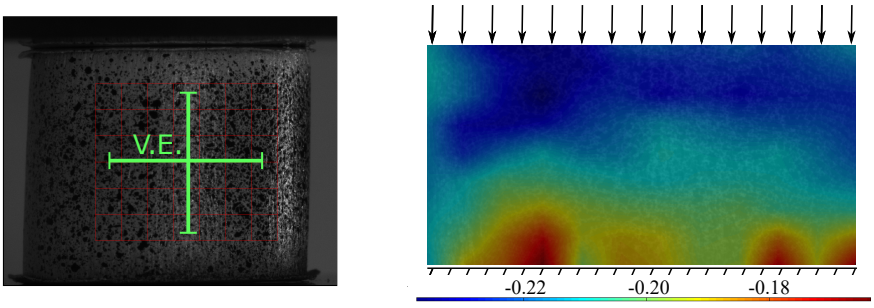

(a) (b)

Figure 2.15.: DIC on compression tests tested in the servo-hydraulic test machine. (a) DIC mesh and VE in initial configuration. (b) Example of principal strain field obtained from compression test at a nominal strain-rate of 10^{-3} s^{-1}.

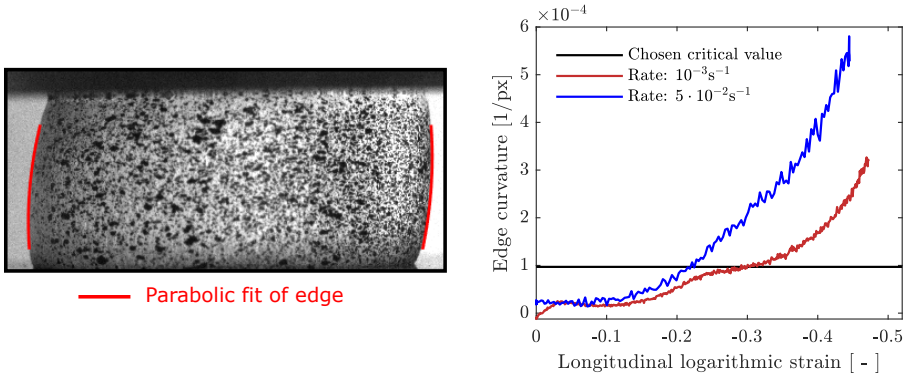

(a) (b)

Figure 2.16.: Edge tracing performed on compression specimens tested in the servo-hydraulic test machine. (a) Example of a fit of the tracked edges. (b) Examples of curvature change during the test for two experiments performed at different nominal strain-rates.

axisymmetric deformation. Compression tests tend to exhibit barrelling, which can be measured using edge tracing to determine the curvature of the specimens. A MATLAB script was used to track the edges, by finding the peak values of change in greyscale value along the x-coordinate of each image to determine the location of the edge. This was done for all lines over the height of the specimens. The pixel coordinates of each edge were then fitted to a second order polynomial dependent on the y-coordinate, as seen in Figure 2.16a. Further, the diameter of the specimens was determined by the difference in the average x-coordinate of the two fitted edges. Barrelling of the specimens was evaluated based on the average curvature of the two fitted second order polynomials. Figure 2.16b show a plot of the average curvature for two tests performed at different nominal strain-rates.

A critical value for the curvature was determined based on the initial curvature of the edges and approximately at the value when it started to accelerate serving as an indication of barrelling. Based on this critical value, a conservative cut-off value for longitudinal logarithmic strain was determined to be at -0.2.

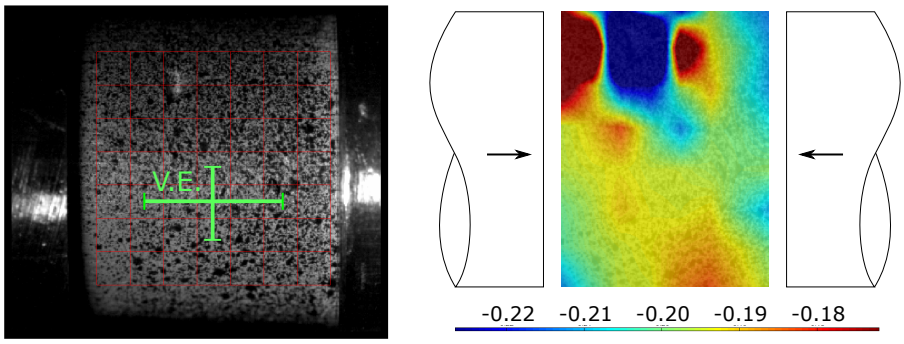

Figure 2.17.: DIC on compression tests tested in the SHPB. (a) DIC mesh and VE in initial configuration. (b) Example of the corresponding principal strain field.

DIC was performed on the tests in the SHPB in a similar fashion to the rest of the compression tests. However, the resolution of the high-speed camera was significantly lower, such that the size of the elements in pixels had to be reduced in order to keep the same spatial discretization. A DIC mesh size of 30 px$\times$30 px equal to 1.5 mm$\times$1.5 mm was used to analyse the SHPB compression tests, as seen in Figure 2.17a. Virtual extensometers were applied to obtain average strain measures, but only the longitudinal strain measure was used. An example of the principal strain field from the chosen representative test is shown in Figure 2.17b. The extremal values in the in the top left of Figure 2.17b is caused by a void on the surface of the specimen, which can be seen in the initial configuration in Figure 2.17a. In order to obtain a more representative strain measure, the location of the virtual extensometer was chosen to avoid this defect.

The Cauchy stress measured from the SHPB tests are based on the force which is obtained from the strain measured on the strain gage of transmitted bar. It is important to verify that the specimen is in equilibrium before using this strain measure to determine the force applied to the specimen. Figure 2.18a shows the strain data obtained from the strain gages on the Hopkinson bars, where the transmitted and reflected wave has been time-shifted on top of the incident wave. For equilibrium to be satisfied, the sum of the reflected and transmitted wave should be equal to incident wave. It is seen from the figure, that this is satisfied at all times except for the first 0.2 ms. The initial discrepancy is most likely linked to the tail of the incident wave. It was observed that the reflected wave reaches the strain gage on the incident bar while the incident wave still has a non-zero magnitude.

It was observed a significant amount of noise in the raw signal from the experiments.

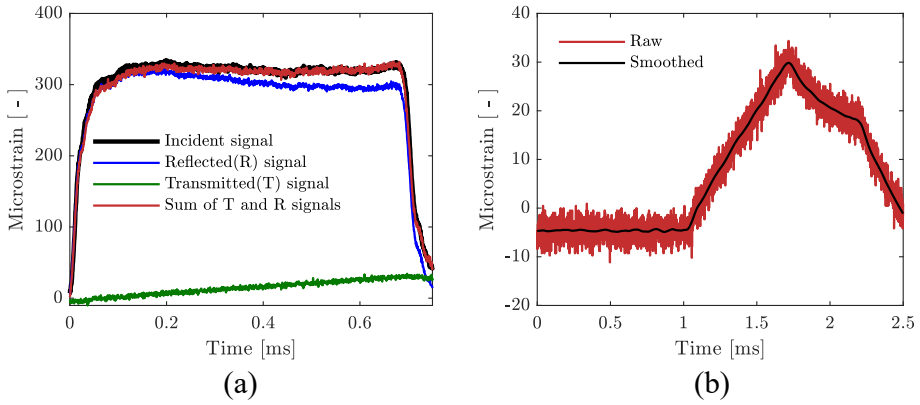

Figure 2.18.: Post-processing of SHPB measurements. (a) Confirmation of equilibrium. (b) Comparison between the measured data and the smoothed data.

However, this noise was seen to be randomly scattered around a smooth base signal, as it was the same noise before the incident wave hit the first strain gage. Therefore, it is believed that the filtered response should be representative of the contact force between the Hopkinson bars and the specimen. The accuracy should at least be satisfactory for giving a good indication of the strain-rate sensitivity of the adhesive material at strain-rates relevant for crash loading. A local regression with weighted linear least square fit smoothing algorithm in MATLAB was applied to smooth the curves. Figure 2.18b shows a comparison between the raw signal from the strain gage and the smoothed signal.

2.3.4. Test results

The Cauchy stress presented in this section is based on the assumption of incompressibility, as there were strong indications of close to incompressible behaviour presented in Section 2.2.4. Furthermore, the transverse strain measures from the compression tests strengthened this assumption. With the larger range of strain-rates obtained from the SHPB tests, it is clear that strain-rate sensitivity is a key phenomenon for this material, especially when modelling crash loading. It can be seen from Figure 2.19a that the strain-rate sensitivity behaves in a multiplicative manner for the compression tests as well. The specimens were deformed to a longitudinal logarithmic strain of approximately -0.5 before unloading. Despite the large deformation, all specimens were seen to return to their initial configuration after unloading, further strengthening the assumption of negligible plastic deformations.

Figure 2.19b shows the scatter present for the compression tests. There is significantly more scatter for the tests performed in the SHPB. This is likely caused by a combination

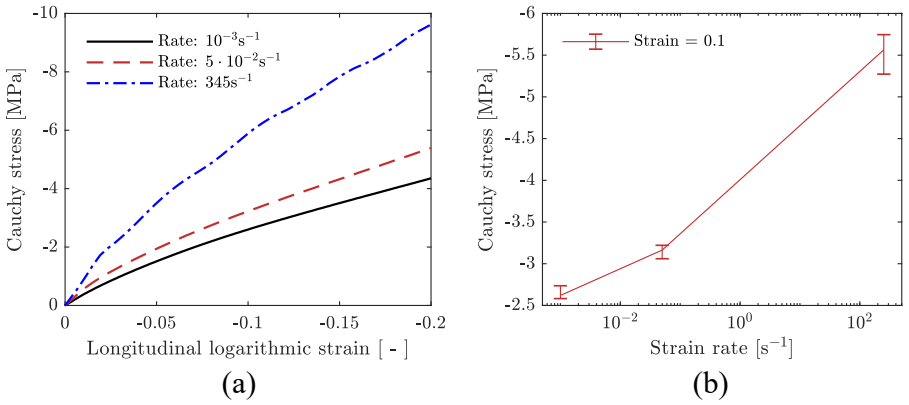

Figure 2.19.: Compression test results. (a) Representative stress-strain curves. (b) Scatter in tensile stress at 0.1 strain for three different nominal strain-rates.

of the difference in impactor velocity, arbitrary differences due to noise and any dynamic effects. Despite the previously mentioned flaws, the compression tests have less scatter than what was reported for the tension tests as the compression tests were made from a single batch.

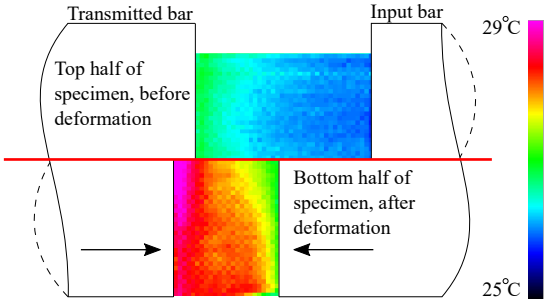

Figure 2.20.: Comparison between temperature measured in the initial configuration and deformed configuration for a SHPB test at a nominal strain-rate of 350 s^{-1}.

A different approach to measure the temperature changes had to be employed for the SHPB compression tests than for the tension tests. As the initial temperature field was inhomogeneous as well as large deformations and displacements of the specimens during the tests, an average measure was not possible to obtain. Therefore, the temperature change had to be estimated by picking a point before deformation and finding that same point after deformation in order to determine the difference. The gradient was seen to be the same both before and after the deformation such that it was possible to recognise the same points. This method does not provide the same level of accuracy as using an average measure as

done with the tension tests.

Figure 2.20 shows the difference of before and after deformation as seen from the thermal camera. There was observed a temperature change of about 2 K by considering the point with the highest temperature in the specimen. It should be noted that the total strain after the stress waves passed through the specimen 3 times was about -0.5, which is considerably less than for the tension test. Comparing the temperature change in the tension test at a strain of 0.5, it is considerably lower than for the SHPB compression test, which is consistent considering the respective strain-rates.

By significantly reducing the resolution of the thermal camera, a recording frequency of 1125 Hz was obtained. This frequency allows for only 5 to 6 pictures during the deformation of the specimens. This relatively low frequency leads to motion blur of the temperature measurements, as the specimen moves considerably in the time between each picture. The potential error caused by the low recording frequency is approximately bounded by the maximum difference in temperature between two pictures, which is roughly 0.5 K.

2.4. Notched tension tests

2.4.1. Test specimens

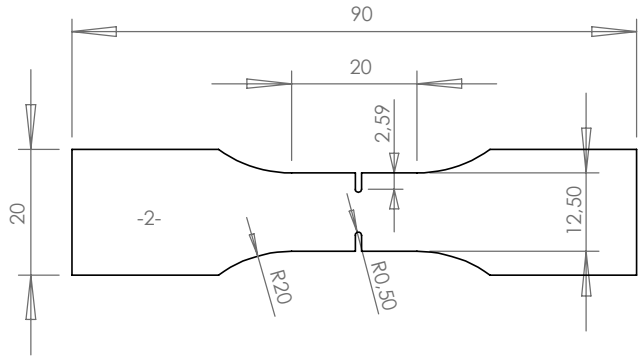

Figure 2.21.: Geometry of the notched tension test specimens.

Figure 2.21 shows the geometry of the notched tension test specimens. These specimens were designed with the intention of studying failure in the material. The notch ensures that failure is initiated in the critical cross-section for all repetitions. In this cross-section there is an increased stress triaxiality ratio with a peak value at the surface in the centre of the notch. Numerical simulations were used to determine the radius of the notch, with a goal of having a stress triaxiality ratio of at least 0.4 at failure. A hyperelastic Mooney-Rivlin

material model was calibrated based on an initial tension test and used to simulate the notched specimens. Failure was assumed to occur at a principal logarithmic strain of 0.7. The width of the notched region was set equal to that of the tension tests to make them comparable. The large deformations of the material before failure makes the notch stretch and converge towards a uniaxial tension test, which in turn meant that a very sharp notch was required to achieve an elevated stress triaxiality ratio at failure. Iterative simulations found that a radius of 0.5 mm was necessary to achieve a stress triaxiality ratio of 0.4 at failure.

The notched tension test specimens were produced from the same plates as the uniaxial tension test specimens and using the same machining techniques as described in Section 2.2.1. Therefore, the notched specimens were subjected to the same flaws as the tension tests. Specifically, the surface flaws caused by the waterjet cutting would likely be critical regarding failure in the notched region, as the stress state is critical at the surface.

2.4.2. Test setup

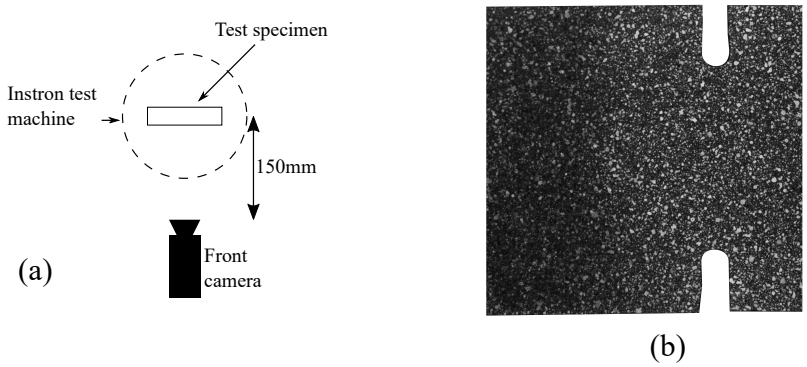

Figure 2.22.: Notched tension test setup. (a) Schematic of the notched tension test setup, as seen from above. (b) View from front camera.

Similar to the tension tests, the Instron 5944 servo-hydraulic test machine with a 2 kN load-cell was used to test the notched tension test specimens. A high-resolution camera was placed a distance of 150 mm away from the specimens as seen in Figure 2.22a. The high-resolution camera of type Ximea CB200MG-CM gives a spatial resolution of $7.17 \cdot 10^{-3}$ mm/px recording at a frequency of 1 Hz. All 6 repetitions of the notched tension tests were tested at a cross-head velocity of 1.2 mm/min corresponding to a nominal strain-rate of $2 \cdot 10^{-2}\,\mathrm{s}^{-1}$ based on the length of the notched region. It was applied a speckled pattern using a fine white spray-paint to facilitate DIC as seen in Figure 2.22b.

2.4.3. Post-processing techniques

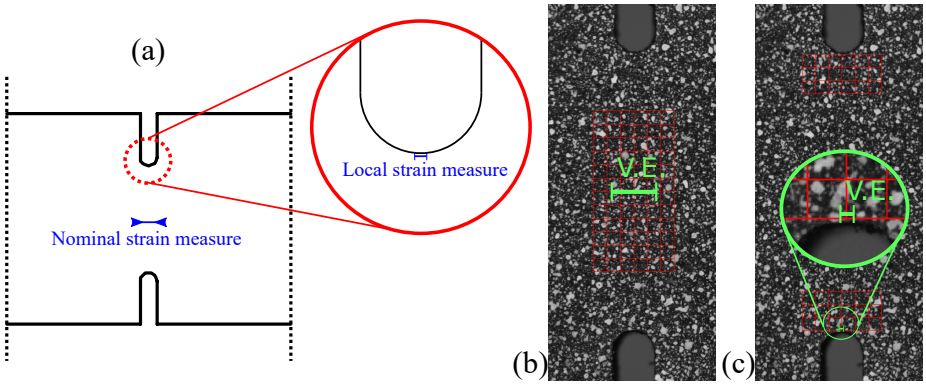

Figure 2.23.: DIC and strain measures for post-processing of notched tension tests. (a) Definitions of strain measures. (b) DIC to obtain the nominal strain. (c) DIC to obtain the local strain.

DIC in combination with high-resolution cameras enables several deformation measures with acceptable accuracy. In this work, it is defined two strain measures as depicted in Figure 2.23a. A nominal strain measure is defined at the centre of the notched region such that it could be used as a reference strain giving an indication of the global loading. The reference length for the nominal strain measure was chosen to be the same length as the length of the notched region equal to 1 mm. The local strain measure is defined in order to obtain a measure of the local behaviour of the notch in the critical region. A length-scale of 0.1 mm was set. This length-scale is smaller than the DIC element size, but the elements are of higher order, so it is expected to provide a sufficiently accurate measure of the local strain.

Two different DIC meshes were used to obtain the different strain measures. Figure 2.23b shows the mesh used to obtain the nominal strain measure. It was used linear elements with a size of $50\,\text{px} \times 50\,\text{px}$ corresponding to $0.36\,\text{mm} \times 0.36\,\text{mm}$. Similarly to the previous tests, it was used a virtual extensometer to extract the nominal strain measure. Figure 2.23c shows the mesh used to obtain the local strain measure. Due to the large strain gradients in this region, it was chosen to use quadratic elements instead of the linear elements. This leads to a larger DIC error, but in turn reduces the finite element error as the strain field is more accurately captured. A similar element size was used for this mesh as with the mesh for the nominal strain measure. The virtual extensometer used to obtain the local strain measure was centred over the location of crack initiation, which was seen to vary from test to test depending on the location of the critical flaw.

2.4.4. Test results

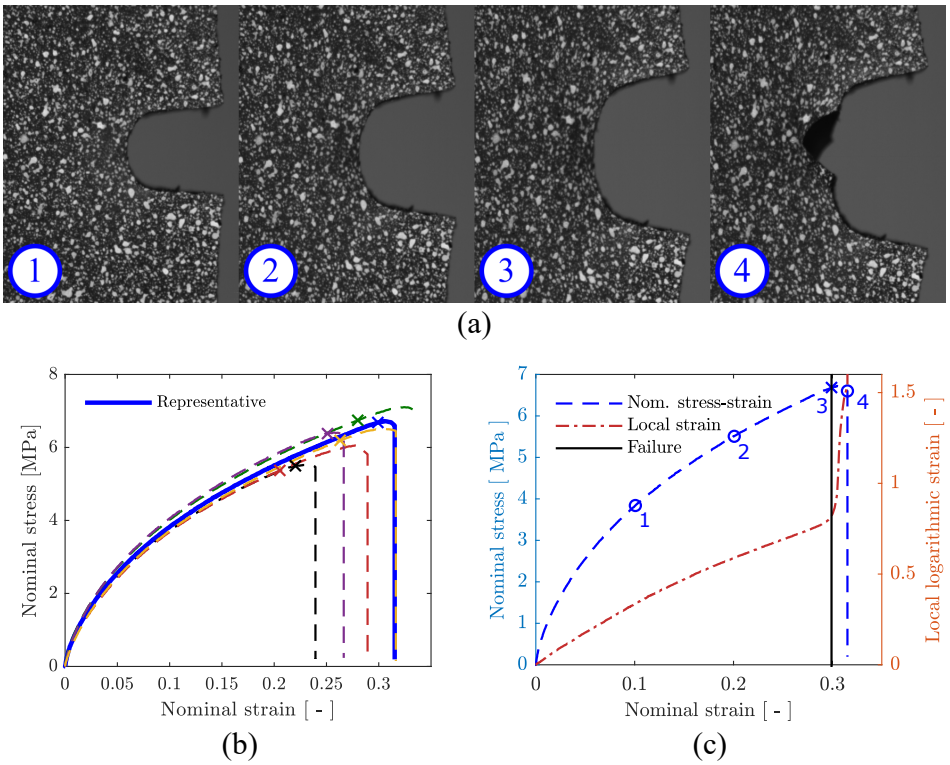

Figure 2.24.: Notch tension test results. (a) States of deformation of the notch corresponding to numbers in Figure 2.24C. (b) Nominal stress-strain curves for the notched tension tests. (c) Plot of nominal stress and local logarithmic strain versus nominal strain, illustrating how failure strain could be defined for these tests.

An example of the stages of deformation is presented in Figure 2.24a, where each frame number corresponds to a number on the curve in Figure 2.24c. It is evident from these stages of deformation that the large elastic strains of the material deform the notch gradually from a notched specimen to something close to a uniaxial tension specimen as discussed in Section 2.4.1. Figure 2.24b shows the nominal stress-strain curves obtained using the previously defined nominal strain measure and a stress measure based on the initial minimum cross-section. The onset of crack propagation is marked with an '×', this failure strain is defined based on the point where the local strain starts to diverge. An example of how this point was determined for a representative test is shown in Figure 2.24c. The blue curve represents the nominal stress-strain curve with values on the left vertical axis, while the red curve corresponds to the local strain versus nominal strain with values on the right vertical axis. It is seen that the behaviour of the local strain changes drastically over

a short span of nominal strain. Failure initiation is determined to occur at the start of this change. However, this is not an exact definition, which in turn introduces some scatter to the problem. Using this failure definition, it is evident that it is possible to detect crack initiation before it is visible on the surface as can be seen from stage 3 in Figures 2.24a and 2.24c. While the failure mechanism itself has been determined to be brittle, it behaves in a ductile manner. This is likely linked to the large elastic deformations, low stiffness and the distribution of flaws in the material.

Figure 2.24b shows that there is significant scatter in the nominal strain at failure initiation, complete loss of load-carrying ability and time from initiation to complete failure. Nominal strain at initiation varied between 0.2 and 0.3, while the local strain at initiation varied between 0.80 and 0.86. It is believed that the previously mentioned surface defects vary in both size and location. Especially the variance in location of the critical defect could lead to large scatter in nominal strain at failure initiation. However, the much smaller scatter in the local strain suggests that a critical defect has to be strained to a certain level before initiation, independent on location. Propagation of the crack would also be dependent on location of initiation and potentially also density of internal flaws such as unmixed adhesive. There was not observed any voids on any of the failed surfaces, indicating that the surface defects caused by the waterjet cutting were critical.

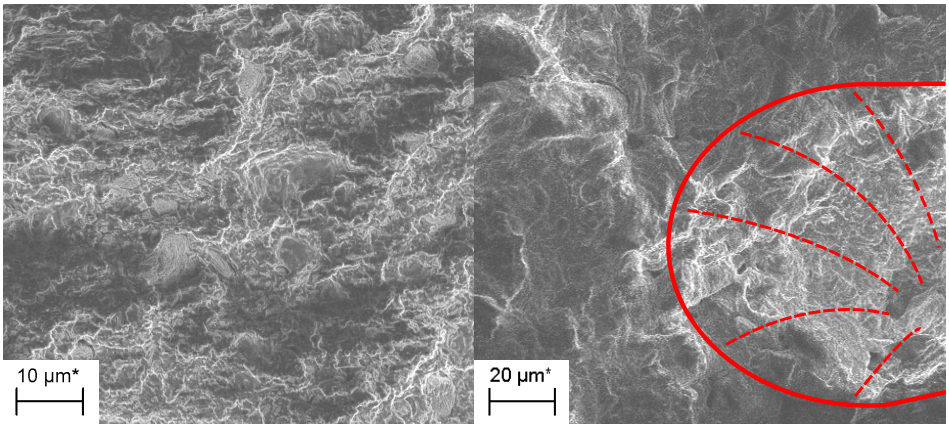

Figure 2.25.: SEM micrographs of the fractured surface of a notched test specimen. (a) Representative area of the fractured surface, pictured with a magnification factor of 726. (b) Fracture surface in area where it is likely that failure initiated, pictured with a magnification factor of 357.

Scanning electron microscopy (SEM) was used to further investigate the failure surface of one of the specimens. Figure 2.25a shows the SEM micrograph of a typical region of the failure surface with a magnification factor of 726. There are no clear ridges, dimples or fibrils visible that could indicate a ductile fracture mechanism unlike typical structural

adhesives. This is consistent with the lack of plasticity previously observed. Figure 2.25b shows a micrograph of the region where failure is likely to have initiated with a magnification factor of 357. This micrograph is taken from the edge of the failure surface, where the surface of the whole specimen would be. The red lines highlight a significant change in topology compared to the rest of the fractured surface, which is believed to be the initial flaw from which the crack initiated.

2.5. Single lap joint tests

2.5.1. Test specimens

In order to further investigate the behaviour of the adhesive in a joint configuration, it was made single lap joint (SLJ) specimens. It was also the intention to obtain an initial indication of the effects of using dissimilar adherents for this type of joint. The chosen adherent materials were carbon fibre reinforced polymer (CFRP) plates with continuous fibres cut from the flanges of a hat-section and a sheet moulding compound (SMC) material cut from flat plates. Ideally, it should have been steel and aluminium adherents, but the adhesive did not bond to these metals without more advanced surface preparations. The specimens could also be used for validation purposes, given that a proper material model for the CFRP and SMC material is calibrated.

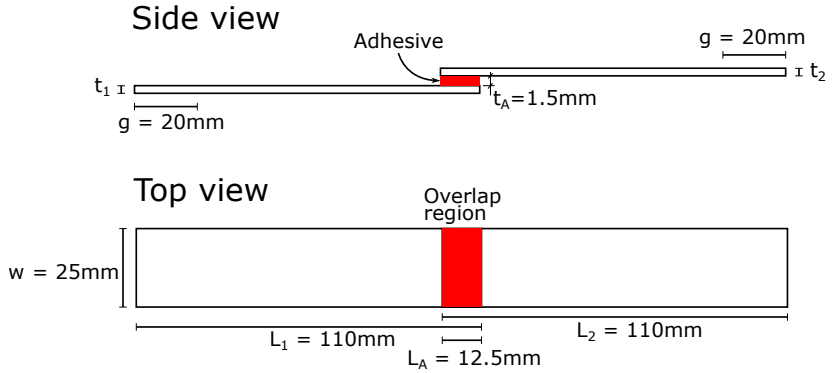

Figure 2.26.: Geometry of the single lap joint specimens.

Figure 2.26 shows the final geometry of the studied SLJ specimens. Dimensions were obtained from an industrial partner, which are almost the same as the geometry presented in the NS-EN 1465:2009 [110] standard. The adhesive thickness was set to be 1.5 mm, which is the nominal thickness used in the industry. This thickness is also comparable to the thickness of the plates used to make the bulk adhesive specimens. The length of the

clamped region at the ends of the specimen was chosen to be 20 mm based on the size of the grips in the test machine. There was used two types of adherent materials making a total of 3 configurations. First configuration is CFRP to CFRP, where the CFRP material has a thickness of 2.25 mm. Second configuration is SMC to SMC, where the SMC material has a thickness of 2.75 mm. Finally, the third and multi-material configuration consists of SMC and CFRP adherents. It was made and tested 5 repetitions of each configuration.

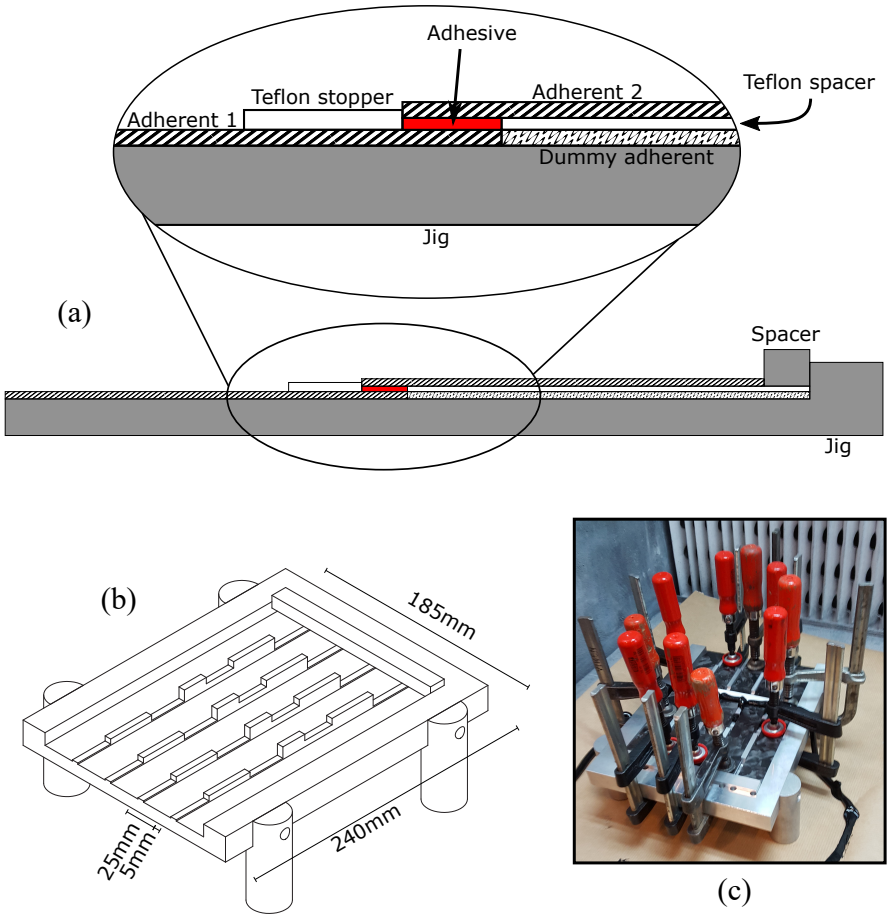

Figure 2.27.: Jig used to create SLJ specimens. (a) Longitudinal cross-section of the jig while in use, illustrating how the correct geometry is obtained. (b) Global view of the jig with key measures. (c) Picture of the jig in use.

Before the SLJ specimens could be produced, a jig had to be made in order to ensure the correct geometry of the specimens. The design of the jig is presented in Figure 2.27. It is intended to be flexible in the thickness direction to allow for different types of adherents

and different adhesive thicknesses. However, it is heavily constrained with respect all other dimensions. Figure 2.27a shows a cross-section of a SLJ specimen in the jig during reticulation, showing how the correct geometry is obtained using this jig. The thickness of the adhesive layer is controlled by the thickness of the Teflon spacer, while the correct overlap length is ensured by the metal spacer in the back. A dummy adherent of the same plate material as adherent 1 is used to ensure flexibility in terms of adherent thickness.

Key dimensions of the jig is shown in Figure 2.27b, where it is evident that the jig allows for 5 specimens at a time. The jig itself and the metal spacer are both made of aluminium. Additionally, the jig is covered with a release agent before use. Adherents were cut using the same waterjet cutting machine as used for the tension tests and the notched tension tests. The stiffness of the CFRP and SMC materials is at least two orders of magnitude higher than the bulk adhesive material. Therefore, waterjet cutting provides much better results for these specimens than for the bulk adhesive specimens. The surface preparation of the adherents consists of cleaning them with isopropanol before bonding. Additionally, the CFRP specimens are grinded with sandpaper to remove pollution from the production process.

In order to make the specimens, the parts were stacked up according to Figure 2.27a. Adhesive was added before the top adherent was placed. It was ensured continuous flow of adhesive while moving the nozzle from one side of the jig to the other, thus reducing the void content of the adhesive layer. The top adherent was then forced in place to squeeze out excess adhesive and complete the joint. Afterwards, fixtures were added to keep the adherents in place during curing as shown in Figure 2.27c. It should be noted that the 3 specimens in the middle of the jig are less securely fastened than the two on the edge, making them more prone to inaccuracies in the geometry. The specimens were fixed in the jig for more than a week before being released.

Before testing, the excess adhesive had to be removed from the specimens. A sharp knife was used to cut off larger pieces excess adhesive as it was difficult to cut with high accuracy. For more detailed cleaning, sandpapers with different grits were used iteratively in an attempt to obtain the nominal geometry of the specimens. As this process was performed manually, the accuracy was not sufficient to avoid significant defects. Particularly, it was difficult to create right angles, and there was also a tendency to grind the adherents in addition to the adhesive layer. Furthermore, there was typically a thin layer of excess adhesive that created a gap between the Teflon spacers and the adherents which was difficult to remove without damaging the adherents significantly. This layer was typically connected to the primary adhesive layer and therefore influencing the failure initiation and propagation for the specimens.

Overall, these issues in the production process reduced the quality of the specimens significantly. Particularly, the first series of 5 CFRP to CFRP specimens were poorly made, as the issues with thickness control was first discovered when inspecting these specimens. A variation of adhesive thickness between 1.63 mm to 2.6 mm was observed for these

specimens. The last two series of SMC to SMC and SMC to CFRP specimens were better, with the adhesive thickness varying between 1.8 mm to 2.25 mm.

2.5.2. Test setup

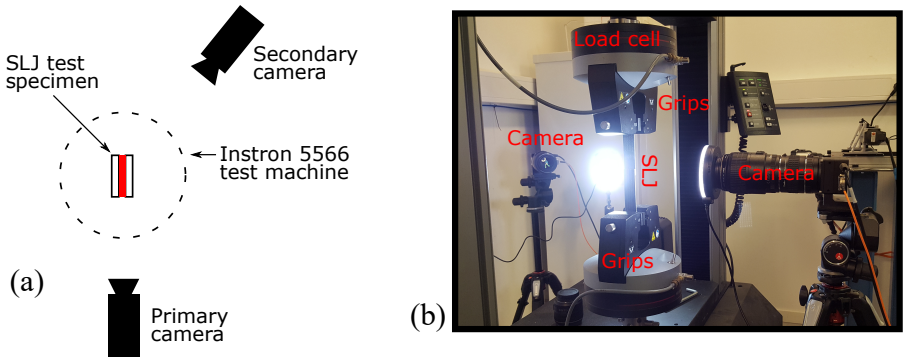

Figure 2.28.: SLJ test setup. (a) Schematic of the SLJ test setup, as seen from above. (b) Picture of the test setup in use.

To test the SLJ specimens, a servo-hydraulic Instron 5566 test machine fitted with a 10 kN load-cell was used. It was used adjustable grips to ensure that the SLJ specimens remained vertical and undeformed in the initial configuration. However, these grips were not flexible enough to fully account for the offset in the SLJ specimens. An angle up to 1.7° from the vertical line was observed on the top adherent of the thickest specimens, for the rest of the specimens this angle was measured to be around 0.5°. The tests were tested at a nominal shear rate of $10^{-2}\,\mathrm{s}^{-1}$. The nominal shear rate, $\gamma_{\mathrm{nominal}}$, was determined according to the equation: $\gamma_{\mathrm{nominal}} = v_{\mathrm{machine}}/t_{\mathrm{adhesive}}$, where v_{machine} is the crosshead velocity of the test machine and t_{adhesive} is the measured adhesive thickness. As the adhesive thickness varied for each specimen, the machine velocity was varied accordingly to ensure the same nominal shear rate.

DIC was employed in order to study the deformation of the SLJ specimens in detail. White spray-paint was used to apply a fine speckled pattern to the side of the specimens to facilitate DIC. It was used two cameras to record the specimens as shown in Figure 2.28a. The primary camera was a high-resolution camera of type Ximea CB200MG-CM, giving a spatial resolution of $4.17 \cdot 10^{-3}$ mm on the side of the specimen. A secondary camera of type Prosilica GC2450 was placed at an angle to the specimens to monitor any events not visible on the side surface. Both cameras recorded at a frequency of 8 Hz. The complete setup with lighting is shown in Figure 2.28b.

2.5.3. Post-processing techniques

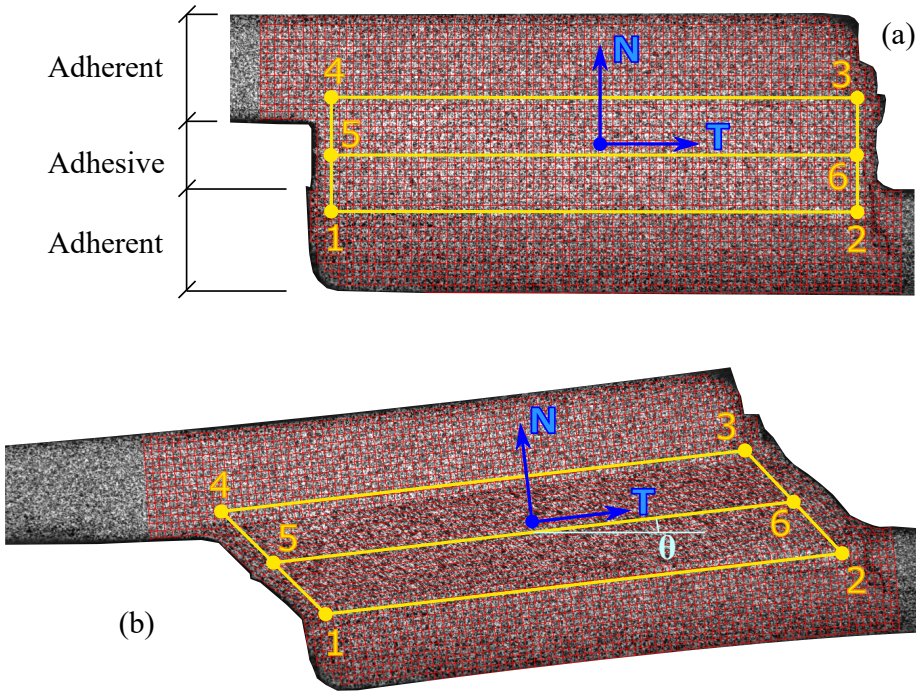

Figure 2.29.: DIC on SLJ test specimens with definition of 2D cohesive element used to obtain separations and rotations. (a) Initial configuration. (b) Deformed configuration.

DIC on the side surface visible to the high-resolution camera was the primary post-processing tool used to analyse the SLJ tests. A typical DIC mesh is presented in Figure 2.29, where it was used linear elements of size 40 px × 40 px equal to 0.17 mm × 0.17 mm. These DIC analyses provided field data allowing for qualitative comparisons between the different configurations. Additionally, point tracking on the DIC mesh was used to obtain deformation measures that more accurately describes the joint behaviour. These deformation measures are based on a 2D cohesive element formulation that takes the nodal coordinates of the corner nodes and returns joint separations and rotations.

The coordinates of the 4 corner nodes numbered 1 to 4 in Figure 2.29a are transformed from pixel coordinates to physical coordinates. Nodes 5 and 6 are defined to have the average coordinates of nodal pairs 1 + 4 and 2 + 3 respectively. These two nodes define the local coordinate system of the 2D cohesive element, where the tangential direction is parallel to the line going from node 5 to 6 and the normal direction being perpendicular to that vector. Separations are initially calculated between the two nodal pairs 1 + 4 and

2 + 3 separately. This is done by defining an initial vector describing the distances between the two nodes in the element coordinate system in the undeformed configuration. The next step is to find the same measure in the current configuration with an updated coordinate system and subtract the vector in the undeformed configuration to obtain the separations for each nodal pair. The global separation measures, Δ_N in the normal direction and Δ_T in the tangential direction, are then defined as the average of the separation calculated for each nodal pair. Finally, the separation in the tangential direction is set to be the absolute value of the measured tangential separation. The rotation angle of the joint is defined by the angle between the vector defining the tangential direction in the undeformed and deformed configurations as seen in Figure 2.29b. In order to keep the output data more compact and understandable, the analyses have been performed with only a single 2D element per joint.

A separate series of DIC analyses were run to investigate the local strain in the critical regions of the joints. The locations of crack initiation, as visible on the side surface of the specimen, were determined by looking through the images of the tests. There were typically 2 locations of crack initiation observed on the monitored side surface of the specimens for each test. These locations were mapped back to the undeformed configuration using the DIC analysis previously used to measure separations. A reference length of 0.2 mm was decided upon to study these failure initiation locations, using a mesh with linear elements of size 48 px × 48 px equal to 0.2 mm × 0.2 mm. The critical element was centred on the coordinates of failure initiation with 2 layers of elements on each side, yielding a 5×5 mesh, in order to increase DIC accuracy of the critical element. An additional 4 analyses were run per failure location, with the mesh offset by 12 px in each direction to find the most critical location.

A representative local failure strain was then calculated using a von Mises equivalent strain measure based on the 4 in-plane strain components, assuming all out-of-plane components equal to 0. Using the principal strains, this measure is simplified to the equation: $\varepsilon_{VMeq} = \sqrt{\frac{4}{9}(\varepsilon_1^2 + \varepsilon_2^2 - \varepsilon_1\varepsilon_1)}$, where ε_{VMeq} is the von Mises equivalent strain, ε_1 is the first principal strain and ε_2 is the second principal strain. The assumption that all out-of-plane strain components being equal to zero is false for these tests, but it is useful to generate a measure for comparisons. Furthermore, it was defined an upper and lower bound for the critical strain values. The lower bound was defined as the equivalent strain at the time when the strain measure started to diverge, while the upper bound was defined by the measured equivalent strain at the last frame before a visible crack.

2.5.4. Test results

There was observed large variations between the tests as will be documented in this section. However, the general behaviour of the SLJ tests is well represented by Figure 2.30. As

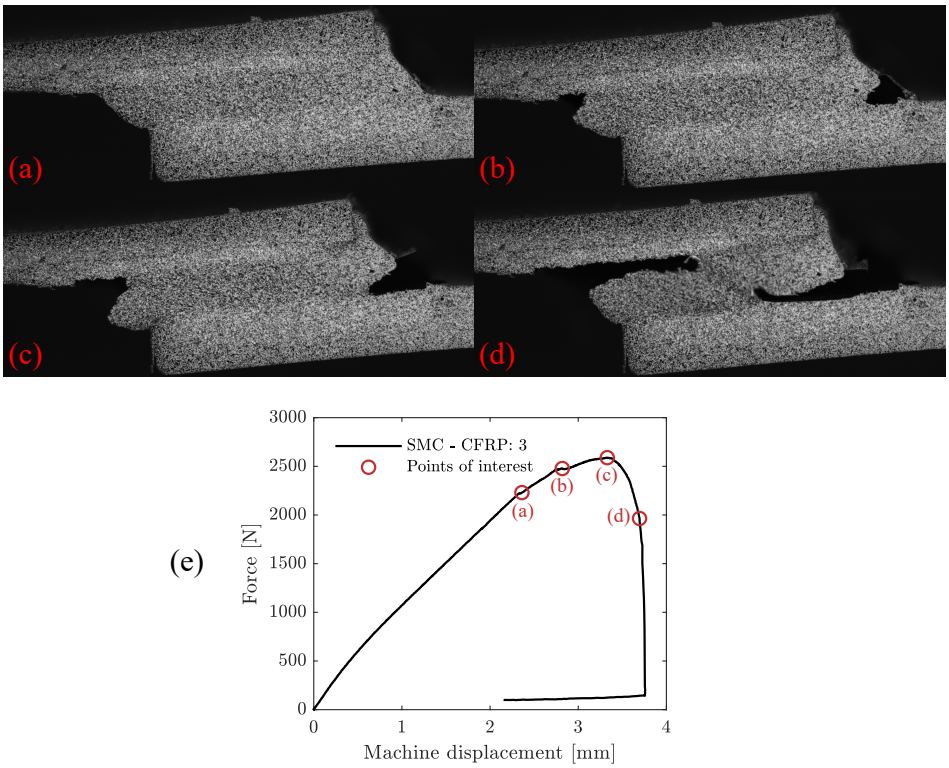

Figure 2.30.: States of deformation for a SLJ test with corresponding force displacement curve. (a) State a, after first failure, which is not visible on this surface. (b) State b, after second visible crack started propagating. (c) State c, peak force. (d) State d, before complete loss of load carrying capabilities. (e) Force displacement curve for the test where deformation states are indicated.

shown in the figure, there was typically observed a crack propagating on each of the two interfaces from two different sides. These cracks were seen to initiate long before the peak force was reached, showing that the responses of the specimens were increasing despite significant damage.

Studying Figure 2.30 in detail, it is clear from Figures 2.30a and 2.30e that the crack is initiated before it is visible on the studied surface. This was confirmed using the second camera. In Figure 2.30b the initial crack has propagated to the monitored surface. A second crack has also started propagating at that point, leading to a temporary loss of stiffness as seen in Figure 2.30e. Peak force is reached in Figure 2.30c, with large visible cracks. Finally, it is shown in Figure 2.30d that the specimens have significant load-carrying capabilities with only a fraction of the adhesive layer still active.

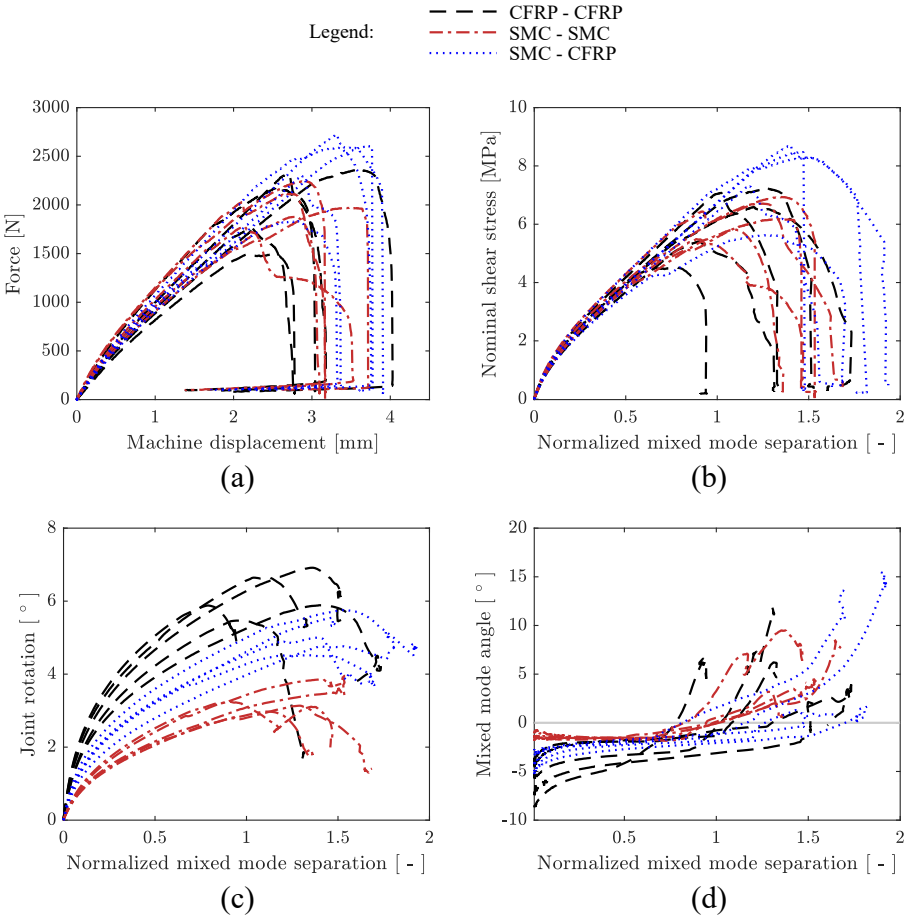

Figure 2.31.: SLJ results for all 5 repetitions for each of the 3 configurations. (a) Force versus machine displacement curves. (b) Nominal shear stress versus normalized mixed mode separation. (c) Rotation of joint versus normalized mixed mode separation. (d) Mixed mode angle versus normalized mixed mode separation.

Based on the measures described in Section 2.5.3, it has been defined 3 key measures to present the results of the SLJ in Figure 2.31. The mixed mode separation, Δ_{MM}, is defined as follows:

$$\Delta_{MM} = \sqrt{\Delta_N^2 + \Delta_T^2} \tag{2.4}$$

where Δ_N is the separation in the normal direction and Δ_T is the separation in the tan-

gential direction as described in Section 2.5.3. The normalized mixed mode separation, $\Delta_{\text{MM\_normalized}}$, is defined by the equation:

$$\Delta_{\text{MM\_normalized}} = \frac{\Delta_{\text{MM}}}{t_{\text{adhesive}}} \tag{2.5}$$

where t_{adhesive} is the adhesive thickness. Finally, the mixed mode angle, α, is defined as follows:

$$\alpha = \frac{180}{\pi}\arctan\left(\frac{\Delta_{\text{N}}}{\Delta_{\text{T}}}\right) \tag{2.6}$$

A mixed mode angle of 0° represents pure tangential separation, while an angle of 90° represents pure normal separation. Mixed mode angles lower than 0° represents negative normal separation, or compression, which is typically mixed with some tangential separation. Note that the tangential separation was defined to be positive, such that the sign of the mixed mode angle always refers to either tension or compression in the normal direction.

Figure 2.31a shows the machine displacement versus force measured in the load-cell representing the raw data from the test machine. All repetitions for the 3 configurations are presented, showing a large amount of scatter. There is seemingly no tendency in the scatter other than that the SMC to CFRP specimens tend to fail later. The results suggest that the specimen quality is the governing parameter regarding failure for these tests. Therefore, it is likely that this trend with later failure for the SMC to CFRP specimens are simply caused by the fact that they were made last and with the highest precision.

The normalized mixed mode separation deformation measure defined by Equation 2.5 is used as a representative deformation measure in Figure 2.31b, emphasizing the adhesive behaviour. Further, the stress measure used is defined by dividing the total force on the in-plane cross-sectional area of the adhesive layer, representing an average shear stress. It should be noted that for all configurations, the stiffnesses of the adherents are much higher than the adhesive layer. Therefore, the deformations localize in the adhesive layer, making the thickness of the adhesive layer a critical parameter. Comparing Figures 2.31a and 2.31b it can be seen that the scatter in stiffness is significantly reduced when the deformation measure is normalized to the adhesive thickness. Looking at two of the outliers, measurements of the geometry suggest that these are significantly flawed specimens. The CFRP to CFRP specimen with the overall worst performance is the specimen with the by far largest adhesive thickness, strongly suggesting a heavily flawed production process. Further, the SMC to CFRP tests with the worst performance was also seen to have a significantly longer overlap length than the nominal value, again suggesting significant production flaws.

Figure 2.31c shows the joint rotation as defined in Figure 2.29 versus the normalized mixed mode separation. While the deformation localizes in the adhesive layer, it is evident that the joint rotation is governed by the stiffness of the adherents. It is clear that the SMC adherents have a higher bending stiffness than the CFRP adherents primarily due to the large adherent thickness. The joint rotation is seen to be decreasing at the end of the tests, this is caused by the damage of the adhesive layer reducing its ability to transfer bending moment to the adherents.

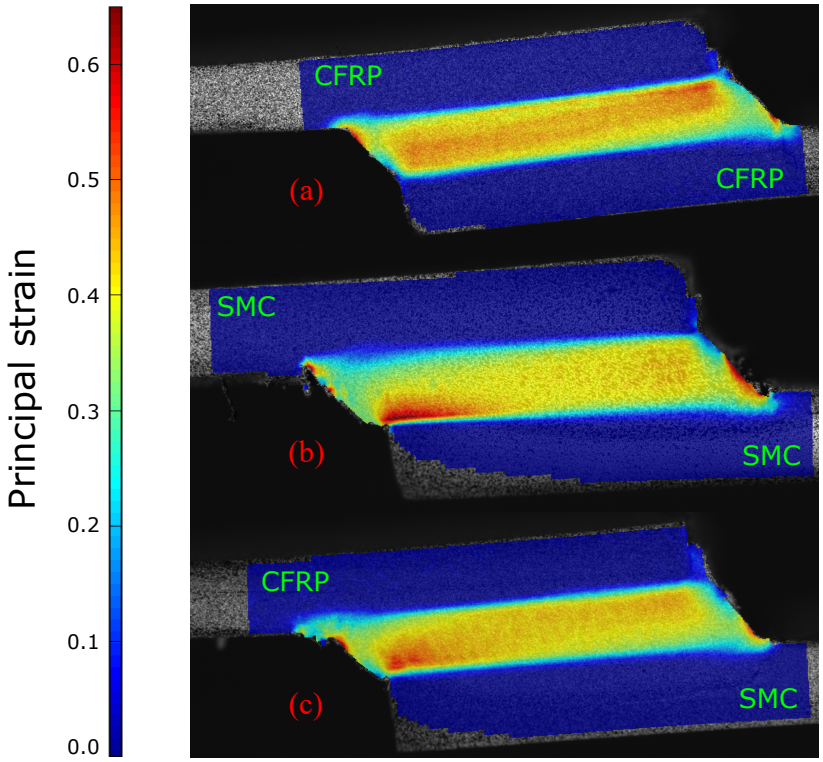

Figure 2.32.: First principal strain field obtained from DIC at a normalized mixed mode separation of 0.935. (a) CFRP to CFRP specimen. (b) SMC to SMC specimen. (c) SMC to CFRP specimen.

The kinematics of the joint can be further studied looking at the ratio between tangential and normal separation defined by the mixed mode angle in Equation 2.6. Figure 2.31d shows how the mixed mode angle changes throughout deformation of the specimen. It is seen that all tests are dominated by tangential separation as to be expected from a SLJ. However, there is initially a compressive component in the normal direction for all specimens that gradually turns into a tension component. This tension component seems to be accelerated by the failure process in the specimens. Similarly to Figure 2.31c, the stiffness of the adherents is a key component influencing the mixed mode angle of the tests. Additionally,

the scatter in the adhesive thickness propagates to the scatter in both joint rotation and mixed mode angle as it influences the initial offset and therefore the bending moment.

Figure 2.32 shows the measured first principal strain field based on DIC at a normalized mixed mode separation of roughly 0.935 for all 3 configurations. The specimens chosen to be displayed in the figure are those that allowed for large deformation before significant crack propagation, thus making the strain fields easier to compare. All the specimen types are seen to have weak strain-gradients in the adhesive layer except for peak values close to or at the edge of the adhesive domain. The measured principal strain in the centre of the adhesive layer is seen to be around 0.42 for all 3 configurations. This indicates that the normalized mixed mode separation is a relevant measure of the state of deformation in the adhesive layer. There seems to be some deformation into the region of the adherents, although it is likely that this effect is caused by excess adhesive that was not removed properly.

Comparing the different configurations to each other, it is seen that both the location and intensity of the peak strain regions vary arbitrarily between them. These differences were also spotted within each configuration of adherents. Therefore, it seems that the production flaws dominate the adhesive behaviour in the critical region, while the multi-material aspect is of less importance for these tests.

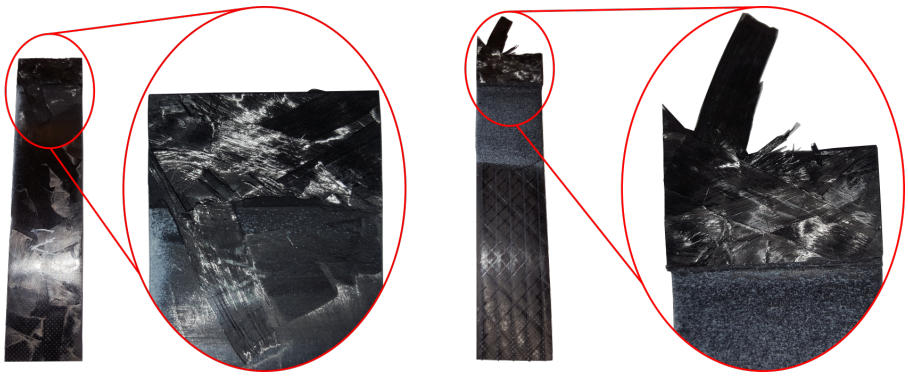

Figure 2.33.: Delamination failure of SMC adherent.

Failure of the specimens seems primarily to be adhesion failure or cohesive superficial. Although it is difficult to differentiate between those two, it was consistently observed large deformations in the adhesive layer adjacent to crack tip. For the tests with the SMC adherents, it was possible to hear continuous cracking in the adherents during the test, with gradually increasing intensity until failure. There was one repetition where either the adhesion was better than the other repetitions or with a larger flaw in the SMC that failed through delamination in the SMC. The failure surfaces of this specimen are presented in Figure 2.33. An indication of the effect of having dissimilar adherents is shown by 4 out of 5 SMC to CFRP specimens initiate failure on the side of the SMC adherent.

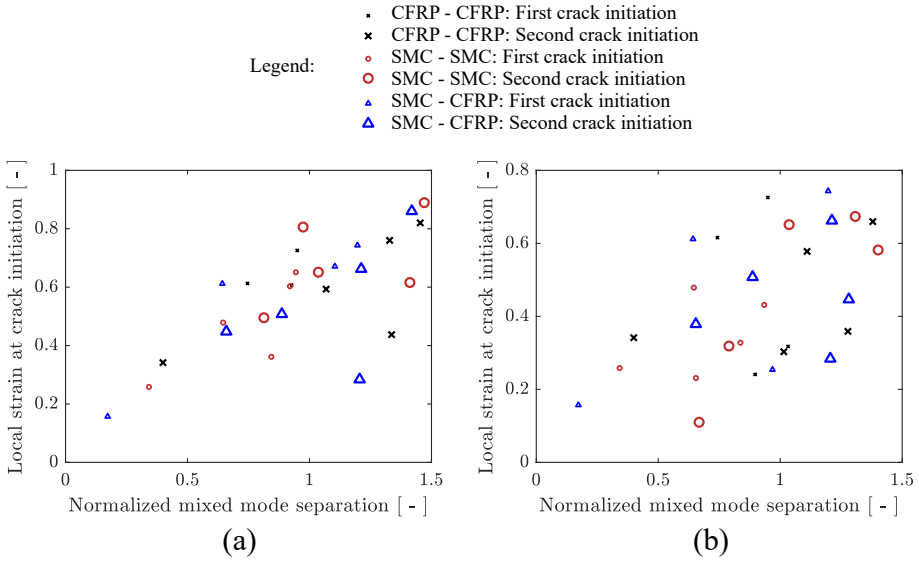

Figure 2.34.: Scatter plots of measured failure strain versus normalized mixed mode separation for all tests with both first and second crack initiation. (a) Upper bound for failure strain using the given measurement technique. (b) Lower bound for failure strain using the given measurement technique.

Figure 2.34 shows the measured failure strain as defined in Section 2.5.3. Overall, there was observed huge scatter in this failure measure indicating that the problem is dominated by production flaws of differing sizes and locations. There is a weak linear relation between the normalized mixed mode separation and measured failure strain for the upper bound criteria as seen in Figure 2.34a. This could be caused by the fact that cracks initiated earlier are less critical and therefore smaller. As there is a constant length-scale of 0.2 mm applied to the failure measurement, these smaller cracks would register with a lower failure strain. This effect is also present when using the lower bound definition. However, a lot of the points are registered at lower failure strains due to an initial crack occurring in the 3D domain of the adhesive layer and not on or close to the monitored surface. This was confirmed by the secondary camera, where there were observed cracks growing significantly before reaching the monitored surface.

2.6. Discussion and concluding remarks

2.6.1. Discussion

The results from the experiments performed in this chapter are for the most part consistent with what is presented in Section 1.2.1. Previous studies on polyurethane based adhesives have shown similar results in terms of large strains before failure ([11], [57], [86]). A significant strain-rate sensitivity was also reported by both Jia et al. [11] and Golaz et al. [86]. Duncan and Dean [10] suggested that flexible adhesives, defined as semi-structural adhesives in the current work, exhibit similar mechanical properties as rubbers. The behaviour reported in this chapter is similar in nature to what was reported by Sasso et al. [16] for a rubber-like material, thus reinforcing the description of the studied adhesive being rubber-like.

Unlike the results presented by Jia et al. [11], there was not observed any large changes in the behaviour of the stress-strain curve with increasing strain-rate. It is likely that this change was caused by the glass transition of the polymer. The glass transition phenomenon is known to be both time and temperature dependent. Further, these two variables interact with each other through the time-temperature equivalence principle [111]. Therefore, the glass transition temperature is not uniquely defined for a given material. The technical data sheet for the material studied in this thesis reported a glass transition temperature of -45 °C, while Jia et al. reported a glass transition temperature of 45.5 °C. This large difference explains the difference in the observed behaviour, however a similar behaviour might still be observed for the studied material if tested at significantly higher strain-rates.

Overall, the test results provide a more complete overview of the mechanical behaviour of this type of adhesives in one experimental campaign compared to previous literature. However, there are some key tests missing that could provide higher accuracy and certainty regarding modelling strategies for the next chapter. Shear tests provide key information to the shear behaviour of the material which is an important deformation mode. It is shown by Bergström [81] that several material models that perform well in tension provide poor results in shear. The lack of shear data introduces a restriction on the model selection which will be further discussed in the next chapter. Similarly, biaxial tension tests provide additional information that could be used to determine more suitable material models. There was not performed any dynamic mechanical analysis (DMA) on the material, which is needed to calibrate a linear viscoelasticity with high accuracy for a large range of strain-rates. The primary reason for not performing these tests was to save time and keep the calibration process as simple as possible while still capturing the key phenomena. Furthermore, it is difficult to design and machine shear tests as they would tend towards uniaxial tension when subjected to large deformations.

Putting the adhesive in context of a joint adds additional challenges as is evident by the

SLJ tests performed in this chapter. While there was observed some scatter in the bulk adhesive specimens that propagates to the joint level, it seems that flaws on the joint level both in terms of geometry and surface quality dominate the behaviour. The joint adds a few key complicating factors such as other failure modes that are not directly linked to the behaviour of the adhesive itself including adhesion failure and adherent failure. Ideally, the joints should only exhibit cohesive failure in the adhesive layer in order to reflect the adhesive behaviour on a joint level. It is also clear that small changes in the geometry has a much larger effect than that of the material scatter documented in the bulk adhesive tests.

The failure strain measurements presented in Section 2.5.4 do not provide any relevant information due to the already mentioned problems. However, these measurements showcase what information could be obtained using the presented method. Given a higher quality of the test specimens yielding more consistent results, it would be possible to use this data as an additional point for calibration and for validation purposes. It is evident that it is possible to obtain significantly more information from these simple SLJ tests than what is typically reported in literature by using the different measures presented in Section 2.5.3.

There are several improvements that could be made to better the results of the SLJ tests in order to make the results useable for further investigations. A new jig design which is able to handle the excess adhesive in a more controlled manner in addition to better fixtures would greatly improve the global geometry of the specimens. This would significantly increase consistency until failure. In order to improve consistency with regards to failure, it would be essential to use machines that could remove the excess adhesive with high precision. The improved geometry of the adhesive layer achieved with these methods would ensure that failure propagates through the width of the specimen faster. This would make the failure strain measurement more consistent. Further, a trigger could be added to ensure that failure initiates at the same place on the monitored surface every time for additional consistency with regards to the failure strain measure.

2.6.2. Conclusions

The experimental campaign performed in this chapter identified the key phenomena governing the mechanical behaviour of the studied two-component polyurethane adhesive. Based on the tension tests, the material was found to exhibit large elastic strains without permanent deformations. It was also seen to be close to incompressible, strain-rate sensitive in a multiplicative manner and exhibit a brittle failure mechanism. The compression tests reinforced these observations in addition to showing insignificant adiabatic heating and symmetric behaviour in tension and compression. SEM images of one of the fractured notched tension test specimens further strengthened the assumption of a brittle failure mechanism. Failure location was seen to vary on the notched tension tests despite the tests having a clear critical point. This suggests that flaws are governing the failure behaviour of the material. Overall, the studied adhesive was seen to exhibit a rubber-like behaviour.

Moving up in scale to a single lap joint, the production flaws were seen to heavily influence the behaviour of the joints with the given production quality.

Nevertheless, the experimental campaign performed in this chapter provides a sufficient experimental basis for determining suitable numerical models and to calibrate them on a mesoscopic scale. This concludes the first step in the overarching research strategy for the semi-structural two-component polyurethane adhesive, which is presented in Section 1.5. Although this adhesive will only be studied numerically on a mesoscopic scale, this chapter shows how an unknown material can be sufficiently characterized in order to model it. It is also shown in later chapters that a similar approach to the one employed here represents the first step in a multi-scale modelling strategy for adhesives.

3. Numerical campaign: Polyurethane adhesive

3.1. Introduction

This section will give a description of the chapter by presenting the goals for the numerical study and putting it in context of the overall objectives and research strategy of the thesis. It will also provide a more detailed review of the relevant hyperelastic material models that have been applied for modelling the adhesive. Finally, the choice of modelling strategy for this chapter will be discussed.

3.1.1. Chapter description

Chapter 2 presented experimental data for the semi-structural two-component polyurethane adhesive BETAFORCE 2816L, which will be used as a basis for all studies performed in this chapter. The goal of this chapter is to use this data to find a suitable numerical framework for meso-scale modelling of that specific adhesive, then calibrate and validate the models. This represents the next step of a multi-scale modelling approach, in line with the objectives and research strategy outlined in Sections 1.3 and 1.5 respectively.

The chapter is structured in two primary sections. Section 3.2 provides a detailed overview of the two material models that have been applied including all the relevant equations. Then, the numerical integration scheme will be outlined with key functions and an algorithmic overview of the stress update, sub-stepping scheme and numerical estimation of the tangent operator is presented. Further, the calibration procedure and results are described in detail. The next section describes the validation process, which is based on the notched tension tests presented in Section 2.4. Numerical issues, validation results and viability of the suggested approach are discussed and concluded upon in Section 3.4.

3.1.2. Background: Hyperelastic constitutive models

An initial study was performed in order to determine a suitable material model for meso-scale modelling of the adhesive BETAFORCE 2816L. As outlined in Section 1.2 and highlighted by Duncan and Dean [10], semi-structural adhesives are typically modelled with a hyperelastic material model combined with linear viscoelasticity. For the initial study, only the quasi-static response was considered. Duncan and Dean suggested that the Neo-Hookean (NH) [77], Arruda-Boyce eight-chain (AB) [79], Mooney-Rivlin (MR) ([75],[76]) and Ogden (OG) [78] models could be applied to these types of adhesives. Furthermore, Lubowiecka et al. [57] found the NH and AB models suitable, while Golaz et al. [86] used a 3-term OG model with success. Therefore, the 4 models NH, AB, MR and OG were considered in this initial study.

A brief description of the 4 models is given below and discussed in light of the experimental results obtained from tension and compression tests ran at a nominal strain-rate of 10^{-3}s^{-1}. The presented calibrations were performed in the Abaqus FEA suite [112] using the test data from Chapter 2. Incompressibility has been assumed for the comparisons to the uniaxial test data. Therefore, the focus of the model descriptions will be on the deviatoric response.

Before continuing, some continuum mechanics measures for finite strain deformations will be defined, as they will be used continuously throughout this chapter. The fundamental kinematic variable is the deformation gradient, $\mathbf{F}$, which represents a mapping between the initial and current configuration. It is defined by the equation:

$$\mathbf{F} = \frac{\partial \mathbf{x}}{\partial \mathbf{X}} \tag{3.1}$$

where $\mathbf{x}$ represents the position in the current configuration and $\mathbf{X}$ represents the position in the initial configuration. Based on the deformation gradient the right and left Cauchy-Green deformation tensors, $\mathbf{C}$ and $\mathbf{B}$ respectively, are defined by the equations:

$$\mathbf{C} = \mathbf{F}^T\mathbf{F} \tag{3.2}$$

$$\mathbf{B} = \mathbf{F}\mathbf{F}^T \tag{3.3}$$

The Jacobian, J, represents the volume change and is defined by the determinant of the deformation gradient:

$$J = \det(\mathbf{F}) \tag{3.4}$$

It is practical to split the models into a volumetric and distortional component. Therefore, the isochoric right and left Cauchy-Green deformation tensors, $\mathbf{C}_{\text{iso}}$ and $\mathbf{B}_{\text{iso}}$ respectively, are defined by the following equations:

$$\mathbf{C}_{\text{iso}} = J^{-\frac{2}{3}}\mathbf{C} \tag{3.5}$$

$$\mathbf{B}_{\text{iso}} = J^{-\frac{2}{3}}\mathbf{B} \tag{3.6}$$

The first of the considered models is the Neo-Hookean (NH) model [77] as it is the simplest of the hyperelastic material models. Only 2 material parameters are required to describe the response of a material using a NH model. The distortional response is defined by the shear modulus, μ, and the volumetric response is defined by the bulk modulus, K. There are several versions of the NH potential used in literature. However, the model presented here has a clear separation between the distortional and volumetric components. The Helmholtz free energy potential per unit reference volume, Ψ_{NH}, is defined as follows:

$$\Psi_{\text{NH}}(I_1^*, J) = \frac{\mu}{2}(I_1^* - 3) + K(J - \log(J)) \tag{3.7}$$

where I_1^* is the first invariant of the isochoric right Cauchy-Green deformation tensor, which is defined by the equation:

$$I_1^* = \text{trace}(\mathbf{C}_{\text{iso}}) \tag{3.8}$$

In order to give a better idea of the response of the model, the Cauchy stress of the model when subjected to uniaxial tension and compression assuming incompressibility will be presented. The deformation gradient for incompressible uniaxial deformation, $\mathbf{F}_{\text{uniax}}$, is given by the equation:

$$\mathbf{F}_{\text{uniax}} = \begin{bmatrix} \lambda_{\text{uniax}} & 0 & 0 \\ 0 & \frac{1}{\sqrt{\lambda_{\text{uniax}}}} & 0 \\ 0 & 0 & \frac{1}{\sqrt{\lambda_{\text{uniax}}}} \end{bmatrix} \tag{3.9}$$

where λ_{uniax} is the stretch in the longitudinal direction of a uniaxial tension and compression test. Given this deformation field, the Cauchy stress in the longitudinal direction, $\sigma_{\text{NH,uniax}}$, is given by the equation:

$$\sigma_{\text{NH,uniax}} = \mu\left(\lambda_{\text{uniax}}^2 - \frac{1}{\lambda_{\text{uniax}}}\right) \tag{3.10}$$

Figure 3.1 shows a comparison between the nominal stress-strain curves of the calibrated NH model and the test data. It is evident that this simple model is not able to capture the strong non-linear behaviour of the test data as it is seen to diverge considerably at larger strains.

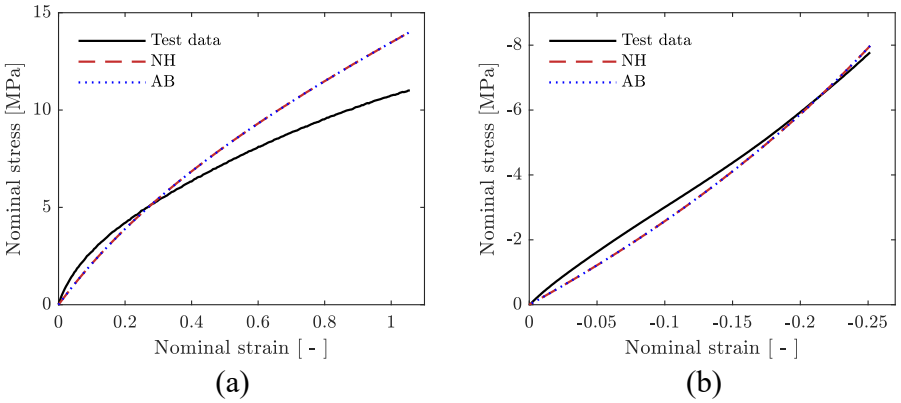

Figure 3.1.: Calibration results of a Neo-Hookean model and an Arruda-Boyce eight-chain model compared to nominal test data from uniaxial tension and compression tests described in Chapter 2. (a) Tension. (b) Compression.

The Arruda-Boyce eight-chain (AB) model [79] is a micromechanically based model as described in Section 1.2. It was originally developed for large stretch behaviour of rubber, which is suitable for the studied adhesive as it was seen to behave in a rubber-like manner. A key feature of this model is that it accounts for the finite length of the polymer chains indirectly through the locking stretch parameter, λ_{lock}. This ensures that the response tends toward infinity as the effective chain stretch, λ_C, approaches the locking stretch, which is a phenomenon that is often observed in rubber-like materials at large strains. Despite the complexity of the model, it only requires 3 parameters for the version used in this thesis. These are the effective shear modulus, μ_{AB}, the locking stretch, λ_{lock}, and the bulk modulus, K. The Helmholtz free energy potential per unit reference volume, Ψ_{AB}, is defined as follows:

$$\Psi_{\mathrm{AB}}(\lambda_C, J) = \mu_{\mathrm{AB}}\lambda_{\mathrm{lock}}^2\left(\left(\frac{\lambda_C}{\lambda_{\mathrm{lock}}}\right)\mathcal{L}_{\mathrm{chain}}^{-1} + \log\left(\frac{\mathcal{L}_{\mathrm{chain}}^{-1}}{\sinh(\mathcal{L}_{\mathrm{chain}}^{-1})}\right)\right) + K(J - \log(J)) \tag{3.11}$$

where $\mathcal{L}_{\mathrm{chain}}^{-1}$ is defined by the equation:

$$\mathcal{L}_{\mathrm{chain}}^{-1} = \mathcal{L}^{-1}\left(\frac{\lambda_C}{\lambda_{\mathrm{lock}}}\right) \tag{3.12}$$

where $\mathcal{L}^{-1}(x)$ is the inverse Langevin function and λ_C is the effective chain stretch defined by the equation:

$$\lambda_C = \sqrt{\mathrm{trace}(\mathbf{B}_{\mathrm{iso}})/3} \tag{3.13}$$

Assuming the uniaxial deformation field given in Equation 3.9, the Cauchy stress in the longitudinal direction, $\sigma_{\mathrm{AB,uniax}}$, is described by the equation:

$$\sigma_{\mathrm{AB,uniax}} = \frac{\mu_{\mathrm{AB}}\lambda_{\mathrm{lock}}}{3\lambda_C}\mathcal{L}^{-1}\left(\frac{\lambda_C}{\lambda_{\mathrm{lock}}}\right)(\lambda_{\mathrm{uniax}}^2 - \frac{1}{\lambda_{\mathrm{uniax}}}) \tag{3.14}$$

A comparison between nominal stress-strain curves of the calibrated AB model and test data is shown in Figure 3.1. It is seen from the figure that the response of the AB model converges towards the NH model due to the locking stretch being much larger than the effective chain stretch. Therefore, the same issues that were noted with the NH model are relevant for the AB model as well for the studied adhesive.

The Mooney-Rivlin (MR) model ([75],[76]) serves as an extension of the NH model, where there is added a dependency of the second invariant of the isochoric right Cauchy-Green deformation tensor, I_2^*, defined by the equation:

$$I_2^* = \frac{J^{-\frac{4}{3}}}{2}\left(\left(\mathrm{trace}(\mathbf{C})\right)^2 + \mathrm{trace}(\mathbf{C}^2)\right) \tag{3.15}$$

Compared to the NH model there is added an additional parameter to scale the contribution from the second invariant to the potential. The parameters governing the distortional deformation are given generic names, C_{10} and C_{01}, as they are not directly linked to the

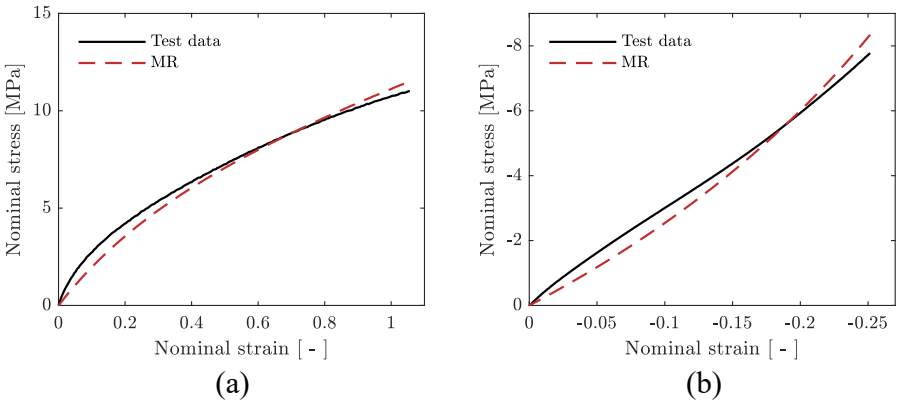

Figure 3.2.: Calibration results of a Mooney-Rivlin model compared to nominal test data from uniaxial tension and compression tests described in Chapter 2. (a) Tension. (b) Compression.

shear modulus. However, the bulk modulus, K, still represent the volumetric response. The Helmholtz free energy potential per unit reference volume, Ψ_{MR}, is defined as follows:

$$\Psi_{\text{MR}}(I_1^*, I_2^*, J) = C_{10}(I_1^* - 3) + C_{01}(I_2^* - 3) + K(J - \log(J)) \tag{3.16}$$

Assuming the deformation field given in Equation 3.9, the Cauchy stress in the longitudinal direction, $\sigma_{\text{MR,uniax}}$, is described by the equation:

$$\sigma_{\text{MR,uniax}} = 2\left(\lambda_{\text{uniax}}^2 - \frac{1}{\lambda_{\text{uniax}}}\right)\left(C_{10} + \frac{C_{01}}{\lambda_{\text{uniax}}}\right) \tag{3.17}$$

Figure 3.2 shows a comparison between nominal stress-strain curves of the calibrated MR model and the test data. It is evident that the extension from the NH model to the MR model allows for a significantly better fit to the test data. Unlike the AB model, the MR model is entirely phenomenological. Thus, it may provide poor results in loading modes that were not used for the calibration such as shear or biaxial tension in this case. Furthermore, negative values of C_{01} could cause numerical instability.

A more general phenomenological model based on a polynomial of the principal stretches is the Ogden (OG) model [78]. It can be expanded with enough parameters to fit perfectly to any set of test data. This is at a cost of potential stability problems as well as a more costly calibration process. A 3-term OG model, such as the one used by Golaz et al. [86], is defined by 9 parameters. These parameters are μ_k, α_k and D_k for $k = 1, 2, 3$, where D_k

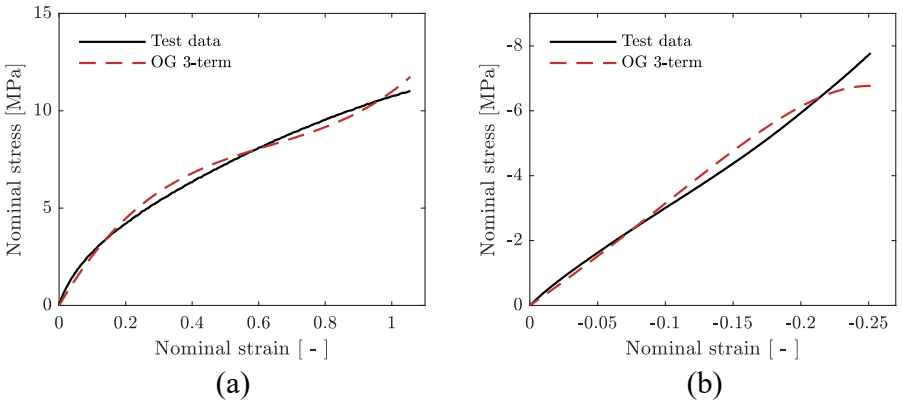

Figure 3.3.: Calibration results of a 3-term Ogden model compared to nominal test data from uniaxial tension and compression tests described in Chapter 2. (a) Tension. (b) Compression.

represents the volumetric response. The Helmholtz free energy potential per unit reference volume, Ψ_{OG}, is defined as follows:

$$\Psi_{\text{OG}}(\lambda_1^*, \lambda_2^*, \lambda_3^*, J) = \sum_{k=1}^{N} \frac{2\mu_k}{\alpha_k^2}\left((\lambda_1^*)^{\alpha_k} + (\lambda_2^*)^{\alpha_k} + (\lambda_3^*)^{\alpha_k} - 3\right) + \sum_{k=1}^{N} \frac{1}{D_k}(J-1)^{2k} \tag{3.18}$$

where N is the number of Ogden terms and λ_I^* is the isochoric principal stretches defined by the equation:

$$\lambda_I^* = J^{-\frac{1}{3}}\lambda_I \tag{3.19}$$

where $I = 1, 2, 3$ and λ_I are the principal stretches. Based on this potential function, the Cauchy stress in the longitudinal direction, $\sigma_{\text{OG,uniax}}$, in uniaxial tension and compression is given by the equation:

$$\sigma_{\text{OG,uniax}} = \sum_{k=1}^{N} \frac{2\mu_k}{\alpha_k}\left(\lambda_{\text{uniax}}^{\alpha_k} - \left(\frac{1}{\sqrt{\lambda_{\text{uniax}}}}\right)^{\alpha_k}\right) \tag{3.20}$$

Figure 3.3 shows a comparison between nominal stress-strain curves of the calibrated OG model and the test data. A decent fit was obtained, but there are obvious stability problems

for the given calibration. According to the calibration software, it is only stable between nominal strains of -0.24 and 0.55. Similar to the MR model, it is entirely phenomenological and therefore suffers the same problems. However, if sufficient calibration data is available and the material itself is suitable then it is possible to obtain good results.

3.1.3. Model selection

It was seen in the previous section that models employed in literature for modelling of semi-structural adhesives are not able to capture the non-linear response observed for the studied adhesive. Only the MR model provided acceptable results, but it has the additional problem of being purely phenomenological. Both shear test data and biaxial tension data are unavailable for calibration purposes, which adds significant uncertainty to a phenomenological model for those deformation modes. Further, linear viscoelasticity would not be able to alter the general behaviour of these models in order to capture the observed behaviour. Additionally, there was not performed any DMA on the studied adhesive, so it would be difficult to accurately calibrate a linear viscoelastic model for a large range of strain-rates. In conclusion, it is necessary to investigate alternative models than what was previously used in literature for these adhesives.

An alternative model should preferably be micro-mechanically based to reduce uncertainty in deformation modes not used for calibration. The model should also have a more complex rheological model to be able to capture more general non-linear behaviour. In addition, a non-linear viscous formulation would be preferable such that the strain-rate sensitivity could be captured with significantly fewer parameters than for linear viscoelasticity.

Given the rubber-like behaviour documented in Chapter 2, it is natural to consider models typically applied for modelling of rubbers. A model commonly applied for modelling of rubbers is the Bergström-Boyce (BB) model [84]. It was shown by Bergström [81] that the model is able to capture the non-linear behaviour of rubbers with relatively few parameters. As described in Section 1.2.5, the BB model is micro-mechanically based and uses a non-linear viscous formulation, making it suitable given the limited test data available. Based on these considerations, the BB model was chosen as the basis for the numerical study performed on the studied semi-structural adhesive. A detailed description of the BB model, including all the relevant equations and numerical implementation, is presented in the following section.

3.2. Numerical framework

It is the intention of this section to provide a sufficient background for the numerical framework used to study the semi-structural adhesive such that it is possible to reproduce the experimental results presented in Chapter 2. Therefore, the Bergström-Boyce (BB) model and the proposed modification are described in detail with the relevant equations. Furthermore, the numerical implementation will be presented with the numerical integration scheme included in a detailed algorithmic overview. Finally, the calibration procedure used to calibrate the studied adhesive is presented.

3.2.1. Description of Bergström-Boyce model

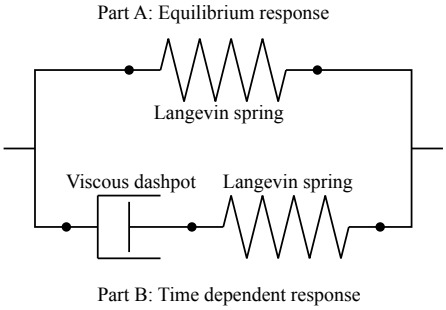

Figure 3.4.: Rheological interpretation of the Bergström-Boyce model.

The BB model [84] assumes that there are two contributions to the deviatoric response of the model, which is shown in the rheological model presented in Figure 3.4. Part A represents the equilibrium response, which is modelled by a simple Langevin spring using the AB model. Part B represents the time dependent response. It is based on the concept that there are free polymer chains that initially stretches affinely with the surrounding material. Then, these chains relax based on reptation theory presented by de Gennes [113]. To capture this phenomenon, the deformation gradient is multiplicatively split into an elastic and inelastic component. The elastic component represents the stretch of the free chains, which is modelled by a Langevin spring similar to Part A. Relaxation of the free chains is captured through the inelastic component, which is modelled by a non-linear viscous dashpot. Finally, the volumetric response is uncoupled from the deviatoric response and is only dependent on the bulk modulus, K. For the implementation studied in this work, the potential for the volumetric response was chosen to be similar to what was used for the NH, AB and MR models as described by the Equations 3.7, 3.11 and 3.16 respectively.

Part A is based on the full deformation gradient. Therefore, the kinematic measures defined by Equations 3.1 to 3.6 are sufficient to obtain the Kirchhoff stress in Part A. The equation for the stress is derived from the Arruda-Boyce eight-chain potential presented in Equation 3.11, but without the volumetric component. Only 2 parameters are needed for Part A, namely the effective shear modulus for Part A, μ_{A}, and the locking stretch for Part A, $\lambda_{\mathrm{lock,A}}$. The Kirchhoff stress for Part A, $\boldsymbol{\tau}_{\mathrm{A}}$, is given by:

$$\boldsymbol{\tau}_{\mathrm{A}} = \frac{\mu_{\mathrm{A}}\lambda_{\mathrm{lock,A}}}{3\lambda_{\mathrm{C}}}\mathcal{L}^{-1}\Big(\frac{\lambda_C}{\lambda_{\mathrm{lock,A}}}\Big)\mathbf{B}'_{\mathrm{iso}} \tag{3.21}$$

where λ_{C} is the effective chain stretch defined by Equation 3.13 and $\mathbf{B}'_{\mathrm{iso}}$ is the deviatoric part of the isochoric left Cauchy-Green deformation tensor.

The split of the deformation gradient for Part B is defined by the following equation:

$$\mathbf{F} = \mathbf{F}_{\mathrm{e}}\mathbf{F}_{\mathrm{i}} \tag{3.22}$$

where $\mathbf{F}_{\mathrm{e}}$ is the elastic part of the deformation gradient and $\mathbf{F}_{\mathrm{i}}$ is the inelastic part of the deformation gradient. This split is used to define the elastic left Cauchy-Green deformation tensor, $\mathbf{B}_{\mathrm{e}}$, and the isochoric elastic left Cauchy-Green deformation tensor, $\mathbf{B}_{\mathrm{e,iso}}$, with the following equations:

$$\mathbf{B}_{\mathrm{e}} = \mathbf{F}_{\mathrm{e}}\mathbf{F}_{\mathrm{e}}^{\mathrm{T}} \tag{3.23}$$

$$\mathbf{B}_{\mathrm{e,iso}} = J^{-\frac{2}{3}}\mathbf{B}_{\mathrm{e}} \tag{3.24}$$

In order to describe time dependency in a finite deformations framework it is necessary to introduce the velocity gradient, $\mathbf{L}$, given by the equation:

$$\mathbf{L} = \frac{\partial \mathbf{v}}{\partial \mathbf{x}} = \dot{\mathbf{F}}\mathbf{F}^{-1} = \mathbf{D} + \mathbf{W} \tag{3.25}$$

where $\mathbf{D}$ is the symmetric part of the velocity gradient, also known as the rate of deformation tensor, and $\mathbf{W}$ is the anti-symmetric part that is named the spin tensor. The velocity gradient can further be split into an elastic, $\mathbf{L}_{\mathrm{e}}$, and an inelastic, $\mathbf{L}_{\mathrm{i}}$, component given by the following equation:

$$\mathbf{L} = \mathbf{L}_\mathrm{e} + \mathbf{L}_\mathrm{i} \tag{3.26}$$

where $\mathbf{L}_\mathrm{e}$ and $\mathbf{L}_\mathrm{i}$ are defined by:

$$\mathbf{L}_\mathrm{e} = \dot{\mathbf{F}}_\mathrm{e}\mathbf{F}_\mathrm{e}^{-1} \tag{3.27}$$

$$\mathbf{L}_\mathrm{i} = \mathbf{D}_\mathrm{i} + \mathbf{W}_\mathrm{i} = \mathbf{D}_\mathrm{i} = \mathbf{F}_\mathrm{e}\dot{\mathbf{F}}_\mathrm{i}\mathbf{F}_\mathrm{i}^{-1}\mathbf{F}_\mathrm{e}^{-1} \tag{3.28}$$

where $\mathbf{D}_\mathrm{i}$ is the inelastic rate of deformation tensor and $\mathbf{W}_\mathrm{i}$ is the inelastic spin tensor. The inelastic spin tensor is constitutively prescribed to be equal to $\mathbf{0}$ for this model. In order to determine the Kirchhoff stress in the Langevin spring of Part B, it is necessary to introduce 2 additional parameters. These are the effective shear modulus for Part B, μ_B, and the locking stretch for Part B, $\lambda_\mathrm{lock,B}$. With the given kinematic considerations and the new parameters, the Kirchhoff stress in Part B, $\boldsymbol{\tau}_\mathrm{B}$, is given by:

$$\boldsymbol{\tau}_\mathrm{B} = \frac{\mu_\mathrm{B}\lambda_\mathrm{lock,B}}{3\lambda_\mathrm{V}}\mathcal{L}^{-1}\Big(\frac{\lambda_V}{\lambda_\mathrm{lock,B}}\Big)\mathbf{B}'_\mathrm{e,iso} \tag{3.29}$$

where λ_V is the viscous chain stretch, which is defined by:

$$\lambda_\mathrm{V} = \sqrt{\mathrm{trace}(\mathbf{B}_\mathrm{e,iso})/3} \tag{3.30}$$

The rate of the elastic isochoric left Cauchy-Green deformation tensor, $\dot{\mathbf{B}}_\mathrm{e,iso}$, is given by:

$$\dot{\mathbf{B}}_\mathrm{e,iso} = \mathbf{L}'\mathbf{B}_\mathrm{e,iso} + \mathbf{B}_\mathrm{e,iso}(\mathbf{L}')^\mathrm{T} - 2\mathbf{D}_\mathrm{i}\mathbf{B}_\mathrm{e,iso} \tag{3.31}$$

This equation can be derived from previously presented kinematic considerations. Further, the inelastic rate of deformation tensor, $\mathbf{D}_\mathrm{i}$, is given by:

$$\mathbf{D}_\mathrm{i} = \dot{\gamma}_\mathrm{i}\mathbf{N}_\mathrm{i} \tag{3.32}$$

where $\dot{\gamma}_\mathrm{i}$ is the effective inelastic shear rate and $\mathbf{N}_i$ is the direction of the inelastic rate of deformation. The direction of the inelastic rate of deformation is based on the Kirchhoff stress in Part B through:

$$\mathbf{N}_{\mathrm{i}} = \frac{\boldsymbol{\tau}_{\mathrm{B}}}{\|\boldsymbol{\tau}_{\mathrm{B}}\|} \tag{3.33}$$

where $\|\boldsymbol{\tau}_{\mathrm{B}}\|$ is the Euclidean norm for the Kirchhoff stress in Part B. It is key to note that the Kirchhoff stress in Part B is deviatoric, such that the inelastic rate of deformation will also be deviatoric. This means that the inelastic deformation is isochoric. Furthermore, the effective inelastic shear rate, $\dot{\gamma}_{\mathrm{i}}$, is constitutively prescribed based on the formulation presented by Dal and Kaliske [114], and it is given by:

$$\dot{\gamma}_{\mathrm{i}} = \dot{\gamma}_0(\lambda_{\mathrm{i}} - 0.999)^c \left(\frac{\|\boldsymbol{\tau}_{\mathrm{B}}\|}{\hat{\tau}\sqrt{2}} \right)^m \tag{3.34}$$

where $\dot{\gamma}_0$, $\hat{\tau}$, c and m are the reference effective inelastic shear rate, the reference driving stress and two power terms for each part of the inelastic flow respectively. Further, the effective inelastic chain stretch, λ_{i}, is given by:

$$\lambda_{\mathrm{i}} = \sqrt{\frac{\mathrm{trace}(\mathbf{F}_{\mathrm{i}}^{\mathrm{T}}\mathbf{F}_{\mathrm{i}})}{3}} \tag{3.35}$$

There was made a slight change to Equation 3.34 compared to the original, where -1 was replaced with -0.999 in order to avoid numerical problems as $c < 0$ and $\lambda_{\mathrm{i}} \geq 1$. The hydrostatic component of the model is based on the previously mentioned potentials, such that the pressure, p, can be described by:

$$p = K(J^{-1} - 1) \tag{3.36}$$

Finally, the Cauchy stress, $\boldsymbol{\sigma}$, of the BB model, as defined in this work, is given by:

$$\boldsymbol{\sigma} = \frac{\boldsymbol{\tau}_{\mathrm{A}} + \boldsymbol{\tau}_{\mathrm{B}}}{J} - p\mathbf{I} \tag{3.37}$$

where $\mathbf{I}$ is the second order identity tensor.

The behaviour of the model when subjected to monotonic loading follows a general pattern divided into two phases. In the beginning the viscous dashpot of Part B will be locked, such that the model acts as two Langevin springs in parallel. During deformation, the stress in Part B will increase, which in turn will increase the effective inelastic shear rate. Due to the power law used in Equation 3.34, the evolution of effective inelastic shear rate is

slow in the first phase, then rapidly increasing in the transition between the two phases. When the effective inelastic shear rate approaches the effective strain-rate of the material, the viscous dashpot will be unlocked to the point where the stress in Part B stabilizes as all deformation in Part B becomes inelastic. This is an indication of the second phase, where the stiffness is dominated by Part A. The evolution of the inelastic chain stretch will have an influence on the response of Part B, but the overall behaviour of the model remains split in two primary phases. This split results in a primarily additive strain-rate sensitivity for the model, which is inconsistent with the experimental observations.

3.2.2. Description of modified Bergström-Boyce model

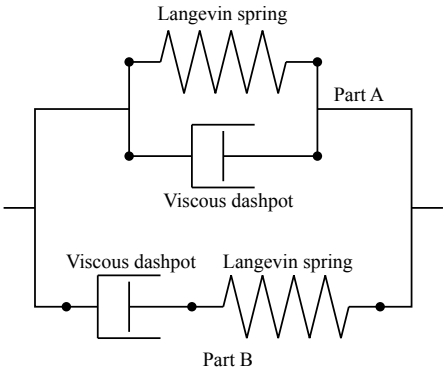

Figure 3.5.: Rheological interpretation of the Bergström-Boyce modified model.

A phenomenological extension to the BB model is proposed such that it can capture the multiplicative strain-rate sensitivity observed in Figures 2.9a and 2.19a. The extension is designed to retain as much as possible of the original behaviour of the BB model, while adding as few parameters as possible to capture the multiplicative strain-rate sensitivity. In order to fulfil these goals, it was chosen to extend Part A of the BB model with a Cowper-Symonds rate sensitivity factor. Figure 3.5 shows the rheology of the Bergström-Boyce modified (BBmod) model, where an additional viscous dashpot has been added to Part A.

The Kirchhoff stress in Part A for the BBmod model, $\boldsymbol{\tau}_{\mathrm{A,BBmod}}$, is based on the Kirchhoff stress in Part A for the BB model, $\boldsymbol{\tau}_{\mathrm{A}}$, which is described by Equation 3.21. This stress tensor is scaled with a Cowper-Symonds rate sensitivity factor, which introduces two new parameters namely the reference strain-rate, $\dot{\varepsilon}_0$, and a power law parameter, R. The Kirchhoff stress in Part A for the BBmod model, $\boldsymbol{\tau}_{\mathrm{A,BBmod}}$, is defined by the following equation:

$$\boldsymbol{\tau}_{\mathrm{A,BBmod}} = \boldsymbol{\tau}_{\mathrm{A}}\left(1 + \mathrm{sgn}(\dot{\psi}_{\mathrm{A}})\left[\frac{\dot{\bar{\varepsilon}}}{\dot{\varepsilon}_0}\right]^R\right) \tag{3.38}$$

where $\mathrm{sgn}(\dot{\psi}_{\mathrm{A}})$ is the sign of the rate of the eight-chain potential for Part A in the BB model and $\dot{\bar{\varepsilon}}$ is the rate of the von Mises equivalent of the Hencky strain tensor.

The factor $\mathrm{sgn}(\dot{\psi}_{\mathrm{A}})$ was added to allow for loading and unloading of the model as well as ensuring positive dissipation of the additional viscous contribution in the BBmod model. Positive dissipation is a necessity for the model to conform with the second law of thermodynamics, which is a basic requirement for any new model to satisfy. It can be proven that this is satisfied by verifying that the viscous stress of Part A in the BBmod model, $\boldsymbol{\sigma}_{\mathrm{v,A}}$, given by the equation:

$$\boldsymbol{\sigma}_{\mathrm{v,A}} = \frac{\boldsymbol{\tau}_{\mathrm{A}}}{J}\mathrm{sgn}(\dot{\psi}_{\mathrm{A}})\left[\frac{\dot{\bar{\varepsilon}}}{\dot{\varepsilon}_0}\right]^R \tag{3.39}$$

always satisfies the inequality:

$$\boldsymbol{\sigma}_{\mathrm{v,A}} : \mathbf{D} \geq 0 \tag{3.40}$$

It can readily be shown that:

$$\dot{\psi}_{\mathrm{A}} = \boldsymbol{\tau}_{\mathrm{A}} : \mathbf{D} \tag{3.41}$$

Equation 3.41 can be inserted into Equation 3.39 such that the left side of the inequality shown in Equation 3.40 becomes:

$$\boldsymbol{\sigma}_{\mathrm{v,A}} : \mathbf{D} = \frac{1}{J}\mathrm{sgn}(\boldsymbol{\tau}_{\mathrm{A}} : \mathbf{D})\boldsymbol{\tau}_{\mathrm{A}} : \mathbf{D}\left[\frac{\dot{\bar{\varepsilon}}}{\dot{\varepsilon}_0}\right]^R \tag{3.42}$$

It is evident that this product is always positive such that the dissipation inequality is satisfied.

The BBmod model is expected to behave similar to the BB model except for a part of the dynamic response is transferred to the multiplicative viscous component of Part A. Another significant change is that the initial stiffness will be dependent on the applied strain-rate. It is also expected to give a better fit than the BB model as there are 2 additional fitting

parameters. The BBmod model is designed for the academic purpose of investigating if better results could be obtained when adding a multiplicative component to the strain-rate sensitivity of the BB model. However, there are several issues with the implementation of this model that will be discussed in the next sections. These issues makes the model infeasible for industrial use, thus emphasizing the academic nature of this model.

3.2.3. Implementation

It was originally chosen to implement the model in Abaqus/Explicit [112] based on previous experience with implementations in that solver. However, the initial implementation in the Abaqus/Explicit was found to be unstable due to the direction of the viscous stress in Part A of BBmod. Therefore, it was chosen to implement the model in Abaqus/Implicit [112] as the larger time-steps would stabilize the problem with the direction of the viscous stress. In order to implement the model in an implicit solver, it is necessary to use a semi-implicit, quasi-implicit or implicit stress update to avoid large errors. This means that iterations are necessary in the stress update. A sub-stepping scheme is also important to ensure convergence. Furthermore, a consistent tangent operator has to be determined to ensure that the global convergence rate remains quadratic. It is cumbersome and difficult to derive an analytical expression for the consistent tangent operator of a new model. Therefore, it was chosen to use a numerical estimation of the consistent tangent operator.

There are some key functions that will be used several times during the overview of the implementation of the BBmod model, they will therefore be presented first. The inverse of the Langevin function, $\mathcal{L}^{-1}(x)$, is used to determine both the potential and the response of the AB model, which is a key component of the implementation. For this implementation, a numerical estimate of the inverse Langevin function is necessary. The estimate presented by Jedynak [115] is used for this implementation due to both its simplicity and accuracy, which is given by:

$$\mathcal{L}^{-1}(x) = x\frac{3 - 2.6x + 0.7x^2}{(1-x)(1+0.1x)} \tag{3.43}$$

Further, the Kirchhoff stress for the AB model, $\boldsymbol{\tau}_{8\text{chain}}$, given an isochoric left Cauchy-Green deformation tensor, $\mathbf{B}_{\text{iso}}$, an effective shear modulus, μ and a locking stretch, λ_{lock} is given by the equation:

$$\begin{aligned} \lambda_{\text{C}}(\mathbf{B}_{\text{iso}}) &= \sqrt{\text{trace}(\mathbf{B}_{\text{iso}})/3} \\ \boldsymbol{\tau}_{8\text{chain}}(\mathbf{B}_{\text{iso}}, \mu, \lambda_{\text{lock}}) &= \frac{\mu\lambda_{\text{lock}}}{3\lambda_{\text{C}}}\mathcal{L}^{-1}\Big(\frac{\lambda_{\text{C}}}{\lambda_{\text{lock}}}\Big)\mathbf{B}'_{\text{iso}} \end{aligned} \tag{3.44}$$

Using the same input as Equation 3.44, the Helmholtz free energy potential per unit reference volume for the AB model, $\Psi_{8\text{chain}}$, is given by:

$$\begin{aligned}
\lambda_{\text{C}}(\mathbf{B}_{\text{iso}}) &= \sqrt{\text{trace}(\mathbf{B}_{\text{iso}})/3} \\
\mathcal{L}_{\text{ch}}^{-1}(\lambda_{\text{C}}, \lambda_{\text{lock}}) &= \mathcal{L}^{-1}\Big(\frac{\lambda_C}{\lambda_{\text{lock}}}\Big) \\
\Psi_{8\text{chain}}(\mathbf{B}_{\text{iso}}, \mu, \lambda_{\text{lock}}) &= \mu\lambda_{\text{lock}}^2\bigg(\Big(\frac{\lambda_C}{\lambda_{\text{lock}}}\Big)\mathcal{L}_{\text{ch}}^{-1} + \log\Big(\frac{\mathcal{L}_{\text{ch}}^{-1}}{\sinh(\mathcal{L}_{\text{ch}}^{-1})}\Big)\bigg)
\end{aligned} \tag{3.45}$$

Before presenting the stress update algorithm, the step and iteration notations have to be defined. Time-steps are defined by the counters n and $n+1$ which represent the previous step and the current step respectively. Similarly, the iteration counters are I and $I+1$, which represent the previous and current iteration respectively.

It was chosen to use a quasi-implicit stress update algorithm, as it proved to converge better than a semi-implicit algorithm and it was less involved than a fully implicit update. That means the direction of the inelastic flow is lagging one iteration behind the current iteration, such that it updates throughout the iterations. Time integration is done through a first order update on the inelastic deformation gradient, $\mathbf{F}_{\text{i}}$, through the equation:

$$(\mathbf{F}_{\text{i},n+1}^{I+1})^{-1} = (\mathbf{1} - \Delta\text{t}\dot{\gamma}_{\text{i},n+1}^{I+1}\mathbf{F}_{n+1}^{-1}\mathbf{N}_{\text{i},n+1}^{I}\mathbf{F}_{n+1})\mathbf{F}_{\text{i},n}^{-1} \tag{3.46}$$

where Δt is the time between the two time-steps. It is necessary to iterate on $\dot{\gamma}_{\text{i},n+1}^{I+1}$ as it is dependent on $(\mathbf{F}_{\text{i},n+1}^{I+1})^{-1}$. The secant method was chosen as the iteration scheme due to its simplicity. A residual function, f_{res}, was defined according to the following equation:

$$f_{\text{res}}^{I+1} = \dot{\gamma}_{\text{i},n+1}^{I+1} - \dot{\gamma}_0(\lambda_{\text{i},n+1}^{I+1} - 0.999)^c\left(\frac{\|\boldsymbol{\tau}_{\text{B},n+1}^{I+1}\|}{\hat{\tau}\sqrt{2}}\right)^m \tag{3.47}$$

The secant method update for $\dot{\gamma}_{\text{i},n+1}^{I+1}$ is then given by the equation:

$$\dot{\gamma}_{\text{i},n+1}^{I+1} = \dot{\gamma}_{\text{i},n+1}^{I} - f_{\text{res}}^{I}\frac{\dot{\gamma}_{\text{i},n+1}^{I} - \dot{\gamma}_{\text{i},n+1}^{I-1}}{f_{\text{res}}^{I} - f_{\text{res}}^{I-1}} \tag{3.48}$$

Based on the previously presented equations, the stress update algorithm is presented in Algorithm 1.

Algorithm 1 BBmod stress update.

Input: Solver variables: $\mathbf{F}_n$, $\mathbf{F}_{n+1}$, Δt and $\boldsymbol{\sigma}_n$
State variables: $\mathbf{F}_{i,n}^{-1}$, $\boldsymbol{\tau}_{B,n}$ and $\dot{\gamma}_{i,n}$
Material parameters: μ_A, $\lambda_{lock,A}$, μ_B, $\lambda_{lock,B}$, $\dot{\gamma}_0$, $\hat{\tau}$, $\dot{\varepsilon}_0$, R, c and m

Output: $\boldsymbol{\sigma}_{n+1}$, $\mathbf{F}_{i,n+1}^{-1}$, $\boldsymbol{\tau}_{B,n+1}$ and $\dot{\gamma}_{i,n+1}$

Calculate kinematic variables:
    Based on $\mathbf{F}_n$, $\mathbf{F}_{n+1}$ and Δt calculate the variables:
    $\mathbf{B}_n$, $\mathbf{B}_{n+1}$, J_n, J_{n+1}, $\mathbf{B}_{iso,n}$, $\mathbf{B}_{iso,n+1}$ and $\mathbf{L}_{n+0.5}$
Calculate Kirchhoff stress in Part A:
    Calculate $\boldsymbol{\tau}_{A,EC,n+1}(\mathbf{B}_{iso,n+1}, \mu_A, \lambda_{lock,A})$ based on Equation 3.44
    Calculate $\Psi_{A,EC,n}(\mathbf{B}_{iso,n}, \mu_A, \lambda_{lock,A})$ and $\Psi_{A,EC,n+1}(\mathbf{B}_{iso,n+1}, \mu_A, \lambda_{lock,A})$ based on Equation 3.45
    Calculate $\operatorname{sgn}(\dot{\psi}_A) = \frac{\Psi_{A,EC,n+1} - \Psi_{A,EC,n}}{\operatorname{ABS}(\Psi_{A,EC,n+1} - \Psi_{A,EC,n})}$
    Calculate $\boldsymbol{\tau}_{A,n+1} = \boldsymbol{\tau}_{A,EC,n+1}\left(1 + \operatorname{sgn}(\dot{\psi}_A)\left[\frac{\dot{\bar{\varepsilon}}}{\dot{\varepsilon}_0}\right]^R\right)$
Calculate Kirchhoff stress in Part B:
    # Trial 1:
        Calculate $\dot{\gamma}_{i,n+1}^{tr1} = \dot{\gamma}_{i,n}$
        Calculate $(\mathbf{F}_{i,n+1}^{tr1})^{-1}(\dot{\gamma}_{i,n+1}^{tr1}, \mathbf{N}_{i,n})$ based on Equation 3.46
        Calculate $\mathbf{B}_{e,iso,n+1}^{tr1}$ and $\lambda_{i,n+1}^{tr1}$ based on Equations 3.22, 3.23, 3.24 and 3.35
        Calculate $\boldsymbol{\tau}_{B,n+1}^{tr1}(\mathbf{B}_{e,iso,n+1}^{tr1}, \mu_B, \lambda_{lock,B})$ based on Equation 3.44
        Calculate f_{res}^{tr1} based on Equation 3.47
    # Trial 2:
        Calculate $\dot{\gamma}_{i,n+1}^{tr2} = \dot{\gamma}_0(\lambda_{i,n+1}^{tr1} - 0.999)^c\left(\frac{\|\boldsymbol{\tau}_{B,n+1}^{tr1}\|}{\hat{\tau}\sqrt{2}}\right)^m$
        Calculate $(\mathbf{F}_{i,n+1}^{tr2})^{-1}(\dot{\gamma}_{i,n+1}^{tr2}, \mathbf{N}_{i,n+1}^{tr1})$ based on Equation 3.46
        Calculate $\mathbf{B}_{e,iso,n+1}^{tr2}$ and $\lambda_{i,n+1}^{tr2}$ based on Equations 3.22, 3.23, 3.24 and 3.35
        Calculate $\boldsymbol{\tau}_{B,n+1}^{tr2}(\mathbf{B}_{e,iso,n+1}^{tr2}, \mu_B, \lambda_{lock,B})$ based on Equation 3.44
        Calculate f_{res}^{tr2} based on Equation 3.47
    # Secant iteration scheme:
        while $\left|\frac{f_{res}^{I+1}}{\dot{\gamma}_{i,n+1}^{I+1}}\right| \geq$ tolerance
            Calculate $\dot{\gamma}_{i,n+1}^{I+1}$ based on Equation 3.48
            Calculate $(\mathbf{F}_{i,n+1}^{I+1})^{-1}(\dot{\gamma}_{i,n+1}^{I+1}, \mathbf{N}_{i,n+1}^{I})$ based on Equation 3.46
            Calculate $\mathbf{B}_{e,iso,n+1}^{I+1}$ and $\lambda_{i,n+1}^{I+1}$ based on Equations 3.22, 3.23, 3.24 and 3.35
            Calculate $\boldsymbol{\tau}_{B,n+1}^{I+1}(\mathbf{B}_{e,iso,n+1}^{I+1}, \mu_B, \lambda_{lock,B})$ based on Equation 3.44
            Calculate f_{res}^{I+1} based on Equation 3.47
        end while
    Set $\boldsymbol{\tau}_{B,n+1} = \boldsymbol{\tau}_{B,n+1}^{I+1}$, $\mathbf{F}_{i,n+1}^{-1} = (\mathbf{F}_{i,n+1}^{I+1})^{-1}$ and $\dot{\gamma}_{i,n+1} = \dot{\gamma}_{i,n+1}^{I+1}$
Update stress
    $\boldsymbol{\sigma}_{n+1} = \frac{\boldsymbol{\tau}_{A,n+1} + \boldsymbol{\tau}_{B,n+1}}{J_{n+1}} - K(J_{n+1}^{-1} - 1)\mathbf{I}$
Return $\boldsymbol{\sigma}_{n+1}$, $\mathbf{F}_{i,n+1}^{-1}$, $\boldsymbol{\tau}_{B,n+1}$ and $\dot{\gamma}_{i,n+1}$

There are some details that are omitted from Algorithm 1 in order to keep it concise. Several initialization steps are omitted as well as conditions that are necessary to avoid singularities in the code. During the secant iterations, boundary values are defined for the effective inelastic shear rate, $0 \leq \dot{\gamma}_{\mathrm{i},n+1}^{I+1} \leq 1/\Delta\mathrm{t}$. This was done to ensure physical predictions of $\dot{\gamma}_{\mathrm{i},n+1}^{I+1}$ and avoid the worst predictions of $\mathbf{N}_{\mathrm{i},n+1}^{I}$ for the next iteration. Furthermore, a requirement to changing the value of $\mathrm{sgn}(\dot{\psi}_{\mathrm{A}})$ was added in order to increase the stability of the stress update algorithm. It is assumed that the sign of the viscous stress of Part A can only change value when the rate of the von Mises equivalent of the Hencky strain tensor, $\dot{\bar{\varepsilon}}$, is less than a critical value. The idea is that the strain-rate has to pass through 0 when going from loading to unloading.

It was seen that the model exhibited strong non-linear behaviour when transitioning from phase 1 to phase 2 of the response of this model. Specifically, the effective inelastic shear rate, $\dot{\gamma}_{\mathrm{i}}$, undergoes large changes over a short period of time causing convergence problems for the stress update algorithm. Therefore, it is necessary to use a sub-stepping scheme to ensure convergence. This sub-stepping scheme should also be flexible to keep the computational cost reasonable, which is done by scaling it with the effective strain-rate. Finally, the details of the sub-stepping scheme are presented as a part of Algorithm 2.

Algorithm 2 Outer loops for stress update

Input: Solver variables: $\mathbf{F}_n$, $\mathbf{F}_{n+1}$, $\Delta\mathrm{t}$ and $\boldsymbol{\sigma}_n$
State variables: $\mathbf{F}_{\mathrm{i},n}^{-1}$, $\boldsymbol{\tau}_{\mathrm{B},n}$ and $\dot{\gamma}_{\mathrm{i},n}$
Material parameters: μ_{A}, $\lambda_{\mathrm{lock,A}}$, μ_{B}, $\lambda_{\mathrm{lock,B}}$, $\dot{\gamma}_0$, $\hat{\tau}$, $\dot{\varepsilon}_0$, R, c and m
Output: $\boldsymbol{\sigma}_{n+1}$, $\mathbf{F}_{\mathrm{i},n+1}^{-1}$, $\boldsymbol{\tau}_{\mathrm{B},n+1}$, $\dot{\gamma}_{\mathrm{i},n+1}$ and $\mathbf{C}_{ij(kl),n+1}^{t}$

Create the 12 perturbations of the deformation gradient at time $n+1$:
  $\delta\mathbf{F}_{\pm,n+1}^{(kl)} = \pm\frac{\epsilon}{2}\left[(\mathbf{e}_k \otimes \mathbf{e}_l)\mathbf{F}_{n+1} + (\mathbf{e}_l \otimes \mathbf{e}_k)\mathbf{F}_{n+1}\right]$, for $(kl) = 11, 22, 33, 12, 13, 23$
  $\mathbf{F}_{\mathrm{pert},\pm,n+1}^{(kl)} = \mathbf{F}_{n+1} + \delta\mathbf{F}_{\pm,n+1}^{(kl)}$
  # Perform sub-stepping for all deformation gradients at step time $n+1$:
    # Determine number of sub-steps:
      $N_{\mathrm{substeps}} = \mathrm{int}\left[\max\left(20\mu_B\bar{\varepsilon}/(\dot{\bar{\varepsilon}}^{\frac{1}{m}}\hat{\tau}\sqrt{2}), 10\right)\right]$
    # Partition the step from $\mathbf{F}_n$ to $\mathbf{F}_{\mathrm{inp},n+1}$ into N_{substeps} steps:
      $\mathbf{L} = \left[\left(\mathbf{F}_{\mathrm{inp},n+1} - \mathbf{F}_n\right)/\Delta\mathrm{t}\right]\mathbf{F}_n^{-1}$
      $\mathbf{F}_q = \left(\mathbf{1} + \frac{q\Delta\mathrm{t}\mathbf{L}}{N_{\mathrm{substeps}}}\right)\mathbf{F}_n$ for sub-step number q
      # Update stress and state variables for each sub-step using Algorithm 1
Calculate the numerical estimate of the consistent tangent operator:
  $\mathbf{C}_{ij(kl),n+1}^{t} = \frac{\boldsymbol{\sigma}_{ij}(\mathbf{F}_{\mathrm{pert},+,n+1}^{(kl)}) - \boldsymbol{\sigma}_{ij}(\mathbf{F}_{\mathrm{pert},-,n+1}^{(kl)})}{2\epsilon}$
Return $\boldsymbol{\sigma}_{n+1}$, $\mathbf{F}_{\mathrm{i},n+1}^{-1}$, $\boldsymbol{\tau}_{\mathrm{B},n+1}$, $\dot{\gamma}_{\mathrm{i},n+1}$ and $\mathbf{C}_{ij(kl),n+1}^{t}$

The numerical estimate of the consistent tangent operator used in this work is similar to the one presented by Johnsen et al. [116], which in turn is based on the work of Miehe

[117] and Sun et al. [118]. It was shown by Sun et al. [118] that it is possible to obtain similar convergence rate with this numerical estimate as with an analytical expression for the consistent tangent operator when using a perturbation factor, ϵ, of 10^{-8}. The numerical estimate is based on a central difference, which requires 12 additional perturbations of the deformation gradient. This makes the algorithm 13 times slower, as all the perturbations have to go through the same sub-stepping scheme and stress update as the original. A complete overview of the numerical estimation of the consistent tangent operator, $\mathbf{C}^t_{ij(kl)}$ in Voigt notation, and sub-stepping scheme is presented in Algorithm 2.

3.2.4. Calibration

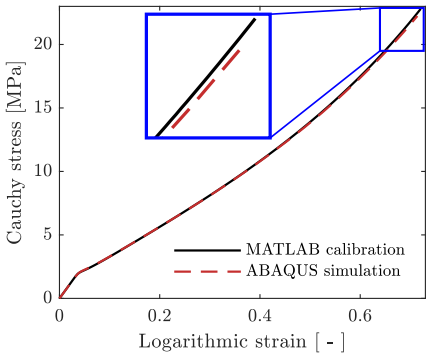

Figure 3.6.: Comparison between the stress-strain response of the BBmod model obtained from MATLAB and full tension test simulation in Abaqus/Standard [112].

Calibration of the BB and BBmod models was performed in MATLAB. The time, strain and stress histories obtained from the gage sections of the representative tension and compression tests were used as a basis for the calibrations. Based on the experimental results and to avoid reverse engineering, incompressibility was assumed, such that the whole strain field was known for the calibration process. A comparison between the stress-strain curve from the MATLAB calibration and the corresponding simulation of a full tension test in Abaqus/Standard [112] with the same parameters is shown in Figure 3.6.

There is a slight difference at large strains between the response obtained in MATLAB compared to the Abaqus/Standard simulation. This is caused by two key differences, the simulation is based on the cross-head and time histories obtained from the representative test and not the measured strain histories. Furthermore, incompressibility is approximately enforced through a penalty formulation, where the bulk modulus is set equal to 1000 MPa, yielding an initial Poisson's ratio of 0.4922. As the calibrated stress-strain response is slightly stiffer initially and softer at higher strain levels, the shoulders are overly stiff

while the gage section is too soft compared to the physical tests. This leads to a higher strain-rate in the gage section initially and a lower strain-rate at larger strains, causing the simulation to initially overestimate the response and underestimate the response at large strains. In addition, the MATLAB calibration assumes perfect incompressibility, which also causes a slightly stiffer response. It is evident that these phenomena explain the difference in response observed in Figure 3.6. In conclusion, the difference between the response obtained from the MATLAB calibration and a full tension test in Abaqus/Standard is negligible and therefore it validates the chosen calibration approach.

The calibration itself used a least square fit method in MATLAB and was split into 3 steps:

1. The time independent parameters μ_A and $\lambda_{lock,A}$ were fitted to the tension test performed at a nominal rate of $10^{-3}s^{-1}$, while keeping the other parameters fixed at values that yielded zero contribution.

2. The time dependent parameters μ_B, $\lambda_{lock,B}$, $\hat{\tau}$, c, m, $\dot{\varepsilon}_0$ and R were fitted to six representative tests in both tension and compression at different rates, with the time independent parameters fixed.

3. Applying the parameters found in the two first steps as initial values, all parameters were relaxed and optimized to fit all six representative tests.

The bulk modulus was set to 1000 MPa to ensure approximate incompressibility and the reference inelastic shear rate, $\dot{\gamma}_0$, was set equal to $0.001\,s^{-1}$ to reduce calibration time. It should be noted that there is a dependency between $\dot{\gamma}_0$ and $\hat{\tau}$, such that model behaviour remains the same with a fixed value for $\dot{\gamma}_0$. Calibrated material parameters are presented in Table 3.1.

Table 3.1.: Calibrated material parameters [119].

Model	BB parameters								BBmod param.	
	μ_A[MPa]	$\lambda_{lock,A}$[−]	μ_B[MPa]	$\lambda_{lock,B}$[−]	$\dot{\gamma}_0$[s^{-1}]	$\hat{\tau}$[MPa]	c[−]	m[−]	$\dot{\varepsilon}_0$[s^{-1}]	R[−]
BB	4.40	3.98	16.0	2.42	0.001	2.42	−1.56	6.68	-	-
BBmod	3.68	2.90	12.0	2.48	0.001	3.23	−3.21	13.7	68.0	0.267

A comparison between the calibrated stress-strain curves of the models and the experimental data is shown in Figure 3.7. Overall, both models are seen to provide a good fit to the material data. However, the two phases described in Section 3.2.1, which are linked to the evolution of the effective inelastic shear rate, are apparent with the presence of a kink on the stress-strain curve. This kink causes the models to be overly stiff initially and then too soft afterwards. It is evident that the issues with this kink are slightly alleviated with the introduction of the modification in the BBmod model due to the multiplicative viscous contribution of Part A. The difference in initial stiffness between the BB and BBmod models is clearly visible in Figure 3.7b, which visualizes the effect of the modification.

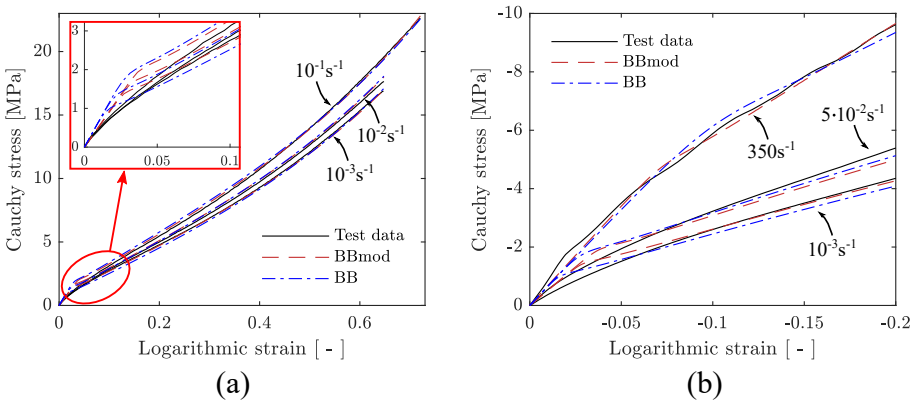

Figure 3.7.: Comparison between calibrated material models to uniaxial test data presented in Chapter 2. (a) Tension. (b) Compression.

3.3. Validation with notched tension tests

In this section, a validation case for the two calibrated models is presented, where the models have to perform outside of the domain used for calibration. The notched tension tests (NTT) presented in Section 2.4 satisfy this criterion, making it suitable for validating the models. All simulations were run in Abaqus/Standard [112] for this section.

3.3.1. Finite element model description

Figure 3.8 shows the finite element (FE) model of the representative notched tension test that is used for validation. Measurements on one representative test specimen are used as a basis for the geometry of the model, such that the simulation is as close to the experiment as possible. The grips are modelled as a fixed boundary condition in one end and as a prescribed velocity on the other end. It is used 2 symmetry planes, in the thickness and width direction of the specimen, to reduce the computational cost of the model. Element formulation C3D8R in Abaqus/Standard, which are linear brick elements with reduced integration and hourglass control, are used for the model. The element size varies from 0.6 mm to 0.1 mm as seen in Figure 3.8, making the total number of elements 15924. Specifically, the critical element highlighted in the figure has a size of 0.1 mm and is located at the front surface of the specimen where the local deformations from the experiments were measured. Therefore, the logarithmic strain in the longitudinal direction for the critical element should be comparable to the local strain measure defined in Figure 2.23a.

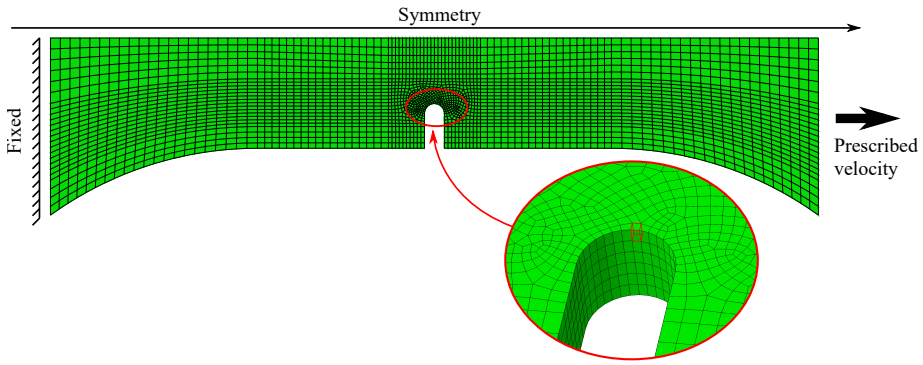

Figure 3.8.: Finite element model of the notched tension tests where the critical element in the notched region is highlighted.

The prescribed velocity applied to the boundary is based on the machine displacement measured on the representative test, giving a velocity of 0.01923 mm/s over a total time of 572 s. Double precision was used for all simulations performed in this section. An initial increment size of 17.5 s was used, while the smallest and largest increments recorded for the simulation using BBmod were 0.247 s and 41.19 s respectively. In summary, this gave a total number of increments of 93, resulting in a total CPU time of 4709 seconds. These stats are comparable to the simulation using the BB model, as it was used the same material model with BBmod parameters set to values ensuring no contribution from the modification.

3.3.2. Simulation results

Initial simulations revealed that the notched tension tests exhibit a range of stress states with strong gradients of the stress and strain fields in the notched region. Specifically, the behaviour is tension dominated with increased stress triaxiality in the critical part of the notch. Additionally, there are significant shear stresses adjacent to the critical region. It is evident that the notched tension tests require the models the perform outside of the domain used for calibration. Therefore, these simulations serve as an indication of the suitability of the models for the studied material.

Figure 3.9a show the simulation results using the BB and BBmod models compared to test data for the representative notched tension test. The reference deformation measure is the nominal strain in the centre of the notched region, as defined in Figure 2.23a, which is used for the horizontal axis. Further, the left vertical axis related to the blue curves shows the nominal stress measure, which is determined by dividing the total force by the initial minimum cross-section of the notched region. The red curves related to the

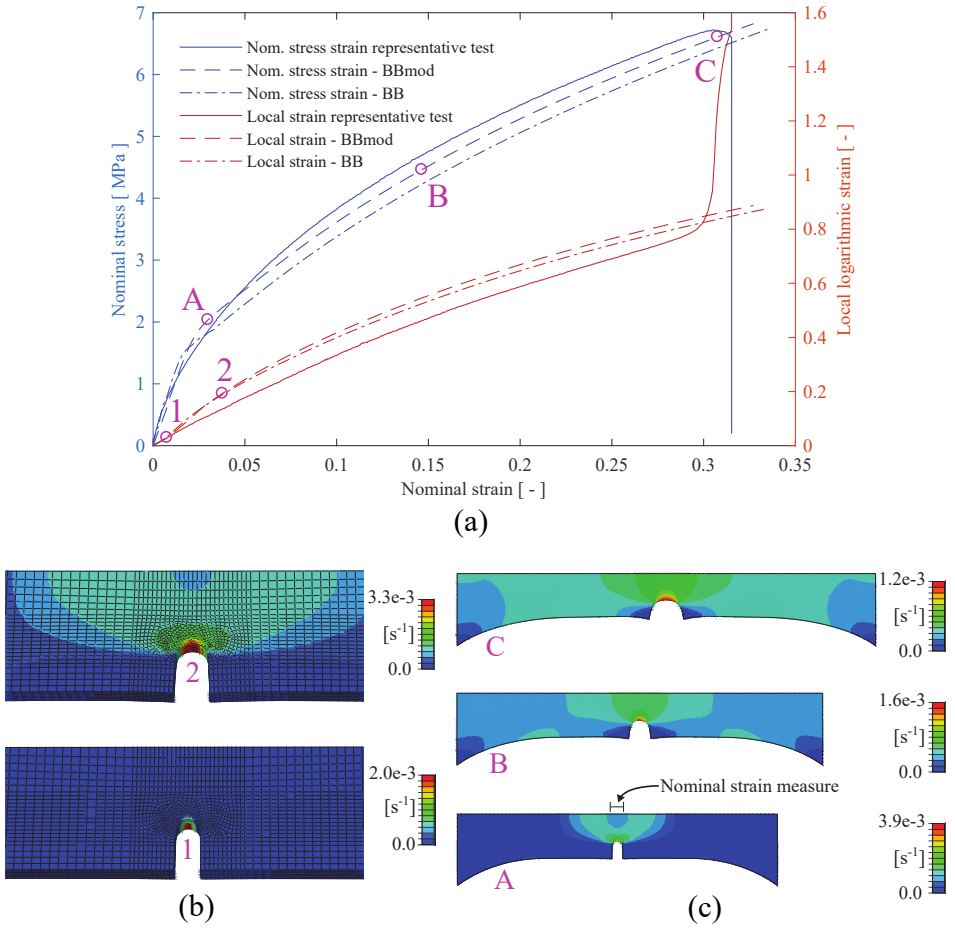

Figure 3.9.: Results of validation simulations. (a) Simulation results compared to the representative test. States 1, 2, A, B and C correspond to the similarly named states presented in sub-figures (b) and (c) respectively. (b) Field output of $\dot{\gamma}_i$ for BBmod simulations corresponding to States 1 and 2 in sub-figure (a). (c) Field output of $\dot{\gamma}_i$ for BBmod simulations corresponding to States A, B, C in sub-figure (a).

right vertical axis present the local logarithmic strain measure defined in Figure 2.23a. Overall, the results are satisfactory considering the complexity of the material and the varied behaviour of the tests. The BBmod model is seen to perform slightly better than the BB model as expected based on the discussions in Section 3.2.4. Initially, there is a significant discrepancy between the simulations and test results. However, the simulations converge towards test data at the end of the simulation. It was not implemented any failure model, such that results past crack initiation in the tests are not relevant.

A key discrepancy between the simulations and the test data occurs almost immediately when the local strain measures diverge shortly after State 1 in Figure 3.9a. Figure 3.9b shows the field output of the effective inelastic shear rate, $\dot{\gamma}_{\mathrm{i}}$, from the simulations using the BBmod model before and after the divergence of the local strain measure. The effective inelastic shear rate in State 1 in Figure 3.9b in the critical element is significantly lower than the peak value, which indicates that the accumulated inelastic deformation is negligible. However, in State 2 the inelastic shear rate in the critical element is fully activated and past the kink in the stress-strain curve. This causes a spurious strain localization effect, as the critical region is significantly softer than the surrounding region, which in turn causes the divergence in the local strain measure.

It is believed that the underestimation of the nominal stress is linked to the same phenomenon as the error in the local strain measure, but on a larger scale. Figure 3.9c shows the field output of the effective inelastic shear rate for the three States A, B and C referenced in Figure 3.9a. In State A, the inelastic deformations are localized in the critical part of the notch, such that the global response is dominated by the overly stiff part of the material response. However, significant inelastic deformations are accumulated in the notched region for State B, leading to the softer phase of the deformation process. Towards the end of the simulation, there is significant inelastic shearing in the whole specimen as well as considerable accumulation in the notched region making the response converge towards the test results. In summary, the kink in the stress-strain curve caused by the evolution of the effective inelastic shear rate is the primary cause of the differences between the tests and the simulations for both the BB and BBmod models. It is the same phenomenon as is observed in the calibration results but amplified by the inhomogeneity of the deformation field in the notched tension tests.

3.4. Discussion and concluding remarks

3.4.1. Discussion

The results show that both the BB model and the BBmod model are viable candidates for modelling of the studied semi-structural adhesive. It was observed a good fit for both tension and compression tests and acceptable results for the notched tension tests. However, there are issues with the implementation and the formulation that complicates the problem. Looking at the numerical implementation, there are significant instabilities present for both models. Incompressibility is a common source of instabilities for rubber-like materials. Depending on the accuracy needed for the incompressibility, there are alternative approaches available. A hybrid formulation, where the pressure is separated into its own field variable in the solver, allows for exact reinforcement of the incompressibility. This formulation adds a new layer of complexity to the problem and makes the model less

available than the approach chosen in this thesis. It was chosen to use a high bulk modulus as a type of penalty formulation to approximately satisfy the incompressibility, which could cause numerical instabilities. The value of the bulk modulus was chosen to be as high as possible without crashing the simulations.

An issue that arose due to the choice of using an implicit solver is the highly non-linear behaviour of the effective inelastic shear rate described by Equation 3.34. A computationally expensive sub-stepping scheme had to be implemented to capture this behaviour. Despite this sub-stepping scheme, the increment size must be small to achieve convergence when the inelastic shear rate is increasing rapidly. Therefore, the increment size would be small throughout the whole simulation for more complex problems where this critical point is reached at different times for different parts. There have been implemented solutions to circumvent this problem in other solvers for the BB model by reformulating the model to have a rate sensitive yield function instead. However, such a formulation further emphasizes the discontinuous response of the model and therefore magnifying the issues discussed in Sections 3.2.4 and 3.3.2.

Specifically for the BBmod model, there is another source of instabilities, as mentioned in Section 3.2.3, regarding the direction of the viscous contribution from Part A. For an implementation in an explicit solver this issue initiates oscillations that creates a feedback loop making the solution diverge rapidly. In an implicit solver, the direction could change during the equilibrium iterations making the simulation unable to converge. A simple solution to this problem was presented in Section 3.2.3 by adding a condition to the change of direction. However, this condition requires relatively small increment sizes. Therefore, it either increases the computational cost of more general problems drastically or it puts strong constraints on the problems regarding loading and unloading. There might be other implementations to solve this issue, but it is considered future work.

Comparing the BB model to the BBmod model, the BBmod model is seen to yield marginally better accuracy as it partially captures the observed multiplicative strain-rate sensitivity. However, the key issue from the BB model is still present, but in a lesser extent. In addition, the BBmod model has an extra numerical instability compared to the BB model, making it unfeasible outside of academic purposes.

The notched tension test simulations give an indication of the performance of the applied material models in some of the loading modes relevant for bonded joints. However, the behaviour is still tension dominated in this case. It would be beneficial to perform validation simulations on the single lap joint (SLJ) tests and peel tests in order to validate the behaviour in a wider range of relevant loading modes. The composite adherents used for the SLJ tests performed in this study as well as the scatter reported in Section 2.5.4 makes these tests unsuitable for validation. Therefore, a better validation process is recommended for future work.

Failure was omitted from the modelling approach as it was found to be governed by a brittle

mechanism, which significantly complicates the failure modelling process. Therefore, it was determined to be out of scope for the current study. A proper validation process and failure model are necessary in order to apply a multi-scale modelling approach. As both are missing for this adhesive, it is unsuitable for further studies in line with the overarching research strategy.

3.4.2. Conclusions

It was shown that material models previously applied to semi-structural adhesives in literature were unsuitable for the studied adhesive. These models were not able to fully capture the non-linear behaviour observed in the experiments or were lacking data for an accurate calibration. Based on the rubber-like behaviour exhibited by the studied adhesive, it was chosen to base the modelling approach on the Bergström-Boyce (BB) model. This model is typically used to model rubbers and it is micro-mechanically based such that physical behaviour is ensured outside of the domain used for calibration. As the calibration was limited to uniaxial tension and compression data, this became a key reason for the choice of model. The BB model exhibits a primarily additive strain-rate sensitivity, which is in contrast to the multiplicative strain-rate sensitivity observed in the experiments. Therefore, it was chosen to implement a modification to the BB model, where the equilibrium response was multiplicatively scaled with a Cowper-Symonds rate sensitivity factor.

The BB model and its modification is seen to be able to predict the response of the material with acceptable accuracy for the calibration cases and the validation case. As expected, the modified model predicts the material response with higher accuracy as it partially captures the observed multiplicative strain-rate sensitivity of the studied material. A significant error present for both models is the initial sudden change of stiffness caused by the formulation of the effective inelastic shear rate with the given material parameters. It is evident that this error is amplified by having an inhomogeneous deformation field. Both models exhibit significant numerical instabilities in terms of incompressibility and the rapid evolution of the effective inelastic shear rate. The modified model has an additional instability caused by the definition and implementation of the direction of the additional viscous contribution. As it is currently implemented, this instability limits the domain of problems where the model is applicable. Therefore, the modification is not recommended for general purpose outside of academic problems.

In line with the research strategy presented in Section 1.5, it is demonstrated how the experimental campaign outlined in Chapter 2 is used to determine and calibrate numerical models for the studied adhesive. There are some previously discussed problems related to validation and failure modelling that makes it difficult to continue with multi-scale modelling approach in this instance. However, the approach demonstrated in Part II has shown to be viable if these specific problems are addressed. Therefore, it was chosen as the basis for the studies performed in Part III.

Part III.

Crash stable epoxy adhesive

4. Basis for studying structural adhesives

4.1. Introduction

This section will give the objectives of the chapter and link it to the rest of the thesis. There will also be presented an overview of the validation approach applied in Part III of the thesis including a brief outline of the chosen meso-scale modelling strategy.

4.1.1. Chapter description

A similar strategy to the one applied to the semi-structural adhesive in Part II has been applied to the structural adhesive which is studied in this part. The goal of this chapter is to present an experimental basis for calibration and validation of meso-scale and macro-scale numerical models of the structural adhesive SikaPower 498 (SP498). Further, it is the goal to choose, calibrate and validate a suitable meso-scale material model for the adhesive. This corresponds to the first 2 steps of the objectives and 3 steps of the research strategy presented in Sections 1.3 and 1.5 respectively. The experimental and numerical work presented in this chapter will then serve as a basis for further studies in Chapters 5 and 6 following the same overarching objectives and research strategy.

SP498 is a single component structural epoxy adhesive that is commonly used to bond structural components in the automotive industry. Further, it is a hot curing adhesive which is applied to the body in white of a car and cured at 180 °C during the electro-deposition coating process. The adhesive is a crash-modified adhesive, meaning it contains rubber particles which increases the ductility of the material by arresting propagating cracks. As will be demonstrated in this chapter, the difficulties present for the semi-structural adhesive studied in Part II are not significant for this adhesive. The ductile nature of failure for this adhesive and the comprehensive experimental basis allows for more reliable modelling of failure on a mesoscopic scale and multi-scale validation. This is the primary reason for the change of the studied adhesive, as it allows for further studies on a macroscopic level and validation for both meso-scale and macro-scale models.

In this chapter it will be presented an overview of the experimental basis in Section 4.2. Then, a detailed outline and calibration of the chosen polymer model will be presented in Section 4.3. Validation of this model is presented in Section 4.4. Finally, the overall results are discussed and concluded in Section 4.5.

4.1.2. Validation strategy for multi-scale modelling of SP498 adhesive

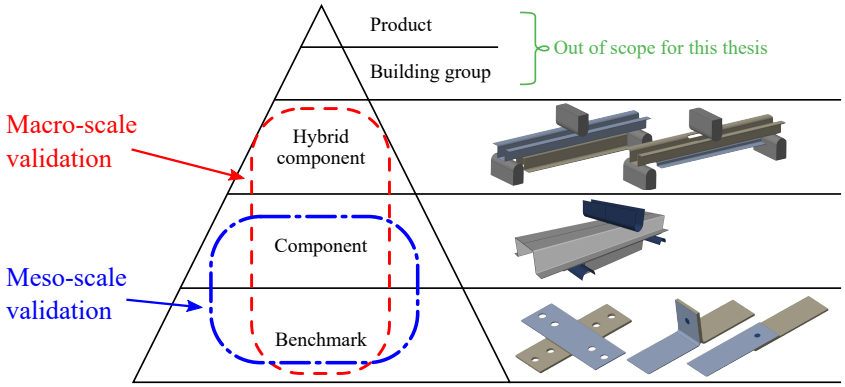

Figure 4.1.: Validation strategy for Part III of the thesis. Benchmark and hybrid component test figures from Reil [120].

The validation strategy for Part III of the thesis is based on investigating the adhesive behaviour in progressively more complex problems. Figure 4.1 shows the validation hierarchy applied for validation of meso-scale and macro-scale models in this work. Benchmark tests represent simple experiments with a single mechanical fastener or a limited adhesive layer. The macroscopic loading mode for the benchmark tests is generally dominated by a primary loading mode, such as macroscopic tension or compression. In contrast, the local stress and strain fields might be significantly more complex. In this work, the benchmark tests consist of cross tests, peel tests and single lap joint tests.

Moving up in the hierarchy, the bonded component test significantly increases the size of the problem. This allows for different loading modes for different parts as well as controlled crack propagation over large displacements. Further, the components tests subject the joints to combined macroscopic loading, making them particularly suitable for validation of macro-scale models. A bonded component loaded in 3-point bending, as seen in Figure 4.1, represents the component level tests in this work. This component subjects the adhesive layer to both macroscopic shear and peel loading. The hybrid component tests represent one step further in the validation process, adding the interaction between adhesive bonding and mechanical fasteners on the component level as an additional complexity. At the top of the hierarchy are the building group and product levels, these are relevant for more mature

models that are intended for industrial applications and are considered out of scope for the current work.

Validation of a meso-scale modelling approach is presented in Section 4.4. The emphasis will be on the benchmark level of experiments, as these are more manageable in terms of simulation time and still provides a sufficient level of complexity. There will also be run a validation case on the component level to get an indication of the performance in a more complex situation. The experiments used for validation of meso-scale models are briefly described in the following section. Validation of macro-scale models will be shown in Chapter 5. For the macro-scale models, the emphasis will be on the bonded component test. There will also be run validation cases on the hybrid benchmark and component tests in Chapter 6, to serve as a further indication on the performance and potential of the applied calibration framework.

4.1.3. Modelling choice

As is outlined in Sections 1.2.1 and 1.2.5, there is significantly more literature available concerning structural adhesives compared to the semi-structural adhesive investigated in Part II. Particularly, Dufour et al. ([5],[44]) studied the same structural adhesive SP498 that is the focus of Part III of this thesis. Therefore, it is possible to determine a suitable meso-scale material model without performing an extensive experimental campaign first.

Dufour et al. [5] reported several phenomena governing the meso-scale behaviour of the SP498 adhesive. In the elastic domain, it was observed viscoelasticity and relatively small elastic strains compared to that of a semi-structural adhesive. The plastic domain was seen to exhibit viscoplasticity, pressure sensitive yielding, non-isochoric plastic flow and a ductile damage mechanism. These phenomena, with the exception of viscoelasticity, was confirmed by the tests reported in Section 4.2.1.

There is an already implemented polymer model available within the SIMLab research group that is able to capture the previously mentioned phenomena. This model is based on the work presented by Polanco-Loria et al. [89] and Morin et al. [121]. The specific components of this model that are necessary to describe the key phenomena of the adhesive are outlined in Section 4.3.1.

4.2. Experimental campaign

4.2.1. Bulk adhesive testing

This section will describe the bulk adhesive tests that was used to calibrate the selected polymer model. The bulk adhesive tests consisted of uniaxial tension tests, uniaxial compression tests and notched tension tests as shown in Figure 4.2. Details regarding the test setups are referred to Reil [120], although some necessary information will be provided here as well. The emphasis of this section will be on the post-processing and results of the bulk adhesive tests. There will also be a brief discussion regarding the consequences of the observed results in a modelling perspective.

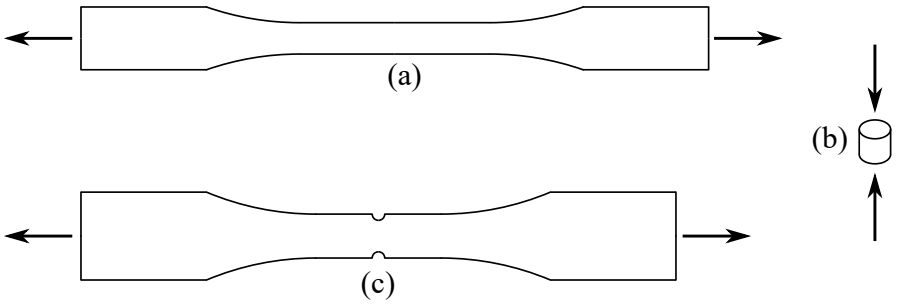

Figure 4.2.: Bulk adhesive tests [120]. (a) Uniaxial tension. (b) Uniaxial compression. (c) Notched tension.

Figure 4.3 shows the detailed geometry of the uniaxial tension test specimens. These specimens were tested at loading velocities of 1.8 mm/min, 18.0 mm/min and 180 mm/min corresponding to nominal strain-rates of $10^{-3}\,s^{-1}$, $10^{-2}\,s^{-1}$ and $10^{-1}\,s^{-1}$ respectively. The tests were monitored with two perpendicular cameras recording at a rate of 15 Hz in order to facilitate digital image correlation (DIC).

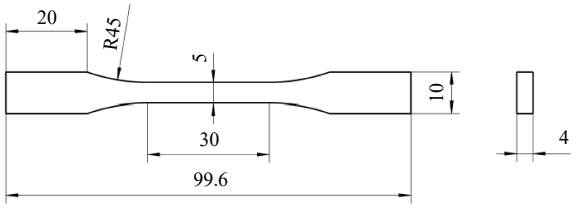

Figure 4.3.: Geometry of tension test specimens [120].

Similar to the bulk adhesive tests reported in Chapter 2, DIC was essential for the post-processing of these experiments. The DIC software [109] used for analyses of the semi-structural adhesive was applied here as well. The analyses were performed using linear elements with a size of 40 px × 40 px equal to 1.06 mm × 1.06 mm for the front surface and 50 px × 50 px equal to 1.47 mm × 1.47 mm for the side surface.

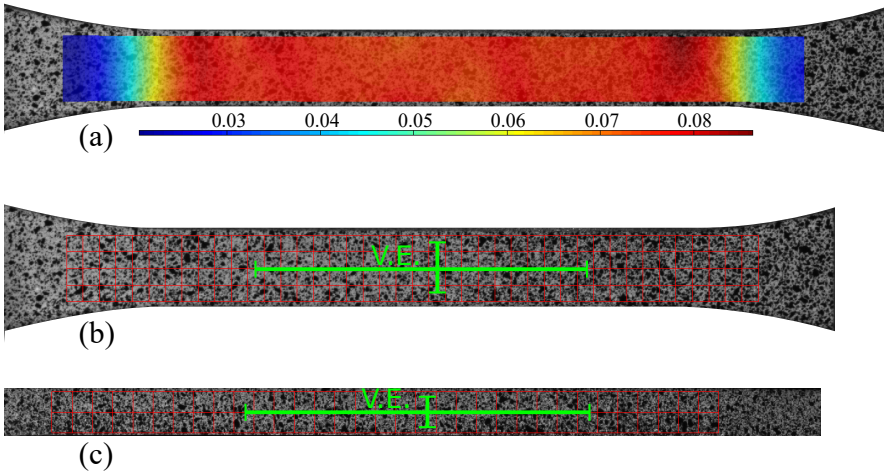

Figure 4.4.: Post-processing of tension tests. (a) Example of principal strain field measured by DIC on a representative tension test at a nominal strain-rate of $10^{-3}\,s^{-1}$. (b) DIC mesh and virtual extensometers (VE) applied to the front surface of the specimen. (c) DIC mesh and VE applied to the side surface of the specimen.

Figure 4.4a shows the principal strain field immediately preceding failure for a representative tension test. It is evident that deformation is localized in the gage section of the specimen. However, there are some gradients through the gage section such that a representative measure has to be defined. Virtual extensometers (VE) were defined in the middle of the observed surfaces covering a significant portion of the length and width of the gage section as seen in Figures 4.4b and 4.4c. The length and position of the VE were chosen to avoid peak strain values, as these peaks were likely caused by DIC error or a non-representative part of the material. Additionally, the VE have the effect of averaging the strain measure, ensuring more representative measurements for the material.

The post-processed results of the uniaxial tension tests are presented in Figure 4.5. Figure 4.5a shows the Cauchy stress versus the logarithmic strain for three representative tests at three different nominal strain-rates. In contrast to the previously studied semi-structural adhesive, there are strong indications of significant plastic strains preceding failure for this adhesive. While there is no significant viscoelasticity, there is a clear effect of viscoplasticity present.

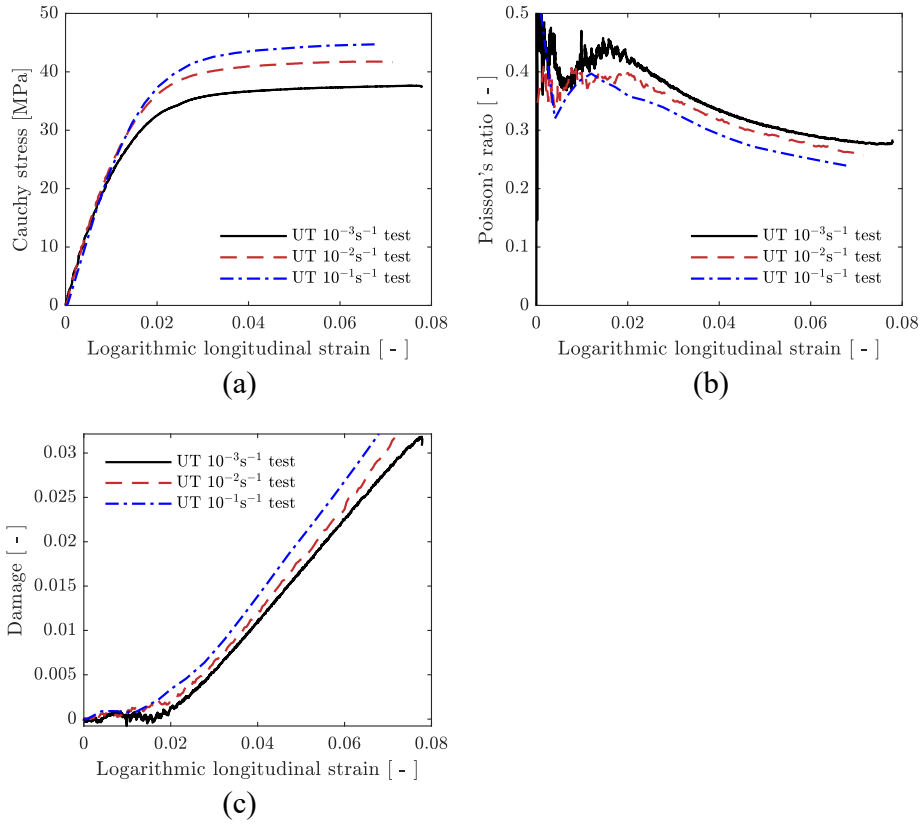

Figure 4.5.: Uniaxial tension test results. (a) Cauchy stress vs. logarithmic longitudinal strain. (b) Poisson's ratio vs. logarithmic longitudinal strain. (c) Damage vs. logarithmic longitudinal strain.

Looking at the evolution of the Poisson's ratio with the logarithmic strain in Figure 4.5b, there is a strong effect of non-isochoric plastic flow. It can be assumed that the that the adhesive consists of a matrix phase and a void phase, where the matrix could be assumed to be isochoric in the plastic domain. The volume fraction of the void phase could then be considered as damage, D, following the equation:

$$D = 1 - \exp(-\varepsilon^{p}_{\text{vol}}) \tag{4.1}$$

where $\varepsilon^{p}_{\text{vol}}$ is the volumetric plastic strain. Figure 4.5c shows the evolution of the damage with the logarithmic strain. The gradual evolution of damage in the plastic domain demonstrates the ductile damage process in the material.

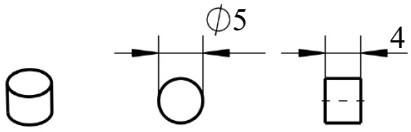

Figure 4.6.: Geometry of compression test specimens [120].

Figure 4.6 shows the geometry of the uniaxial compression test specimens. These specimens were tested at a loading velocity of 0.24 mm/min corresponding to a nominal strain-rate of $10^{-3}\,s^{-1}$. The tests were monitored with two perpendicular cameras recording at a rate of 2 Hz in order to facilitate DIC.

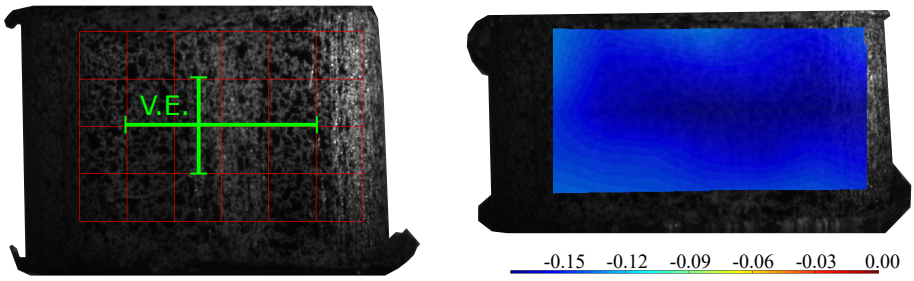

Figure 4.7.: Post-processing of compression tests. (a) DIC mesh and VE applied to the surface of the specimen. (b) Example of principal strain field measured by DIC on a representative compression test at a nominal strain-rate of $10^{-3}\,s^{-1}$.

Strain measurements from the compression tests were obtained using the same DIC software as the tension tests. The linear DIC elements had a size of 100 px × 100 px equal to 0.57 mm × 0.57 mm and 0.66 mm × 0.66 mm for the front and side cameras respectively. Figure 4.7a shows the VE used to define the longitudinal and transverse strains. Similar to the tension tests, these VE are used to obtain a more representative strain measure than the strain measured in a single DIC element. The location of the different virtual extensometers were chosen to avoid the extreme values of the principal strain field shown in Figure 4.7b.

A comparison between the stress-strain curves of a representative tension test and compression test run at a nominal strain-rate of $10^{-3}\,s^{-1}$ is shown in Figure 4.8a. It is evident that yielding of the material is subjected to a strong pressure sensitivity. Figure 4.8b shows the damage evolution for a representative compression test calculated using Equation 4.1. There is significant damage evolution in the material when subjected to positive pressure, suggesting that there might be local buckling around particles in the adhesive.

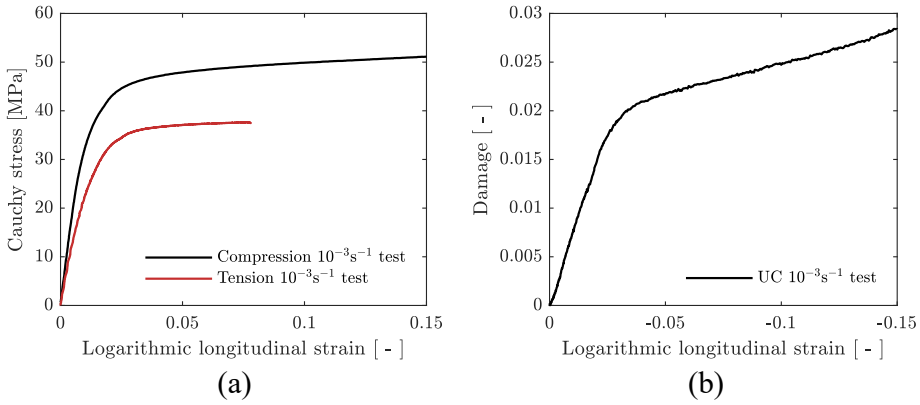

Figure 4.8.: Uniaxial compression test results. (a) Cauchy stress vs. logarithmic longitudinal strain. (b) Damage vs. logarithmic longitudinal strain.

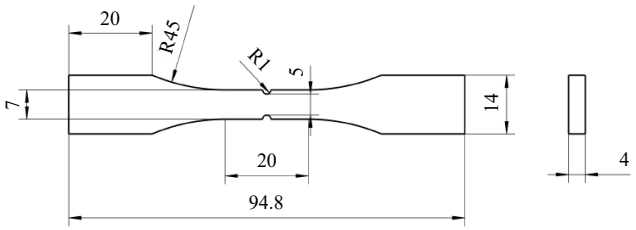

Figure 4.9.: Geometry of notched tension test specimens [120].

Figure 4.9 shows the geometry of the notched tension test specimens. These specimens were tested at a loading velocity of 1.8 mm/min corresponding to a nominal strain-rate of $1.5 \cdot 10^{-2}\,s^{-1}$ using the initial length of the notched region as a reference. Similar to previous bulk adhesive tests, the specimens were covered with a speckled pattern and monitored by two perpendicular cameras recording at a rate of 10 Hz in order to facilitate DIC.

Post-processing of the notched tension tests involved defining two different strain measures for correlation. A nominal strain measure with initial length equal to the length of the notched region of 2 mm was used as a reference strain indicating the global deformation. A key advantage with this deformation measure is that it is not particularly sensitive to the boundary conditions, thus removing a potential source of error. There was also defined a transverse strain measure in the centre of the notched region as seen in Figure 4.10a. This strain measure provided an additional curve for evaluating correlation between experiments and simulation results. These measures were obtained from DIC analyses using a linear elements with a size of 40 px × 40 px equal to 0.23 mm × 0.23 mm. An example of the

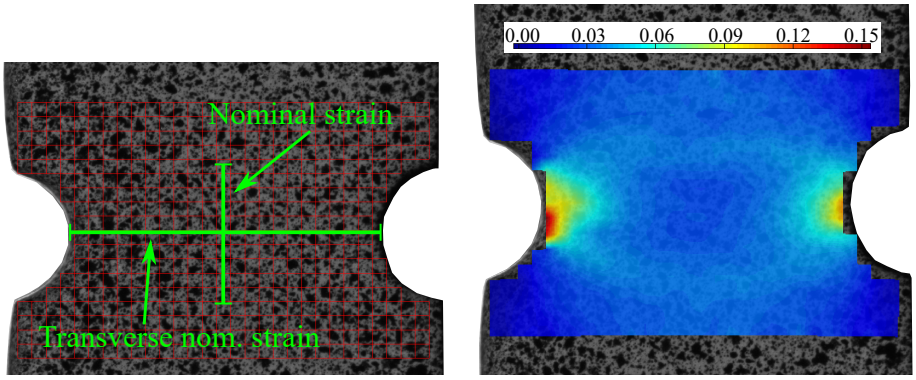

Figure 4.10.: Post-processing of notched tension tests. (a) DIC mesh and virtual extensometers used to measure the nominal strain measure and transverse strain measure. (b) Example of principal strain field measured by DIC on a representative notched tension test.

principle strain field obtained from one such analysis is shown in Figure 4.10b.

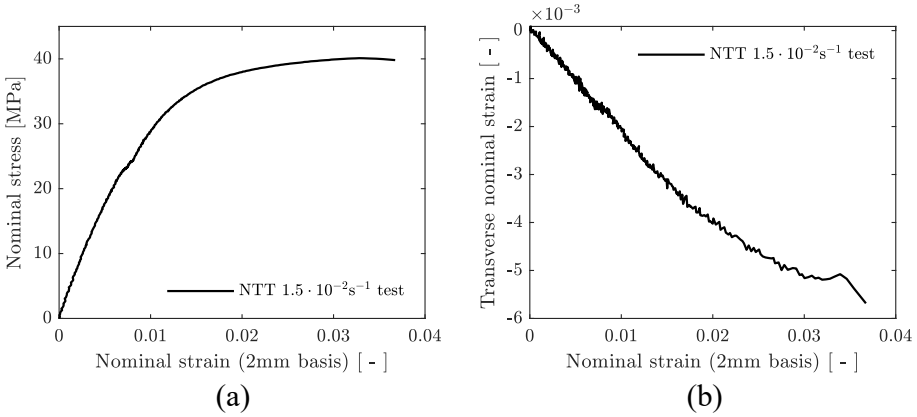

Figure 4.11.: Notched tension test results. (a) Nominal stress vs. nominal strain. (b) Transverse nominal strain vs. nominal strain.

Results of the notched tension tests are presented in Figure 4.11. The nominal stress measure was calculated by dividing the total force by the initial cross-section area of the smallest cross-section in the notched region. Nominal stress versus nominal strain for a representative notched tension test is shown in Figure 4.11a. Comparisons between the nominal strain measure and the machine displacement revealed that there was slippage in the grips. The shift of the stress-strain curve before a nominal strain of 0.01 is believed to be caused by this issue. Figure 4.11b shows the evolution of the transverse nominal strain

in the notched region. It should be noted that the transverse nominal strain is an order of magnitude lower than the nominal strain measure, which suggests significant plastic dilatation in the notched region.

Overall, the quality of the bulk adhesive experiments was sufficient for the intended purpose. However, there are some issues which should be kept in mind when correlating these experiments with numerical simulations. Specifically, the compression test specimens were very small, which adds significant uncertainty to the geometry of the specimens. Further, small specimens are prone to exhibit a non-representative response due to an uneven distribution of particles and flaws. Therefore, the compression tests are primarily used to determine the ratio between the yield stress in tension and compression. The details of the notched tension tests are also relatively small compared to the machining tools used. Figure 4.10 shows that the geometry of the physical specimens is rounded compared to the nominal geometry. Measurements on images of the specimens also revealed that that notch on one side of the representative test had a 10 % larger radius. These issues could contribute to any divergence between experimental and numerical results.

In summary, the experiments exhibited a range of phenomena relevant for numerical modelling of the adhesive. Based on tension tests, the elastic domain seems to be insensitive to the strain-rate with relatively small elastic strains compared to a semi-structural adhesive. This suggests that a hypo-elastic formulation would be sufficient for modelling the elastic domain. Further, the tension tests show a clear effect of viscoplasticity, which is further emphasized by the additional data reported by Dufour [44] for this adhesive. The results presented in Figure 4.8 highlight the pressure sensitivity of the yielding of the material. Additionally, all of the bulk adhesive tests exhibited evidence of non-isochoric plastic flow. Damage was seen to grow steadily in the plastic domain for the tension tests suggesting a ductile damage mechanism.

4.2.2. Benchmark tests

A series of benchmark tests were performed by Reil [120] and used in the current work. This section will give a brief description of the different benchmark tests that is used for validation purposes in Sections 4.4.1 and 4.4.2. These tests include bonded cross tests, hybrid single lap joint tests and hybrid peel tests.

Reil [120] performed cross tests between steel and aluminium adherents in the cross test rig shown in Figure 4.12. The cross test rig allowed for testing in three different configurations; a macroscopic tension case, CT00, a mixed mode case, CT45, and a shear dominated case, CT90. It was reported by Reil [120] that the stiffness of these bonded specimens was too high in order to get accurate displacement measures for comparisons to numerical models. However, the tests still serve as a partial validation to the meso-scale modelling

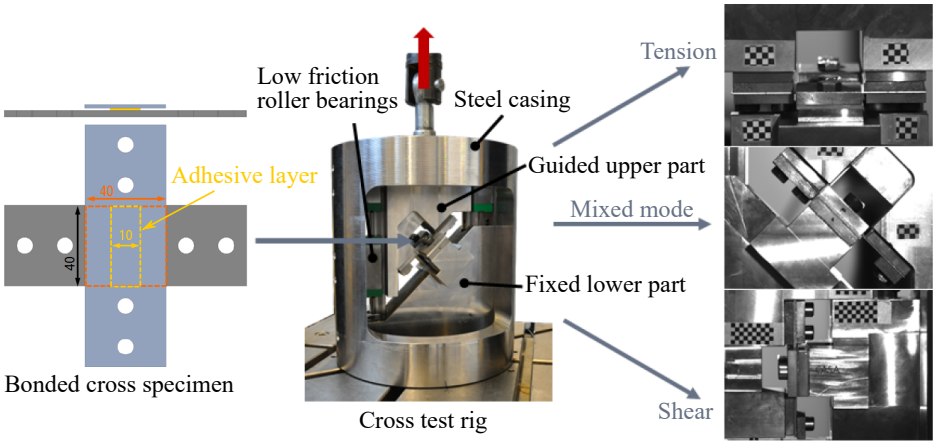

Figure 4.12.: Overview of cross test setup [120].

framework chosen for the given adhesive. A more in-depth discussion of the validation case is presented in Section 4.4.1.

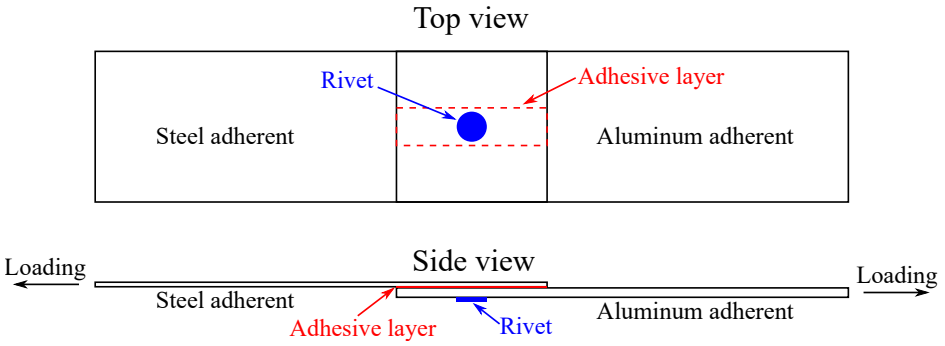

Figure 4.13.: Overview of hybrid single lap joint test setup [120].

Hybrid single lap joints (SLJ) tests with steel and aluminium substrates, see Figure 4.13, were also tested by Reil [120]. The substrates were bonded together using the SP498 adhesive in addition to being fastened with a self-piercing rivet (SPR). Due to the high stiffness of the adhesive compared to the SPR, the initial behaviour was seen to be dominated by the adhesive layer until failure of the adhesive. In contrast to the cross tests, it was possible to obtain an optical displacement measure that was representative, thus enabling direct comparisons between tests and numerical simulations. Therefore, it was found to be suitable for validation of numerical models as discussed in Section 4.4.2.

Hybrid peel tests with similar materials and joining method as the hybrid SLJ tests were

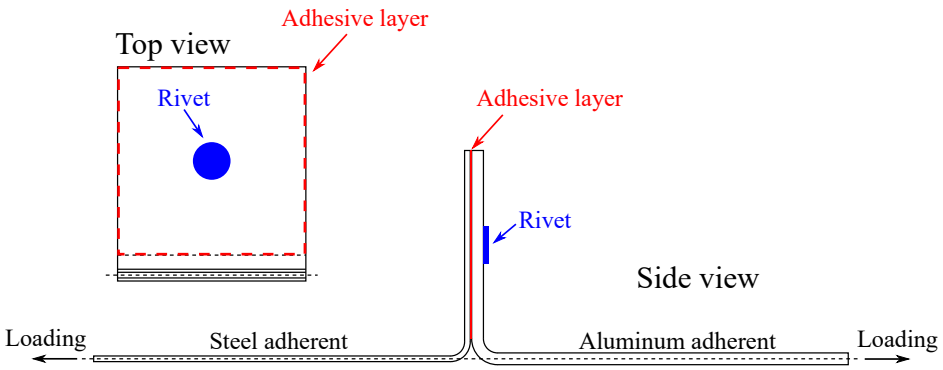

Figure 4.14.: Overview of hybrid peel test setup [120].

performed by Reil [120]. An overview of the peel tests is shown in Figure 4.14, where the adhesive covers the whole overlap region. Similar to the hybrid SLJ tests, the initial behaviour was dominated by the adhesive layer until the crack reached the rivet. Therefore, these tests serve a similar purpose as the hybrid SLJ tests, but with a tension dominated macroscopic loading instead of shear dominated. Further discussions regarding the validation tests are covered in Section 4.4.2.

4.2.3. Component testing

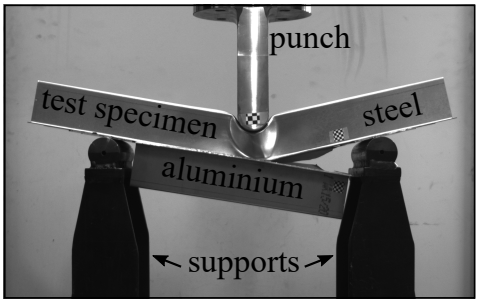

Figure 4.15.: Overview of bonded component test setup [122].

This section presents a detailed description of the test specimens, test setup, post-processing techniques and results for the bonded component tests shown in Figure 4.15. Production of the specimens was performed externally and will not be covered. However, some of the visible production flaws will be mentioned. Finally, there will be a brief discussion regarding the results.

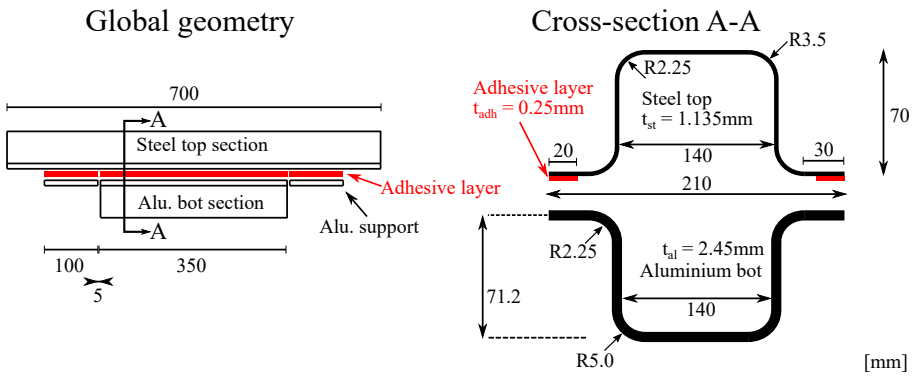

Figure 4.16.: Detailed overview of the global and cross-section geometry of the bonded component test.

The bonded component tests consist of two hat profiles bonded together with the SP498 adhesive in addition to two support plates as seen in Figure 4.16. A rolled micro-alloyed steel sheet is used to make the top hat section, while the bottom hat section and support plates are made from the same 6XXX series aluminium alloy with a T4 temper. The support plates ensure that there are no local deformations at the contact between the supports and the specimen. Detailed measures of the global geometry and cross-section are given in Figure 4.16.

There was observed an initial twist of the specimens, which was likely caused by the heat treatment during curing of the adhesive. The twist was estimated by measuring the maximum lift of the specimens from the supports in a unloaded state. This measure was used to calculate the angle of twist over the 439 mm distance between the supports. For Specimens 1 and 3, there was measured a twist between the supports of 0.68° and 1.01° respectively, while there was no measurable twist for Specimen 2.

The thickness of the adhesive line was found by measuring the total thickness of the two flanges bonded together, then subtracting the thickness of the steel and aluminium sheets. Measurements were taken at the inner and outer part of the bonded area of the flange at 6 different points along the length of the bonded area. A variation of about ±0.05 mm was found for the adhesive thickness in the length direction of the specimens. Further, it was found a gradient in the adhesive thickness in the transverse direction, where the inner part of the bonded area of the flange was approximately 0.2 mm thicker than the outer part. The average thickness of the adhesive layer for the 3 different specimens was approximately 0.25 mm.

Figure 4.17a shows an overview of the test setup for the bonded component tests. The specimen is loaded in 3-point bending with a loading velocity of 10 mm/min. Three different cameras were used to monitor the experiments, an overview camera to observe the

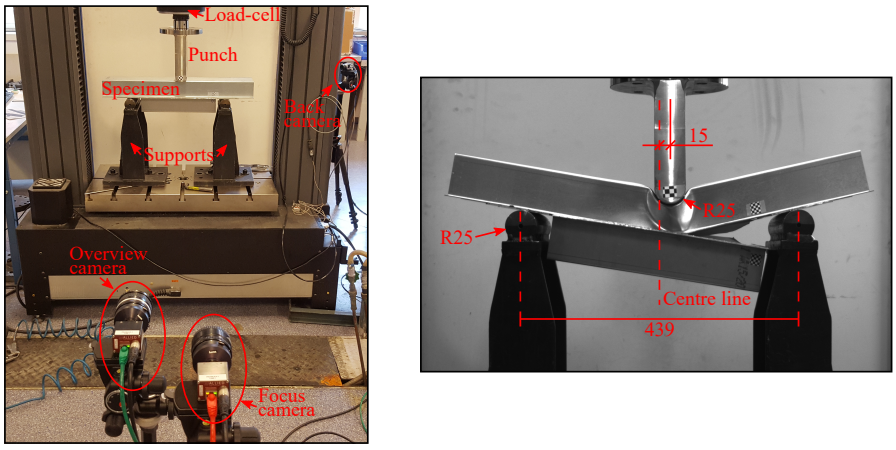

Figure 4.17.: Overview of bonded component test setup. (a) Overview of setup including camera positions. (b) Key measurements of 3-point bending setup.

global deformation mode, a focus camera to track the crack propagation and a back camera to verify that the deformation mode remained symmetric. All cameras recorded at a rate of 1 Hz. Chequered stickers were added to the specimens above and below the planned initiation point for the cracks as well as on the punch to facilitate point-tracking in order to obtain accurate displacement measures.

Key dimensions of the test setup are presented in Figure 4.17b. Specifically, the punch is offset with 15 mm to the centre line between the two supports. This was done in order to ensure that the crack initiated at the right side for all three replicates, thus allowing the focus camera to track its propagation. It was considered using Teflon spacers at the contact points between the supports, the punch and the specimens to reduce the friction between them. However, similar experiments performed by Reil [120] suggested that the influence of these spacers were limited. Therefore, it was chosen to not use spacers in order to reduce the number of variables.

Post-processing of the experiments was done through point-tracking, where it was used the same DIC software as previously in Section 4.2.1. An initial study tracked the displacement of the punch and compared it to the crosshead displacement measured by the machine. These measures were seen to coincide within a reasonable margin of error, such that the machine displacement could be used as a reference displacement measure. Figure 4.18 shows the locations of the points used to measure the crack opening displacement, which was defined as the absolute change of distance between the two points. These locations were chosen in such a way to coincide with the nodes of a finite element model using a general mesh size of 4 mm. This ensured that experimental results and simulation results could be

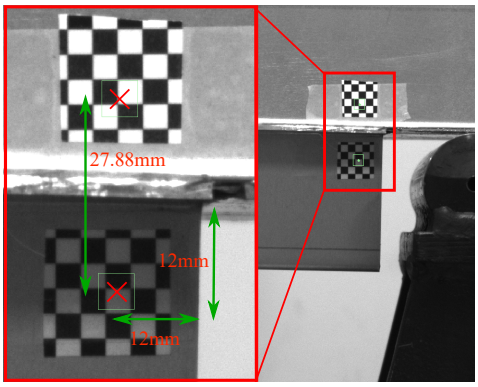

Figure 4.18.: Location of tracking points used to measure and define the crack opening displacement.

directly compared. It should be noted that this measure is influenced by significant bending of the flanges as well as some deformation in the webs of the hat profiles. Therefore, it does not accurately represent the crack propagation. However, it does serve as an indication of the crack propagation.

The results of the component tests are presented in Figure 4.19. The raw data from the test machine is represented by the force versus machine displacement curves in Figure 4.19a. Force versus crack opening displacement and the relationship between the machine displacement and crack opening displacement is shown in Figures 4.19b and 4.19c respectively.

An analysis of the response of the component indicates that it goes through several stages where the dominant mechanism changes. The initial response is purely elastic until local buckling at the contact between the punch and the specimen occurs. This local buckling softens the response, but strain hardening of the metal keeps the force level rising. It is evident from Figure 4.19b that the peak force is reached once the adhesive starts failing. This is further emphasized by the fact that the initial change in crack opening displacement is governed by bending of the flanges. Visual inspection of the crack from the focus camera and the evolution presented in Figure 4.19c confirmed this phenomenon. The response is then governed by the propagation of the crack until it reaches the punch. At that point, strain hardening of the metals would again increase the force level. However, the tests were stopped roughly when the crack stopped propagating. In terms of validation, the bonded component tests seem particularly suitable as the post-peak response of the component is dominated by crack propagation in the adhesive layer. Therefore, these tests are used as a basis for the validation performed in Chapter 5, in addition to providing an indication of the viability of the polymer model as shown in Section 4.4.3.

It is evident that the repeatability of the experiments is good despite the inaccuracies from

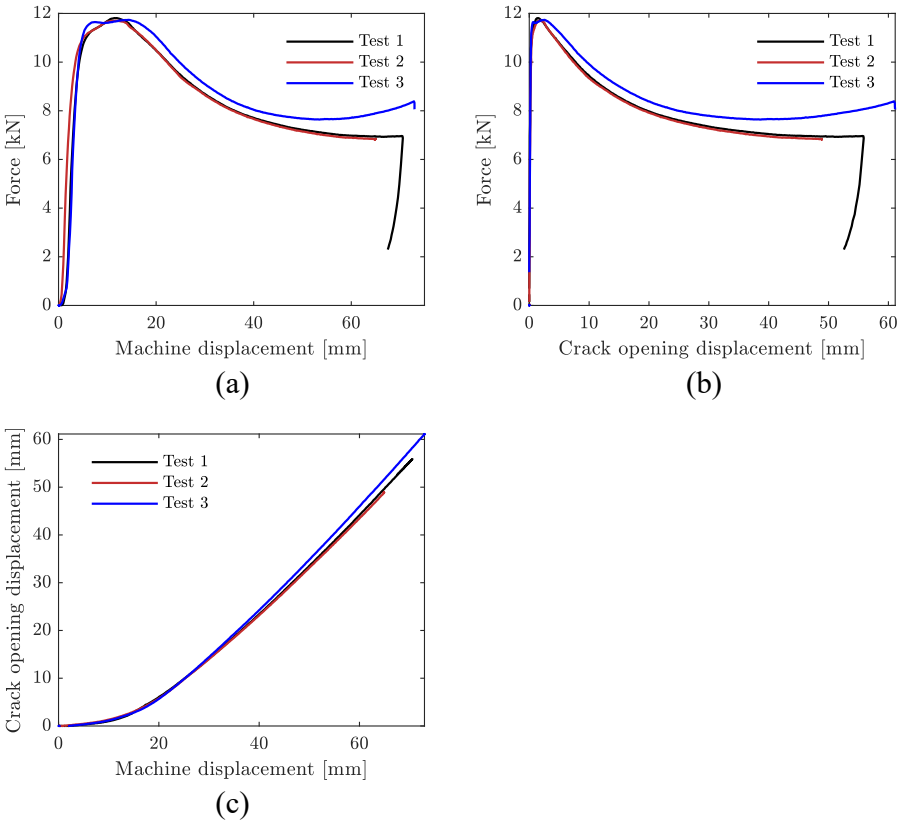

Figure 4.19.: Results of bonded component tests. (a) Force vs. machine displacement. (b) Force vs. crack opening displacement. (c) Crack opening displacement vs. machine displacement.

the production process. The initial twist of Specimen 1 and 3 does not seem to influence the results significantly. It is believed that the minor shift in the elastic response of the specimens seen in Figure 4.19a is caused by the specimens straightening themselves until full contact is achieved between the supports and the specimen.

Figure 4.20a shows the local buckling in the region close to the punch. While there are large strains in the region, there is no failure in the metal. This significantly reduces the complexity of the problem, making it more suitable for validation of the adhesive behaviour. One of the failed adhesive lines from Specimen 2 is shown in Figure 4.20b. There are some flaws present at the end of the adhesive layer, which suggests that the exact timing and strength of the adhesive before crack initiation is subjected to some uncertainty. However, the failure of the adhesive layer is dominated by cohesive failure, which is the preferred

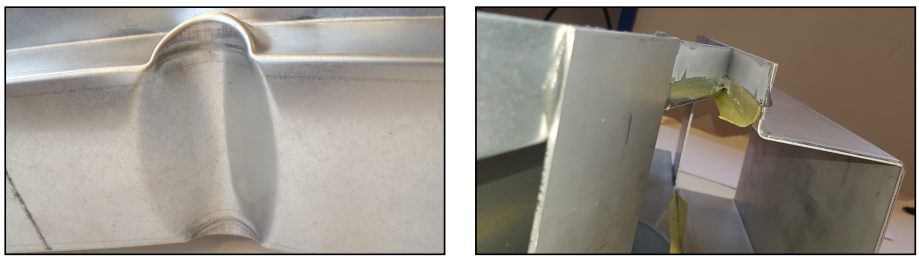

(a) (b)

Figure 4.20.: Post-failure pictures of key locations of bonded component test number 2. (a) Local buckling at impact location. (b) Failure of adhesive layer.

failure mode as the numerical models assume a cohesive failure.

4.3. Meso-scale modelling

This section gives an outline of the numerical framework required for meso-scale modelling of the SP498 adhesive. It is based on the model choice described in Section 4.1.3. Further, the model is calibrated based on the experimental data presented in Section 4.2.1.

4.3.1. Polymer model description

The polymer model presented in this section is based on an in-house model developed with the intention of capturing the phenomena typically present in ductile polymers. While the original implementation contains a range of modules, only the ones relevant for the current work will be presented here.

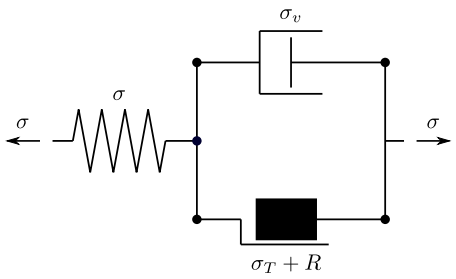

Figure 4.21.: Rheological interpretation of the polymer model.

A finite strain framework forms the basis for the presented polymer model. A corotational formulation is used to retain an objective stress rate for large rotations. This corotational formulation is based on the polar decomposition of the deformation gradient, $\mathbf{F}$, as shown:

$$\mathbf{F} = \mathbf{R} \cdot \mathbf{U} \tag{4.2}$$

where $\mathbf{R}$ is the rotation tensor and $\mathbf{U}$ is the right stretch tensor. Using this rotation tensor, the corotational rate of deformation tensor, $\hat{\mathbf{D}}$, and the corotational Cauchy stress tensor, $\hat{\boldsymbol{\sigma}}$, can be defined:

$$\hat{\mathbf{D}} = \mathbf{R}^T \cdot \mathbf{D} \cdot \mathbf{R} \tag{4.3}$$

$$\hat{\boldsymbol{\sigma}} = \mathbf{R}^T \cdot \boldsymbol{\sigma} \cdot \mathbf{R} \tag{4.4}$$

where is $\mathbf{D}$ is the rate of deformation tensor and $\boldsymbol{\sigma}$ is the Cauchy stress tensor. Based on the rheological model presented in Figure 4.21, the corotational rate of deformation, $\hat{\mathbf{D}}$, can be split into an elastic and plastic component:

$$\hat{\mathbf{D}} = \hat{\mathbf{D}}^e + \hat{\mathbf{D}}^p \tag{4.5}$$

where $\hat{\mathbf{D}}^e$ is the elastic part of the rate of deformation tensor and $\hat{\mathbf{D}}^p$ is the plastic part of the rate of deformation tensor.

Given the relatively small elastic deformations observed in the experiments, a hypo-elastic formulation is applicable to describe the elastic domain of the model. Using this formulation, the rate of the corotational Cauchy stress tensor, $\dot{\hat{\boldsymbol{\sigma}}}$, is given by:

$$\dot{\hat{\boldsymbol{\sigma}}} = \hat{\mathbf{C}} : \hat{\mathbf{D}}^e \tag{4.6}$$

where $\hat{\mathbf{C}}$ is the isotropic tensor of elastic moduli.

The plastic domain is defined by the yield function, f, given by:

$$f(\hat{\boldsymbol{\sigma}}, R) = \varphi(\hat{\boldsymbol{\sigma}}) - (\sigma_T + R) \tag{4.7}$$

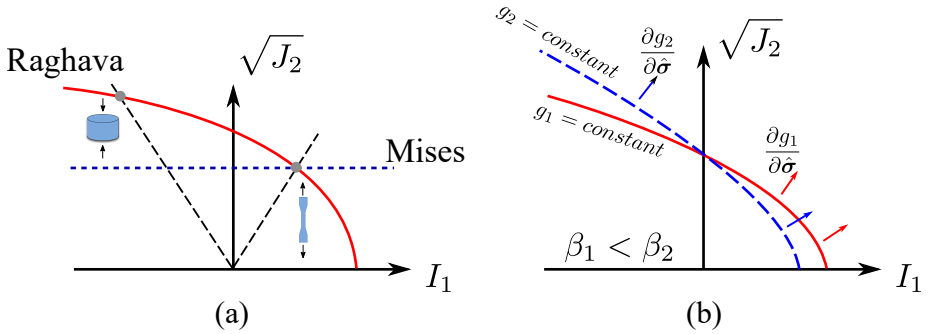

Figure 4.22.: Visualization of yield function and plastic potential in $\sqrt{J_2} - I_1$ space. (a) Raghava yield function and von Mises yield function. (b) Influence of dilatation parameter on the plastic potential.

where $\varphi(\hat{\boldsymbol{\sigma}})$ is the equivalent stress. In order to introduce pressure sensitivity to the model, the Raghava yield function [87] was adopted. For this yield function, the equivalent stress, $\varphi(\hat{\boldsymbol{\sigma}})$, is given by the following equation:

$$\varphi(\hat{\boldsymbol{\sigma}}) = \frac{(\alpha - 1)\text{trace}(\hat{\boldsymbol{\sigma}}) + \sqrt{(\alpha - 1)^2(\text{trace}(\hat{\boldsymbol{\sigma}}))^2 + 6\alpha(\hat{\boldsymbol{\sigma}}' : \hat{\boldsymbol{\sigma}}')}}{2\alpha} \tag{4.8}$$

where $\hat{\boldsymbol{\sigma}}'$ is the deviatoric part of the corotational Cauchy stress tensor and α is the pressure sensitivity parameter which is defined by:

$$\alpha = \frac{\sigma_C}{\sigma_T} \geq 1 \tag{4.9}$$

where σ_C is the yield stress in uniaxial compression and σ_T is the yield stress in uniaxial tension.

Figure 4.22a shows a representation of the Raghava yield function in $\sqrt{J_2} - I_1$ space with a comparison to the von Mises yield function. I_1 is the first invariant of the Cauchy stress tensor and J_2 is the second invariant of the deviatoric part of the Cauchy stress tensor. It should be noted that setting $\alpha = 1$ reduces the Raghava yield function to the von Mises yield function.

Plastic flow in the model is constitutively prescribed according to:

$$\hat{\mathbf{D}}^p = \lambda \frac{\partial g}{\partial \hat{\boldsymbol{\sigma}}} \tag{4.10}$$

where $\dot{\lambda}$ is the plastic multiplier and g is the plastic potential. It is assumed a non-associated plastic flow where the plastic potential is described by:

$$g(\hat{\boldsymbol{\sigma}}) = \frac{(\beta-1)\text{trace}(\hat{\boldsymbol{\sigma}}) + \sqrt{(\beta-1)^2(\text{trace}(\hat{\boldsymbol{\sigma}}))^2 + 6\beta(\hat{\boldsymbol{\sigma}}' : \hat{\boldsymbol{\sigma}}')}}{2\beta} \tag{4.11}$$

where β is the dilatation parameter. A visualization of the influence of the parameter β on the plastic potential is shown in Figure 4.22b. It is evident that a larger dilatation parameter increases the isotropic component of the gradient of the plastic potential, thus accelerating plastic dilatation and damage. Further, it should be noted that the isotropic component of the gradient of this potential is always positive, meaning there is positive plastic dilation in compression. Given that it is non-associated plastic flow, the rate of the equivalent plastic strain, $\dot{p}$, is defined by:

$$\dot{p} = \dot{\lambda}\frac{g}{\varphi(\hat{\boldsymbol{\sigma}})} \tag{4.12}$$

Strain hardening, R, is described by a Voce hardening law, which is given by the following equation:

$$R = \sum_{i=1}^{N_R} Q_{Ri}\Big[1 - \exp\Big(-\frac{\theta_{Ri}}{Q_{Ri}}p\Big)\Big] \tag{4.13}$$

where N_R is the number of Voce terms, θ_{Ri} is the initial hardening rate for Voce term i and Q_{Ri} is the saturation value the corresponding Voce hardening term. In this work, it was found to be sufficient with only two hardening terms.

Viscoplasticity is introduced by constitutively prescribing the rate of the equivalent plastic strain, $\dot{p}$, through the following equation:

$$\dot{p} = \begin{cases} 0 & \text{if } f \leq 0 \\ \dot{p}_0\Big\{\exp\Big[\frac{1}{C}\Big(\frac{\varphi(\hat{\boldsymbol{\sigma}})}{\sigma_T+R} - 1\Big)\Big]\Big\} & \text{if } f > 0 \end{cases} \tag{4.14}$$

where $\dot{p}_0$ is a reference plastic strain-rate and C is the strain-rate sensitivity parameter. Based on Equation 4.14, the viscous overstress, σ_v, is given by:

$$\sigma_v = C(\sigma_T + R)\ln\Big(1 + \frac{\dot{p}}{\dot{p}_0}\Big) \tag{4.15}$$

It is evident that the viscous overstress is scaled multiplicatively with the size of the elastic domain through $\sigma_T + R$.

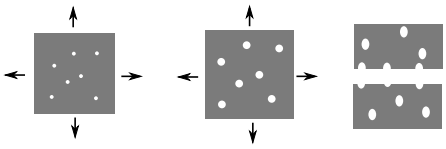

Figure 4.23.: Damage process in ductile materials: Void nucleation, growth and coalescence.

Figure 4.23 shows the basis for failure in ductile materials. It is assumed that there are some initial voids in the material in addition to voids that nucleate during deformation. When the material deforms, these voids will grow dependent on the stress state until the material between the voids starts to neck. This phenomenon is called coalescence and it is believed to be immediately preceding failure in the material. As described in Section 4.2.1, the void growth is assumed to be linked to volumetric plastic deformations described by the damage parameter D. The rate of the damage, $\dot{D}$, is given by the following equation:

$$\dot{D} = (1 - D)\text{trace}(\hat{\mathbf{D}}^p) \tag{4.16}$$

Further, it is assumed that the void phase is unable to carry any load. This is modelled by introducing an effective stress tensor, which represents the stress that the matrix material is subjected to. The corotated Cauchy stress tensor in the previous equations is substituted by the effective corotated Cauchy stress tensor, $\hat{\boldsymbol{\sigma}}_{\text{eff}}$, through a damage coupling according to:

$$\hat{\boldsymbol{\sigma}} \rightarrow \hat{\boldsymbol{\sigma}}_{\text{eff}} = \frac{\hat{\boldsymbol{\sigma}}}{1 - D} \tag{4.17}$$

Failure is captured by a simple model, where it is assumed that coalescence occurs when the damage, D, reaches a critical value, D_C, following:

$$D \geq D_C \rightarrow \hat{\boldsymbol{\sigma}} = \mathbf{0} \tag{4.18}$$

Generally, failure in the material is dependent on the stress state through the Lode parameter and the stress triaxiality ratio. The presented failure criterion is independent on the Lode parameter and only indirectly dependent on the stress triaxiality ratio through the gradient of the plastic potential and thus the rate of plastic dilatation. Furthermore, there is no

length scale normalization for the damage evolution or the critical value. Thus, failure in the material will be fundamentally mesh dependent with the presented model. The consequences of these issues will be discussed further throughout Part III.

4.3.2. Calibration process

Overall, there are 12 parameters that needs to be calibrated for the presented polymer model. The elastic domain is described by the elastic modulus, E, and the Poisson's ratio, ν. The plastic domain is described by the yield stress in tension, σ_T, the pressure sensitivity parameter, α, the dilatation parameter, β, and the hardening parameters $\theta_{R1/R2}$ and $Q_{R1/R2}$. Viscoplasticity is described by the strain-rate sensitivity parameter C and the reference plastic strain-rate, $\dot{p}_0$. Finally, failure is described by a single critical damage parameter, D_C.

The calibration process is split into six different steps. Some of the parameters are determined based on a rough estimate from a visual inspection of the experimental results, while others are directly calculated from the curves. There are also parameters that needs to be fitted using a least square fit algorithm in MATLAB. A few parameters are determined through reverse engineering of finite element (FE) simulations.

Step 1: Determine elasticity parameters. The elastic modulus, E, is fitted to the elastic domain in Figure 4.5a, while the Poisson's ratio, ν, is approximated to fit the initial Poisson's ratio shown in Figure 4.5b.

Step 2: Determine key plasticity parameters. For this part, the effective stress measure calculated based on Equations 4.1 and 4.17 is used. An initial estimate of the yield stress in tension, σ_{T0}, was approximated by considering the effective stress-strain curve at a nominal strain-rate of 10^{-3}s^{-1} in tension. The value was set to 20MPa, while a more precise yield stress in tension, σ_T, was later calculated by adjusting for viscoplasticity.

The pressure sensitivity parameter, α, was determined by comparing the effective stress in uniaxial tension to the effective stress in uniaxial compression at a nominal strain-rate of 10^{-3}s^{-1}. In order to avoid issues with determining exactly at what point the response becomes non-linear, it was chosen to use an elastic offset to compare the effective flow stress at approximately 0.02 plastic strain. As the ratio between the flow stress in tension and compression remains constant according to the model, these two data points were used to determine the pressure sensitivity parameter, α, following Equation 4.9.

Step 3: Calibrate viscoplasticity parameters. It can be shown that the viscoplasticity parameters, $\dot{p}_0$ and C, can be determined independent on the yield stress and hardening. This is done by comparing the ratio of the flow stress at the same plastic strain for tests at different plastic strain-rates using an elastic offset similar to Step 2. Experimental data

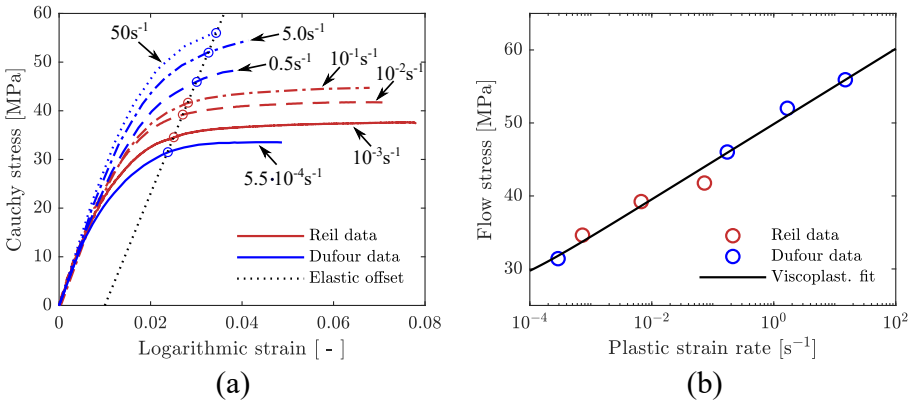

Figure 4.24.: Calibration of viscoplasticity parameters. (a) Stress-strain curves used as basis for viscoplasticity calibration including data from Dufour [44]. (b) Polymer model viscoplasticity fit.

from uniaxial tension tests presented in Section 4.2.1 are limited to nominal strain-rates ranging from 10^{-3} s^{-1} to 10^{-1} s^{-1}. This data set was expanded by data reported by Dufour [44] for the same adhesive, making the calibration relevant for higher rate problems as well. Figure 4.24a shows how the flow stress at the different plastic strain-rates were obtained from the data set. Based on these data points, it was used a least square fit algorithm in MATLAB to determine the viscoplasticity parameters, $\dot{p}_0$ and C. These parameters were then used to determine the yield stress in tension such that it gave a value of 20 MPa at a nominal strain-rate of 10^{-3} s^{-1}.

Results of the viscoplasticity calibration fit is shown in Figure 4.24b. Compared to the data presented in Section 4.2.1, there is a discrepancy especially for the tension test at a nominal strain-rate of 10^{-1} s^{-1}. However, the overall fit is seen to be satisfactory. It is evident from Figure 4.24a that the tests reported by Dufour [44] exhibit significantly less ductility than the ones reported by Reil [120]. This represents an additional source of uncertainty, as the two datasets might not be directly comparable due to unknown reasons.

Step 4: Determine hardening parameters. Before fitting the parameters, the effective stress versus plastic strain was calculated based on the updated yield stress in tension and adjusted for viscoplasticity parameters determined in Step 3. Based on these curves and the viscoplasticity parameters, the hardening parameters were fitted using a least square fit algorithm in MATLAB. Only the uniaxial tension test data presented in Section 4.2.1 was used for the calibration of the hardening parameters.

Step 5: Determine the dilatation parameter. Reverse engineering using FE simulations was used to determine the dilatation parameter, β. The parameter was iterated upon until

a satisfactory agreement between the simulations and experiments for the evolution of the Poisson's ratio and damage in the uniaxial tension tests was obtained.

Step 6: Determine the critical damage parameter. The last parameter that needed to be determined is the critical damage parameter, D_C. As everything but failure was available, FE simulations of the experiments could be run with confidence. In order to calibrate the critical damage parameter, it was decided to run simulations of the notched tension tests and then retrieve the damage value from the critical element at the time of failure in the representative experiment.

The limited flexibility of the given failure model forced decisions on which experiments and what mesh size to use for calibration purposes. It was seen that obtaining a critical damage parameter from the uniaxial tension tests would have given a value of roughly 0.03 compared to the notched tension tests that gave a value of 0.115. The notched tension tests exhibit an increased stress triaxiality ratio which closer represents the stress state in an adhesive layer. Further, the uniaxial tension tests are mesh insensitive with respect to determining a critical damage value, which makes them unsuitable for this purpose as the problem is in general mesh sensitive. Therefore, it was chosen to use the notched tension tests for calibration of the critical damage.

The element size of the notched tension test simulations in the critical region was set to 0.1 mm. This was done to match the element size in the through-thickness direction of a typical adhesive layer with a nominal thickness of 0.3 mm. There was also performed a mesh sensitivity study with regards to the damage parameter for the notched tension test simulations. Based on the baseline reference length of 0.1 mm, it was determined a critical damage value of 0.115. For comparison, a reference element length of 0.033 mm gave a critical damage value of roughly 0.125, while a reference length of 0.3 mm gave a critical damage value of 0.099.

Table 4.1.: Calibrated material parameters for the presented polymer model.

Polymer model parameters					
E[MPa]	ν[−]	σ_T[MPa]	α[−]	β[−]	θ_{R1}[MPa]
2300	0.43	15.0	1.29	1.50	4134
Q_{R1}[MPa]	θ_{R2}[MPa]	Q_{R2}[MPa]	C[−]	$\dot{p}_0$[s^{-1}]	D_c[−]
7.70	469	6.36	0.0851	$2.77 \cdot 10^{-5}$	0.115

Calibrated material parameters for the polymer model are given in Table 4.1. Comparisons between experimental data and simulations using the presented model and parameters are shown in Figures 4.25, 4.26 and 4.27. The overall prediction of the stress-strain response is satisfactory as seen in Figure 4.25a. However, there is an both an over and underestimation of the stress level for tests performed at a nominal strain-rate of $10^{-1}\,\mathrm{s}^{-1}$ and $10^{-3}\,\mathrm{s}^{-1}$ respectively. This is a direct consequence of using the additional data reported by Dufour [44] in the calibration of the viscoplasticity parameters. The evolution of the Poisson's

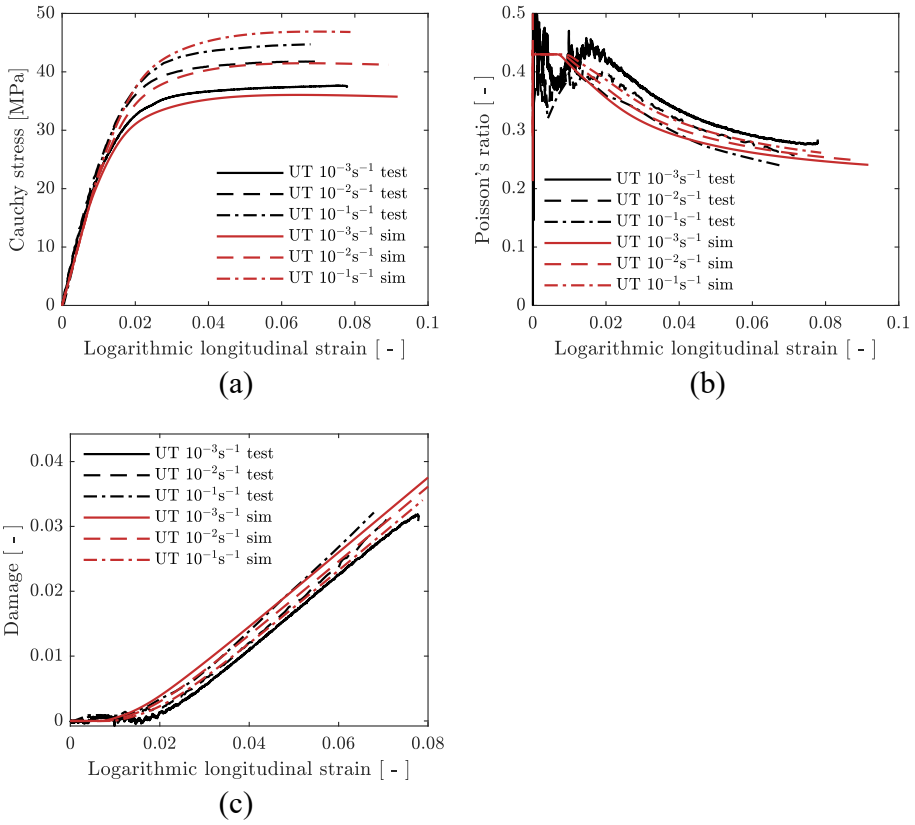

Figure 4.25.: Comparison between experimental results and simulation results using the polymer model for tension tests. (a) Cauchy stress vs. logarithmic longitudinal strain. (b) Poisson's ratio vs. logarithmic longitudinal strain. (c) Damage vs. logarithmic longitudinal strain.

ratio and damage shows good agreement between tests and simulations as they were used as the basis for determination of the dilatation parameter.

Figure 4.26a shows the Cauchy stress versus logarithmic strain in uniaxial compression. While the overall stress level is well predicted, the trend is not captured. There is a weak hardening present in the experiments, while the simulations predict significant softening. This is directly linked to the damage evolution shown in Figure 4.26b. The damage evolution is linked to the gradient of the plastic potential, which always has a positive isotropic component for the given potential as seen in Figure 4.22b. Therefore, the model is not able to capture the damage evolution in the experiments leading fictitious softening of the Cauchy stress.

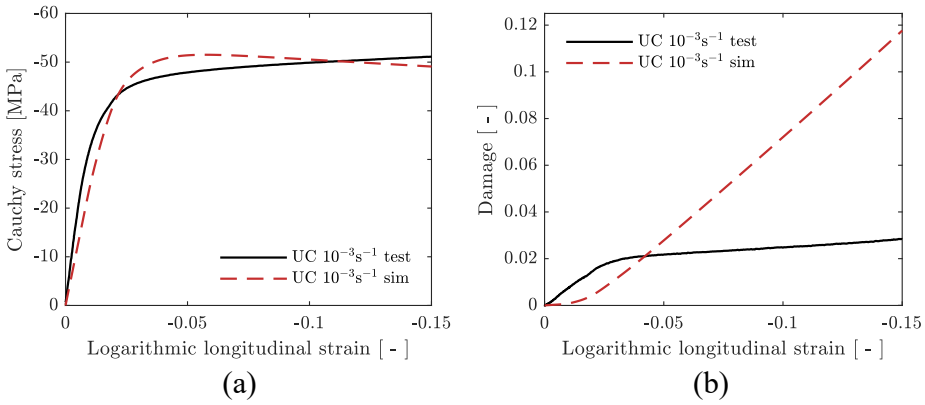

Figure 4.26.: Comparison between experimental results and simulation results using the polymer model for compression tests. (a) Cauchy stress vs. logarithmic longitudinal strain. (b) Damage vs. logarithmic longitudinal strain.

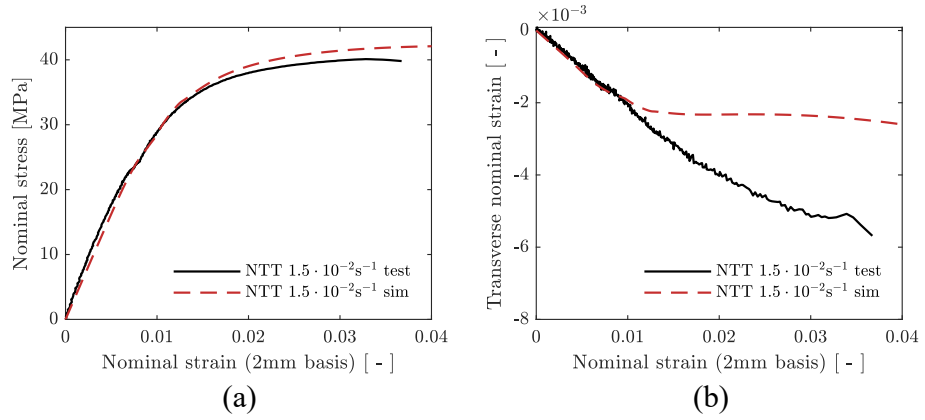

Figure 4.27.: Comparison between experimental results and simulation results using the polymer model for notched tension tests. (a) Nominal stress vs. nominal strain. (b) Transverse nominal strain vs. nominal strain.

Comparisons between the experimental data and simulation results for a representative notched tension test is shown in Figure 4.27. The overall nominal stress-strain response is seen to be acceptable, while the transverse strain measure is deviating significantly outside the elastic domain. Although the transverse strain is one order of magnitude lower than the longitudinal strain, it gives an indication that there are issues with the plastic domain in the presented model. A parameter study on the dilatation parameter revealed that it was possible to obtain a good fit for the transverse strain by setting the parameter equal to 1.35. However, the damage evolution for the uniaxial tension tests would then be

significantly underestimated. As a result, there is an additional uncertainty to the damage value calibrated based on the notched tension test simulations.

It is seen from the calibration process that the experimental data presented in Section 4.2.1 is sufficient to calibrate the presented polymer model. However, there are several tests that could have assisted in determining better parameters such as a shear test to investigate the shear behaviour of the material. Additionally, it would be of interest to perform a variety of tests at different stress triaxiality ratios and Lode angles. These experiments could facilitate calibration of more advanced failure models, which would be of importance for future development of the methodology presented in Part III.

4.4. Validation of polymer model for structural adhesive

This section presents the results of a series of validation tests for the previously calibrated polymer model according to the strategy outlined in Section 4.1.2. These will be based on experiments presented in Sections 4.2.2 and 4.2.3. The bonded component test simulation will be described in more detail as it will be used further in Chapters 5 and 6.

4.4.1. Cross tests

Section 4.2.2 gives a brief description of the bonded cross tests, with geometry and test configuration given in Figure 4.12. Details regarding the experiments are given by Reil [120]. However, simulations for validation purposes were performed as a part of the current work and are reported in this section.

The simulations were run with Abaqus/Explicit [112] using significant mass scaling to reduce the computational time of the quasi-static tests. It was used linear brick elements with reduced integration for the model. Further, the mesh consisted of 3 elements through the thickness for both the metal adherents and the adhesive layer with a $0.4\,\text{mm} \times 0.4\,\text{mm}$ in plane mesh size for the bonded region. One symmetry plane was used for all three configurations, which allowed for non-symmetric crack propagation in the tension dominated case. The fixtures were modelled as rigid boundaries and prescribed velocities at the edge of the clamped region.

Figure 4.28 shows the simulation results of the cross tests compared to the experimental data. Overall, the peak force level seems to be well predicted for all three configurations. However, the stiffness is severely overestimated in the simulations compared to the experiments. The discrepancy in stiffness is seen to increase with the stiffness of the given configuration with the shear dominated CT90 case showing the largest error. It is believed

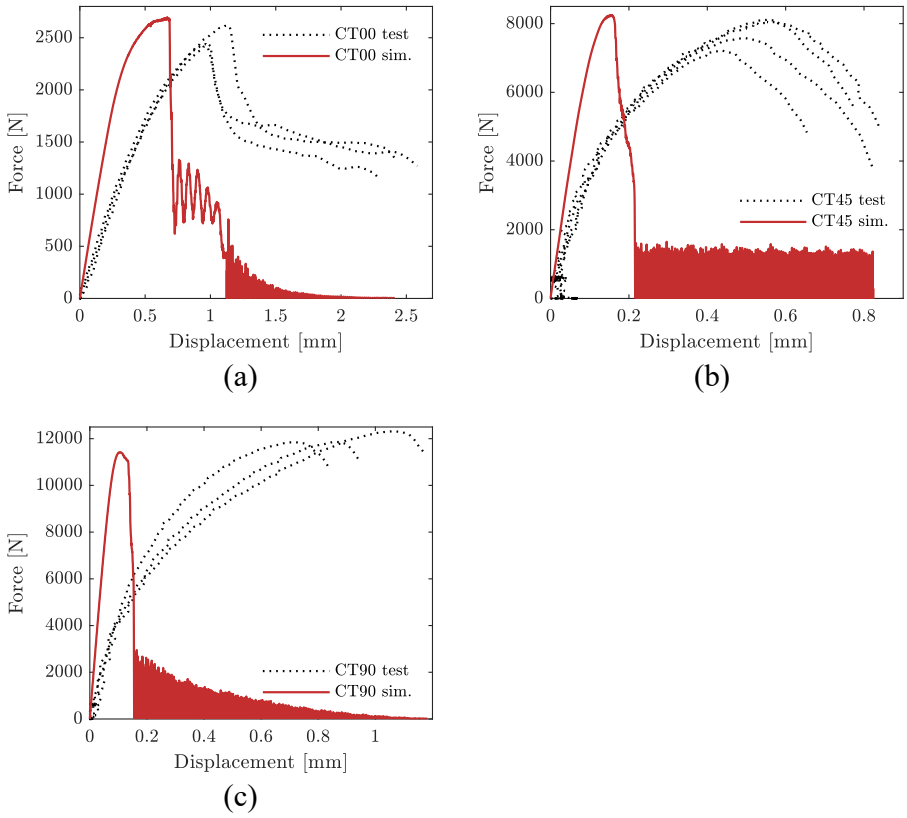

Figure 4.28.: Comparison between experimental results and simulation results for bonded cross tests. (a) CT00 - tension dominated. (b) CT45 - Mixed mode. (a) CT90 - shear dominated.

that this is caused by compliance in the clamping system, which was not captured by the optical measurements. Results presented in Section 4.4.2 further suggests that this error is linked to problems with the experimental measurements rather than the performance of the numerical models. There are also significant oscillations present for all simulations after failure in the adhesive layer which is caused by the employed mass scaling.

4.4.2. Hybrid benchmark tests

Hybrid single lap joint (SLJ) tests and hybrid peel tests form the benchmark tests which are used for further validation of the polymer model. Both experiments and simulations were

performed by Reil [120] and are briefly presented in Section 4.2.2. However, the simulations presented in this section were run with the polymer model and material parameters outlined in Section 4.3. The initial behaviour of both experiments were seen to be dominated by the behaviour and failure of the adhesive layer making them suitable for further validation.

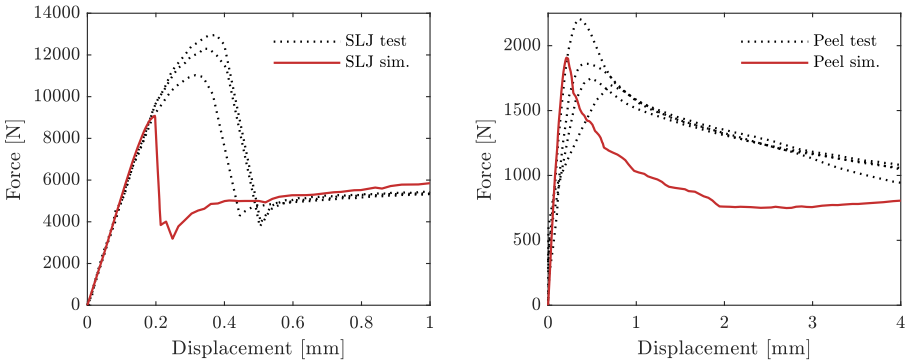

Figure 4.29.: Comparison between experimental results and simulation results for hybrid benchmark tests by Reil [120]. (a) Single lap joint tests. (b) Peel tests.

Results of the benchmark test simulations compared to the experiments are presented in Figure 4.29. In contrast to the results presented in Figure 4.28, the initial stiffness is seen to be captured well for the benchmark tests. This indicates that the previously presented stiffness issue was related to experimental measurements rather than the material model and calibration.

The force level for the SLJ tests, as shown in Figure 4.29a, is significantly underestimated in addition to an overestimation of the crack propagation velocity. Both errors could be linked to the inflexibility of the failure model and its mesh dependency. It was seen from the simulations that the crack propagated from the elements closest to the rivet which had a much smaller size than the baseline element size of 0.1 mm used for calibration of the failure parameter. Further, the stress state present in the adhesive layer for the SLJ tests is significantly different than the one in the notched tension tests used for calibration of the failure parameter.

Figure 4.29b shows the initial response of the hybrid peel tests. It is seen that the peak force level is well predicted, and a better prediction of the crack propagation velocity compared to the SLJ tests. The geometry of the peel tests forces the crack to initiate at a location where the mesh size is equal to the reference size of 0.1 mm through the thickness of the adhesive layer. This ensures a significantly better representation of failure in the proposed failure model. There is no control of the crack propagation velocity in the proposed polymer model, as well as no calibration case with crack propagation. Therefore, crack propagation

is generally not accurately predicted by the proposed model.

4.4.3. Bonded component tests

Component level validation was performed on the bonded component tests presented in Section 4.2.3. As discussed previously, the post-peak behaviour of these components were dominated by crack propagation in the adhesive layer, making them ideal for validation purposes. Due to the size of the problem, there was only used one element through the thickness of the adhesive layer to obtain a reasonable computational time. Therefore, the purpose of this section is to provide an indication of the behaviour of the material model when subjected to more complex loading. The finite element (FE) model presented in this section will be actively used throughout Chapters 5 and 6, and it is therefore described in detail here.

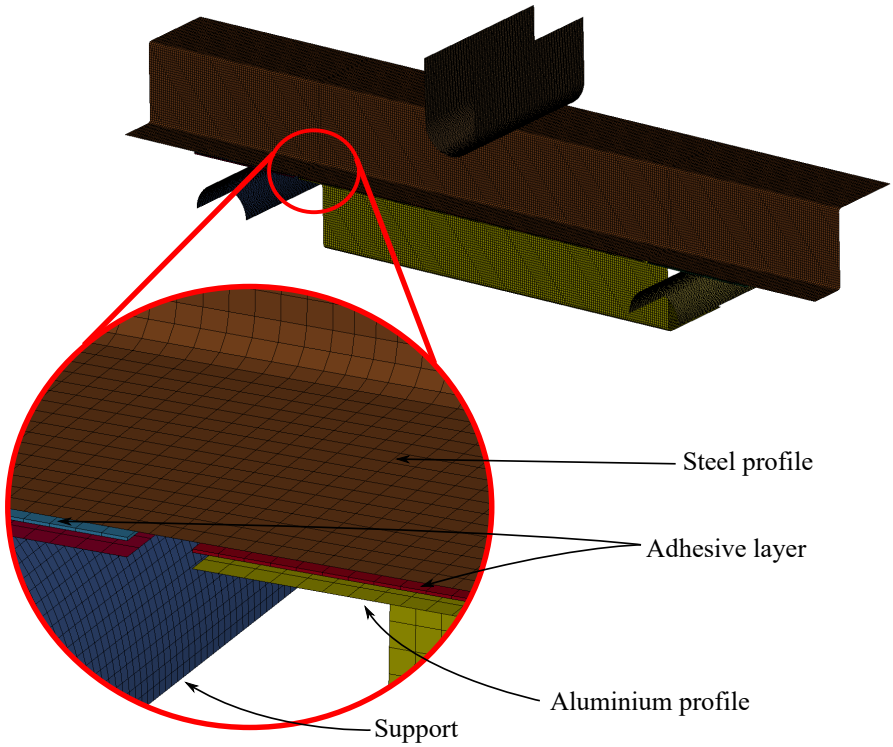

Figure 4.30.: Mesh of bonded component test.

Bonded component test simulations were run with LS-DYNA version 9.3 [123] to facilitate

user defined cohesive zone models for the next chapters. Figure 4.30 shows the FE model of the bonded component test with a general mesh size of 2 mm for the shell elements. Shell element formulation 2 [93] with 1 integration point in the plane and 5 through the thickness of the element was used. The solid elements used for the adhesive layer followed the in-plane mesh size of 2 mm with a thickness of 0.25 mm corresponding to the average thickness of the adhesive layer. Element formulation 1 [93] with reduced integration was used for the solid elements. These elements were linked to the metal hat profiles using the contact keyword CONTACT_TIED_SHELL_EDGE_TO_SURFACE_CONSTRAINED_OFFSET [93].

Boundary conditions were applied by introducing two rigid supports with a fixed position and a rigid punch with a prescribed velocity. An automatic surface to surface contact algorithm was used between the rigid parts and the specimen. Additionally, it was used the same contact algorithm between the two metal profiles to capture the direct contact beneath the punch. Symmetry boundary conditions were applied to the plane defined by the longitudinal axis and vertical axis in the centre of the specimen.

In order to model the metal materials, a standard material model in LS-DYNA, MAT_258 [72], was employed. This model allows for a Hershey-Hosford high exponent yield function and a Voce hardening law. The parameters used to model the aluminium and steel profiles were calibrated by Reil [120]. It was performed simplified forming simulations of the two hat profiles in order to estimate the initial history variables in the corners of the hat sections. Further, the adhesive layer was modelled with the previously presented polymer model and parameters shown in Table 4.1.

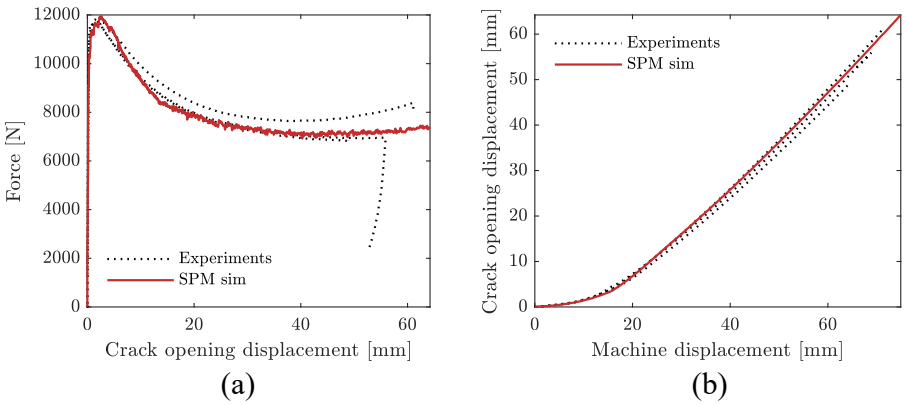

Figure 4.31.: Comparison between experimental results and simulation results for bonded component tests. (a) Force vs. crack opening displacement. (b) Crack opening displacement vs. machine displacement.

Figure 4.31 shows the results of the bonded component test simulations compared to the experimental data. The results show a very good agreement between experiments and

simulations results. This suggest that failure and crack propagation was captured well when exposed to industry relevant loading modes. It is key to note that it was only used one element through the thickness of the adhesive layer. Therefore, failure and crack propagation are delayed due to the intrinsic mesh sensitivity of the problem. As such, these results are not directly comparable to the ones presented in Section 4.4.2.

4.5. Discussion and concluding remarks

4.5.1. Discussion

This chapter presented a meso-scale polymer model and an experimental basis for calibration and validation of the model. This model form the basis for the multi-scale calibration approach presented in Chapter 5, as well being used to better understand the adhesive behaviour in different types of joints. The multi-scale calibration process uses virtual benchmark tests to generate target curves for optimization. Based on the validation cases presented in Section 4.4, it is evident that there are uncertainties linked to failure and crack propagation in the polymer model. Further, this seems to have a significant impact on the estimated maximum resistance of a test as well as the post-peak behaviour. These discrepancies will then propagate to the macro-scale simulations, thus reducing the overall value of this approach.

The presented polymer model lacks two aspects of failure modelling. Generally, failure in ductile materials, such as the SP498 adhesive, is dependent on the stress state through the Lode parameter and stress triaxiality ratio. The presented model has a weak indirect dependency on the stress triaxiality ratio through plastic dilatation and damage coupling. However, this dependency is not calibrated and it is not able to capture the difference between notched tension and pure tension as shown in Section 4.3.2. Further, the model has no dependency on the deviatoric stress state through the Lode parameter. In order to expand the model to account for these variables, it would be necessary to perform a series of additional tests exhibiting the different stress states. These tests are typically more complex and more expensive than the basic ones presented in Section 4.2.1.

The calibration of the critical damage parameter revealed an intrinsic mesh dependency of the problem. However, there are no mesh regularization schemes in the applied polymer model, which contributes to the scatter in performance seen in Section 4.4. These issues could be alleviated by modifying the failure parameter based on the reference element length along the lines of what was done by Costas et al. [72]. This would require additional post-processing of the experimental results, as well as additional computational time in the calibration process. A different approach shown by Balieu et al. [92] is to use a non-local damage model, where the damage is averaged based on an intrinsic length of the

failure process. However, such a formulation would add additional computational cost and increase the complexity of the implementation. Further, it could be difficult to determine a suitable intrinsic length scale.

Ultimately, it was decided to continue with the simple failure model presented in Section 4.3.1 due to its simplicity. The purpose of this study is to investigate the potential of the proposed methodology. Therefore, it is not necessary to obtain very accurate results as long as the results are reasonable and the issues causing the errors are known. These issues will be further discussed in the coming chapters, where the impact on the macro-scale becomes apparent.

4.5.2. Conclusions

The purpose of this chapter is to create a basis for the studies presented in the following chapters by providing experimental data to calibrate and validate a suitable polymer model. For calibration purposes, uniaxial tension tests, compression tests and notched tension tests were performed. There was also performed benchmark tests in the form of cross tests, single lap joint tests and peel tests. These were used for primary validation of the implemented model. Finally, it was performed a series of bonded component tests for higher level validation of the polymer model performance.

Based on previous literature and the results of the calibration tests it was decided to use parts of an already implemented polymer model. This model was able to capture the key phenomena governing the mechanical behaviour. Further, the bulk adhesive tests were used to calibrate the model and validation was performed on the benchmark tests and the bonded component test. While the proposed model provided decent results, the validation performed on the benchmark tests revealed significant flaws with respect to failure in the model. Particularly, a lack of mesh regularization was found to be critical as well as a limited dependency on the stress state. It is evident that these issues would influence the results of the following chapters, where the calibration method is based on simulations using this polymer model.

The work presented in this chapter mirrors the research strategy of Part II, by following the first three steps outlined in Section 1.5. This was done to facilitate the next steps in the research strategy, which will be outlined in Chapter 5. Further, those results will be used to explore the feasibility of a multi-scale modelling approach, which is in line with the overarching objectives of this thesis.

5. Macro-scale modelling of structural adhesives

5.1. Introduction

This section will give a description of the chapter by presenting the objectives of the chapter and putting it in context of the rest of the thesis. A short summary of the cohesive zone modelling framework for LS-DYNA [123] will also be presented. Finally, the selection of macro-scale material models is discussed.

5.1.1. Chapter description

This chapter serves as a continuation of the results presented in Chapter 4, continuing with numerical studies of the SikaPower 498 (SP498) adhesive. The purpose of this chapter is to bridge the gap from a meso-scale modelling framework to a macro-scale modelling framework through a partial virtual laboratory calibration procedure. Using this procedure, several macro-scale models are investigated in order to facilitate multi-material analyses in Chapter 6. This is in line with the objectives and research strategy outlined in Sections 1.3 and 1.5, respectively.

An outline of the three macro-scale models applied in this work is given in Section 5.2. The three cohesive zone models are MAT_240 in LS-DYNA [123], a modified version of MAT_240 and a Gurson-based cohesive zone model (GCZM). The implementation of the GCZM is presented in Section 5.2.4. Further, the virtual laboratory calibration procedure is described in Section 5.3. Calibration results and an initial validation step using the bonded component tests are presented in Section 5.4. Finally, the results and observations made throughout this chapter are discussed and concluded in Section 5.5.

5.1.2. Cohesive zone model framework

All macro-scale simulations run as a part of this work were carried out in version 9.3 of the LS-DYNA solver [123]. This solver was chosen due to its baseline cohesive zone modelling framework, which only requires user subroutines to define a traction-separation law.

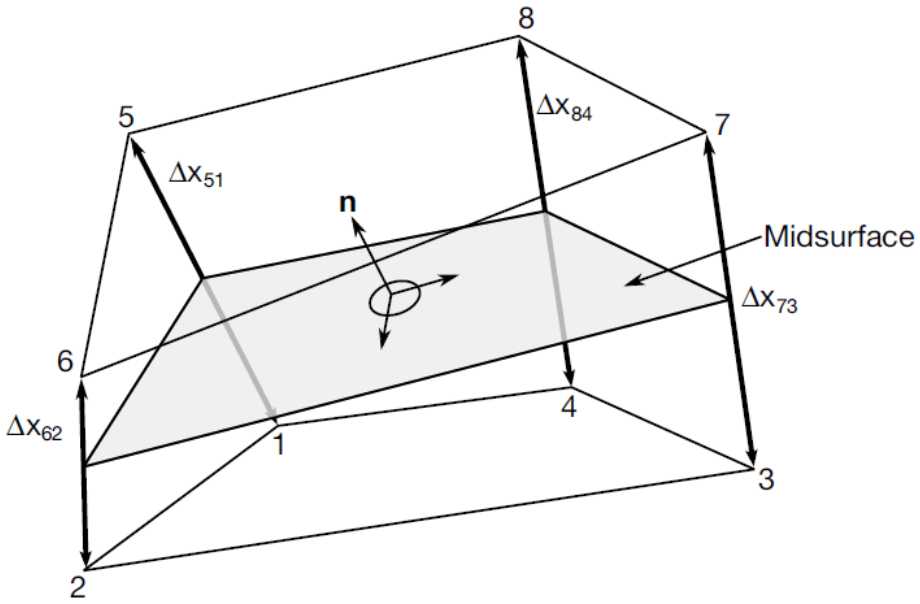

Figure 5.1.: Definitions of separations for cohesive solid element in LS-DYNA [93].

The cohesive zone modelling framework in LS-DYNA is implemented through solid element formulations 19 and 20 [93]. These are essentially the same except for formulation 20 accounting for thickness of adjacent shell elements. Figure 5.1 shows how the cohesive elements are defined in LS-DYNA, where the separations between each nodal pair are interpolated to calculate the separations for each of the four integration points. Additionally, the solver accounts for finite rotations of the elements.

For each integration point, the solver calculates three separation measures in the local coordinate system. These are the normal separation, u_{n}, and the two tangential separations, u_{t1} and u_{t2}, based on the local element plane in Figure 5.1. Together they define the separation vector, $\mathbf{u}$:

$$\mathbf{u} = \begin{bmatrix} u_{\mathrm{n}} \\ u_{\mathrm{t1}} \\ u_{\mathrm{t2}} \end{bmatrix} \tag{5.1}$$

For each of the local element directions, there are the corresponding tractions in each integration point. These are the normal traction, σ_n, and the two tangential shear tractions, τ_1 and τ_2. These three tractions are the elements of the traction vector $\mathbf{t}$:

$$\mathbf{t} = \begin{bmatrix} \sigma_n \\ \tau_1 \\ \tau_2 \end{bmatrix} \tag{5.2}$$

The traction vector, $\mathbf{t}$, is numerically integrated over the cross-section surface of the cohesive element to determine the nodal forces. In order to obtain the traction vector, the separation vector, $\mathbf{u}$, is sent to the material subroutine which calculates the tractions based on a traction-separation law. Through the material subroutine, it is possible to implement user defined subroutines that describe traction-separation laws which are not part of the baseline solver.

5.1.3. Model selection

The primary purpose of this chapter is to perform a preliminary study of the potential of the proposed methodology. Therefore, a model which is used in the industry that captures some of the key phenomena of the studied adhesive is chosen as a baseline for the study. Further, there is an exploratory component to this study, where it is natural to include novel models presented in recent literature.

MAT_240 in LS-DYNA ([69],[104]) is chosen as a baseline model for this study. The model is applied in the industry, as it is a simple model that includes a basic description of elasticity, viscoplasticity, damage and failure. This is captured in the form of a tri-linear traction separation law which is outlined in Section 5.2.1.

A modification of MAT_240 was chosen as one of the exploratory models as it was already implemented by Sønstabø et al. [53]. This modification adds four parameters that control the mixed mode interaction for stiffness, yield separation, critical damage separation and failure separation. Therefore, it is possible to investigate the importance of flexibility in terms of the mixed mode interactions for the adhesive in a multi-scale perspective. These additional parameters does add a significant computational cost with respect to calibration of the model compared to MAT_240. Details regarding the modification are presented in Section 5.2.2.

The last model to be studied in this chapter is a Gurson-based cohesive zone model (GCZM), which is based on the article by Said Schicchi et al. [106]. Being a novel model, it is of academic interest to study its performance with respect to adhesive bonding. However, the

primary reason for exploring this model is that it captures important features of the physics of the adhesive. Chapter 4 discussed that damage and failure in the SP498 adhesive is governed by void nucleation, growth and finally coalescence at a critical value. The GCZM is a direct extension of the Gurson-Tvergaard-Needleman (GTN) [124] porous plasticity model to a macro-scale traction-separation law. Therefore, the GCZM is an interesting model to study for the given adhesive.

A key advantage with this model is that the matrix response can be assumed to be similar to the undamaged response of the polymer model calibrated in Chapter 4. A modification to the hardening law of the original GCZM [106] is implemented in this work, such that the plasticity parameters could be directly transferred. This significantly reduces the computational cost of calibrating the GCZM model, making it easier to calibrate than the baseline MAT_240 model as shown in Section 5.4.3. A detailed description of the GCZM model as well as an algorithmic overview of the implementation of this model is presented in Sections 5.2.3 and 5.2.4 respectively.

5.2. Model descriptions and implementation

This section presents a detailed outline of the three different macro-scale material models applied in this work. Descriptions including the relevant equations for MAT_240, MAT_240 modified and the Gurson based cohesive zone model (GCZM) are presented in Sections 5.2.1, 5.2.2 and 5.2.3 respectively. Further, the implementation of the GCZM is presented in Section 5.2.4.

5.2.1. MAT_240

MAT_240 was originally presented by Marzi et al. [104] and represents a tri-linear traction separation law as seen in Figure 5.2. The original model and its implementation in LS-DYNA include a rate-dependency. However, the problems studied in this chapter are quasi-static such that only the rate-independent part of the model will be presented. This section will present the required equations needed to calculate a traction vector, $\mathbf{t}$, from an arbitrary separation vector, $\mathbf{u}$, which in turn defines the traction-separation law.

For the quasi-static implementation, there are eight parameters needed to define the traction-separation law. The effective Youngs modulus, E_{mod}, and shear modulus, G_{mod}, are used to calculate the stiffness in normal direction, E_{n}, and tangential direction, E_{t} according to:

$$E_{\text{n}} = E_{\text{mod}}/t_{\text{rep}} \tag{5.3}$$

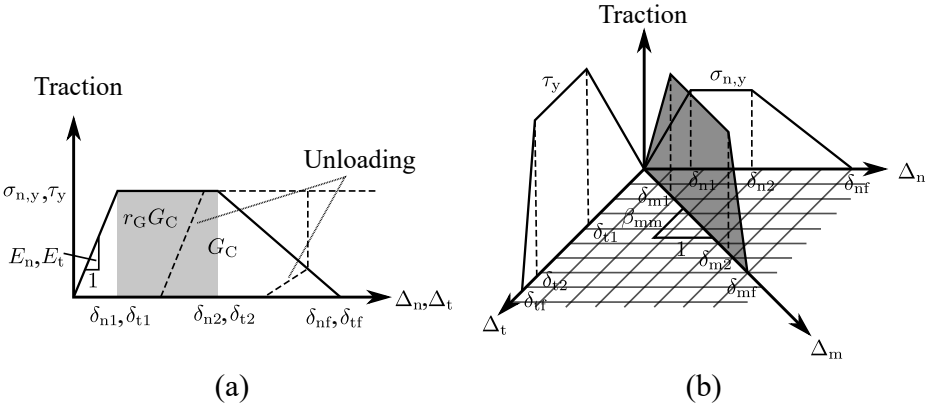

Figure 5.2.: Definition of traction-separation law for MAT_240 [104]. (a) Definitions of key parameters for mode I and mode II. (b) Traction-separation law including the mixed mode.

$$E_t = G_{mod}/t_{rep} \tag{5.4}$$

where t_{rep} is the representative thickness. This thickness is typically calculated by the solver, but it can also be given as an input parameter. The energy release rate in mode I, G_{1C}, and mode II, G_{2C}, represents the traction integrated over the separation until failure for the two different modes as seen in Figure 5.2a. Further, the ratio between the total energy release rate for each mode and the energy release rate for the plastic domain, as shown in Figure 5.2a, are defined by the factors r_{G1} and r_{G2} for mode I and mode II respectively. The last parameters needed to define the traction-separation law are the effective yield traction in mode I, $\sigma_{n,y}$, and mode II, τ_y.

These parameters are then used to define the key separations for mode I and mode II which are shown in Figure 5.2a. Onset of yield occurs at the separation at yield initiation for mode I, δ_{n1}, and mode II, δ_{t1}. Further, onset of damage occurs at the separations δ_{n2} and δ_{t2} for mode I and II respectively. Finally, failure occurs at the failure separations δ_{nf} and δ_{tf} for the respective modes. These separations are calculated according to:

$$\begin{aligned} \delta_{n1} &= \frac{\sigma_{n,y}}{E_n}, \quad & \delta_{n2} &= \delta_{n1} + \frac{r_{G1} G_{1C}}{\sigma_{n,y}}, \quad & \delta_{nf} &= \delta_{n1} - \delta_{n2} + 2\frac{G_{1C}}{\sigma_{n,y}} \\ \delta_{t1} &= \frac{\tau_y}{E_t}, \quad & \delta_{t2} &= \delta_{t1} + \frac{r_{G2} G_{2C}}{\tau_y}, \quad & \delta_{tf} &= \delta_{t1} - \delta_{t2} + 2\frac{G_{2C}}{\tau_y} \end{aligned} \tag{5.5}$$

As seen in Figure 5.2b, the traction-separation law is defined in the mode I and mode II domain with mixed mode describing the interaction between the two. However, the input from the solver is the separation vector, **u**, given in Equation 5.1. These separations are then used to calculate the effective separations used for the traction-separation law. The effective normal separation, Δ_n, is defined by:

$$\Delta_n = \max(u_n, 0) \tag{5.6}$$

Further, the effective tangential separation, Δ_t, is calculated according to:

$$\Delta_t = \sqrt{u_{t1}^2 + u_{t2}^2} \tag{5.7}$$

These two separations are then used to calculate the effective mixed mode separation, Δ_m, according to:

$$\Delta_m = \sqrt{\Delta_n^2 + \Delta_t^2} \tag{5.8}$$

The mixed mode domain is further defined by the mixed mode ratio, β_{mm}, which is defined as:

$$\beta_{mm} = \frac{\Delta_t}{\Delta_n} \tag{5.9}$$

A mixed mode angle, γ_{mm}, is also used to describe the ratio between the normal and tangential separation according to:

$$\gamma_{mm} = \arccos\left(\frac{\Delta_n}{\Delta_m}\right) \tag{5.10}$$

Similar to the individual deformation modes, there the key separation measures for the mixed mode case. These are calculated based on the parameters and key separations used to define mode I and II in addition to the mixed mode ratio, β_{mm}, and mixed mode angle, γ_{mm}. Mixed mode separation at yield initiation, δ_{m1}, is calculated according to:

$$\delta_{m1} = \delta_{n1}\delta_{t1}\sqrt{\frac{1 + \beta_{mm}^2}{\delta_{t1}^2 + \left(\beta_{mm}\delta_{n1}\right)^2}} \tag{5.11}$$

Similarly, the mixed mode separation at onset of damage, δ_{m2}, is given by:

$$\delta_{m2} = \delta_{n2}\delta_{t2}\sqrt{\frac{1+\beta_{mm}^2}{\delta_{t2}^2 + \left(\beta_{mm}\delta_{n2}\right)^2}} \tag{5.12}$$

Mixed mode separation at failure, δ_{mf}, is defined by:

$$\delta_{mf} = \frac{\delta_{m1}\left(\delta_{m1}-\delta_{m2}\right)\left(E_n G_{2C}\left[\cos(\gamma_{mm})\right]^2 + E_t G_{1C}\left[\sin(\gamma_{mm})\right]^2\right) + 2G_{1C}G_{2C}}{\delta_{m1}\left(E_n G_{2C}\left[\cos(\gamma_{mm})\right]^2 + E_t G_{1C}\left[\sin(\gamma_{mm})\right]^2\right)} \tag{5.13}$$

In order to describe the loading and unloading in the plastic domain, the plastic separations must be defined. Plastic separation in the normal direction, $u_{n,p}$, is defined by the equation:

$$u_{n,p} = \max\left(u_{n,p,t_{i-1}},\, u_n - \delta_{m1}\cos(\gamma_{mm}),\, 0\right) \tag{5.14}$$

where $u_{n,p,t_{i-1}}$ is the plastic separation in the normal direction from the previous time-step, which is used to ensure that the plastic separation is irreversible. An elastic predictor is used to determine if there are plastic separations in the tangential direction. The elastic shear separation predictor, $\delta_{t,y}$, is calculated according to:

$$\delta_{t,y} = \sqrt{\left(u_{t1} - u_{t1,p,t_{i-1}}\right)^2 + \left(u_{t2} - u_{t2,p,t_{i-1}}\right)^2} \tag{5.15}$$

where $u_{t1,p,t_{i-1}}$ and $u_{t2,p,t_{i-1}}$ are the plastic separations in the two tangential directions for the previous time-step. If $\delta_{t,y} > \delta_{m1}\sin(\gamma_{mm})$ then the tangential separation is considered plastic. The plastic separations in the two tangential directions, $u_{t1,p}$ and $u_{t2,p}$, are updated following:

$$\begin{aligned} u_{t1,p} &= u_{t1,p,t_{i-1}} + u_{t1} - u_{t1,t_{i-1}} \\ u_{t2,p} &= u_{t2,p,t_{i-1}} + u_{t2} - u_{t2,t_{i-1}} \end{aligned} \tag{5.16}$$

where $u_{t1,t_{i-1}}$ and $u_{t2,t_{i-1}}$ are the separations in the respective tangential directions from the previous time-step.

If $\Delta_m > \delta_{m2}$ damage evolution is initiated. The damage, D, is determined by:

$$D = \max\left(\frac{\Delta_m - \delta_{m2}}{\delta_{mf} - \delta_{m2}}, D_{t_{i-1}}, 0\right) \tag{5.17}$$

where $D_{t_{i-1}}$ is the damage from the previous time-step, ensuring a monotonic increase of the damage.

With all these parameters determined, it is possible to calculate the tractions. The traction in the normal direction, σ_n, is calculated according to:

$$\sigma_n = \begin{cases} E_n(u_n - u_{n,p}) & \text{if } u_n - u_{n,p} < 0 \\ E_n(1-D)(u_n - u_{n,p}) & \text{if } u_n - u_{n,p} \geq 0 \end{cases} \tag{5.18}$$

where the split based on the sign of $u_n - u_{n,p}$ ensures an undamaged response in compression. Finally, the shear tractions, τ_1 and τ_2, are determined:

$$\tau_1 = E_t(1-D)(u_{t1} - u_{t1,p}) \tag{5.19}$$

$$\tau_2 = E_t(1-D)(u_{t2} - u_{t2,p}) \tag{5.20}$$

In summary, these equations describe how the material subroutine for MAT_240 calculates the tractions in each integration point for the cohesive elements given a set of separations and the relevant history variables.

5.2.2. MAT_240 modified

The second model applied in this study is a modification of MAT_240, which adds significant flexibility in the description of the mixed mode interactions. However, the response in the normal and the tangential directions are unchanged from MAT_240, such that the visualizations of the traction-separation law in Figure 5.2 are also valid for MAT_240 modified.

Although the response is similar in the normal and tangential directions, the input parameters used to define this behaviour are different. The energy release rates, ratios and elastic stiffnesses are replaced with the key separation measures as input parameters. Separation

at yield initiation, δ_{n1} and δ_{t1}, separation at damage initiation, δ_{n2} and δ_{t2}, separation at failure, δ_{nf} and δ_{tf}, and traction at yield, $\sigma_{n,y}$ and τ_y, define the traction separation law for their respective modes. Four additional parameters are added to describe the mixed mode interactions. These are the mixed mode stiffness interaction parameter, α_0, the mixed mode yield initiation interaction parameter, α_1, the mixed mode damage initiation interaction parameter, α_2, and the mixed mode failure interaction parameter, α_f.

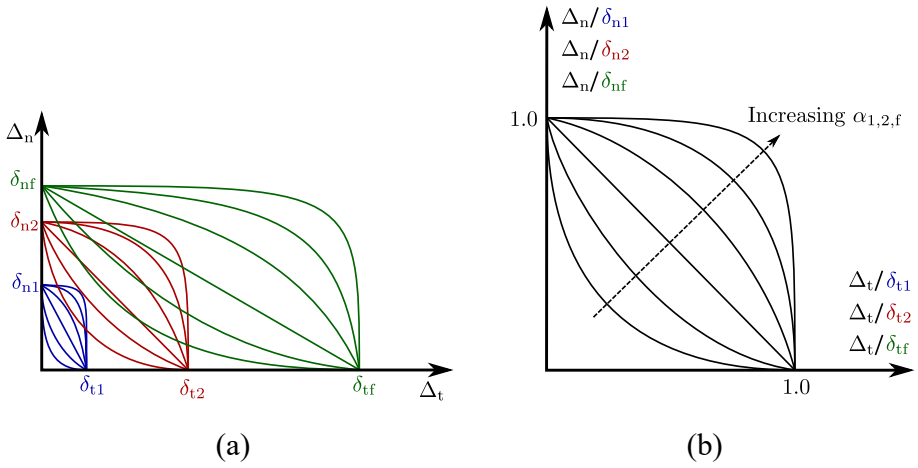

Figure 5.3.: Mixed mode interaction for MAT_240 modified. (a) Examples of potential yield, damage initiation and failure separation interactions. (b) Examples of separation interactions with normalized axes, showing the influence of $\alpha_{1,2,f}$.

Due to the similarities between MAT_240 and its modification, a series of equations are also applicable for the modified model. Equations 5.1, 5.2, 5.6, 5.7, 5.8 and 5.10 form the basis for MAT_240 modified.

The stiffness in normal direction, E_n, and tangential direction, E_t, are generalized for the modified model to include a mixed mode interaction. A mixed mode stiffness separation, $\delta_{mm,y}$, is introduced to alter the stiffness depending on the mixed mode angle, γ_{mm}, according to:

$$\delta_{mm,y} = \frac{\delta_{n1}\delta_{t1}}{\left[\left(\delta_{t1}\cos(\gamma_{mm})\right)^{\alpha_0} + \left(\delta_{n1}\sin(\gamma_{mm})\right)^{\alpha_0}\right]^{1/\alpha_0}} \tag{5.21}$$

which is used to calculate the stiffnesses following:

$$\begin{aligned} E_{\mathrm{n}} &= \sigma_{\mathrm{n,y}}/\delta_{\mathrm{mm,y}} \\ E_{\mathrm{t}} &= \tau_{\mathrm{y}}/\delta_{\mathrm{mm,y}} \end{aligned} \tag{5.22}$$

It is readily seen that a mixed mode angle of 0° and 90° makes $\delta_{\mathrm{mm,y}}$ equal to δ_{n1} and δ_{t1} respectively, such that Equation 5.22 returns the same relation seen in Equation 5.5.

In order to describe the mixed mode interactions for yield initiation, damage initiation and failure, normalized mixed mode angles, $\gamma_{\mathrm{mm,1}}$, $\gamma_{\mathrm{mm,2}}$ and $\gamma_{\mathrm{mm,f}}$, are introduced for their respective interactions. These are defined using the following equations:

$$\begin{aligned} \gamma_{\mathrm{mm,1}} &= \arctan\left(\frac{\Delta_{\mathrm{t}}}{\Delta_{\mathrm{n}}}\frac{\delta_{\mathrm{n1}}}{\delta_{\mathrm{t1}}}\right) \\ \gamma_{\mathrm{mm,2}} &= \arctan\left(\frac{\Delta_{\mathrm{t}}}{\Delta_{\mathrm{n}}}\frac{\delta_{\mathrm{n2}}}{\delta_{\mathrm{t2}}}\right) \\ \gamma_{\mathrm{mm,f}} &= \arctan\left(\frac{\Delta_{\mathrm{t}}}{\Delta_{\mathrm{n}}}\frac{\delta_{\mathrm{nf}}}{\delta_{\mathrm{tf}}}\right) \end{aligned} \tag{5.23}$$

Using these mixed mode angles, the mixed mode separation at yield initiation, δ_{m1}, damage initiation, δ_{m2}, and failure, δ_{mf}, are defined according to:

$$\begin{aligned} \delta_{\mathrm{m1}} &= \frac{\delta_{\mathrm{n1}}\delta_{\mathrm{t1}}}{\left[\left(\delta_{\mathrm{t1}}\cos(\gamma_{\mathrm{mm,1}})\right)^{\alpha_1} + \left(\delta_{\mathrm{n1}}\sin(\gamma_{\mathrm{mm,1}})\right)^{\alpha_1}\right]^{1/\alpha_1}} \\ \delta_{\mathrm{m2}} &= \frac{\delta_{\mathrm{n2}}\delta_{\mathrm{t2}}}{\left[\left(\delta_{\mathrm{t2}}\cos(\gamma_{\mathrm{mm,2}})\right)^{\alpha_2} + \left(\delta_{\mathrm{n2}}\sin(\gamma_{\mathrm{mm,2}})\right)^{\alpha_2}\right]^{1/\alpha_2}} \\ \delta_{\mathrm{mf}} &= \frac{\delta_{\mathrm{nf}}\delta_{\mathrm{tf}}}{\left[\left(\delta_{\mathrm{tf}}\cos(\gamma_{\mathrm{mm,f}})\right)^{\alpha_f} + \left(\delta_{\mathrm{nf}}\sin(\gamma_{\mathrm{mm,f}})\right)^{\alpha_f}\right]^{1/\alpha_f}} \end{aligned} \tag{5.24}$$

Figure 5.3a shows how these mixed mode separations could vary in the normal and tangential separation domain illustrating the potential flexibility of the model. By plotting these curves with normalized axes, the influence of the interaction parameters, α_1, α_2 and α_{f}, are visualized in Figure 5.3b. With the key mixed mode separations defined, the plasticity, damage and tractions are calculated similarly to MAT_240 following Equations 5.14 to 5.20.

5.2.3. Gurson-based cohesive zone model

The final model to be studied in this work is a Gurson-based cohesive zone model (GCZM) originally presented by Said Schicchi et al. [106]. There are several changes from the original model to the one presented in this work. The model presented here is extended from 2D to 3D. Further, the hardening law is modified to a Voce hardening law in order to conform with the polymer model calibrated in Chapter 4. Finally, the void nucleation was changed to be linear with the effective plastic separation in contrast to the original exponential model. There is uncertainty in the effect of void nucleation for the studied adhesive, such that it is reasonable to assume a simple nucleation model. It should be noted that void nucleation is needed to enable failure in shear for the model. An additional advantage with this change is that it reduces the number of parameters to calibrate.

There are 18 parameters needed to define the model as implemented in this work. A reference thickness, t_{rep}, which is the thickness of the adhesive layer have to be given as an input. An effective elastic modulus, E_{eff}, and an effective shear modulus, G_{eff}, define the elastic domain for this model. Plasticity in the matrix material is defined by the yield stress, σ_{y}, and the Voce parameters $\theta_{\text{R1,R2,R3}}$ and $Q_{\text{R1,R2,R3}}$. In addition to the 3 fitting parameters used in the GTN model [124], q_1, q_2 and q_3, there is a fitting parameter for the matrix yield contribution, q_4. The void nucleation parameter, A_{n}, the initial void volume fraction, f_0, the critical void volume fraction, f_{C}, and the void volume fraction at failure, f_{F}, describe the failure component of the model.

Similar to the previously described models in this section, the separations and tractions presented in Equations 5.1 and 5.2 are the input and output from the material subroutine. In contrast to the previous models, the GCZM is formulated on a rate form. The rate of the separations, $\dot{\mathbf{u}}$, are split into an elastic, $\dot{\mathbf{u}}^{\text{e}}$, and plastic component, $\dot{\mathbf{u}}^{\text{p}}$ according to:

$$\dot{\mathbf{u}} = \dot{\mathbf{u}}^{\text{e}} + \dot{\mathbf{u}}^{\text{p}} \tag{5.25}$$

The elastic rate of separation can be calculated following:

$$\dot{\mathbf{u}}^{\text{e}} = \mathbf{C}^{-1} \cdot \dot{\mathbf{t}} \tag{5.26}$$

where $\mathbf{C}^{-1}$ is the inverse of the elastic stiffness matrix and $\dot{\mathbf{t}}$ is the rate of the traction vector. Using these two equations, the rate of the traction vector, $\dot{\mathbf{t}}$, can be determined using the total rate of separation and the plastic rate of separation vectors according to:

$$\dot{\mathbf{t}} = \mathbf{C} \cdot \left(\dot{\mathbf{u}} - \dot{\mathbf{u}}^{\text{p}}\right) \tag{5.27}$$

where the elastic stiffness matrix for this model is defined as:

$$\mathbf{C} = \begin{bmatrix} k_n & 0 & 0 \\ 0 & k_t & 0 \\ 0 & 0 & k_t \end{bmatrix}, \quad k_n = \frac{E_{\text{eff}}}{t_{\text{rep}}}, \quad k_t = \frac{G_{\text{eff}}}{t_{\text{rep}}} \tag{5.28}$$

where k_n and k_t are the elastic stiffness in the normal and tangential directions respectively.

Plastic rate of separation, $\dot{\mathbf{u}}^{\text{p}}$, is constitutively prescribed using an associated flow rule:

$$\dot{\mathbf{u}}^{\text{p}} = \dot{\lambda}\mathbf{n} \tag{5.29}$$

where $\dot{\lambda}$ is the plastic multiplier and $\mathbf{n}$ is the gradient of the yield function according to:

$$\mathbf{n} = \frac{\partial \phi}{\partial \mathbf{t}} \tag{5.30}$$

where ϕ is the yield function.

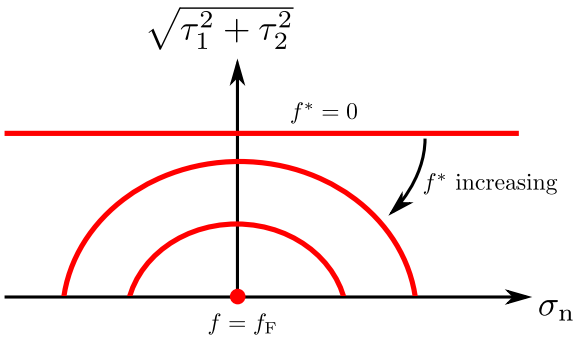

Figure 5.4.: Influence of the effective void volume fraction, f^*, on the yield surface of the GCZM.

The yield function, ϕ, is almost identical to its meso-scale counterpart in the GTN model with the exception that the matrix yield term is scaled by a new factor q_4. It is determined using the traction vector, $\mathbf{t}$, the equivalent plastic separation, $\bar{u}$, and the void volume fraction, f, as input variables according to:

$$\phi(\mathbf{t}, \bar{u}, f) = q_4 \frac{\tau_1^2 + \tau_2^2}{\sigma_{\mathrm{M}}^2} + 2q_1 f^* \cosh\left(\frac{3}{2} q_2 \frac{\sigma_{\mathrm{n}}}{\sigma_{\mathrm{M}}}\right) - \left(1 + q_3 f^{*2}\right) \tag{5.31}$$

where σ_{M} is the matrix flow stress and f^* is the effective void volume fraction defined as:

$$f^* = \begin{cases} f & \text{if} \quad f \leq f_{\mathrm{C}} \\ f_{\mathrm{C}} + \frac{\frac{1}{q_1} - f_{\mathrm{C}}}{f_{\mathrm{F}} - f_{\mathrm{C}}}\left(f - f_{\mathrm{C}}\right) & \text{if} \quad f_{\mathrm{C}} < f < f_{\mathrm{F}} \end{cases} \tag{5.32}$$

Figure 5.4 shows a sketch of the yield function in tangential and normal stress domain with the influence of the effective void volume fraction illustrated. It is seen that Setting $f = f_{\mathrm{F}}$ in Equation 5.32 gives $f^* = 1/q_1$. Assuming $q_3 = q_1^2$, the yield surface reduces to a point meaning the material cannot carry any load.

The rate of the void volume fraction, $\dot{f}$, is given by:

$$\dot{f} = \dot{f}_{\mathrm{gro}} + \dot{f}_{\mathrm{nuc}} \tag{5.33}$$

where $\dot{f}_{\mathrm{gro}}$ is the contribution from void growth due to volumetric plastic deformations and $\dot{f}_{\mathrm{nuc}}$ is the contribution due to void nucleation. The rate of the void volume fraction due to void growth, $\dot{f}_{\mathrm{gro}}$, is determined according to:

$$\dot{f}_{\mathrm{gro}} = (1 - f)\frac{\dot{u}_{\mathrm{n}}^{\mathrm{p}}}{t_{\mathrm{rep}}} \tag{5.34}$$

where $\dot{u}_{\mathrm{n}}^{\mathrm{p}}$ is the plastic separation in the normal direction. As the tangential separations are isochoric, the normal separation represents the hydrostatic component in the GTN model. Further, the rate of the void volume fraction due to void nucleation, $\dot{f}_{\mathrm{nuc}}$, is defined as:

$$\dot{f}_{\mathrm{nuc}} = A_{\mathrm{N}} \dot{\bar{u}} \tag{5.35}$$

where $\dot{\bar{u}}$ is the rate of the equivalent plastic separation and A_{N} is the void nucleation parameter. The rate of the equivalent plastic separation is defined by assuming a power equivalence between the macroscopic power and the undamaged matrix power:

$$(1-f)\sigma_{\mathrm{M}}\dot{\bar{u}} = \mathbf{t}\cdot\dot{\mathbf{u}}^{\mathrm{p}} \tag{5.36}$$

This gives the equation for the rate of the equivalent plastic separation, $\dot{\bar{u}}$:

$$\dot{\bar{u}} = \frac{\mathbf{t}\cdot\dot{\mathbf{u}}^{\mathrm{p}}}{(1-f)\sigma_{\mathrm{M}}} \tag{5.37}$$

The matrix flow stress, σ_{M}, is based on a Voce hardening law analogous to the one presented in Section 4.3.1. However, the equivalent plastic strain is replaced with the equivalent plastic separation normalized with the thickness of the adhesive layer resulting in:

$$\sigma_{\mathrm{M}} = \sigma_{\mathrm{y}} + \sum_{i=1}^{3} Q_{Ri}\Big[1-\exp\Big(-\frac{\theta_{Ri}}{Q_{Ri}}\frac{\bar{u}}{t_{\mathrm{rep}}}\Big)\Big] \tag{5.38}$$

In order to calculate the plastic separations, it is necessary to determine the plastic multiplier, $\dot{\lambda}$. Using the Kuhn-Tucker conditions, the following expression for the plastic multiplier can be obtained:

$$\dot{\lambda} = \frac{\mathbf{n}\cdot\mathbf{C}}{\mathbf{n}\cdot\mathbf{C}\cdot\mathbf{n}+\bar{H}}\cdot\dot{\mathbf{u}} \tag{5.39}$$

where $\bar{H}$ is the softening parameter:

$$\bar{H} = -\frac{\partial\phi}{\partial f}\left((1-f)\frac{\partial\phi}{\partial\sigma_{\mathrm{n}}} + A_{\mathrm{N}}\frac{\mathbf{t}\cdot\mathbf{n}}{(1-f)\sigma_{\mathrm{M}}}\right) - \frac{\partial\phi}{\partial\bar{u}}\frac{\mathbf{t}\cdot\mathbf{n}}{(1-f)\sigma_{\mathrm{M}}} \tag{5.40}$$

There are two contributions to the softening parameter, one related to the void volume fraction and one related to the hardening of the material. These two contributions typically have different signs. The derivatives needed to determine the softening parameter are given in Equations 5.41 to 5.46:

$$\frac{\partial\phi}{\partial\sigma_{\mathrm{n}}} = \frac{3f^{*}q_1q_2\sinh\left(\frac{3}{2}q_2\frac{\sigma_{\mathrm{n}}}{\sigma_{\mathrm{M}}}\right)}{\sigma_{\mathrm{M}}} \tag{5.41}$$

$$\frac{\partial\phi}{\partial\tau_1} = \frac{2q_4\tau_1}{\sigma_{\mathrm{M}}}, \qquad \frac{\partial\phi}{\partial\tau_2} = \frac{2q_4\tau_2}{\sigma_{\mathrm{M}}} \tag{5.42}$$

$$\frac{\partial f^*}{\partial f} = \begin{cases} 1 & \text{if} \quad f \leq f_C \\ \frac{\frac{1}{q_1} - f_C}{f_F - f_C} & \text{if} \quad f_C < f < f_F \end{cases} \tag{5.43}$$

$$\frac{\partial \phi}{\partial f} = \frac{\partial \phi}{\partial f^*}\frac{\partial f^*}{\partial f} = \left[2q_1 \cosh\left(\frac{3}{2}q_2\frac{\sigma_n}{\sigma_M}\right) - 2q_3 f^*\right]\frac{\partial f^*}{\partial f} \tag{5.44}$$

$$\frac{\partial \sigma_M}{\partial \bar{u}} = \sum_{i=1}^{3}\frac{\theta_{Ri}}{t_{rep}}\exp\left(-\frac{\theta_{Ri}}{Q_{Ri}}\frac{\bar{u}}{t_{rep}}\right) \tag{5.45}$$

$$\frac{\partial \phi}{\partial \bar{u}} = \frac{\partial \phi}{\partial \sigma_M}\frac{\partial \sigma_M}{\partial \bar{u}} = -\frac{3f^* q_1 q_2 \sigma_n \sigma_M \sinh\left(\frac{3}{2}q_2\frac{\sigma_n}{\sigma_M}\right) + 2q_4(\tau_1^2 + \tau_2^2)}{\sigma_M^3}\frac{\partial \sigma_M}{\partial \bar{u}} \tag{5.46}$$

Figure 5.5 shows the response of the GCZM in pure mode I and II using the material parameters presented in Table 5.3. The stiffness in the normal direction is comparatively high, with an almost brittle behaviour. It should be noted that without an initial void volume fraction this model will not yield or fail when subjected to pure normal separation. Further, the mode II behaviour is seen to be significantly softer with comparatively high ductility. This increase in ductility is caused by the void volume fraction being driven entirely by the void nucleation contribution for pure tangential separation. In summary, Initial studies of this model demonstrate that the behaviour of the model is dominated by the void volume fraction and its evolution.

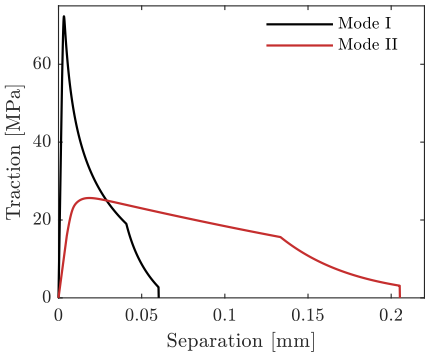

Figure 5.5.: Example of traction separation law in mode I and mode II for the GCZM.

There is a kink in the traction separation curves presented in Figure 5.5. This kink is caused by the void volume fraction reaching the critical value, f_C, where the evolution

of the effective void volume fraction is accelerated towards failure. Further, the sudden failure is caused by a simplification in the numerical implementation of the model which is discussed further in Section 5.2.4.

The GCZM model has a single damage variable in the form of the void volume fraction, f, which typically has a non-zero initial value, f_0. This could facilitate a statistically based distribution of the initial void volume fraction in order to model potential defects and a general variance of the quality of the adhesive layer.

5.2.4. Implementation: GCZM

The GCZM model is implemented in the LS-DYNA explicit solver [123] as a user subroutine for solid element formulations 19 and 20. As it is an explicit solver, there is no need to calculate a consistent tangent stiffness. Further, the time increments are generally very small, such that the sub-stepping requirements are not as strict compared to an implementation in an implicit solver. The user subroutine is only required to return a traction vector for a provided separation vector. Therefore, the equations provided in Section 5.2.3 are sufficient for the numerical implementation when reformulated to an incremental form.

A semi-implicit stress update algorithm was chosen due to the small time-steps in the explicit solver. This means that the gradient of the yield function is calculated based on the previous time-step. A quasi-implicit update, where the gradient of the yield function is updated after every iteration, was also considered. However, it was seen to cause numerical instabilities as there could be poor predictions of the gradient within the iteration loop.

A secant iteration scheme is used to iterate on the change in the plastic multiplier over the time-step, $\Delta\lambda = \Delta t\dot{\lambda}$, where the yield function is used as a residual function in this implementation. As previously, the time steps are noted with n and $n+1$ corresponding to previous and current time-step respectively. Further, the iteration counts are noted as I and $I+1$ corresponding to previous and current iteration, with $I-1$ being the iteration before I. Based on this, the secant update on the increment of the plastic multiplier, $\Delta\lambda_{n+1}^{I+1}$, for iteration $I+1$ and step $n+1$ is estimated according to:

$$\Delta\lambda_{n+1}^{I+1} = \Delta\lambda_{n+1}^{I} - \phi_{n+1}^{I} \frac{\Delta\lambda_{n+1}^{I} - \Delta\lambda_{n+1}^{I-1}}{\phi_{n+1}^{I} - \phi_{n+1}^{I-1}} \tag{5.47}$$

Initialization of the secant iteration scheme requires a non-zero estimate of the incremental change in the plastic multiplier, $\Delta\lambda_{n+1}^{I}$, by multiplying both sides of Equation 5.39 with the time increment:

$$\Delta\lambda_{n+1}^{I}(\bar{H}_n, \mathbf{n}_n) = \frac{\mathbf{n}_n \cdot \mathbf{C}}{\mathbf{n}_n \cdot \mathbf{C} \cdot \mathbf{n}_n + \bar{H}_n} \cdot \Delta\mathbf{u} \tag{5.48}$$

where $\Delta\mathbf{u}$ is the increment in the separation vector, $\bar{H}_n$ is the softening parameter calculated based on the previous time-step using Equation 5.40 and $\mathbf{n}_n$ is the gradient of the yield function from the previous time-step.

In order to evaluate the yield function for the given prediction, ϕ_{n+1}^{I}, it is necessary to determine the corresponding equivalent plastic separation and void volume fraction. An incremental update of the equivalent plastic separation, $\bar{u}_{n+1}^{I}$, is determined by substituting the plastic separations in Equation 5.37 with a function of $\Delta\lambda_{n+1}^{I}$:

$$\bar{u}_{n+1}^{I}(\Delta\lambda_{n+1}^{I}, \mathbf{t}_n, \mathbf{n}_n, f_n, \sigma_{\mathrm{M},n}, \bar{u}_n) = \bar{u}_n + \Delta\bar{u}_{n+1}^{I} = \bar{u}_n + \frac{\mathbf{t}_n \cdot \mathbf{n}_n}{(1 - f_n)\sigma_{\mathrm{M},n}}\Delta\lambda_{n+1}^{I} \tag{5.49}$$

Similarly, an incremental update of the void volume fraction, f_{n+1}^{I}, is determined by using $\Delta\lambda_{n+1}^{I}$ and $\bar{u}_{n+1}^{I}$ in Equations 5.33, 5.34 and 5.35:

$$f_{n+1}^{I}(\Delta\lambda_{n+1}^{I}, \Delta\bar{u}_{n+1}^{I}, f_n, \mathbf{n}_n) = f_n + \Delta f_{n+1}^{I} = f_n + (1 - f_n)\frac{n_{1,n}}{t_{\mathrm{rep}}}\Delta\lambda_{n+1}^{I} + A_{\mathrm{N}}\Delta\bar{u}_{n+1}^{I} \tag{5.50}$$

where $n_{1,n}$ is the first component of the gradient, $\mathbf{n}_n$.

A compact list of operations describing the numerical implementation of the GCZM is presented in Algorithm 3. The algorithm is structured in an initialization phase where the number of sub-steps for the outer sub-stepping loop is determined. For each sub-step, the converged history variables and tractions are used as new input variables representing increment n in the algorithm. Each sub-step is structured with an elastic predictor and then a plastic correction, where the plastic correction is done with a trial step before the secant iterations.

Failure in the GCZM is initially captured by letting the yield surface reduce to a point when the void volume fraction reaches its failure value. However, a quasi-implicit algorithm had to be employed in order to converge towards this type of failure. This introduced further numerical instabilities due to the volatility in the initial plastic predictions, making the semi-implicit algorithm the appropriate choice for this implementation. Therefore, it was chosen to use a cut-off value for the void volume fraction. The integration point is considered to have failed if $f_{n+1} > 0.95 f_{\mathrm{F}}$, where f_{n+1} is the converged value of the void volume fraction for the given sub-step.

Algorithm 3 GCZM traction-separation law subroutine.

Input: Solver variables: $\mathbf{u}_{n+1}$, $\mathbf{t}_n$ and Δt
State variables: $\mathbf{u}_n$, $\bar{u}_n$, $\sigma_{\mathrm{M},n}$ and f_n
Material parameters: t_{rep}, E_{eff}, G_{eff}, $q_{1/2/3/4}$, σ_{y}, $\theta_{R1/2/3}$, $Q_{R1/2/3}$, A_{n}, f_0, f_{C}, f_{F}
Output: $\mathbf{t}_{n+1}$, $\mathbf{u}_{n+1}$, f_{n+1}, $\bar{u}_{n+1}$ and $\sigma_{\mathrm{M},n+1}$

Initialization and sub-stepping:
    # Determine k_n, k_t based on Equation 5.28
    # Determine $\Delta\mathbf{u}_{\mathrm{tot}} = \mathbf{u}_{n+1} - \mathbf{u}_n$
    # Determine number of sub-steps:
    $N_{\mathrm{sub}} = \mathrm{int}\left[\max\left(\frac{\mathrm{abs}(\Delta u_{\mathrm{n,tot}})}{0.05\sigma_{\mathrm{y}}/k_n}, \frac{\mathrm{abs}(\Delta u_{\mathrm{t1,tot}})}{0.05\sigma_{\mathrm{y}}/k_t}, \frac{\mathrm{abs}(\Delta u_{\mathrm{t2,tot}})}{0.05\sigma_{\mathrm{y}}/k_t}, \frac{f_{\mathrm{F}}}{f_{\mathrm{F}}-f_n}, 1\right)\right]$
    # Determine change in separation per sub-step: $\Delta\mathbf{u} = \Delta\mathbf{u}_{\mathrm{tot}}/N_{\mathrm{sub}}$
Loop over N_{sub} sub-steps
    # Elastic predictor:
        # Determine predictor tractions: $\mathbf{t}^{\mathrm{tr1}}_{n+1} = \mathbf{t}_n + \mathbf{C}\Delta\mathbf{u}$
        # Determine yield function, $\phi^{\mathrm{tr1}}_{n+1}(\mathbf{t}^{\mathrm{tr1}}_{n+1}, \bar{u}_n, f_n)$, based on Equation 5.31
        # **if** $\phi^{\mathrm{tr1}}_{n+1}(\mathbf{t}^{\mathrm{tr1}}_{n+1}, \bar{u}_n, f_n) < 0$
            then write updated values and continue to next sub-step
            else Continue with plastic update
    # Initial plastic predictor:
        # Determine gradient for the previous increment/sub-step, $\mathbf{n}_n$,
        using Equations 5.30, 5.41 and 5.42
        # Determine $\Delta\lambda^{tr2}_{n+1}$ using Equation 5.48
        # Determine tractions $\mathbf{t}^{\mathrm{tr2}}_{n+1} = \mathbf{t}_n + \mathbf{C}\left(\Delta\mathbf{u} - \Delta\lambda^{tr2}_{n+1}\mathbf{n}_n\right)$
        # Determine history variables, $\sigma^{tr2}_{\mathrm{M},n+1}$, $\bar{u}^{tr2}_{n+1}$ and f^{tr2}_{n+1},
        using Equations 5.38, 5.49 and 5.50 respectively
        # Determine yield function, $\phi^{\mathrm{tr2}}_{n+1}(\mathbf{t}^{\mathrm{tr2}}_{n+1}, \bar{u}^{tr2}_{n+1}, f^{tr2}_{n+1})$, based on Equation 5.31
    # Secant iterations:
        # Initialize values: $\Delta\lambda^1_{n+1} = \Delta\lambda^{tr1}_{n+1}$, $\phi^1_{n+1} = \phi^{tr1}_{n+1}$, $\Delta\lambda^2_{n+1} = \Delta\lambda^{tr2}_{n+1}$, $\phi^2_{n+1} = \phi^{tr2}_{n+1}$
        # **while** $\mathrm{abs}\left(\phi^{I+1}_{n+1}\right) \geq$ tolerance
            # Determine $\Delta\lambda^{I+1}_{n+1}$ using Equation 5.47
            # Determine tractions $\mathbf{t}^{\mathrm{I+1}}_{n+1} = \mathbf{t}_n + \mathbf{C}\left(\Delta\mathbf{u} - \Delta\lambda^{I+1}_{n+1}\mathbf{n}_n\right)$
            # Determine history variables, $\sigma^{I+1}_{\mathrm{M},n+1}$, $\bar{u}^{I+1}_{n+1}$ and f^{I+1}_{n+1},
            using Equations 5.38, 5.49 and 5.50 respectively
            # Determine yield function, $\phi^{\mathrm{I+1}}_{n+1}(\mathbf{t}^{\mathrm{I+1}}_{n+1}, \bar{u}^{I+1}_{n+1}, f^{I+1}_{n+1})$, based on Equation 5.31
    # Write final values of iteration scheme as sub-step tractions and state variables
End sub-step loop
Return $\mathbf{t}_{n+1}$, $\mathbf{u}_{n+1}$, f_{n+1}, $\bar{u}_{n+1}$ and $\sigma_{\mathrm{M},n+1}$

The calculation of the number of sub-steps is primarily based on avoiding too large increments in the separations by relating them to the elastic separation before yielding. There is an additional term for determining the number of sub-steps related to the void volume fraction. As the gradient of the yield function is changing rapidly as the void volume fraction approaches the failure value, it is necessary to add additional sub-steps to ensure convergence. Due to the cut-off value on the void volume fraction, the number of sub-steps due to the void volume fraction is limited to a maximum of 20.

The model seems to be numerically unstable when loaded primarily in the normal direction while at a low void volume fraction. This effect is emphasized with a compression phase before continuing to load in tension. A low void volume fraction makes the effective yield traction in pure normal direction very high, such that small changes in the void volume fraction causes a large change in the effective yield traction. This effect can in some cases become strong enough that the yield surface is shrinking faster than what the plastic corrector can adjust for, making the solution unable to converge. The issue is alleviated by using a sub-stepping scheme.

5.3. Virtual laboratory calibration procedure

This section will give an overview of the partial virtual laboratory approach applied in the calibration process for the macro-scale material models. The idea and concept behind the approach is presented first. Then, the considerations and the resulting numerical models used for the calibration process are presented. Finally, the reverse engineering process used to calibrate the material parameters is described in general terms.

5.3.1. Concept and strategy

Traditionally, macro-scale material models are calibrated based on physical tests, either by reverse engineering of benchmark tests or a combination of material tests and fracture mechanics tests. These tests are expensive to perform in addition of being complex. Further, one such set of tests gives one calibration of the given material model. If the joint configuration is changed by altering the adherents or the adhesive thickness, a new set of tests have to be performed to obtain new parameters for that specific configuration. It is evident that replacing these experiments with numerical experiments could significantly reduce cost. The flexibility of a numerical calibration approach and its low cost make it especially suitable when exploring possible joint configurations.

The key idea behind the partial numerical calibration process is to use a validated meso-scale modelling framework, such as the one presented in Chapter 4, to simulate virtual

benchmark tests. These virtual benchmark tests are then used in the reverse engineering process instead of physical benchmark tests. Since they are numerical models, they can be parametrized in order to calibrate and investigate a range of configurations with limited effort.

In the initial study of this work, it was chosen to use three types of benchmark tests to ensure that the key loading modes of the adhesive is captured in the calibration process. Therefore, there is one test which is dominated by macroscopic tension, mode I, one test with primarily macroscopic shear, mode II, and a mixed mode case. The tension dominated load case was designed to allow for significant crack propagation before failure to ensure that crack propagation is accounted for in the calibration process. In order to facilitate parametrization of the models, the goal was to keep the models as simple as possible while still exhibiting the relevant loading modes.

5.3.2. Baseline geometries

For the respective meso-scale and macro-scale models, there is a set of common decisions for the three benchmark test configurations. All the meso-scale simulations are run with the Abaqus/Explicit [112] solver. The scope is limited to metal adherents for this study. Further, for these simulations it is assumed elastic adherents for the sake of simplicity and to put emphasis on the adhesive performance. The polymer model presented in Chapter 4 with the parameters given in Table 4.1 is used to model the adhesive. Fully integrated linear brick elements of type C3D8 are used for the adhesive layer to avoid excessive distortion and significant hourglass energy. For the adherents, reduced integrated linear brick elements of type C3D8R are used. Three elements through the thickness of both adherents and the adhesive layer are used in the meso-scale models. Further, the in-plane mesh size is set to $0.5\,\text{mm} \times 0.5\,\text{mm}$ in the bonded region and expanding with a factor of 1.7 for the rest of the models. A mesh sensitivity study suggested that the influence of the in-plane mesh size was negligible, thus allowing for significantly larger elements in-plane than through-thickness.

All the macro-scale simulations are run with the LS-DYNA [123] solver. Similar to the meso-scale simulations it is assumed elastic adherent materials. The adhesive is modelled with the given macro-scale material model that needs to be calibrated, which in this work means the three models presented in Section 5.2. Fully integrated shell elements with formulation 16 [93] are used for the adherents, while the adhesive layer is modelled using cohesive zone elements with solid element formulation 20 [93]. An in-plane mesh size of 2 mm is used for the macro-scale models applied in this chapter. This mesh size represents the finest mesh size currently applied in full-scale simulations in the automotive industry, thereby ensuring relevancy of this work.

Both the thickness and materials for the different parts of the virtual benchmark tests are

adjustable depending on the geometry and materials of the joint the calibration is for. For the calibrations performed in this chapter, the target joint is between the flanges of the bonded component tests. Therefore, the adherents are represented by a 1.135 mm thick steel plate and a 2.45 mm thick aluminium plate. Further, the adhesive layer has its thickness set to 0.25 mm, corresponding to the average thickness of the adhesive layer measured from the component test specimens.

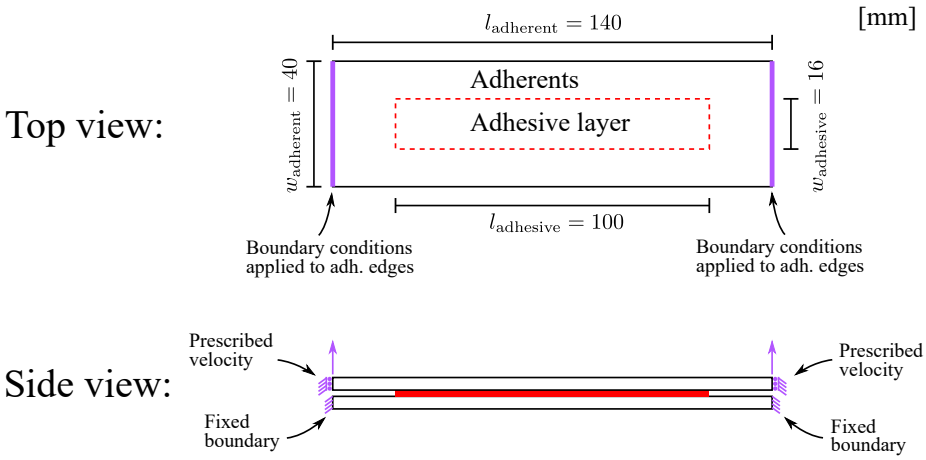

Figure 5.6.: Geometry and loading of the peel dominated virtual test case.

Figure 5.6 shows the chosen baseline geometry of the virtual benchmark test dominated by macroscopic tension. There are two goals to achieve with this geometry. Failure should be dominated by a peeling type of failure mode and it should allow for significant crack propagation before complete loss of load-carrying ability. The key variables influencing these goals are the boundary conditions and the length of the adhesive layer. Fixed boundaries are applied to the bottom adherent, while a rotationless boundary with a prescribed velocity is applied to top adherent as seen in Figure 5.6. The goals are achieved by using these boundary conditions in combination with a long adhesive line where the crack could propagate.

The width of the adhesive layer is based on approximately the width of a typical adhesive layer in the industry, while the rest of the dimensions use the bonded cross tests from Figure 4.12 as a basis. A sensitivity study on the adherent dimensions indicated that the problem was not particularly sensitive to the adherent dimensions when considering the total energy absorbed in the adhesive layer. Therefore, the baseline geometry in Figure 5.6 is used in these studies. Finally, the applied loading velocity is adjusted such that the adhesive layer fail within 100 s of modelling time, giving a loading velocity of 0.1 mm/s.

Figure 5.7 shows the corresponding meso-scale and macro-scale numerical models in deformed configuration to the geometry presented in Figure 5.6. Two symmetry planes are

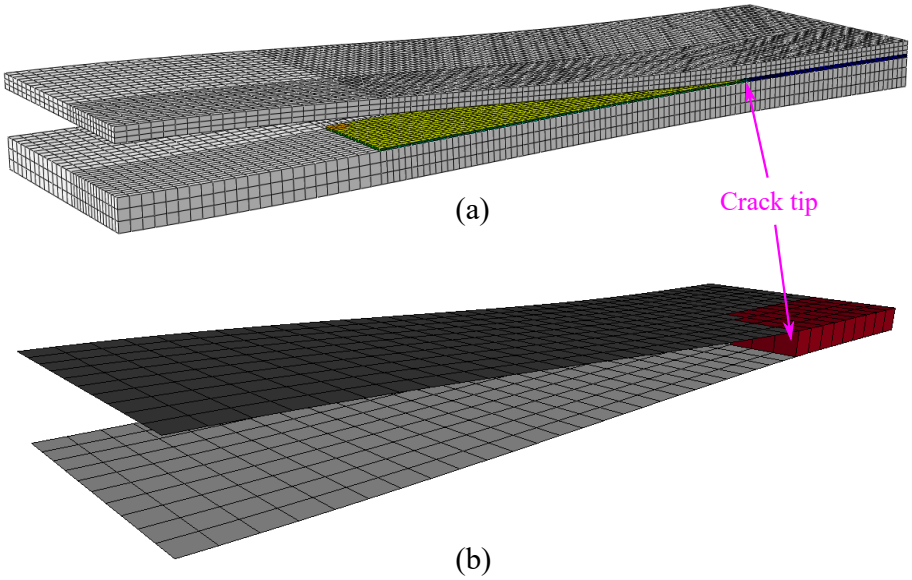

Figure 5.7.: Finite element meshes for the peel dominated virtual test case in deformed configuration. (a) Meso-scale. (b) Macro-scale.

applied to reduce the computational time. The adherents are seen to deform in an S-shape along the length of the tests, which propagates all the way until complete failure. Further, the adhesive ahead of the crack tip in the direction of crack propagation is seen to first be subjected to a compression loading before changing to tension when failing. For the meso-scale model, there is also a significant shear component in the elements connected to the adherents at the crack tip.

Figure 5.8 shows the chosen baseline geometry of the virtual benchmark test dominated by macroscopic shear. The goal is to have a shear dominated failure in the adhesive layer. This is achieved by using a slightly modified version of the previously mentioned cross tests. Width of the adhesive layer is based on the same industry standard as for the tension dominated tests, while the length corresponds to the cross tests. Similar to the tension case, it was performed a sensitivity study on the in-plane geometry of the adherents. This study suggested that the influence on the adhesive layer of the in-plane geometry of the adherents were minor. Therefore, the baseline geometry is used. Fixed rotationless boundaries are applied with the exception of the prescribed velocity indicated in Figure 5.8. The base model has a prescribed loading velocity of $2.5 \cdot 10^{-3}$ mm/s to achieve failure within approximately 100 s of modelling time.

The meso-scale and macro-scale numerical models of the shear dominated loading is shown in Figure 5.9. One symmetry plane is applied to reduce computational time. The

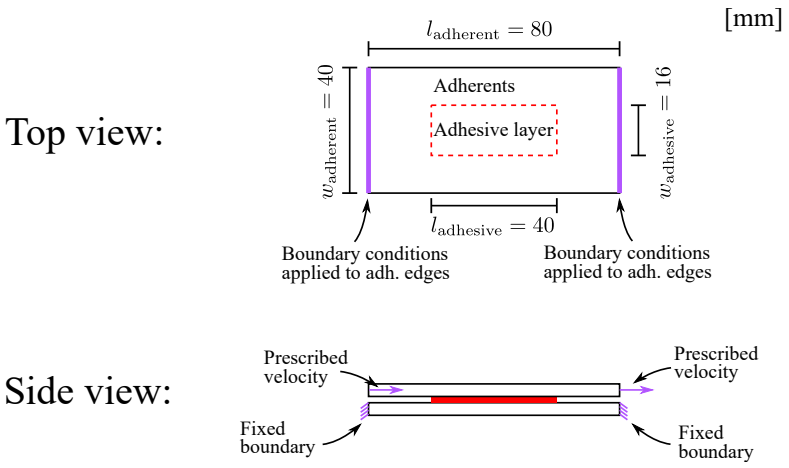

Figure 5.8.: Geometry and loading of the shear dominated virtual test case.

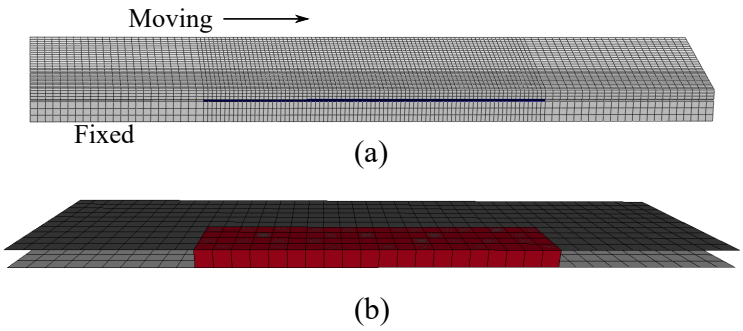

Figure 5.9.: Finite element meshes for the shear dominated virtual test case. (a) Meso-scale. (b) Macro-scale.

deformation mode in the of the adhesive layer is close to uniform with the only exception being the edges influenced by edge effects. Therefore, the adhesive layer fails completely almost immediately after the initial crack starts propagating due to this nearly uniform deformation state.

The mixed mode benchmark model, shown in Figure 5.10, has the same geometry and boundary conditions as the shear dominated model. However, the prescribed velocity is applied at a 45° angle for the top adherent as indicated by the figure. This change means that the adhesive layer is subjected to both macroscopic tension and shear satisfying the goal of applying a mixed mode load. With the given geometry, there is some additional out of plane flexibility such that the loading mode exhibited on the adhesive layer is skewed towards the shear mode. Similar to the previously described tests, the goal is that the

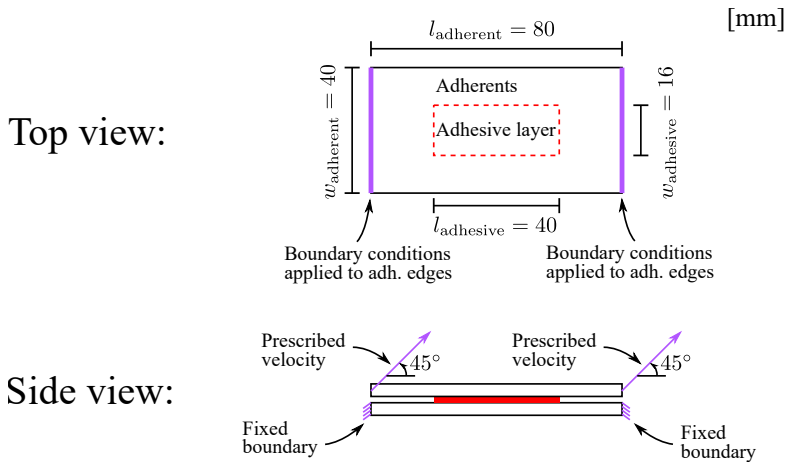

Figure 5.10.: Geometry and loading of the mixed mode virtual test case.

adhesive layer should fail within 100 s modelling time, which gives a prescribed velocity of $2.5 \cdot 10^{-3}$ mm/s as baseline.

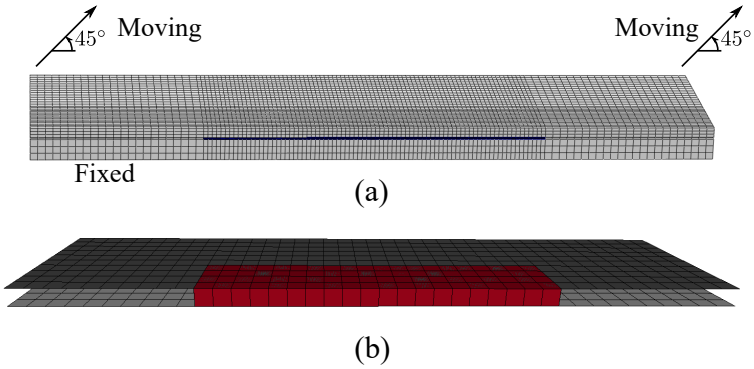

Figure 5.11.: Finite element meshes for the mixed mode virtual test case. (a) Meso-scale. (b) Macro-scale.

Figure 5.11 shows the numerical models used to simulate the mixed mode virtual benchmark tests. The behaviour of the mixed case is close to that of the shear dominated case. However, there is an additional peel component. Due to the flexibility in the out of plane direction, the separation in the normal direction is an order of magnitude less than in the shear direction for this case. The peel traction is on the same order of magnitude as the shear traction, making it relevant for the mixed mode case. With the additional peel forces, the peak force is lowered. However, failure is slightly more gradual for the mixed mode case than the shear dominated case as the peel forces are stronger at the edges and takes more time to

propagate through the adhesive layer.

5.3.3. Calibration by reverse engineering

In order to calibrate the material parameters, a reverse engineering process is used. The results of the meso-scale simulations are used as target curves for their corresponding macro-scale simulations, thus replacing the physical experiments. LS-OPT [125] connected with LS-DYNA [123] runs an optimization algorithm where the macro-scale models presented in Section 5.3.2 are run as predictions and compared to the target curves. The square error between the target curves and the estimated responses for the three different configurations are summed up to create the error function. Optimization is performed by minimizing this error function.

LS-OPT uses a polynomial metamodel in order to estimate the new optimal values of the parameters. For each iteration the domain is reduced such that the solution converges. However, it does not necessarily converge towards a global optimum. Therefore, the optimization process is strongly dependent on user input with regards to deciding initial values and realistic ranges to the relevant parameters. The calibration process is also heavily dependent on the material model to be calibrated. Particularly, the computational cost is significantly reduced by reducing the number of parameters to calibrate. Further, this increases the likelihood of finding an acceptable optimum.

The influence and sensitivity of each parameter in each model are subjected to large variance with respect to the optimization process and response. Therefore, the optimization strategy varies from model to model. The strategy changes in terms of how many iterations are needed to obtain a converged solution and how many times the optimization scheme has to be rerun with updated inputs. Specifics regarding this procedure for the different models are given in Sections 5.4.1, 5.4.2 and 5.4.3.

5.4. Calibration results and initial validation

This section will cover the specific details of the calibration process for the three macro-scale models studied in this chapter. Both the process and calibration results will be presented for each of the models. Finally, an initial validation of these calibrations performed on the bonded component tests will be presented in Section 5.4.4.

5.4.1. Calibration and results for MAT_240

Calibration of MAT_240 was performed in several steps using the process discussed in Section 5.3.3. Initial values of the effective Youngs modulus, E_{mod}, effective shear modulus, G_{mod}, energy release rate in mode I, G_{1C}, energy release rate in mode II, G_{2C}, effective yield traction in mode I, $\sigma_{n,y}$, and effective yield traction in mode II, τ_y, were all estimated based on the stress-strain response reported in Chapter 4. However, the stress and strain-state in the adhesive layer, especially within the size of a cohesive element, is not uniform. Therefore, the macro-scale response can diverge from the local material response, such that the boundaries for these parameters were set quite loose for the initial run. Further, the ratio between the total energy release rate and plastic release rate for both modes, r_{G1} and r_{G2}, were guessed and given wide ranges for the first optimization run. Due to these wide ranges, the optimization procedure had to be rerun with updated estimates and ranges to the parameters in order to converge towards an acceptable solution. In general, the optimization process of this material model was seen to require several runs dependent on the accuracy of the initial predictions and ranges.

Figure 5.12 shows the comparison between the target curves produced by the meso-scale benchmark tests and the predictions of the macro-scale benchmark tests using optimized parameters for MAT_240. The responses of the peel dominated case presented in Figure 5.12a are smoothed for sake of visibility. Due to the large element size of the macro-scale model, failure of each element causes significant oscillations in the response. Overall, it could be considered a decent fit between the sets of virtual benchmark tests. This suggests that a satisfactory calibration has been obtained and that the MAT_240 material model provides sufficient accuracy for the studied adhesive.

Table 5.1.: Calibrated material parameters for MAT_240.

MAT_240 parameters							
E_{mod}[MPa]	G_{mod}[MPa]	$\sigma_{n,y}$[MPa]	τ_y[MPa]	$G_{1C}[\frac{N}{mm}]$	$G_{2C}[\frac{N}{mm}]$	$r_{G1}[-]$	$r_{G2}[-]$
4289	4230	22.9	25.3	1.48	2.64	0.510	0.482

Calibrated material parameters are shown in Table 5.1 and the corresponding traction separation law is shown in Figure 5.13. As expected, there is a weaker response in the peel dominated mode compared to the shear dominated mode which has a 78% higher energy release rate.

5.4.2. Calibration and results for MAT_240 modified

Due to the similarities between MAT_240 and the modified version, the calibration procedure of the modified model was heavily influenced by the results of the MAT_240 calibration. The two models exhibit identical behaviour in pure mode I and II, with the

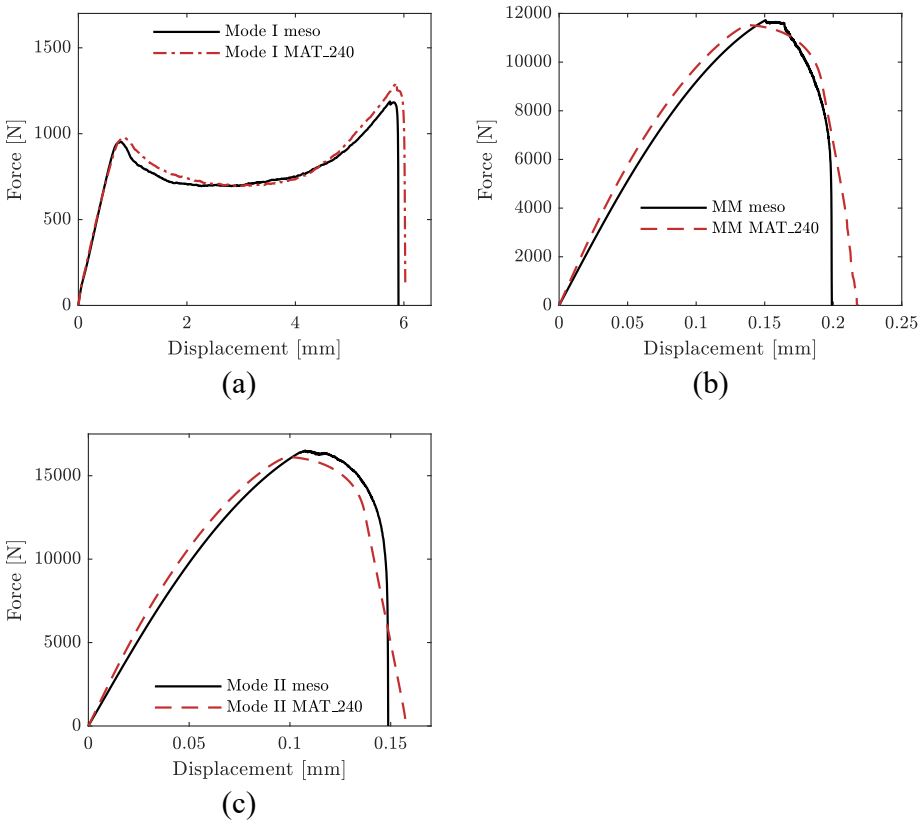

Figure 5.12.: Comparisons between meso-scale target curves and macro-scale predictions using MAT_240. (a) Peel dominated case. (b) Mixed mode case. (c) Shear dominated case.

mixed mode being the only exception. Therefore, the 8 parameters used to describe the pure mode I and II behaviour for MAT_240 modified was calculated based on the MAT_240 parameters and set as fixed values for the initial optimization run. The mixed mode interaction parameters, α_0, α_1, α_2 and α_f, were set to an initial value of 2 assuming a quadratic interaction. Boundaries for the interaction parameters were set to range from linear, 1, to cubic, 3. Similar to MAT_240, several runs of the optimization process were require to obtain decent results.

Figure 5.14 shows the comparison between the target curves produced by the meso-scale benchmark tests and the predictions of the macro-scale benchmark tests using optimized parameters for MAT_240 modified. As previously, the response of the peel dominated case is smoothed for visibility. The overall fit between the meso-scale and macro-scale

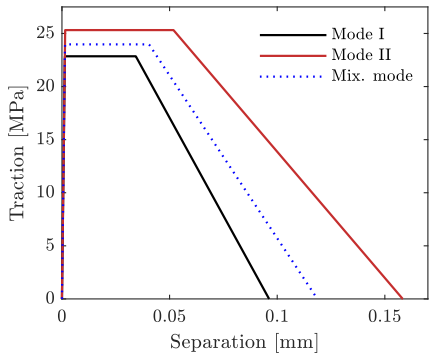

Figure 5.13.: Traction separation law for MAT_240 in mode I, mode II and mixed mode with a load angle of 45° according to Equation 5.10.

simulations when using MAT_240 modified is seen to be very good. It is noticeably better than the performance of the unmodified version, though both could be considered acceptable. However, the computational cost of calibration increases significantly without a previous calibration of MAT_240. An additional layer of user sensitivity is added to the calibration procedure with the additional complexity of the modified model. The oscillations found in Figure 5.14c were likely caused by instabilities in the numerical implementation of the modified model as these were not observed in any other simulations. No further investigations were performed regarding these instabilities as the model was not implemented as a part of this work.

Table 5.2.: Calibrated material parameters for MAT_240 modified.

MAT_240 modified parameters					
$\sigma_{n,y}$[MPa]	τ_y[MPa]	δ_{n1}[mm]	δ_{t1}[mm]	δ_{n2}[mm]	δ_{t2}[mm]
22.9	25.4	$1.31 \cdot 10^{-3}$	$1.41 \cdot 10^{-3}$	$3.43 \cdot 10^{-2}$	$5.79 \cdot 10^{-2}$
δ_{nf}[mm]	δ_{tf}[mm]	α_0[−]	α_1[−]	α_2[−]	α_f[−]
$9.63 \cdot 10^{-2}$	0.163	1.71	1.98	2.65	1.0

Calibrated material parameters are shown in Table 5.2 and the corresponding traction separation law is shown in Figure 5.15. The effect of the mixed mode parameters is clearly visible in the traction and separations, where the mixed mode has significantly lower energy release rate than the two pure modes. This is caused by the low value of the mixed mode interaction parameter for failure, α_f.

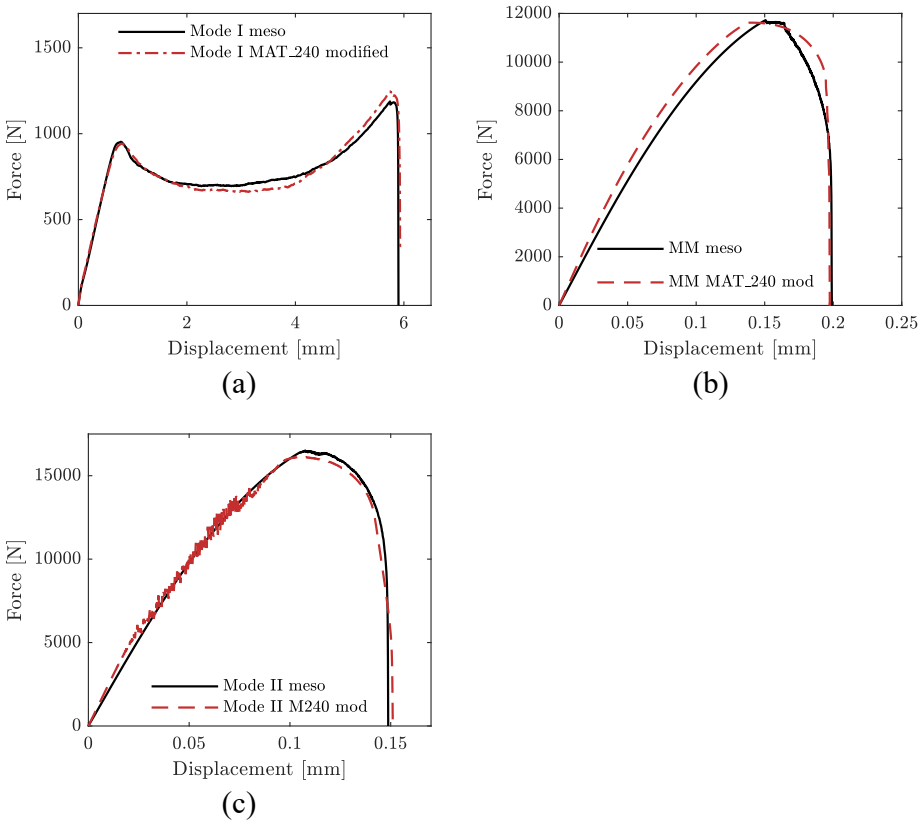

Figure 5.14.: Comparisons between meso-scale target curves and macro-scale predictions using MAT_240 modified. (a) Peel dominated case. (b) Mixed mode case. (c) Shear dominated case.

5.4.3. Calibration and results for GCZM

In contrast to the two previous models, the GCZM model used many of the same parameters previously calibrated for the polymer model discussed in Chapter 4. The effective elastic modulus, E_{eff}, in the normal direction is calculated using the Young's modulus and Poisson's ratio assuming a uniaxial strain state, as there are no transverse strains in the cohesive elements. Similarly, the effective shear modulus, G_{eff}, was calculated using the same elastic parameters. Common values of the GTN model fitting parameters, q_1 and q_2, were assumed and q_3 was calculated as the square of q_1. The additional fitting parameter for the GCZM model, q_4, was initially given an estimated value based on the pressure sensitivity parameter reported in Section 4.3.2. However, the parameter was set as a variable in the optimization scheme as it proved to be important for the shear response of the model.

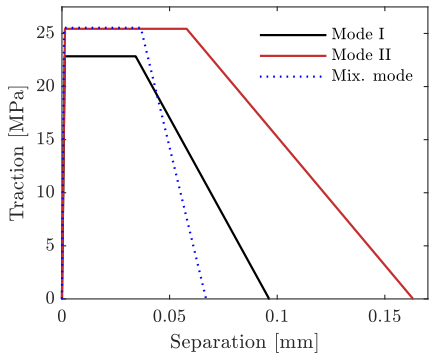

Figure 5.15.: Traction separation law for MAT_240 modified in mode I, mode II and mixed mode with a load angle of 45° according to Equation 5.10.

Further, the parameters governing the matrix flow stress, the yield stress and Voce hardening parameters, were all taken from the previously mentioned polymer model.

Table 5.3.: Calibrated material parameters for GCZM.

GCZM parameters					
E_{eff}[MPa]	G_{eff}[MPa]	q_1[−]	q_2[−]	q_3[−]	q_4[−]
6548	800	1.5	1.0	2.25	1.53
σ_y[MPa]	θ_{R1}[MPa]	Q_{R1}[MPa]	θ_{R2}[MPa]	Q_{R2}[MPa]	θ_{R3}[MPa]
20.0	4134	7.70	469	6.36	0.0
Q_{R3}[MPa]	f_0[−]	f_C[−]	f_F[−]	A_N[1/mm]	
0.0	0.0105	0.289	0.385	2.96	

The initial void volume fraction, f_0, was arbitrarily set to 0.001 with large range as there was no information to base an estimate upon. Void volume fraction at failure, f_F, was assumed equal to the critical damage for the polymer model, as these two represent a similar type of failure criterion. However, there are significant assumptions made in the transition from meso-scale to macro-scale such that these cannot be directly compared. Therefore, a wide range was given to this parameter. The critical void value fraction, f_C, was set equal to 75 % of f_F based on initial studies. The void nucleation parameter, A_N, was estimated such that a reasonable equivalent plastic separation would result in failure. Wide ranges were also given to this parameter due to the uncertainty in what could be considered reasonable. Unlike the previous material models, the optimization process was seen to converge towards an acceptable solution without additional runs for the GCZM.

Figure 5.16 shows the comparison between the target curves produced by the meso-scale benchmark tests and the predictions of the macro-scale benchmark tests using optimized parameters for the GCZM. The correlation is good in the peel dominated case, while the peak force is predicted with decent accuracy for the mixed mode and shear dominated

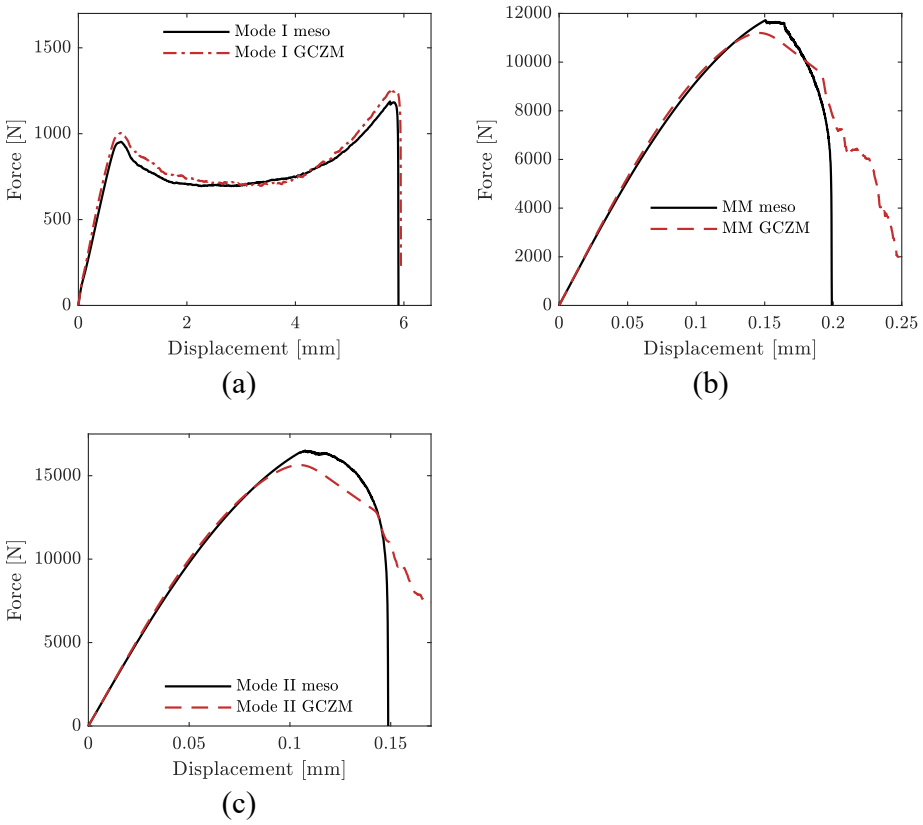

Figure 5.16.: Comparisons between meso-scale target curves and macro-scale predictions using GCZM. (a) Peel dominated case. (b) Mixed mode case. (c) Shear dominated case.

cases. However, the post-peak behaviour in the two latter cases is poorly predicted as a compromise between the peel and shear response had to be made. Overall, the performance is acceptable considering that only four parameters had to be optimized. The sensitivity to user input is much lower than for the MAT_240 model as the GCZM seems to converge towards acceptable solutions with large ranges for the different parameters.

Calibrated material parameters are shown in Table 5.3 and the corresponding traction separation law is shown in Figure 5.17.

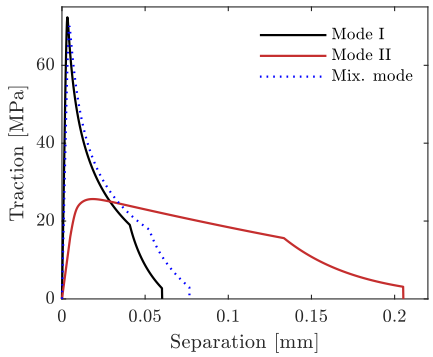

Figure 5.17.: Traction separation law for GCZM in mode I, mode II and mixed mode with a load angle of 45° according to Equation 5.10.

5.4.4. Macro-scale validation on bonded component test

Initial validation of the macro-scale models for simulating the adhesive layer is performed on the bonded component tests presented in Section 4.2.3. The numerical model applied in this section is the same as the model presented in Section 4.4.3 with the exception of the element formulation in the adhesive layer. Solid element formulation 19 [93], corresponding to cohesive zone elements without correction for shell thickness, is used for the adhesive layer in the following simulations.

Two deformation measures are introduced to analyse how the adhesive layer in the bonded component test is loaded. Figure 5.18 shows how the local element coordinate system is defined for the elements studied, where the directions correspond to the separation notations given in Equation 5.7. Further, for the given elements u_{t2} corresponds to mode II behaviour and u_{t1} corresponds to mode III behaviour. The mixed mode angle, α_{mma}, is defined according to:

$$\alpha_{mma} = \arctan\left(\frac{u_n}{\Delta_t}\right) \tag{5.51}$$

A mixed mode angle close to 0° corresponds to a shear dominated loading, while a value close to 90° corresponds to peel dominated loading. Further, negative values represent compression in the normal direction. A shear angle, α_{sha}, is introduced according to:

$$\alpha_{sha} = \arctan\left(\frac{u_{t2}}{\text{abs}(u_{t1})}\right) \tag{5.52}$$

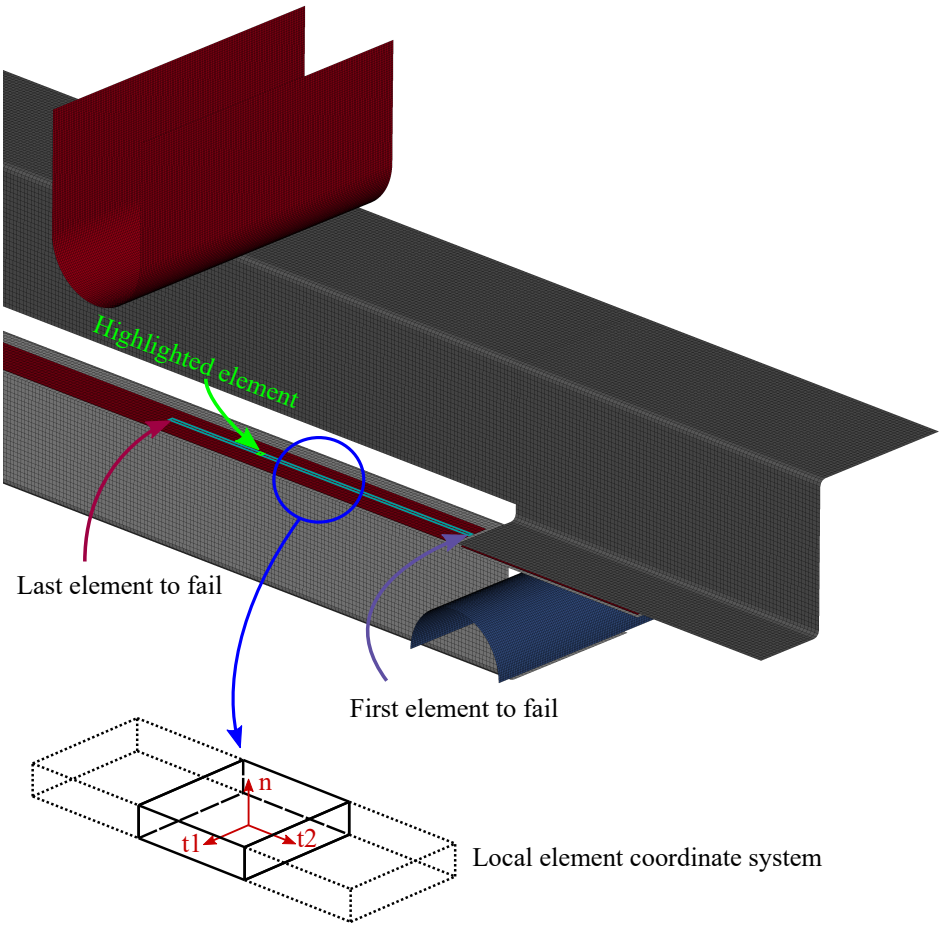

Figure 5.18.: Highlighted elements in the adhesive layer form the basis for the data presented in Figures 5.19c and 5.19d. The local coordinate system for the elements of the separation analysis is shown in the bottom figure.

A shear angle close to 0° corresponds to mode III dominated shear state, while a value close to 90° corresponds to mode II dominated shear state.

Figure 5.19a shows the separations for the element highlighted in green in Figure 5.18, while Figure 5.19b shows the corresponding deformation measures defined in Equations 5.51 and 5.52. A cut-off value at 3% of the maximum resultant separation is used to reduce the noise in these plots for the deformation measures. Figures 5.19c and 5.19d show the evolution of the mixed mode angle and shear angle for all elements failing along the centre line of the adhesive layer as highlighted in Figure 5.18. The trends for these plots

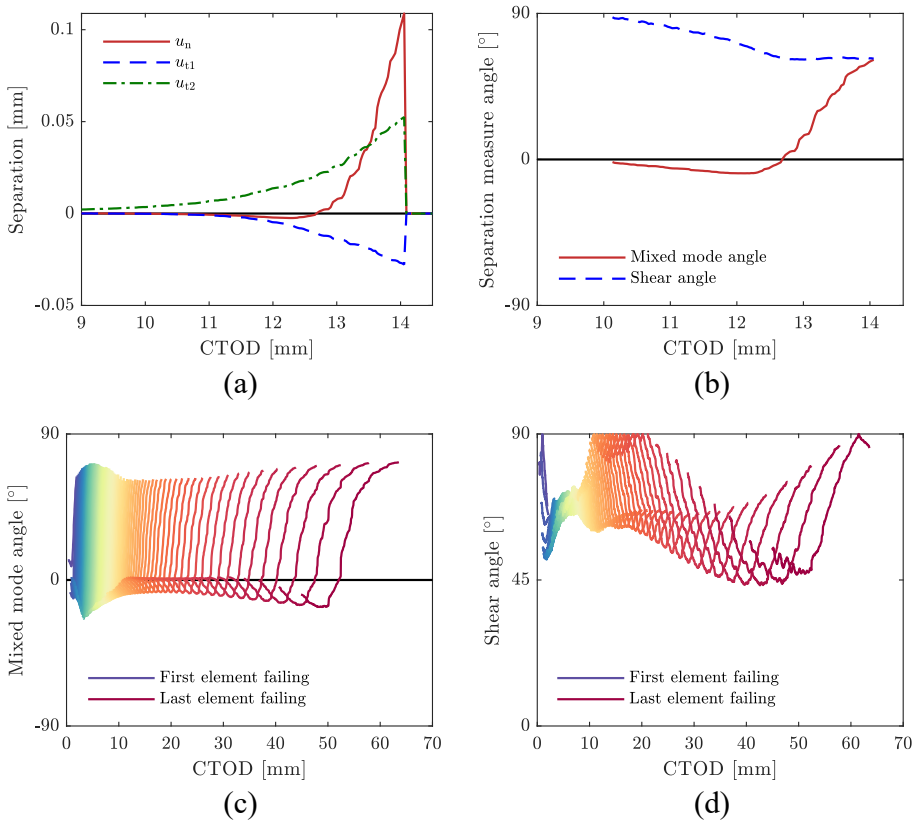

Figure 5.19.: Separation analysis of the failing adhesive elements of the bonded component test. (a) Example of separations for the element highlighted in green in Figure 5.18. (b) Mixed mode angle, α_{mma}, and shear angle, α_{sha}, for the example element in Figure 5.19a calculated using Equations 5.51 and 5.52 respectively. (c) Mixed mode angle, α_{mma}, for all elements shown in Figure 5.18. (d) Shear angle, α_{sha}, for all elements shown in Figure 5.18.

are comparable to the innermost and outermost elements in the adhesive layer. Based on Figure 5.19c, the adhesive layer seems to be subjected to a shear loading initially, then a combination of shear and compression and finally a peel dominated failure. The shear mode seems to be predominantly mode II for the bonded component tests according to Figure 5.19d.

It is evident that the bonded component test subjects the adhesive layer to a more complex loading mode than typical benchmark tests. Further, failure is peel dominated which tends to be the critical loading mode in most applications of bonded joints. Section 4.2.3

established that the behaviour of the adhesive was critical for the global response of the bonded component tests. Combining these observations, the bonded component test is seen to be very suitable as a validation test with regards to modelling of adhesives.

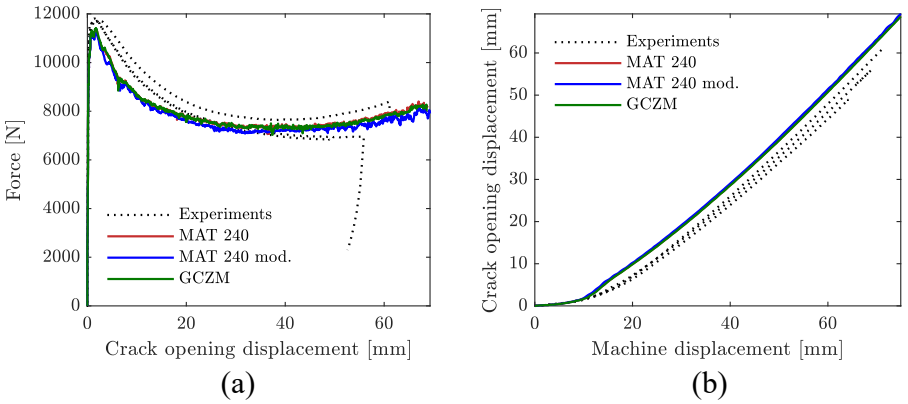

Figure 5.20.: Comparison between experimental results and simulation results using MAT_240, MAT_240 modified and GCZM for the bonded component tests. (a) Force vs. crack opening displacement. (b) Crack opening displacement vs. machine displacement.

Comparisons between the experimental results and the simulation results using the three models calibrated in Sections 5.4.1, 5.4.2 and 5.4.3 are shown in Figure 5.20. Overall, the force vs. crack opening displacement curves in Figure 5.20a shows that all three models perform well for this validation case. However, the peak force is underestimated and the crack propagates too fast initially as seen in Figure 5.20b. The underestimation in peak force is seen to be linked to the premature crack initiation present in the simulations.

All three adhesive models provide approximately the same results on the component level. This is expected as their predictions for the virtual benchmark tests are all acceptable. Therefore, the observed discrepancy on the component level is likely caused by the meso-scale virtual benchmark tests underestimating the response. This is consistent with the observations regarding the validation of the meso-scale adhesive modelling approach on the physical benchmark tests reported in Section 4.4.2. Improvements on the meso-scale modelling approach should enable accurate predictions at the macro-scale following the proposed method.

5.5. Discussion and concluding remarks

5.5.1. Discussion

Three different macro-scale material models were studied as a part of this chapter. Two of them are quite similar except for the mixed mode formulation, while the GCZM is significantly different. Despite the dissimilarities, all three models provide approximately the same accuracy on the component level. This indicates that the integrated properties of the models, such as the energy release rates, are more important with respect to the global behaviour of larger components.

Comparing MAT_240 with the modified version, there is a small increase of accuracy with respect to the virtual benchmark tests for the modified version. However, the increase in performance seems to be negligible for these adhesively bonded joints. Further, the increase in computational cost is very high as the four additional parameters complicates the optimization process. This is clearly shown in Section 5.4.2, where two additional runs of the optimization procedure were required when using previous data from the calibration of MAT_240. Therefore, it is reasonable to conclude that this modification is not recommended for the modelling of structural adhesives.

The difference between MAT_240 and the GCZM is much larger with respect to the traction-separation laws. However, the difference in performance on the virtual benchmark tests is probably not coupled to this difference in behaviour but instead the number of parameters used as variables in the calibration process. For the calibrations presented in Sections 5.4.1 and 5.4.3, only 4 parameters were used as variables for the calibration of GCZM compared to the 8 of MAT_240. A close-to-perfect fit would likely be possible to obtain by using all 16 parameters in Table 5.3 as variables. This would come at a high additional cost with limited benefit in terms of accuracy on the component level. Further, this would remove the key benefit of the GCZM in this framework, which is the computational cost and simplicity of the calibration process. Considering the results on the bonded component test, the GCZM seems to be particularly suitable for modelling of structural adhesives when applying the presented virtual calibration procedure.

Considering this as an initial exploration of the proposed method, the results are very good suggesting that the approach is viable. With the viability of the approach, significant cost saving measures and explorative studies are enabled. As long as the base materials are characterized for meso-scale modelling, any combination of them could be used to generate virtual test. These could then be used to calibrate macro-scale models within a relatively short timeframe and with a reasonable computational cost. If it is shown that the difference in configuration between each joint warrants a new calibration, this method has the potential to significantly reduce costs. Further, the flexibility of this approach could be used to calibrate more advanced models that accounts for adherent properties. This

could then be used to investigate and facilitate modelling of multi-material joints without extensive experimental campaigns.

5.5.2. Conclusions

Three different cohesive zone models are presented in this chapter including MAT_240, a modification of MAT_240 and a Gurson based cohesive zone model (GCZM). While MAT_240 represents a model used in the industry, the GCZM is a fundamentally different model based on recent literature. Further, a 3D version of GCZM is implemented as a part of this thesis.

A partial virtual-laboratory calibration procedure is presented, which uses a multi-scale approach to calibrate macro-scale material models based on meso-scale virtual benchmark tests. However, the material models used in the meso-scale simulations are based on physical material tests. Given that the meso-scale models are calibrated, the traction-separation law for any joint configuration of this type can be calibrated with a relatively low cost. The three previously mentioned models were calibrated using this approach and showed acceptable results on the bonded component test validation case. Despite the significant differences in the response on virtual benchmark tests, the three models gave almost identical results for the bonded component tests. These component tests subjected the adhesive layer to a more complex loading mode than the benchmark tests as well as failing in peel dominated loading. Considering the results of the validation simulations, this suggests that the applied calibration approach is viable.

The observed discrepancy between the validation simulations and the experimental results are caused by premature crack initiation and too fast crack propagation in the simulations. This issue seems to be caused by the underestimated response of the meso-scale simulations, which is consistent with the observation made in Chapter 4. Further studies regarding these issues are presented in Chapter 6.

Following the research strategy, this chapter uses the results from Chapter 4 to enable a multi-scale partial virtual laboratory calibration procedure. Further, the work presented in this chapter facilitates the analyses presented in Chapter 6, where the potential of the methodology is explored. Particularly, the virtual calibration approach allows for a numerical study regarding the influence of the adherent properties with respect to the adhesive performance. This follows the primary objective of this thesis which is to study multi-material joints.

6. Further studies regarding modelling of structural adhesives

6.1. Introduction

This chapter represents the culmination of the thesis, where the results of the previous chapters are used to address the overall objectives of this work as presented in Section 1.3. In particular, the numerical study on the influence of adherents on the material parameters of a macro-scale model for the SikaPower 498 adhesive, see section 6.3, directly addresses the issue of multi-material joining. A higher level validation of the calibration approach presented in Chapter 5 according to Section 4.1.2 is used to illustrate the potential of the approach. Additionally, this validation step gives an indication of the performance of the adhesive models in combination with self-piercing rivets (SPR), which represents a case relevant for industrial applications.

The initial validation of the macro-scale modelling approach presented in Section 5.4.4 suggests that the observed discrepancies are caused by problems with the meso-scale model used for calibration. These issues will be further studied in Section 6.2 by looking at alternatives for the meso-scale models. Additionally, the stress state in the critical integration points are analysed to get an improved understanding of the problem.

Section 6.3 presents the numerical study on the influence of the adherent properties when using the multi-scale calibration approach presented in Chapter 5. The elastic material parameters of the adherents are varied to represent the influence of the material, while the thicknesses of the adherents are varied to study the influence of the geometry. Although this numerical study is limited in terms of scope, it provides an indication of the importance of the multi-material aspect of a joint, as well as putting it in contrast to the influence of the geometry.

The hybrid benchmark tests presented in Section 4.2.2 along with two configurations of a hybrid component test subjected to 3-point bending are used for validation in Section 6.4.1. Finally, Section 6.5 contains a broader discussion and conclusions that lay the foundation for Chapter 7, which concludes this thesis.

6.2. Study of meso-scale influence

This section will present the additional studies performed in order to better understand the influence of the meso-scale models with regards to the multi-scale calibration approach. An outline and description of the studies will be presented first. Then, the results of the altered meso-scale model with 1 element through the thickness of the adhesive layer will be presented. Finally, the stress state of the critical integration points in the meso-scale models will be analysed and discussed.

6.2.1. Concept and study outline

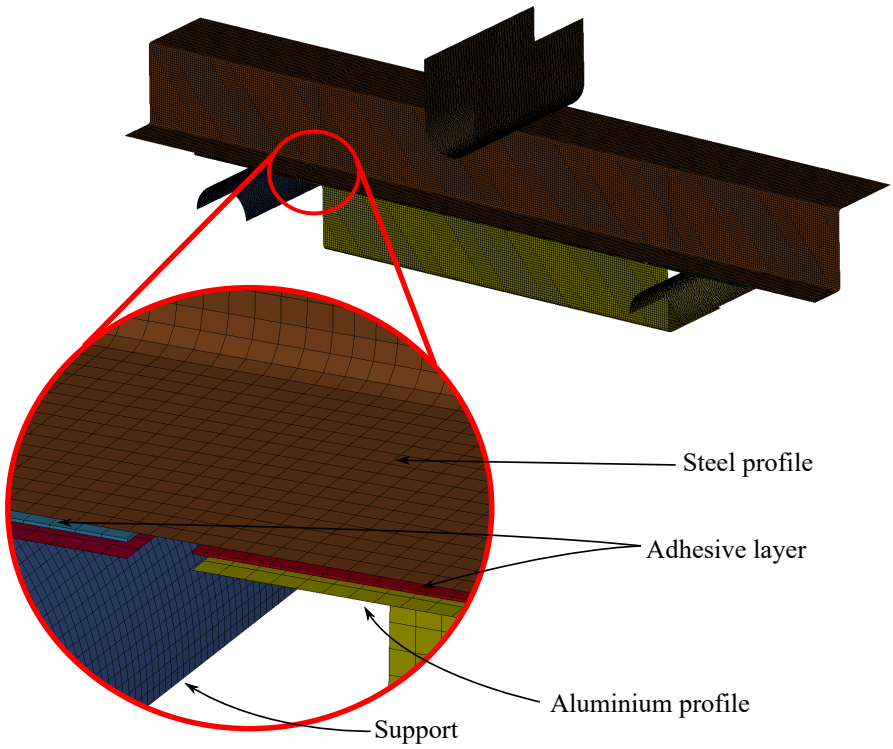

Figure 6.1.: Mesh of the bonded component tests used for validation.

A part of the validation of the meso-scale polymer model, presented in Section 4.4.3, is done on the bonded component tests shown in Figure 6.1. This validation case suggests that using 1 element through the thickness of the adhesive layer with the parameters calibrated

in Chapter 4 could provide good results for the meso-scale model. Based on these results, it would be of interest to apply this to the meso-scale models in the partial virtual calibration approach to investigate its influence on the previously observed issues.

The calibration process presented in Chapter 5 is repeated for MAT_240 and GCZM. However, only a single element through the thickness of the adhesive layer is used for the meso-scale models. These new calibrations are then validated on the bonded component tests to evaluate the performance of this method compared to the original approach. In addition to this altered calibration approach, the stress states in the critical integration points of the different virtual benchmark tests and the notched tension test (NTT) are investigated. By analysing the stress states in the different situations and comparing them to each other, a better understanding of the failure process is obtained. This could be used to explain the differences between the approaches and therefore facilitate further work on the method.

6.2.2. Results of 1 element through thickness basis

The meso-scale virtual benchmark tests are rerun with 1 element through the thickness of the adhesive layer to generate the target curves for the new calibrations of the MAT_240 and GCZM. Figure 6.2 shows the fit between the two calibrated models, MAT_240 and GCZM, and the meso-scale benchmark simulations using 1 element through the thickness of the adhesive layer. In addition, the curves of the meso-scale models with 3 elements through the thickness of the adhesive layer is plotted to highlight the influence of the this change on the response of the virtual benchmark tests.

The fit between the meso-scale target curves and the macro-scale predictions is seen to be decent for both calibrated models. Additionally, a significant increase in the response is seen for all 3 benchmark tests when going from 3 elements through the thickness of the adhesive layer to 1. This could in part be explained by the change of discretization, which reduces the localization of the damage such that the adhesive layer absorbs more energy. However, both the stress state and damage evolution are altered by this change as analysed further in Section 6.2.3.

Table 6.1.: Calibrated material parameters for MAT_240 using 1 element through thickness of the adhesive layer on the meso-scale models and the parameters from the original calibration.

MAT_240 parameters (1 element)							
E_{mod}[MPa]	G_{mod}[MPa]	$\sigma_{\text{n,y}}$[MPa]	τ_{y}[MPa]	$G_{1\text{C}}[\frac{\text{N}}{\text{mm}}]$	$G_{2\text{C}}[\frac{\text{N}}{\text{mm}}]$	$r_{\text{G1}}[-]$	$r_{\text{G2}}[-]$
6548	800	45.2	27.0	2.61	3.14	0.595	0.609
Original MAT_240 parameters							
E_{mod}[MPa]	G_{mod}[MPa]	$\sigma_{\text{n,y}}$[MPa]	τ_{y}[MPa]	$G_{1\text{C}}[\frac{\text{N}}{\text{mm}}]$	$G_{2\text{C}}[\frac{\text{N}}{\text{mm}}]$	$r_{\text{G1}}[-]$	$r_{\text{G2}}[-]$
4289	4230	22.9	25.3	1.48	2.64	0.510	0.482

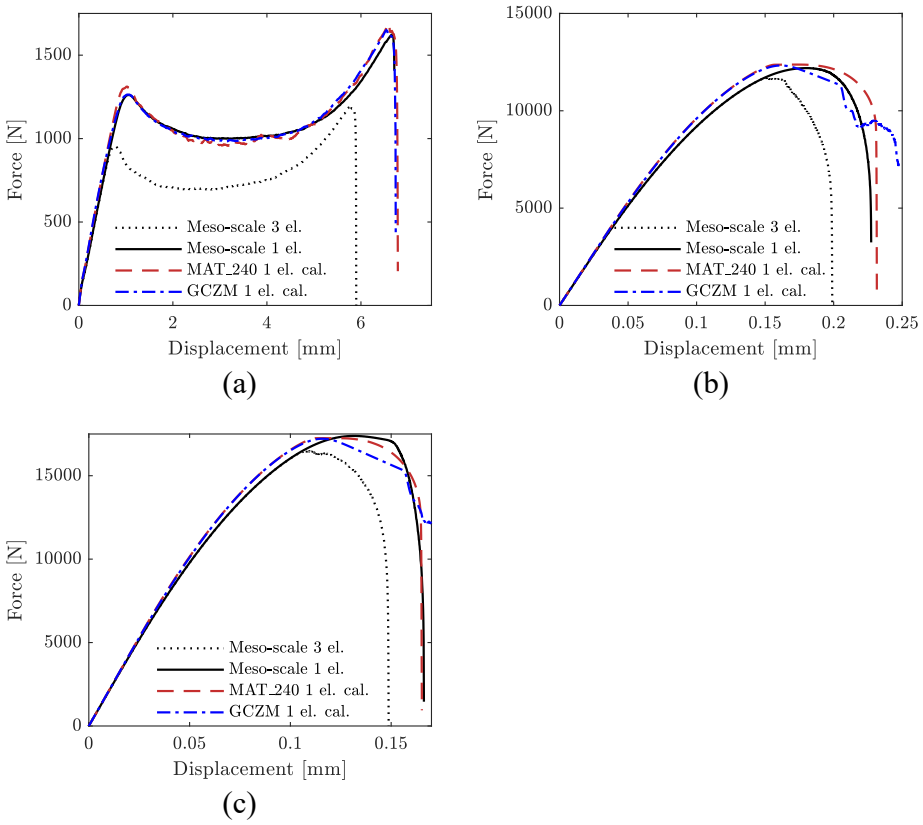

Figure 6.2.: Meso-scale target curves from models using 1 and 3 elements through thickness compared to macro-scale predictions using MAT_240 and GCZM. (a) Peel dominated case. (b) Mixed mode case. (c) Shear dominated case.

Table 6.1 shows the material parameters calibrated for the MAT_240 material model using target curves based on the 1 element through thickness meso-scale models. The key parameters for the MAT_240 model are the energy release rates in mode I and II, G_{1C} and G_{2C} respectively. A 76 % increase in the value of G_{1C} and a 19 % increase in the value of G_{2C} is seen when compared to the original material parameters reported in the second part of Table 6.1. This suggests that there is a much stronger effect of the change in discretization with respect to the peeling mode compared to the shear dominated mode.

Table 6.2 shows the material parameters calibrated for the GCZM fitted to the target curves based on the 1 element through thickness meso-scale models. The original material parameters are reported in the second part of Table 6.2. There are two key changes between the two calibrations, a significant reduction of the A_n parameter by 41 % and an increase of

Table 6.2.: Calibrated material parameters for GCZM using 1 element through thickness of the adhesive layer on the meso-scale models and the parameters from the original calibration.

GCZM parameters (1 element)					
E_{eff}[MPa]	G_{eff}[MPa]	q_1[−]	q_2[−]	q_3[−]	q_4[−]
6548	800	1.5	1.0	2.25	1.30
σ_{y}[MPa]	θ_{R1}[MPa]	Q_{R1}[MPa]	θ_{R2}[MPa]	Q_{R2}[MPa]	θ_{R3}[MPa]
20.0	4134	7.70	469	6.36	0.0
Q_{R3}[MPa]	f_0[−]	f_{C}[−]	f_{F}[−]	A_{N}[1/mm]	
0.0	0.0207	0.406	0.542	1.75	
Original GCZM parameters					
E_{eff}[MPa]	G_{eff}[MPa]	q_1[−]	q_2[−]	q_3[−]	q_4[−]
6548	800	1.5	1.0	2.25	1.53
σ_{y}[MPa]	θ_{R1}[MPa]	Q_{R1}[MPa]	θ_{R2}[MPa]	Q_{R2}[MPa]	θ_{R3}[MPa]
20.0	4134	7.70	469	6.36	0.0
Q_{R3}[MPa]	f_0[−]	f_{C}[−]	f_{F}[−]	A_{N}[1/mm]	
0.0	0.0105	0.289	0.385	2.96	

the void volume fraction at failure by 41 %. In contrast to MAT_240, these changes does not have a preference for the peel dominated case, rather there is a weak preference for the shear response of the model. This highlights a point of inflexibility with the GCZM when using this calibration approach with only 4 parameters used as variables.

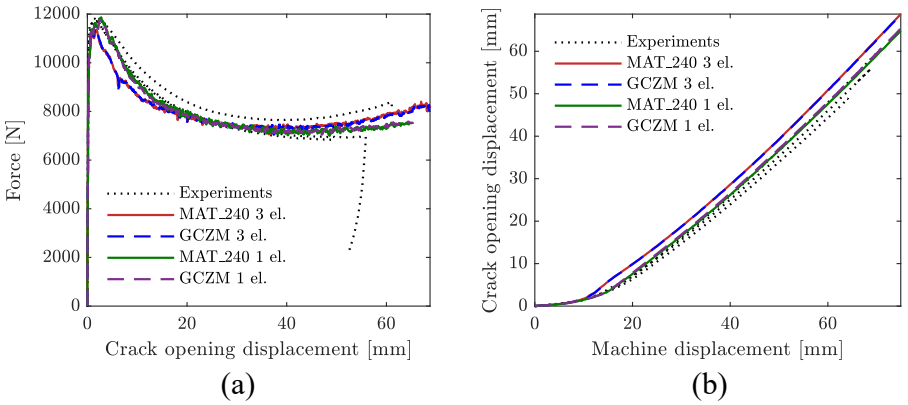

Figure 6.3.: Comparison between experimental results and simulation results using MAT_240 and GCZM calibrated based on meso-scale models using 1 element through thickness for the bonded component tests. (a) Force vs. crack opening displacement. (b) Crack opening displacement vs. machine displacement.

The new calibrations are validated against the bonded component tests described in Section

4.2.3. Figure 6.3 shows the validation results of the two new calibrations presented in this section compared to the ones based on 3 elements through the thickness in the meso-scale models. The average peak force for the experiments is 11.75 kN, while the peak force of the new calibrations is approximately 11.8 kN compared to 11.3 kN for the old calibrations. As previously, there are no significant difference between MAT_240 and GCZM in terms of the response on a component level.

A significant improvement of the results is seen for the new calibrations compared to the ones based on the meso-scale models using 3 elements through the thickness of the adhesive layer. Both the peak force and crack propagation are improved with the new calibrations. The response of the new calibrations are comparable to the validation case reported in Section 4.4.3, where the meso-scale polymer model was used in the adhesive layer of the bonded component test. However, the cohesive zone models have a larger critical time-step, which significantly reduces the computational cost.

6.2.3. Stress analysis and discussion

In order to obtain a better understanding of the failure process in the meso-scale models, stress analyses are performed on the virtual benchmark tests and the notched tension test (NTT). Specifically, the first integration point to fail in each of these models is studied as they are critical for crack initiation in the models. These analyses investigate the stress triaxiality ratio and the Lode parameter as they are commonly considered to influence the plastic strain to failure in ductile materials. The NTT was used to calibrate the critical damage of the meso-scale polymer model. Therefore, it represents the baseline model which is directly linked to the physical tests.

Figure 6.4 shows the stress triaxiality ratio and Lode parameter evolution with plastic strain in the critical integration point for the different meso-scale models. The stress triaxiality ratio, σ^*, is defined according to:

$$\sigma^* = \frac{\sigma_{\mathrm{H}}}{\sigma_{\mathrm{VM}}} \tag{6.1}$$

where σ_{H} is the hydrostatic stress and σ_{VM} is the von Mises stress. Further, the Lode parameter, L, is given by:

$$L = \frac{2\sigma_2 - \sigma_1 - \sigma_3}{\sigma_1 - \sigma_3} \tag{6.2}$$

where $\sigma_{1/2/3}$ are the principal stresses. The virtual benchmark tests with both 1 and 3

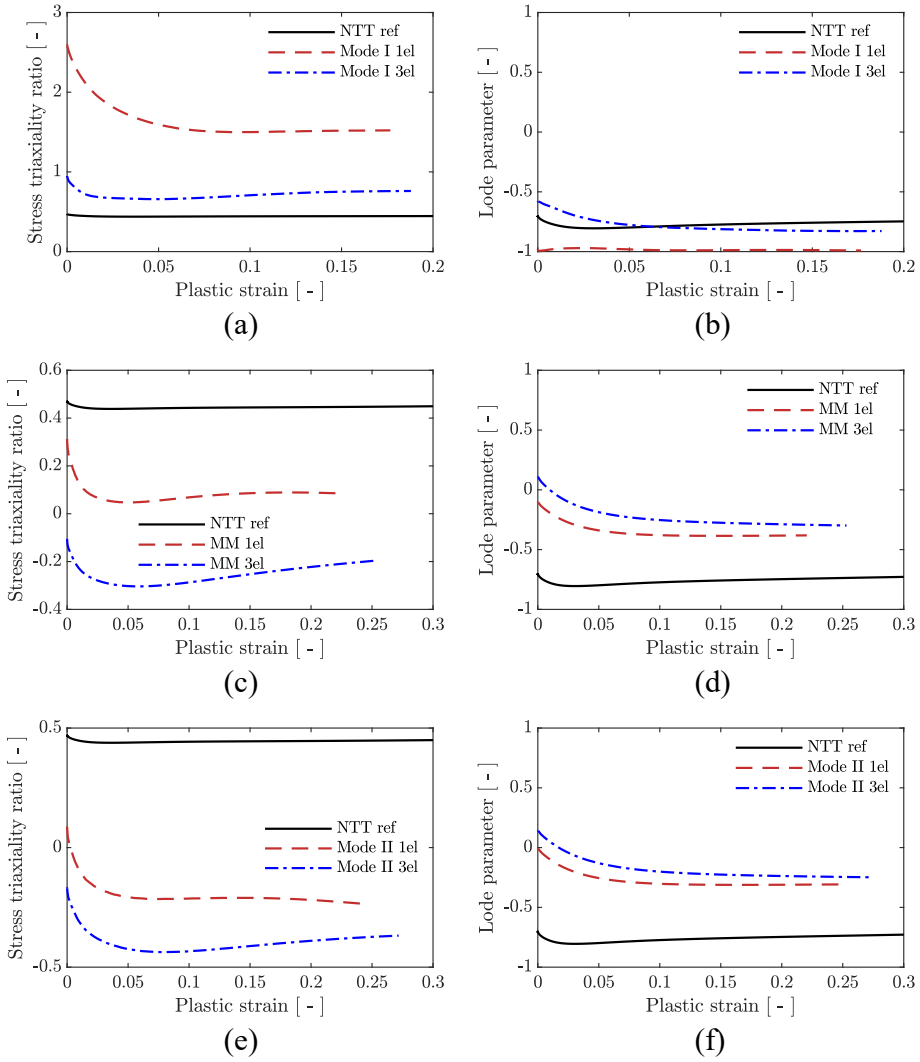

Figure 6.4.: Evolution of stress state in first integration point to fail for the notched tension test (NTT) compared to the critical integration point in the virtual benchmark tests using 1 and 3 elements through thickness of the adhesive layer. (a) Stress triaxiality ratio for the peel case. (b) Lode parameter for the peel case. (c) Stress triaxiality ratio for the mixed mode case. (d) Lode parameter for the mixed mode case. (e) Stress triaxiality ratio for the shear case. (f) Lode parameter for the shear case.

elements through the thickness of the adhesive layer are included to highlight the differences between the two. It is evident from Figure 6.4 that only the peel dominated virtual

benchmark tests with 3 elements through the thickness of the adhesive layer reproduce a comparable stress state to the NTT. All other configurations have a significantly different stress state from the reference NTT.

A comparison between the two types of virtual benchmark tests suggests that any increase of accuracy is not related to the change in stress state. Particularly, the models with 1 element through the thickness of the adhesive layer have a much higher stress triaxiality ratio in the peel dominated case. This leads to an earlier local failure, which emphasizes that the increased strength of these models is predominantly caused by less localization due to the change in discretization.

The virtual benchmark tests with 3 elements through the thickness of the adhesive layer were originally chosen as baseline as they have the same spatial discretization as the NTT. However, there are much stronger gradients in the stress and strain fields through the thickness of an adhesive layer compared to a notched tension test. As a result, the discretization with respect to the gradients is significantly different between the baseline case and the NTT case used for calibration of the damage parameter. This could be one of the reasons why the performance in peeling is poorly predicted for the baseline case despite having a similar stress state and spatial discretization.

Another problem that is not properly addressed with these studies is the potential mismatch between the edge geometry of physical tests and virtual tests. Failure in an adhesively bonded joint is typically initiated at the edge of the adhesive layer. These edges are perfectly straight edges in the virtual benchmark tests used in this study. In contrast, the edges of the adhesive layer in physical benchmark tests and bonded component tests are prone to significant imperfections. Therefore, the importance of the issues related to the flexibility and accuracy of the failure modelling approach might be minor in contrast to the geometric problems. This would suggest that using a simple modelling approach with an adjustment, such as using 1 element through the thickness of the adhesive layer, is preferred over more advanced methods.

6.3. Influence of adherents on macro-scale adhesive model properties

This section will present the numerical studies performed to study the influence of the adherent properties on the calibrated macro-scale material parameters for the adhesive layer. First, an outline of the study will be presented, then the results of the studies are shown. Finally, there will be a short discussion regarding the results.

6.3.1. Outline of adherent influence study

The idea behind this study is the use the flexibility of the partial virtual calibration approach presented in Chapter 5 to calibrate a series of MAT_240 material cards for different adherent configurations. Thus, the influence of the difference between these configurations can be studied. MAT_240 was chosen as the macro-scale material model for this study as there is a clear distinction between mode I and II with regards to the material parameters. Therefore, it is possible to determine if the influence of the adherents is stronger for one of the deformation modes. Further, both 1 and 3 elements through the thickness of the adhesive layer are studied to evaluate the importance of the discretization with respect to the influence of the adherents. For simplicity, the steel and aluminium sheets of the experiments reported in Section 4.2 are used as the reference configuration for the adherents. The other configurations are then based on this reference configuration.

Table 6.3.: List of adherent configurations for the adherent influence study, including elastic stiffness of both adherents and their thickness.

Adherent configurations for influence study.				
Name	$E_{\text{adh.1}}$ [GPa]	$E_{\text{adh.2}}$ [GPa]	$t_{\text{adh.1}}$ [mm]	$t_{\text{adh.2}}$ [mm]
mm0	210	70	1.135	2.45
mm1	70	70	2.45	2.45
mm2	70	210	2.45	2.45
mm3	70	70	1.637	2.45
mm4	70	70	1.637	1.637

The different adherent configurations are listed in Table 6.3. Each of the different configurations are intended to address specific characteristics of the adherents in order to identify the influence of these characteristics. The baseline multi-material joint used for previous calibrations is represented by the mm0 configuration. A case of similar adherents with a large thickness is represented by the mm1 configuration, while the corresponding configuration with thin adherents is represented by the mm4 configuration. The mm2 configuration is similar to the mm1 configuration, but with different elastic properties for one of the adherents to create a multi-material joint. Finally, the mm3 configuration is exactly equal to the mm0 configuration in terms of the bending stiffness of the different adherents, but with similar material properties for both adherents. In summary, these configurations should give an indication regarding the importance of the adherent materials, the difference in bending stiffness between the adherents and the total stiffness of the adherents.

6.3.2. Results of adherent influence study

The energy release rates in mode I and II, G_{1C} and G_{2C} respectively, are considered the key parameters based on previous observations. These will be used to quantify the influence

of the different configurations. One of the goals is to consider the influence of similar adherents compared to dissimilar adherents. A good indicator for the dissimilarity of the adherents is the ratio of bending stiffness between the two adherents, R_{bend}, which is calculated according to:

$$R_{\text{bend}} = \frac{E_{\text{adh.2}} \cdot t_{\text{adh.2}}^3}{E_{\text{adh.1}} \cdot t_{\text{adh.1}}^3} \tag{6.3}$$

where $E_{\text{adh.2}}$ and $t_{\text{adh.2}}$ are the elastic modulus and thickness of the stiffer of the two adherents, while $E_{\text{adh.1}}$ and $t_{\text{adh.1}}$ represent the same for the other adherent.

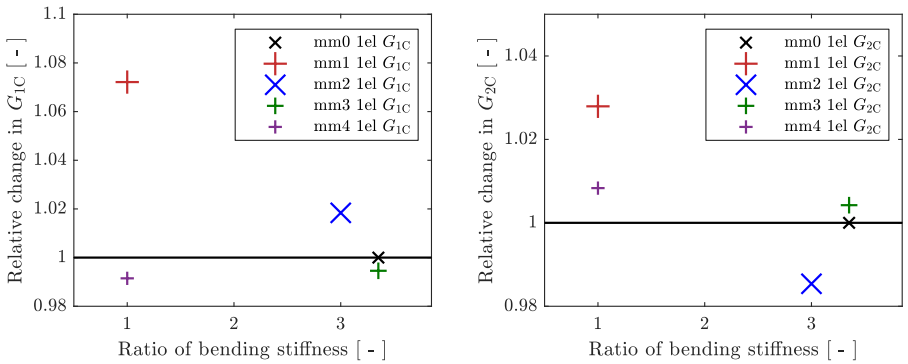

Figure 6.5.: Relative change in energy release rates of the 5 different configurations listed in Table 6.3 plotted against the ratio of bending stiffness between the two adherents in each configuration. The meso-scale models used for the calibrations have 1 element through the thickness of the adhesive layer. (a) Relative change of G_{1C}. (b) Relative change of G_{2C}.

Figures 6.5a and 6.5b show the relative change in G_{1C} and G_{2C} with respect to the reference configuration mm0 where the meso-scale models used 1 element through the thickness of the adhesive layer. The points marked with a cross, '×', represent configurations with different elastic modulus for the two adherents, while the points marked with a plus sign, '+', have similar elastic properties. Further, the size of each of the markers is scaled with the square root of the sum of the bending stiffness of both adherents. The order of the configurations in terms of relative size of their markers is mm4, mm0 which is equal to mm3, mm1 and mm2, where mm2 has a 6.7 times higher total bending stiffness than mm4. Maximum relative difference from the baseline model for G_{1C} is 7.2 % and only 2.8 % for G_{2C}. This suggests that the adherent properties influence the peel mode significantly more than the shear mode.

Figure 6.6 is the same figure as Figure 6.5, but it shows the data of the calibrations based

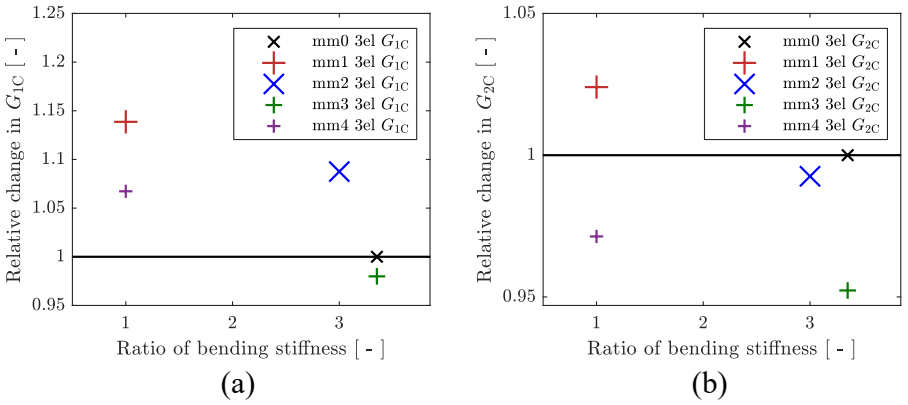

Figure 6.6.: Relative change in energy release rates of the 5 different configurations listed in Table 6.3 plotted against the ratio of bending stiffness between the two adherents in each configuration. The meso-scale models used for the calibrations have 3 elements through the thickness of the adhesive layer. (a) Relative change of G_{1C}. (b) Relative change of G_{2C}.

on the meso-scale models with 3 elements through the thickness of the adhesive layer. The maximum differences between the baseline configurations and the alternatives are 13.9 % for G_{1C} and 4.8 % for G_{2C} for these calibrations. It is evident that the discretization of the meso-scale models plays a significant role regarding the sensitivity of the calibrations with respect to the adherent properties.

The accuracy of the calibration process introduces some uncertainty into this study. This is caused by the fact that there are many combinations of parameters that can give comparable values of the optimization function. While the energy release rates are much less sensitive to this phenomenon than the other parameters, there is still a noticeable effect. Additionally, there are oscillations in the macro-scale peel dominated virtual benchmark tests during propagation of the crack in the adhesive layer. These oscillations further reduce the accuracy of the calibration process with an emphasis on mode I parameters. As a countermeasure, an effort was made to ensure that the different calibrations had a similar type of fit to the meso-scale target curves. The variation in the calibrated values of the energy release rates has not been quantitatively evaluated, but it is reasonable to assume a variation of a few percent in the presented results.

Overall, the influence of the adherents on the calibrated material parameters is small. Considering the inaccuracy of the calibration method, the influence on the adhesive properties related mode II behaviour seems to be negligible. The mm1 configuration is the only significant outlier for the study based on the calibrations using 1 element through the thickness of the adhesive layer. With a finer discretization in the meso-scale models, the mm1 and mm2 configurations represent a substantial variation from the baseline mm0 configuration.

Based on these observations, there is a weak trend indicating that the total stiffness of the adherents leads to higher values of the energy release rate for mode I. Further, a low ratio between the bending stiffness of the adherents seems to positively influence the value of G_{1C}.

A comparison between the energy release rate in mode I for the mm0 and mm3 configurations shows that they are close to identical. These two configurations are identical in terms of the bending stiffness, but mm0 has dissimilar materials between the adherents and mm3 has similar material properties in the adherents. This indicates that the influence of the material of the adherents is of less importance compared to the overall bending properties for the calibration of the macro-scale adhesive properties in mode I.

6.3.3. Discussion regarding the influence of adherents

An explanation to why the configurations with overall higher bending stiffness leads to a higher calibrated energy release rate in mode I is that the load is distributed more evenly. This reduces the localization effect in the adhesive layer such that more energy would be absorbed in the surrounding integration points before the critical one fails. Further, dissimilar bending stiffness of the adherents introduces rotations in the joint due to a lack of symmetry. These rotations could potentially alter the deformation field leading to a stronger localization effect and therefore less energy absorption in the adhesive layer. The influence of the meso-scale discretization is caused by the increased ability of the models to reproduce the gradients through the adhesive layer when refining the mesh. Therefore, any change in the gradients through the adhesive layer as an effect of different adherent configurations is more accurately captured with a finer mesh.

Figure 6.7 shows the response of the bonded component test validation case when using the different calibrations based on the study presented in Figure 6.6. All 5 calibrations have a similar response with the peak force varying between 11407 N and 11492 N. Given the domain of adherent configurations studied in this study, the influence on the component level is negligible in this case. A benefit of this observation is that there seems to be some margin in terms of the accuracy of the calibration procedure for the adhesives. This increases the confidence in a partial virtual laboratory calibrations approach.

It should still be noted that the maximum increase of the G_{1C} with 14 % could be significant in other cases. This change in G_{1C} could potentially initiate different deformation modes on a larger scale in more complex systems and therefore have a significant impact on the overall performance. Further, a stronger influence might be observed when using adherents that are much more dissimilar than studied in this study, such as the joints presented by Lubowiecka et al. [57].

Finally, these results have some potential implications for calibration of these macro-scale

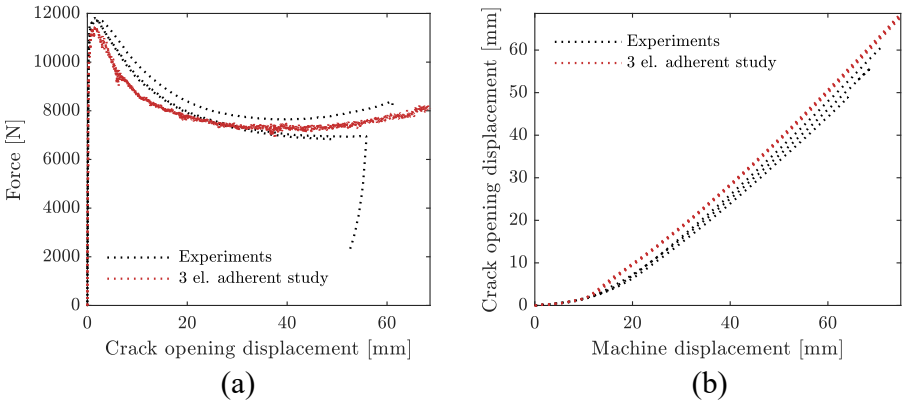

Figure 6.7.: Comparison between experimental results and simulation results using calibrations of MAT_240 based on the 5 configurations listed in Table 6.3 for the bonded component tests. These are the calibrations based on meso-scale models using 3 elements through the thickness of the adhesive layer. (a) Force vs. crack opening displacement. (b) Crack opening displacement vs. machine displacement.

material models using physical tests. An example would be a double cantilevered beam test, which is standard fracture mechanics test used to calibrate energy release rate in mode I, that typically has very stiff adherents. This could lead to non-conservative results when applying the calibrated material parameters to a real application with flexible adherents.

6.4. Further validation of proposed calibration procedure

This section will present validation simulations performed on hybrid benchmark tests and hybrid component tests using a macro-scale adhesive model calibrated with the partial virtual laboratory approach. An outline of the validation simulations will be presented first, including some considerations regarding modelling of self-piercing rivets and adhesive bonding together. Then, the results will be presented in addition to a brief discussion regarding the results.

6.4.1. Outline of hybrid test simulations

Adhesive bonding is typically combined with mechanical fasteners, such as self-piercing rivets (SPR), in an industrial context. Therefore, validation of the proposed method for calibration of the macro-scale adhesive parameters in a hybrid joint configuration is of high

relevance. Further, the inclusion of mechanical fasteners into the validation process adds an additional layer of complexity, thus representing the next step in the validation strategy following Section 4.1.2. This section will present simulation results validated against hybrid benchmark tests and hybrid component tests performed by Reil [120]. These simulations were in part performed by Morin et al. [126] using material cards for the adhesive layer generated as a part of this thesis.

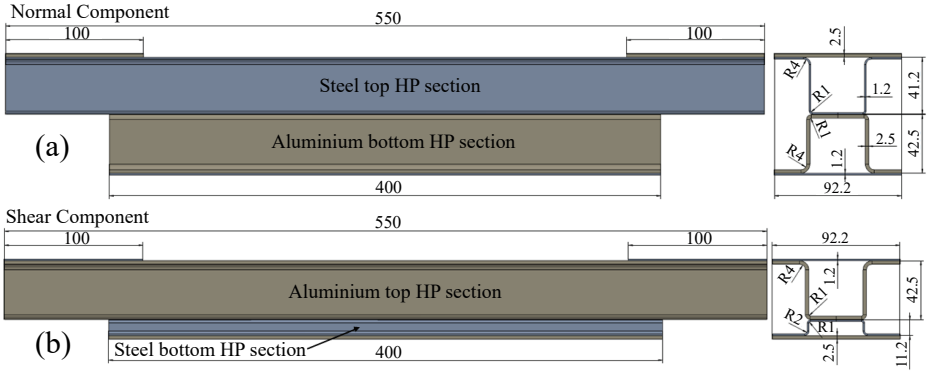

Figure 6.8.: Geometry of the two configurations of the hybrid component tests which are tested in 3-point bending [120]. (a) Normal component with peel dominated failure. (b) Shear component with shear dominated failure.

The hybrid benchmark tests used for this part of the validation process are presented previously in Section 4.2.2. Figure 6.8 shows the geometry of the two hybrid component test configurations. Both hybrid components are loaded in 3-point bending with a 15 mm offset for the impactor to ensure consistent crack initiation on one side of the components. The hybrid normal component test shown in Figure 6.8a is designed in order to induce a peel dominated loading mode for the adhesive layer and SPR joining the two parts of the component. Figure 6.8b shows the shear configuration of the hybrid component tests, which is designed to induce a shear dominated loading on the joint. Detailed descriptions of these experiments are presented by Reil [120].

Table 6.4.: Calibrated material parameters for MAT_240 using 1 element through the thickness of the adhesive layer on the meso-scale models. Specifically generated for the configurations in these hybrid joint tests.

MAT_240 parameters (Hybrid)							
E_{mod}[MPa]	G_{mod}[MPa]	$\sigma_{\mathrm{n,y}}$[MPa]	τ_{y}[MPa]	$G_{1\mathrm{C}}[\frac{\mathrm{N}}{\mathrm{mm}}]$	$G_{2\mathrm{C}}[\frac{\mathrm{N}}{\mathrm{mm}}]$	$r_{\mathrm{G1}}[-]$	$r_{\mathrm{G2}}[-]$
6548	800	43.6	27.1	3.12	3.74	0.607	0.577

All simulations presented in this section were run with the LS-DYNA solver [123]. The steel and aluminium sheet material are the same as used for the bonded component tests presented

in Section 4.2.3. These were modelled using calibrations of the MAT_258 [72] mentioned in Section 4.4.3. The SPR are modelled using the keyword CONSTRAINED_SPR2 ([53],[93],[127]). This model was calibrated based 3 different configurations of cross tests with a single SPR connecting the two sheets. MAT_240 [69] is used to model the adhesive layer which was calibrated as part of this thesis using the method presented in Chapter 5 with 1 element through the thickness of the adhesive layer. An additional calibration was made for these validation simulations to adjust for the nominal thickness of the adhesive layer being 0.3 mm. Calibrated material parameters for MAT_240 used in this section are presented in Table 6.4.

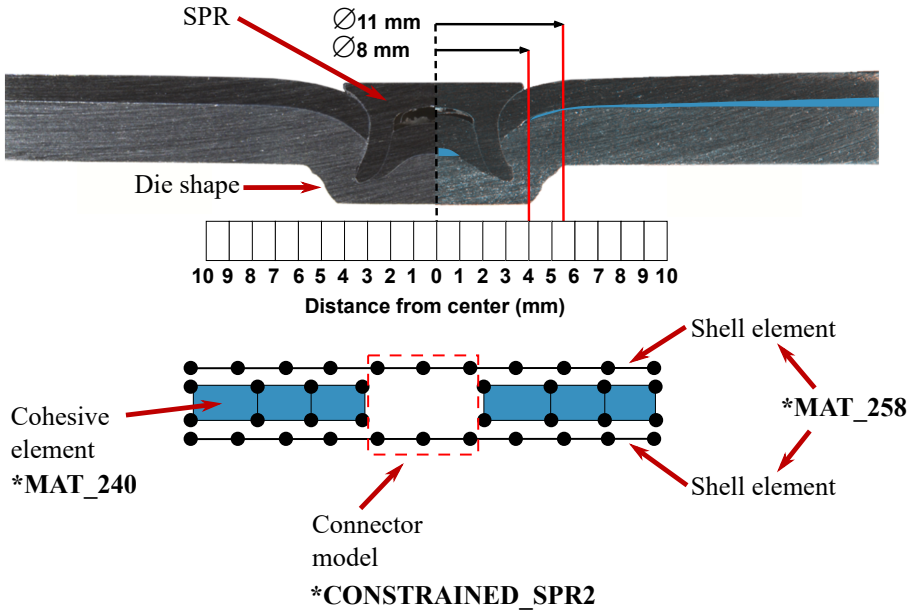

Figure 6.9.: Cross section of hybrid joint with adhesive bonding and a self-piercing rivet (SPR) showing key dimensions. The corresponding schematic of the macro-scale numerical implementation is shown in the bottom part of the figure [126].

A hybrid joint is made by first applying the adhesive and then the SPR. The application of the SPR squeezes some of the adhesive out of that region as shown in Figure 6.9. Therefore, the contribution of the adhesive in the region influenced by the SPR process is small [120]. In terms of modelling this on a macroscopic scale, the simplest approach is not to adjust the adhesive layer in the numerical model to account for this effect. Another approach is to remove the adhesive elements within the diameter of the rivet itself as shown in the bottom part of Figure 6.9. A more conservative approach is to assume that most of the adhesive is squeezed out of the area within the radius of the die used in the SPR process. These three approaches are used for both of the hybrid benchmark test simulations. However, the hybrid component test simulations have the adhesive elements removed within the 4 mm

radius of the rivet.

Figure 6.10.: Macro-scale numerical model of the hybrid single lap joint (SLJ) [126].

Figure 6.10 shows the numerical model and applied loading of the hybrid single lap joint tests. A general mesh size of 2 mm is used for the shell elements and as a reference for the in-plane mesh size of the adhesive layer. The in-plane mesh size is varying between 1 mm and 2 mm around the SPR for the two configurations influenced by the SPR.

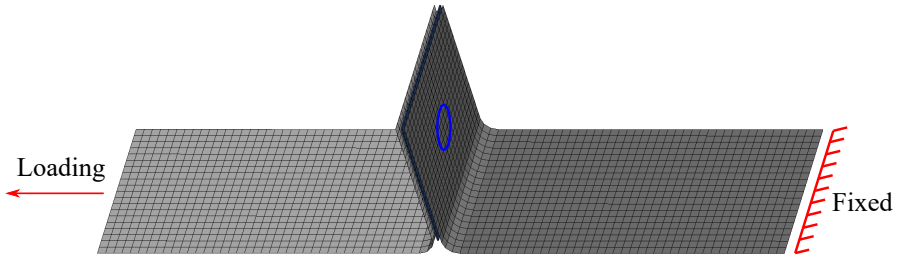

Figure 6.11.: Macro-scale numerical model of the hybrid peel test [126].

Figure 6.11 shows the numerical model and applied load of the hybrid peel tests. Similar to the hybrid SLJ simulations, the general mesh size is 2 mm with some variation in the adhesive layer due to the SPR.

Figure 6.12 shows the numerical model of the hybrid normal component test. A general mesh size of 2 mm is used for the shell elements, while the adhesive layer is adjusted for the size of the rivet and therefore some variations in the mesh size. In total, there are 10 rivets joining the two components with an equal distance of 40 mm between each.

Figure 6.13 shows the numerical model of the hybrid shear component test. In terms of the mesh, the two types of hybrid component tests are identical.

6.4.2. Results of hybrid validation tests

The results of the validation simulations on the hybrid tests will be compared to the experimental data and the corresponding simulations performed by Reil [120]. Particularly,

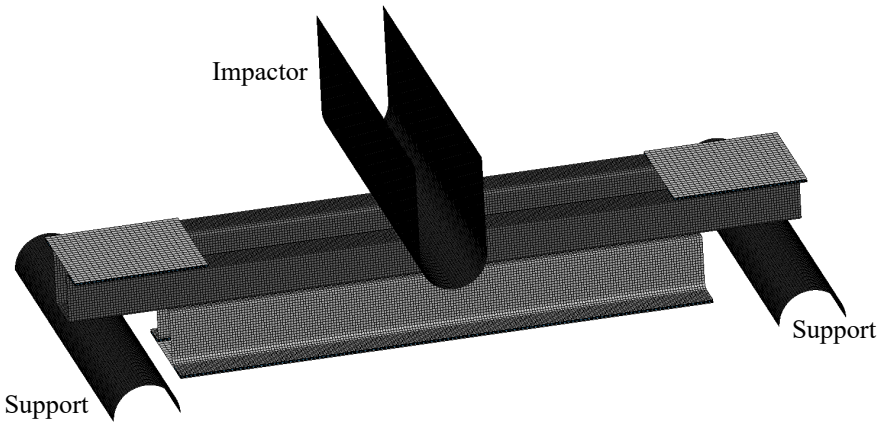

Figure 6.12.: Macro-scale numerical model of the hybrid normal component test [126].

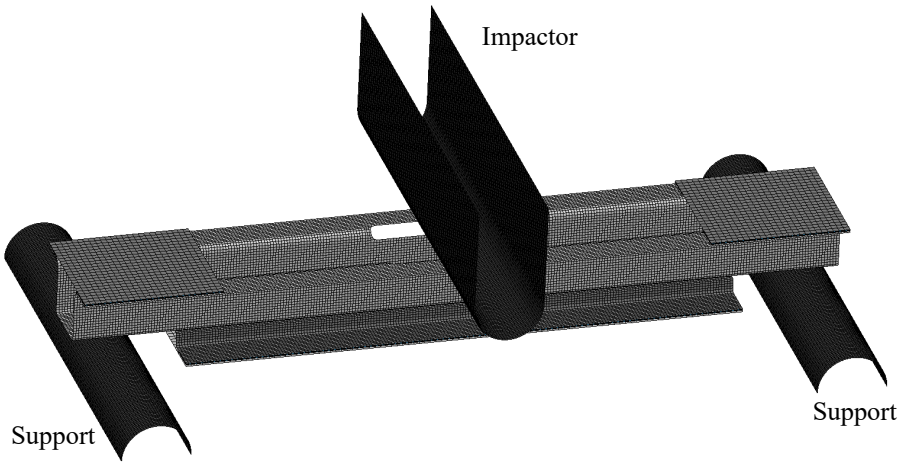

Figure 6.13.: Macro-scale numerical model of the hybrid shear component test [126].

the comparison to these simulations are of interest as they used a significantly different modelling approach for the adhesive layer. A triangular traction-separation law, which was calibrated from physical experiments, was used to model the adhesive for the simulations performed by Reil [120]. Therefore, this comparison gives insight into the difference in performance between the partial virtual calibration approach and the traditional calibration approach using physical experiments. It should be noted that Reil [120] used a different solver, Abaqus [112], as well as other minor differences in the numerical model which could impact the results.

Figure 6.14 shows a comparison between the experimental data and the three simulations

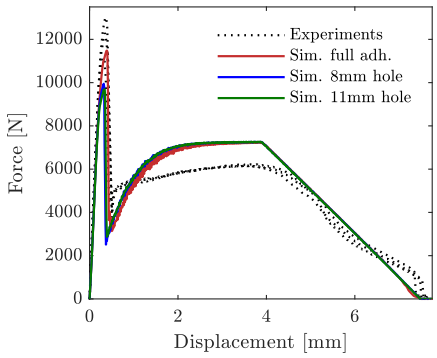

Figure 6.14.: Comparison between experimental results and simulation results for the hybrid SLJ test. Simulations were performed with 3 different configurations for the region of the adhesive layer influenced by the SPR.

with different approaches for the discretization of the adhesive layer for the SLJ test. The response of the SLJ is dominated by the performance of the adhesive until the first significant drop in force, which is caused by failure of the adhesive. Inspecting this domain of the response, the average peak force of the experiments is 12.1 kN while the simulations have a peak force of 9.7 kN, 9.9 kN and 11.5 kN for the three different configurations.

The simulation without adjustments of the adhesive layer to account for the SPR has a good prediction of the peak force, but it is non-conservative. Results of the two more realistic configurations are seen to underestimate the response in line with what was previously seen for the meso-scale models. For comparison, the peak force of the simulation performed by Reil [120] is 10.0 kN, which is similar to the performance of the virtually calibrated adhesive model.

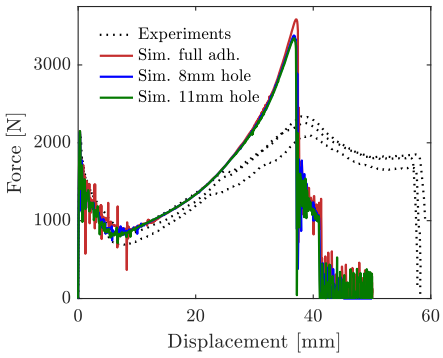

Figure 6.15.: Comparison between experimental results and simulation results for the hybrid peel test. Simulations were performed with 3 different configurations for the region of the adhesive layer influenced by the SPR.

Figure 6.15 shows a comparison between the experimental data and the three simulations with different approaches for the discretization of the adhesive layer for the peel test. Similar to the SLJ test, the initial peak is dominated by the behaviour of the adhesive. The average initial peak force of the experiments is 1.95 kN, while the three simulations gives the same initial peak force of 2.15 kN. There is a significant discrepancy between the experiments and the simulations at larger displacement. This is caused by the failure mode of the rivet which is not possible to model with a macro-scale model. The initial peak force reported by Reil [120] is 1.8 kN, which is slightly better than the prediction using the virtual calibration approach. However, there is significant scatter in the experimental results for these tests with respect to the initial peak response, such that both predictions are within the scatter of the experiments.

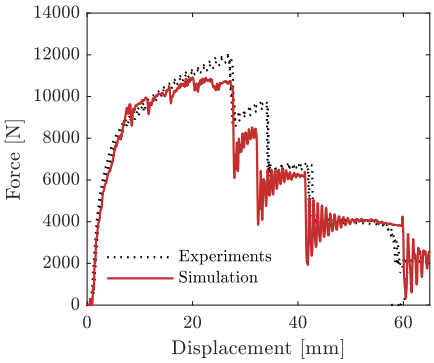

Figure 6.16.: Comparison between experimental results and simulation results for the hybrid normal component test.

Figure 6.16 shows the experimental results compared to the corresponding simulation for the hybrid normal component. Overall, the performance of the numerical model is very good for this validation case considering that the adhesive properties are calibrated using the partial virtual calibration approach. The adhesive seems to propagate a bit too fast before failure of the first rivet at a displacement of 27.6 mm, which is consistent with previous observations. Reil [120] presented comparable results to what is shown in Figure 6.16, but with a better fit before failure of the first rivet. The results of the of the hybrid peel tests suggests that the peeling response of the adhesive model presented in this work is stronger than the one used by Reil [120]. Therefore, the discrepancy observed in Figure 6.16 could potentially be caused by issues not related to the modelling of the adhesive. There are several effects that could cause the observed discrepancy, such as an underestimation of the stiffness of the rivets or poor predictions of the buckling patterns. This is the result of the overall complexity of the component and the potential interactions between the different phenomena governing the response.

Figure 6.17 shows the experimental results compared to the corresponding simulation for the hybrid shear component. The simulated response is significantly underestimated for the

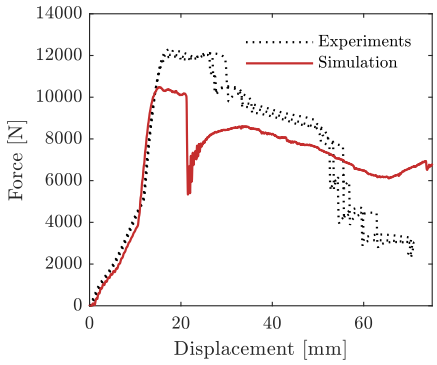

Figure 6.17.: Comparison between experimental results and simulation results for the hybrid shear component test.

hybrid shear component, which is consistent with previous observations on the hybrid SLJ in Figure 6.14. However, the adhesive layer is seen to fail from one edge and all the way to underneath the impactor almost instantaneously at a displacement of 21.2 mm. This would suggest that the adhesive layer is not accurately loaded as the crack should propagate more gradually as a consequence of the global loading mode. The results presented by Reil [120] are better than what is presented in Figure 6.17, with slower crack propagation and a much better prediction of the failure of the rivets. Similar to the hybrid normal component, the results of the validation on the hybrid SLJ suggest that there should not be such a difference between the two approaches. Therefore, the observed discrepancies might not be entirely caused by the modelling of the adhesive.

Overall, the performance of the adhesive model calibrated using the method presented in this work is comparable to the one presented by Reil [120] which is calibrated based on physical tests. Additionally, it is evident that the mechanical fasteners are responsible for the majority of the response, which reduces the risk related to inaccuracies in the modelling of the adhesive. Therefore, these validation results would indicate that the proposed partial virtual laboratory calibration approach is feasible.

6.5. Discussion and concluding remarks

Chapter 5 established that the issues with the meso-scale models propagate through the multi-scale calibration approach leading to similar discrepancies for the macro-scale models. It is shown in this chapter that using a rougher discretization of the adhesive layer in the virtual benchmark tests alleviates these issues. Further, the validation cases indicate that this approach produces results that are comparable to what is currently used in the

industry. The drawback of this approach is that some information is lost with the rougher discretization. This reduces the flexibility of the calibration procedure with respect to the influence of the joint configuration, which is one of the advantages of this method.

For future developments of this calibration approach, the meso-scale modelling strategy should preferably be altered such that a finer discretization could be used. However, there is an inherent problem with regards to a discrepancy between the geometry of the edge of the adhesive layer in a virtual model compared to their physical counterparts. This would suggest that using a more complex meso-scale model for the adhesive to account for changes in stress state and discretization is not a suitable approach. Instead, the current meso-scale adhesive model could be used with altered parameters. The method for altering the parameters would be considered future work.

A key aspect with respect to this partial virtual calibration approach is the cost of the method. Only three types of material tests are required to initialize the calibration procedure. These include a compression test, a tension test and a notched tension test, which are common material tests. In contrast, the industry standard typically requires a combination of material tests and more complex fracture mechanics tests to calibrate a macro-scale material model for an adhesive. It is evident that there is a significant cost saving potential with the proposed method. In its current state there is some uncertainty in the accuracy of the approach, although the validation tests suggest that it is satisfactory. However, this method could be very advantageous in the exploratory phase of a project, where the flexibility and cost of the method allows for exploration of a larger domain of solutions.

This chapter shows how to improve the previously presented partial virtual calibration approach, which in turn gives good results on the validation tests. Further, the key research question of the thesis is addressed implicitly through the study of the influence on the adherent properties on the calibrated macro-scale material parameters. While the influence of the adherents seems to be minor, the study suggests that it is not necessarily the material of the adherents that is causing this influence. Instead, the bending stiffness and ratio of bending stiffness between the two adherents seems to have a larger effect. Finally, the higher-level validation of this method on the hybrid benchmark and component tests illustrates the potential of the proposed method. Further conclusions with respect to the complete thesis are covered in Chapter 7.

Part IV.

Conclusion and outlook

7. Conclusions and outlook

7.1. Conclusions

The topic of multi-material joining is closely linked to adhesives as they are particularly suited for joining materials that behave differently. Two adhesives have been studied as a part of this thesis to illuminate this topic. A semi-structural two-component polyurethane adhesive, BETAFORCE 2816L (PU), was explored first as the behaviour was unknown when starting. Then, the structural toughened epoxy adhesive, SikaPower 498 (SP498), was studied in more detail as there are many numerical models already available for this adhesive. Together, these two adhesives are used in this thesis to build an experimental basis and a modelling strategy step by step from an unknown adhesive until a comprehensive modelling procedure. With the experimental basis and the modelling procedure generated, the characteristics of multi-material joints have been studied.

7.1.1. Studies on two-component polyurethane adhesive

In order to identify the behaviour of the PU adhesive, BETAFORCE 2816L, it was performed a series of tension tests at different strain-rates using two perpendicular cameras and a thermal camera to monitor the specimens. The two perpendicular cameras were used to facilitate digital image correlation (DIC), which gave field data for the deformation field exhibited by the specimens. Compression tests were also performed at different rates, including tests in a split Hopkinson pressure bar with strain-rates relevant for impact problems. These compression tests were also monitored with a similar setup as the tension tests, with a high-speed camera for the dynamic tests. A series of notched tension tests were run at quasi-static conditions in order to generate a validation case and to look closer at failure. Scanning electron microscopy images were taken of one of the fractured surfaces. Finally, single lap joint (SLJ) tests were performed in three different configurations. Two types of adherents were used in the different configurations, a carbon fibre reinforced polymer (CFRP) adherent with continuous fibres and a sheet mould compound (SMC) adherent. These SLJ tests were monitored using a high-resolution camera in combination with DIC to capture the strain field on the side of the adhesive layer.

From the experiments, the mechanical behaviour of the PU adhesive is seen to be rubber-like with large strains and no permanent deformations. This is fundamentally different from typical structural adhesives such as the toughened epoxy adhesive also studied in this thesis. The presented experimental campaign is seen to be sufficient in terms of characterizing the adhesive for meso-scale modelling. Although, additional experiments such as a bi-axial tension tests and a shear test would further strengthen the modelling strategy. The SLJ tests suggests that there is a coupling between the adhesive and the adherents which has to be accounted for when modelling these types of joints. This is due to the crack propagating from the adhesive and into the adherents in several of the tests.

Based on the experiments on the PU adhesive, several existing constitutive models were considered for meso-scale modelling of the adhesive. The Bergström-Boyce (BB) model was chosen as a baseline as it provided good results with relatively few parameters. Additionally, the BB model is based on micromechanical considerations with regards to deformation of rubbers, which increases the confidence in the modelling strategy for this adhesive. Further, a modified version of the BB model (BBmod) was implemented as a user subroutine in Abaqus. This modification added multiplicative strain-rate sensitivity to the BB model to better account for the observed behaviour. Both models were calibrated based on the tension tests and compression tests and then validated on the notched tension tests.

The results of these numerical studies suggest that the BB model is suitable for modelling the response of the PU adhesive. Further, the BBmod model is seen to provide a slight increase in accuracy at the cost of having to calibrate two additional parameters. However, this increase in accuracy is minor and it is expected given the two additional parameters used to obtain a better fit with the calibration data. A failure model in addition to benchmark tests and component tests are needed for further studies of this adhesive and macro-scale modelling.

7.1.2. Studies on toughened epoxy adhesive

The experimental basis for the studies of the SikaPower 498 (SP498) adhesive consisted of several types of bulk adhesive material tests, benchmark tests and component tests. All experiments with the exception of the bonded component tests were performed by Reil [120]. The material tests consisted of tension tests at varying strain-rates, compression tests and notched tension tests. Steel and aluminium sheets were used as adherents for the rest of the tests, always combining both to make the joints multi-material. Bonded cross tests were tested in a tension dominated mode, a shear dominated mode and a mixed mode. Two hat-profiles were bonded together along their flanges to create the bonded component test specimen which was tested in 3-point bending. For the hybrid joints, self-piercing rivets (SPR) were used in combination with adhesive bonding to generate a joint more relevant for industrial applications. Hybrid benchmark tests in the form of a single lap

joint (SLJ) and a typical peeling specimen were tested to represent simple benchmark case with a single SPR combined with adhesive. Two configurations of a hybrid component test were tested in 3-point bending. Both configurations consisted of two hat profiles bonded and riveted together along the top of the hat sections. However, the profiles had different geometry for the different configurations leading to different primary loading modes for the joints. In summary, these experiments provide a sufficient basis for calibration and validation of a multi-scale modelling approach.

Meso-scale modelling of the SP498 adhesive was done with a previously implemented polymer model which was calibrated based on the tension, compression and notched tension tests. This model was then validated against the bonded cross tests, hybrid SLJ tests, hybrid peel tests and bonded component tests. A partial virtual laboratory calibration procedure was developed, where the meso-scale polymer model was used to generate virtual benchmark tests. The responses of these virtual benchmark tests were then used as target curves to enable reverse engineering of material parameters for macroscopic models of the adhesive layer.

Three different macro-scale models were evaluated for modelling of the adhesive including MAT_240 as baseline, a modification of MAT_240 and a Gurson-based cohesive zone model (GCZM). The GCZM was implemented as a user subroutine in the LS-DYNA solver. All three models were calibrated using the proposed partial virtual laboratory and then validated against the bonded component tests. An adjustment to the discretization of the meso-scale models, by reducing the number of elements through the thickness of the adhesive layer, was proposed to improve the accuracy of the method. Based on this adjustment, new parameters were calibrated for the MAT_240 model. These were then validated against the bonded component tests, the hybrid benchmark tests and the hybrid component tests. Finally, a numerical study on the influence of the adherents on the macro-scale properties of the adhesive was performed.

Validation of the meso-scale modelling approach shows that it is gives reasonable results. However, the model seems to underestimate the response in shear as well as too early crack initiation and too fast crack propagation. These issues are alleviated by applying the previously mentioned adjustment. There is still a more fundamental problem with respect to the discrepancy in geometry between the virtual edges of the adhesive layers and physical ones which are subject to significant imperfections. This suggests that using more advanced meso-scale material models for the adhesive layer does not necessarily mean a better prediction of the physical response due to this fundamental issue. Therefore, it is recommended to make adjustments to a simple modelling approach than spending resources on more complex models.

MAT_240, MAT_240 modified and GCZM provide an almost identical response when validated against the bonded component tests. This is despite the three models having significantly different traction-separation laws. Based on these results, the calibration process seems to be critical in terms of obtaining good results on larger components.

As a consequence, the GCZM seems to be viable despite only requiring calibration of four parameters when using the proposed partial virtual calibration procedure. Another benefit with the GCZM is that it is not based on traditional fracture mechanics unlike typical cohesive zone models. The validation of the partial virtual laboratory calibration procedure shows that the method has the potential to produce results comparable to what is achieved with physical experiments. However, the procedure is seen to be dependent on the quality of the meso-scale modelling approach, which is still subject to some uncertainty.

The study regarding the influence of the adherents shows that there is generally a negligible effect, especially when considering the response on a component level. There are some outliers that suggest that the overall bending stiffness of the adherents as well as the ratio between the bending stiffness of the adherents have a noticeable impact. Specifically, the influence of using of two different materials in the different adherents seems to have a negligible effect on the macro-scale material parameters of the adhesive. However, it should be noted that these conclusions are sensitive to the parameters of the partial virtual calibration approach, such as the discretization on the meso-scale models. Therefore, the limitations of this approach have to explored further before making any final conclusions on the subject.

7.1.3. Concluding remarks

The results of this thesis suggest that having a multi-material joint does not seem to have a significant impact on the performance or modelling of the joint in general. Further, the bending properties of the adherents are seen to be more important than the material of the adherents with respect to the behaviour of the adhesive layer. There are also specific cases where the properties of the adherent may induce different failure modes in the adhesive layer, as observed with certain types of fibre reinforced polymers. However, further work regarding the methods used to obtain these observations are needed to make stronger conclusions on the matter.

Significant differences were found for the two adhesives studied in this work which would entail different modelling approaches for each of them. Based on the observations in this thesis, modelling of the toughened epoxy adhesive can be decoupled from the adherents. In contrast, the PU adhesive was seen interacting with the adherents during failure. A larger study outlining these interactions with respect to both adhesives and adherents is needed to further explore these interactions.

The partial virtual laboratory calibration procedure has shown great potential as it is able to produce comparable results to calibrations based on physical experiments. While it has a limited use in an academic context, the cost and time saving potential in an industrial context is significant. However, further research is required to eliminate the uncertainties present in the approach in its current form.

7.2. Suggestions for further work

A natural evolution of the partial virtual calibration procedure would be to include further phenomena known to govern the mechanical behaviour of an adhesive. One such effect could be accounted for by expanding the procedure to dynamic problems by including strain-rate sensitivity and potentially temperature in the models. These new procedures would also have to be validated, which would require significantly more complex experiments to be performed. Another phenomenon that is present for structural adhesives, such as the toughened epoxy in this thesis, is the ageing effect. This effect could be implemented for the meso-scale models, which would then propagate to the macro-scale models without having to perform complex experiments with ageing effects. Similar to the dynamic effects, this would have to be validated first, thus requiring relevant experiments in the research process.

As suggested in the concluding remarks, there are still uncertainties with respect to the limitations and generality of the work presented in this thesis. Therefore, it would be of interest to apply the presented methods to a larger range of adhesives and adherents. This would identify potential outliers and confirm whether the conclusions remain.

The final step for the partial virtual calibration procedure would be an industrial implementation. Further validation on the product level would be required before the method could be generally applied. Additionally, the different steps of the process would have to be refined. Particularly the user sensitive steps, such as the optimization component, would have to be improved before the method could be considered mature enough for industrial applications. Finally, recommendations for robust application of the virtual calibration procedure in an industrial environment would have to be made.

Bibliography

[1] D. Morin, Experiments and models until failure of bonded joints for crashworthiness, Thesis, Université de Valenciennes et du Hainaut-Cambrésis (2010).

[2] Multi-material space frame of the Audi A8, https://www.audi-mediacenter.com/de/fotos/album/leichtbau-240 (2019).

[3] K. Martinsen, S. J. Hu, B. E. Carlson, Joining of dissimilar materials, CIRP Annals - Manufacturing Technology 64 (2) (2015) 679–699. doi:10.1016/j.cirp.2015.05.006.

[4] J. D. Venables, Adhesion and durability of metal-polymer bonds, Journal of Materials Science 19 (8) (1984) 2431 – 2453. doi:10.1007/BF00550796.

[5] L. Dufour, B. Bourel, F. Lauro, G. Haugou, N. Leconte, A viscoelastic-viscoplastic model with non associative plasticity for the modelling of bonded joints at high strain rates, International Journal of Adhesion and Adhesives 70 (2016) 304–314. doi:10.1016/j.ijadhadh.2016.07.015.

[6] D. Morin, G. Haugou, B. Bennani, F. Lauro, Experimental characterization of a toughened epoxy adhesive under a large range of strain rates, Journal of Adhesion Science and Technology 25 (13) (2011) 1581–1602. doi:10.1163/016942410X524417.

[7] L. Goglio, L. Peroni, M. Peroni, M. Rossetto, High strain-rate compression and tension behaviour of an epoxy bi-component adhesive, International Journal of Adhesion and Adhesives 28 (7) (2008) 329–339. doi:10.1016/j.ijadhadh.2007.08.004.

[8] J. Johnsen, F. Grytten, O. S. Hopperstad, A. H. Clausen, Influence of strain rate and temperature on the mechanical behaviour of rubber-modified polypropylene and cross-linked polyethylene, Mechanics of Materials 114 (Supplement C) (2017) 40–56. doi:10.1016/j.mechmat.2017.07.003.

[9] D. Morin, G. Haugou, B. Bennani, F. Lauro, Identification of a new failure criterion

for toughened epoxy adhesive, Engineering Fracture Mechanics 77 (17) (2010) 3481–3500. doi:10.1016/j.engfracmech.2010.09.016.

[10] B. Duncan, G. Dean, Measurements and models for design with modern adhesives, International Journal of Adhesion and Adhesives 23 (2) (2003) 141–149. doi:10.1016/S0143-7496(03)00006-X.

[11] Z. Jia, G. Yuan, H.-l. Ma, D. Hui, K.-t. Lau, Tensile properties of a polymer-based adhesive at low temperature with different strain rates, Composites Part B: Engineering 87 (2016) 227–232. doi:10.1016/j.compositesb.2015.10.013.

[12] F. Lauro, B. Bennani, D. Morin, A. F. Epee, The seė method for determination of behaviour laws for strain rate dependent material: Application to polymer material, International Journal of Impact Engineering 37 (6) (2010) 715–722. doi:10.1016/j.ijimpeng.2009.11.007.

[13] F. Pierron, S. Avril, V. T. Tran, Extension of the virtual fields method to elasto-plastic material identification with cyclic loads and kinematic hardening, International Journal of Solids and Structures 47 (22) (2010) 2993–3010. doi:10.1016/j.ijsolstr.2010.06.022.

[14] D. Notta-Cuvier, B. Langrand, E. Markiewicz, F. Lauro, G. Portemont, Identification of johnson-cook's viscoplastic model parameters using the virtual fields method: Application to titanium alloy ti6al4v, Strain 49 (1) (2013) 22–45. doi:10.1111/str.12010.

[15] J. A. García, A. Chiminelli, B. García, M. Lizaranzu, M. A. Jiménez, Characterization and material model definition of toughened adhesives for finite element analysis, International Journal of Adhesion and Adhesives 31 (4) (2011) 182–192. doi:10.1016/j.ijadhadh.2010.12.006.

[16] M. Sasso, G. Palmieri, G. Chiappini, D. Amodio, Characterization of hyper-elastic rubber-like materials by biaxial and uniaxial stretching tests based on optical methods, Polymer Testing 27 (8) (2008) 995–1004. doi:10.1016/j.polymertesting.2008.09.001.

[17] H. Kolsky, An investigation of the mechanical properties of materials at very high rates of loading, Proceedings of the Physical Society. Section B 62 (11) (1949) 676.

[18] W. Chen, F. Lu, M. Cheng, Tension and compression tests of two polymers under quasi-static and dynamic loading, Polymer Testing 21 (2) (2002) 113–121. doi:10.1016/S0142-9418(01)00055-1.

[19] J. Shim, D. Mohr, Using split hopkinson pressure bars to perform large strain

compression tests on polyurea at low, intermediate and high strain rates, International Journal of Impact Engineering 36 (9) (2009) 1116–1127. doi:10.1016/j.ijimpeng.2008.12.010.

[20] V. Tarigopula, C. Albertini, M. Langseth, O. Hopperstad, A. Clausen, A hydropneumatic machine for intermediate strain-rates: Set-up, tests and numerical simulations, in: DYMAT-International Conference on the Mechanical and Physical Behaviour of Materials under Dynamic Loading, Vol. 1, EDP Sciences, 2009, pp. 381–387.

[21] L. F. M. Da Silva, D. A. Dillard, B. Blackman, R. D. Adams (Eds.), Testing Adhesive Joints: Best Practices, John Wiley & Sons, 2012. doi:10.1002/9783527647026.

[22] M. Hildebrand, Non-linear analysis and optimization of adhesively bonded single lap joints between fibre-reinforced plastics and metals, International Journal of Adhesion and Adhesives 14 (4) (1994) 261–267. doi:10.1016/0143-7496(94)90039-6.

[23] S. A. Nassar, K. Sakai, Effect of cyclic heat, humidity, and joining method on the static and dynamic performance of lightweight multimaterial single-lap joints, Journal of Manufacturing Science and Engineering, Transactions of the ASME 137 (5) (2015). doi:10.1115/1.4030080.

[24] R. H. Goudarzi, M. R. Khedmati, An experimental investigation of static load capacity of al-gfrp adhesively bonded single lap and double butt lap joints, Latin American Journal of Solids and Structures 12 (8) (2015) 1583–1594. doi:10.1590/1679-78251760.

[25] A. Ozel, B. Yazici, S. Akpinar, M. D. Aydin, Ş. Temiz, A study on the strength of adhesively bonded joints with different adherends, Composites Part B: Engineering 62 (2014) 167–174. doi:10.1016/j.compositesb.2014.03.001.

[26] G. Kelly, Quasi-static strength and fatigue life of hybrid (bonded/bolted) composite single-lap joints, Composite Structures 72 (1) (2006) 119–129. doi:10.1016/j.compstruct.2004.11.002.

[27] F. Lambiase, Mechanical behaviour of polymer-metal hybrid joints produced by clinching using different tools, Materials & Design 87 (2015) 606–618. doi:10.1016/j.matdes.2015.08.037.

[28] K. Zhao, L. R. Xu, Size effect of the adhesive bonding strengths of metal/polymer similar and dissimilar material joints, The Journal of Adhesion 91 (12) (2015) 978–991. doi:10.1080/00218464.2014.988328.

[29] A. Spaggiari, D. Castagnetti, E. Dragoni, Experimental tests on tubular bonded butt

specimens: Effect of relief grooves on tensile strength of the adhesive, Journal of Adhesion 88 (4-6) (2012) 499–512. doi:10.1080/00218464.2012.660831.

[30] J. K. Sønstabø, P. H. Holmstrom, D. Morin, M. Langseth, Macroscopic strength and failure properties of flow-drill screw connections, Journal of Materials Processing Technology 222 (2015) 1–12. doi:10.1016/j.jmatprotec.2015.02.031.

[31] L. Arcan, M. Arcan, I. M. Daniel, Sem fractography of pure and mixed-mode interlaminar fractures in graphite/epoxy composites, ASTM Special Technical Publication 948 (1987) 41–67. doi:10.1520/STP25614S.

[32] G. Stamoulis, N. Carrere, J. Y. Cognard, P. Davies, C. Badulescu, Investigating the fracture behavior of adhesively bonded metallic joints using the arcan fixture, International Journal of Adhesion and Adhesives 66 (2016) 147–159. doi:10.1016/j.ijadhadh.2016.01.001.

[33] J. Y. Cognard, P. Davies, B. Gineste, L. Sohier, Development of an improved adhesive test method for composite assembly design, Composites Science and Technology 65 (3-4) (2005) 359–368. doi:10.1016/j.compscitech.2004.09.008.

[34] X. Jiang, X. Qiang, H. Kolstein, F. Bijlaard, Analysis on adhesively-bonded joints of frp-steel composite bridge under combined loading: Arcan test study and numerical modeling, Polymers 8 (1) (2016). doi:10.3390/polym8010018.

[35] J. K. Sønstabø, D. Morin, M. Langseth, Static and dynamic testing and modelling of aluminium joints with flow-drill screw connections, International Journal of Impact Engineering 115 (2018) 58–75. doi:j.ijimpeng.2018.01.008.

[36] M. Adamvalli, V. Parameswaran, Dynamic strength of adhesive single lap joints at high temperature, International Journal of Adhesion and Adhesives 28 (6) (2008) 321–327. doi:10.1016/j.ijadhadh.2007.10.005.

[37] V. Srivastava, A. Shukla, V. Parameswaran, Experimental evaluation of the dynamic shear strength of adhesive-bonded lap joints, Journal of Testing and Evaluation 28 (6) (2000) 438–442. doi:10.1520/JTE12134J.

[38] M. May, O. Hesebeck, S. Marzi, W. Böhme, J. Lienhard, S. Kilchert, M. Brede, S. Hiermaier, Rate dependent behavior of crash-optimized adhesives - experimental characterization, model development, and simulation, Engineering Fracture Mechanics 133 (2015) 112–137. doi:10.1016/j.engfracmech.2014.11.006.

[39] R. Brefort, Characterisation and fe modelling of structural adhesive for high strain rate, Master's thesis, Université de Valenciennes (2011).

[40] A. Janin, A. Constantinescu, D. Weisz-Patrault, R. Neviere, M. Stackler, W. Albouy, An experimental technique for the characterization of adhesive joints under dynamic multiaxial loadings, Procedia Engineering 197 (Supplement C) (2017) 52–59. doi:10.1016/j.proeng.2017.08.081.

[41] T. Yokoyama, H. Shimizu, Evaluation of impact shear strength of adhesive joints with the split hopkinson bar, JSME International Journal Series A 41 (4) (1998) 503–509. doi:10.1299/jsmea.41.503.

[42] S. L. Raykhere, P. Kumar, R. K. Singh, V. Parameswaran, Dynamic shear strength of adhesive joints made of metallic and composite adherents, Materials & Design 31 (4) (2010) 2102–2109. doi:10.1016/j.matdes.2009.10.043.

[43] C. Sato, K. Ikegami, Strength of adhesively-bonded butt joints of tubes subjected to combined high-rate loads, The Journal of Adhesion 70 (1-2) (1999) 57–73. doi:10.1080/00218469908010487.

[44] L. Dufour, Caractérisation et modélisation du collage structural multi-matériaux sous sollicitation dynamique, Thesis, Université de Valenciennes et du Hainaut-Cambrésis (2017).

[45] L. Goglio, M. Rossetto, Impact rupture of structural adhesive joints under different stress combinations, International Journal of Impact Engineering 35 (7) (2008) 635–643. doi:10.1016/j.ijimpeng.2007.02.006.

[46] T. L. Anderson, Fracture mechanics: fundamentals and applications, CRC press, 2005. doi:10.1201/9781420058215.

[47] K. Hasegawa, A. D. Crocombe, F. Coppuck, D. Jewel, S. Maher, Characterising bonded joints with a thick and flexible adhesive layer - part 1: Fracture testing and behaviour, International Journal of Adhesion and Adhesives 63 (2015) 124–131. doi:10.1016/j.ijadhadh.2015.09.003.

[48] R. M. R. P. Fernandes, J. A. G. Chousal, M. F. S. F. de Moura, J. Xavier, Determination of cohesive laws of composite bonded joints under mode ii loading, Composites Part B: Engineering 52 (2013) 269–274. doi:10.1016/j.compositesb.2013.04.007.

[49] J. Simón, E. Johnson, D. Dillard, Characterizing dynamic fracture behavior of adhesive joints under quasi-static and impact loading, Journal of ASTM International 2 (7) (2005) 1–19. doi:10.1520/JAI12955.

[50] C. Sun, M. D. Thouless, A. M. Waas, J. A. Schroeder, P. D. Zavattieri, Rate effects in

mode-ii fracture of plastically deforming, adhesively bonded structures, International Journal of Fracture 156 (2) (2009) 111–128. doi:10.1007/s10704-009-9339-2.

[51] B. R. K. Blackman, A. J. Kinloch, F. S. Rodriguez-Sanchez, W. S. Teo, The fracture behaviour of adhesively-bonded composite joints: Effects of rate of test and mode of loading, International Journal of Solids and Structures 49 (13) (2012) 1434–1452. doi:10.1016/j.ijsolstr.2012.02.022.

[52] S. Oshima, H. Ishida, T. Kusaka, T. Takeda, Experimental characterization of dynamic crack growth behavior in cfrp adhesive interface, Advanced Composite Materials 27 (4) (2018) 397–411. doi:10.1080/09243046.2017.1401336.

[53] J. K. Sønstabø, D. Morin, M. Langseth, Macroscopic modelling of flow-drill screw connections in thin-walled aluminium structures, Thin-Walled Structures 105 (2016) 185 – 206. doi:10.1016/j.tws.2016.04.013.

[54] M. Clarke, M. Buckley, J. Broughton, A. Hutchinson, Characterisation and simulation of structural adhesives, in: 7th European LS-DYNA Conference, Salzburg, Austria, 2009.

[55] D. Morin, B. Bourel, B. Bennani, F. Lauro, D. Lesueur, A new cohesive element for structural bonding modelling under dynamic loading, International Journal of Impact Engineering 53 (2013) 94–105. doi:10.1016/j.ijimpeng.2012.02.003.

[56] T. Carlberger, U. Stigh, Dynamic testing and simulation of hybrid joined bi-material beam, Thin-Walled Structures 48 (8) (2010) 609–619. doi:10.1016/j.tws.2010.03.003.

[57] I. Lubowiecka, M. Rodríguez, E. Rodríguez, D. Martínez, Experimentation, material modelling and simulation of bonded joints with a flexible adhesive, International Journal of Adhesion and Adhesives 37 (2012) 56–64. doi:10.1016/j.ijadhadh.2012.01.010.

[58] S. Joannès, Mechanical characterisation and numerical tool for the design of structural adhesive joints, Theses, École Nationale Supérieure des Mines de Paris (Dec. 2007).
URL https://pastel.archives-ouvertes.fr/tel-00288527

[59] L. E. B. Dæhli, D. Morin, T. Børvik, O. S. Hopperstad, Influence of yield surface curvature on the macroscopic yielding and ductile failure of isotropic porous plastic materials, Journal of the Mechanics and Physics of Solids 107 (2017) 253 – 283. doi:10.1016/j.jmps.2017.07.009.

[60] M. Leuschner, F. Fritzen, J. A. W. van Dommelen, J. P. M. Hoefnagels, Potential-

based constitutive models for cohesive interfaces: Theory, implementation and examples, Composites Part B: Engineering 68 (2015) 38–50. doi:10.1016/j.compositesb.2014.08.024.

[61] M. I. Okereke, A. I. Akpoyomare, M. S. Bingley, Virtual testing of advanced composites, cellular materials and biomaterials: A review, Composites Part B: Engineering 60 (2014) 637–662. doi:10.1016/j.compositesb.2014.01.007.

[62] A. Hershey, The elasticity of an isotropic aggregate of anisotropic cubic crystals, Journal of Applied mechanics-transactions of the ASME 21 (3) (1954) 236–240.

[63] W. Hosford, A generalized isotropic yield criterion, Journal of Applied Mechanics 39 (2) (1972) 607–609. doi:10.1115/1.3422732.

[64] R. Hill, A theory of the yielding and plastic flow of anisotropic metals, Proceedings of the Royal Society of London. Series A. Mathematical and Physical Sciences 193 (1033) (1948) 281–297. doi:10.1098/rspa.1948.0045.

[65] F. Barlat, J. C. Brem, J. W. Yoon, K. Chung, R. E. Dick, D. J. Lege, F. Pourboghrat, S. H. Choi, E. Chu, Plane stress yield function for aluminum alloy sheetsâ€"part 1: theory, International Journal of Plasticity 19 (9) (2003) 1297–1319. doi:10.1016/S0749-6419(02)00019-0.

[66] A. L. Gurson, Continuum theory of ductile rupture by void nucleation and growth: Part I - Yield criteria and flow rules for porous ductile media, Journal of Engineering Materials and Technology 99 (1) (1977) 2–15. doi:10.1115/1.3443401.

[67] V. Tvergaard, Influence of voids on shear band instabilities under plane strain conditions, International Journal of Fracture 17 (4) (1981) 389–407. doi:10.1007/BF00036191.

[68] K. Nahshon, J. Hutchinson, Modification of the gurson model for shear failure, European Journal of Mechanics-A/Solids 27 (1) (2008) 1–17. doi:10.1016/j.euromechsol.2007.08.002.

[69] Livermore Software Technology Corporation, LS-DYNA Keyword User's Manual Volume II (2017).

[70] G. R. Johnson, W. H. Cook, Fracture characteristics of three metals subjected to various strains, strain rates, temperatures and pressures, Engineering Fracture Mechanics 21 (1) (1985) 31–48. doi:10.1016/0013-7944(85)90052-9.

[71] M. G. Cockcroft, D. J. Latham, Ductility and the workability of metals, J Inst Metals 96 (1) (1968) 33–39.

[72] M. Costas, D. Morin, O. S. Hopperstad, T. Børvik, M. Langseth, A through-thickness damage regularisation scheme for shell elements subjected to severe bending and membrane deformations, Journal of the Mechanics and Physics of Solids 123 (2019) 190 – 206, the N.A. Fleck 60th Anniversary Volume. doi:10.1016/j.jmps.2018.08.002.

[73] J. Lemaitre, A continuous damage mechanics model for ductile fracture, Journal of Engineering Materials and Technology 107 (1) (1985) 83–89. doi:10.1115/1.3225775.

[74] O. H. Yeoh, Some forms of the strain energy function for rubber, Rubber Chemistry and Technology 66 (5) (1993) 754–771. doi:10.5254/1.3538343.

[75] M. Mooney, A theory of large elastic deformation, Journal of applied physics 11 (9) (1940) 582–592.

[76] R. S. Rivlin, D. Saunders, Large elastic deformations of isotropic materials vii. experiments on the deformation of rubber, Philosophical Transactions of the Royal Society of London. Series A, Mathematical and Physical Sciences 243 (865) (1951) 251–288.

[77] L. Treloar, The elasticity of a network of long-chain molecules — II, Transactions of the Faraday Society 39 (1943) 241–246.

[78] R. W. Ogden, Non-linear elastic deformations, Courier Corporation, 1997.

[79] E. M. Arruda, M. C. Boyce, A three-dimensional constitutive model for the large stretch behavior of rubber elastic materials, Journal of the Mechanics and Physics of Solids 41 (2) (1993) 389–412. doi:10.1016/0022-5096(93)90013-6.

[80] M. Kaliske, G. Heinrich, An extended tube-model for rubber elasticity: Statistical-mechanical theory and finite element implementation, Rubber Chemistry and Technology 72 (4) (1999) 602–632. doi:10.5254/1.3538822.

[81] J. S. Bergström, Mechanics of Solid Polymers, William Andrew Publishing, 2015. doi:10.1016/C2013-0-15493-1.

[82] H. F. Brinson, L. C. Brinson, Polymer engineering science and viscoelasticity, Springer, 2015.

[83] H. Khajehsaeid, J. Arghavani, R. Naghdabadi, S. Sohrabpour, A visco-hyperelastic constitutive model for rubber-like materials: A rate-dependent relaxation time scheme, International Journal of Engineering Science 79 (Supplement C) (2014) 44–58. doi:10.1016/j.ijengsci.2014.03.001.

[84] J. S. Bergström, M. C. Boyce, Constitutive modeling of the large strain time-dependent behavior of elastomers, Journal of the Mechanics and Physics of Solids 46 (5) (1998) 931–954. doi:10.1016/S0022-5096(97)00075-6.

[85] K. Osnes, J. K. Holmen, O. S. Hopperstad, T. Børvik, Fracture and fragmentation of blast-loaded laminated glass: An experimental and numerical study, International Journal of Impact Engineering 132 (2019) 103334. doi:https://doi.org/10.1016/j.ijimpeng.2019.103334.

[86] B. Golaz, V. Michaud, J. A. E. Månson, Adhesion of thermoplastic polyurethane elastomer to galvanized steel, International Journal of Adhesion and Adhesives 31 (8) (2011) 805–815. doi:10.1016/j.ijadhadh.2011.07.009.

[87] R. Raghava, R. M. Caddell, G. S. Y. Yeh, The macroscopic yield behaviour of polymers, Journal of Materials Science 8 (2) (1973) 225–232. doi:10.1007/BF00550671.

[88] H. Y. Jeong, A new yield function and a hydrostatic stress-controlled void nucleation model for porous solids with pressure-sensitive matrices, International Journal of Solids and Structures 39 (5) (2002) 1385–1403. doi:10.1016/S0020-7683(01)00260-8.

[89] M. Polanco-Loria, A. H. Clausen, T. Berstad, O. S. Hopperstad, Constitutive model for thermoplastics with structural applications, International Journal of Impact Engineering 37 (12) (2010) 1207–1219. doi:10.1016/j.ijimpeng.2010.06.006.

[90] R. Balieu, F. Lauro, B. Bennani, R. Delille, T. Matsumoto, E. Mottola, A fully coupled elastoviscoplastic damage model at finite strains for mineral filled semi-crystalline polymer, International Journal of Plasticity 51 (2013) 241–270. doi:10.1016/j.ijplas.2013.05.002.

[91] M. F. S. F. de Moura, J. A. G. Chousal, Cohesive and continuum damage models applied to fracture characterization of bonded joints, International Journal of Mechanical Sciences 48 (5) (2006) 493–503. doi:10.1016/j.ijmecsci.2005.12.008.

[92] R. Balieu, F. Lauro, B. Bennani, T. Matsumoto, E. Mottola, Non-associated viscoplasticity coupled with an integral-type nonlocal damage model for mineral filled semi-crystalline polymers, Computers & Structures 134 (2014) 18–31. doi:10.1016/j.compstruc.2013.12.006.

[93] Livermore Software Technology Corporation, LS-DYNA Keyword User's Manual Volume I (2017).

[94] D. S. Dugdale, Yielding of steel sheets containing slits, Journal of the Mechanics and Physics of Solids 8 (2) (1960) 100–104. doi:10.1016/0022-5096(60)90013-2.

[95] A. Hillerborg, M. Modéer, P. E. Petersson, Analysis of crack formation and crack growth in concrete by means of fracture mechanics and finite elements, Cement and Concrete Research 6 (6) (1976) 773–781. doi:10.1016/0008-8846(76)90007-7.

[96] A. Needleman, A continuum model for void nucleation by inclusion debonding, Journal of applied mechanics 54 (3) (1987) 525–531. doi:10.1115/1.3173064.

[97] V. Tvergaard, Effect of fibre debonding in a whisker-reinforced metal, Materials Science and Engineering: A 125 (2) (1990) 203–213. doi:10.1016/0921-5093(90)90170-8.

[98] V. Tvergaard, J. W. Hutchinson, The relation between crack growth resistance and fracture process parameters in elastic-plastic solids, Journal of the Mechanics and Physics of Solids 40 (6) (1992) 1377–1397. doi:10.1016/0022-5096(92)90020-3.

[99] A. A. Zadpoor, J. Sinke, R. Benedictus, The mechanical behavior of adhesively bonded tailor-made blanks, International Journal of Adhesion and Adhesives 29 (5) (2009) 558–571. doi:10.1016/j.ijadhadh.2009.01.003.

[100] G. Alfano, M. Crisfield, Finite element interface models for the delamination analysis of laminated composites: mechanical and computational issues, International journal for numerical methods in engineering 50 (7) (2001) 1701–1736. doi:10.1002/nme.93.

[101] P. P. Camanho, C. G. Dávila, M. F. De Moura, Numerical simulation of mixed-mode progressive delamination in composite materials, Journal of Composite Materials 37 (16) (2003) 1415–1438. doi:10.1177/0021998303034505.

[102] G. P. Marques, R. D. S. G. Campilho, F. J. G. da Silva, R. D. F. Moreira, Adhesive selection for hybrid spot-welded/bonded single-lap joints: Experimentation and numerical analysis, Composites Part B: Engineering 84 (2016) 248–257. doi:10.1016/j.compositesb.2015.09.002.

[103] K. Hasegawa, A. D. Crocombe, F. Coppuck, D. Jewell, S. Maher, Characterising bonded joints with a thick and flexible adhesive layer. part 2: Modelling and prediction of structural joint responses, International Journal of Adhesion and Adhesives 63 (2015) 158–165. doi:10.1016/j.ijadhadh.2015.09.004.

[104] S. Marzi, O. Hesebeck, M. Brede, F. Kleiner, A rate-dependent, elasto-plastic cohe-

sive zone mixed-mode model for crash analysis of adhesively bonded joints, in: 7th European LS-DYNA conference, 2009.

[105] A. M. G. Pinto, A. G. Magalhães, R. D. S. G. Campilho, M. F. S. F. de Moura, A. P. M. Baptista, Single-lap joints of similar and dissimilar adherends bonded with an acrylic adhesive, The Journal of Adhesion 85 (6) (2009) 351–376. doi:10.1080/00218460902880313.

[106] D. Said Schicchi, A. Caggiano, A porous-based discontinuous model for ductile fracture in metals, Engineering Fracture Mechanics 138 (2015) 19–32. doi:10.1016/j.engfracmech.2015.03.008.

[107] NF T 76-142: Méthode de préparation de plaques d'adhésifs structuraux pour la réalisation d'éprouvettes d'essai de caractérisation (1988).

[108] ISO 37:2017(E): Rubber, vulcanized or thermoplastic — determination of tensile stress-strain properties (2017).

[109] E. Fagerholt, Field measurements in mechanical testing using close-range photogrammetry and digital image analysis, Ph.D. thesis, Norwegian University of Science and Technology (2012).

[110] NS-EN 1465: Adhesives - Determination of tensile lap-shear strength of bonded assemblies (2009).

[111] J. L. Halary, F. Lauprêtre, L. Monnerie, Polymer materials: macroscopic properties and molecular interpretations, John Wiley & Sons, 2011.

[112] Abaqus, Version 6.14. Dassault Systemès Simulia Corporation. Providence, Rhode Island, USA (2014).

[113] P. G. de Gennes, Reptation of a polymer chain in the presence of fixed obstacles, The Journal of Chemical Physics 55 (2) (1971) 572–579. doi:10.1063/1.1675789.

[114] H. Dal, M. Kaliske, Bergström–boyce model for nonlinear finite rubber viscoelasticity: theoretical aspects and algorithmic treatment for the fe method, Computational Mechanics 44 (6) (2009) 809–823. doi:10.1007/s00466-009-0407-2.

[115] R. Jedynak, Approximation of the inverse langevin function revisited, Rheologica Acta 54 (1) (2015) 29–39. doi:10.1007/s00397-014-0802-2.

[116] J. Johnsen, A. H. Clausen, F. Grytten, A. Benallal, O. S. Hopperstad, A thermo-elasto-viscoplastic constitutive model for polymers, Journal of the Mechanics and

Physics of Solids 124 (2019) 681–701. doi:https://doi.org/10.1016/j.jmps.2018.11.018.

[117] C. Miehe, Numerical computation of algorithmic (consistent) tangent moduli in large-strain computational inelasticity, Computer Methods in Applied Mechanics and Engineering 134 (3) (1996) 223–240. doi:https://doi.org/10.1016/0045-7825(96)01019-5.

[118] W. Sun, E. L. Chaikof, M. E. Levenston, Numerical approximation of tangent moduli for finite element implementations of nonlinear hyperelastic material models, Journal of Biomechanical Engineering 130 (6) (2008). doi:10.1115/1.2979872.

[119] J. F. Berntsen, D. Morin, A. H. Clausen, M. Langseth, Experimental investigation and numerical modelling of the mechanical response of a semi-structural polyurethane adhesive, International Journal of Adhesion and Adhesives 95 (2019) 102395. doi:10.1016/j.ijadhadh.2019.102395.

[120] M. Reil, Connections between steel and aluminium using adhesive bonding combined with self-piercing riveting: Testing, modelling and analysis, Ph.D. thesis, Norwegian University of Science and Technology (2019).

[121] D. Morin, T. Berstad, A. H. Clausen, O. S. Hopperstad, Macroscopic modelling of polymeric materials, in: 10th European LS-DYNA conference, 2015.

[122] J. F. Berntsen, D. Morin, A. H. Clausen, M. Langseth, Modelling of bonded component test - comparing mat_240 to state-of-the-art models, in: 12th European LS-DYNA conference, 2019.

[123] J. O. Hallquist, LS-DYNA theory manual, Livermore Software Technology Corporation (2006).

[124] V. Tvergaard, A. Needleman, Analysis of the cup-cone fracture in a round tensile bar, Acta Metallurgica 32 (1) (1984) 157 – 169. doi:10.1016/0001-6160(84)90213-X.

[125] N. Stander, W. Roux, T. Goel, T. Eggleston, K. Craig, LS-OPT User's manual, Livermore Software Technology Corporation (2010).

[126] D. Morin, M. Reil, T. Berstad, M. Costas, M. Langseth, Modelling of steel-aluminium components using structural adhesive and self-piercing rivets, in: 12th European LS-DYNA conference, 2019.

[127] A. G. Hanssen, L. Olovsson, R. Porcaro, M. Langseth, A large-scale finite element point-connector model for self-piercing rivet connections, European Journal of Me-

chanics - A/Solids 29 (4) (2010) 484–495. doi:10.1016/j.euromechsol.2010.02.010.